Dissertation
submitted to the
Combined Faculties for the Natural Sciences and for Mathematics
of the Ruperta-Carola University of Heidelberg, Germany
for the degree of
Doctor of Natural Sciences

presented by

Diplom-Physiker:	Markward Britsch
born in:	Lahr (Schwarzwald)

Oral examination: 15$^{\text{th}}$ of November 2006

Gravitational instability and fragmentation of self-gravitating accretion disks

Referees: Prof. Dr. Wolfgang J. Duschl
Prof. Dr. Burkhard Fuchs

Abstract

Gravitational instability and fragmentation of self-gravitating accretion disks — We know from observations that supermassive black holes (SMBH) of masses up to $10^{10}\,M_\odot$ existed in quasars when the universe was only about 10^9 years old. The rapid formation of SMBHs can be understood as the outcome of the collision of two large gas-rich galaxies followed by disk accretion. This model relies on a large enough turbulent viscosity in the disk. We show in a linear stability analysis of thin self-gravitating viscous disks that the gravitational instability can drive a turbulence generating the β-viscosity. For simulating a self-gravitating accretion disk in polar coordinates the hydrodynamics code NIRVANA2.0 is adapted for our needs which includes cooling. The results are disk fragmentation, strong accretion at the inner radial boundary of the calculation domain and strong outflow at the outer boundary which both come about by interactions between clumps. The accretion time scale for a disk mass of $6{\cdot}10^8\,M_\odot$ in a radial extent of 29 pc to 126 pc is about $1.2{\cdot}10^7$ a, corresponding to a viscosity parameter $\beta \approx 0.04$. We can confirm the β-viscosity interpretation by the turbulent velocity and length scale and by the scaling of the accretion time scale. All this supports the SMBH-formation model.

Zusammenfassung

Gravitationsinstabilität und Fragmentation von eigengravitierenden Akkretionsscheiben — Wir wissen von Beobachtungen, dass supermassereiche Schwarze Löcher (SMBH) mit Massen von bis zu $10^{10}\,M_\odot$ schon in Quasaren existierten als das Universum nur etwa 10^9 Jahre alt war. Das schnelle Entstehen der SMBHs kann als Produkt einer Kollision zwischen zwei großen gasreichen Galaxien mit anschließender Scheibenakkretion verstanden werden. Dieses Modell braucht eine turbulente Viskosität der Scheibe, die groß genug ist. Wir zeigen mittels einer linearen Stabilitätsanalyse für dünne eigengravitierende viskose Scheiben, dass die Gravitationsinstabilität eine Turbulenz antreiben kann, die die β-Viskosität erzeugt. Um eigengravitierende Akkretionsscheiben in Polarkoordinaten zu simulieren haben wir den Hydrodynamik Code NIRVANA2.0 für unsere Zwecke umgeändert, was auch Kühlung beinhaltet. Die Ergebnisse sind Scheibenfragmentation, starke Akkretion am radialen Innenrand und starker Ausfluss am Außenrand des Rechengebietes. Beides kommt durch Wechselwirkung zwischen Klumpen zustande. Die Akkretionszeitskala für Scheibenmassen von $6{\cdot}10^8\,M_\odot$ in radialer Ausdehnung von 29 pc bis 126 pc liegt bei etwa $1.2{\cdot}10^7$ a, was einem Viskositätsparameter $\beta \approx 0.04$ entspricht. Wir können die β-Viskositätsinterpretation durch die turbulente Geschwindigkeit und Längenskala, und dadurch wie die viskose Zeitskala skaliert, bestätigen. Dies alles stützt auch das SMBH-Entstehungsmodell.

Contents

List of Figures

List of Tables

Äneas mußte das Ende Didos, das sein Leichtsinn herbeigeführt hatte, obgleich ihm von den Göttern selbst geboten worden, sie zu verlassen, mit neuen Irrfahrten und wiederholten Unglücksfällen büßen. Ein Sturm verschlug ihn rückwärts nach Sizilien, wo er vom König Acestes, dessen Mutter eine Trojanerin war, gütig aufgenommen wurde und dem Schatten seines Vaters Anchises, welchen er ein Jahr zuvor bei Drepanum begraben hatte, bei der Wiederkehr dieses Tages herrliche Leichenspiele feierte.

Aus *Äneas* in *Sagen des Klassischen Altertums* von Gustav Schwab

Chapter 1

Introduction

It is amazing how much we can know about the distant past universe. With telescopes we can see light of objects for which it took it almost 13 billion years to reach us, that is more than 90 % of the age of the universe! It is also a wonder that we know the age of the universe and its cosmological parameters. Indeed partly we know these things because we see light that comes almost directly from the beginning of the universe itself when it was a mere few hundred thousand years old. It was the new technology of telescopes and space borne instruments that made these discoveries possible. But what is maybe even more amazing is that we already understand many of these things and how they work. Perhaps in the future we will understand them all. This is achieved mainly by theoretical studies (helped by the always growing computational power) like the present one but also by more observations and experiments. This thesis is an attempt to shed a little more light on the processes that build up quasars and on the process of disk accretion itself. Quasars are some of the most powerful and oldest objects in the cosmos that we know of, and disk accretion is not only the driver of these quasars but also responsible for the build up of completely different kinds of objects like stars or planets.

1.1 Quasars and cosmology

A short introduction to cosmology can be found, *e.g.*, in Unsöld and Baschek (2002) or with more detail (although without the particle physics) in any book about General Relativity like Fliessbach (1995). From observations we know today that the further a galaxy is away from us the more the wavelengths of lines and other features in the electromagnetic spectrum are shifted to longer wavelengths. This is called redshift z, or cosmological redshift in this context, defined by

$$z = \frac{\Delta\lambda}{\lambda_0} = \frac{\lambda - \lambda_0}{\lambda_0}, \tag{1.1}$$

where λ_0 is the wavelength of the line or feature measured in the laboratory, and λ the wavelength in the spectrum of the galaxy. This is interpreted in a way that space itself is expanding with the current rate $H_0 = \dot{R}_0 \cdot R_0^{-1}$ (where R_0 is the

current scalelength of the universe) such that for $z \ll 1$

$$z = \frac{H_0 r}{c}. \tag{1.2}$$

Here r is the distance to the galaxy, $c = 2.9979{\cdot}10^8\,\mathrm{m\,s^{-1}}$, the speed of light, and H_0 is called the Hubble constant. This also means that any cosmological redshift corresponds to a well defined time after the Big Bang, *i.e.*, the hot beginning of the universe. The theory of General Relativity with some additional assumptions like isotropy of the universe leads directly to a description of it, leaving only a few parameters to be measured. When these parameters are fixed, the cosmological evolution is fixed, too. Mainly from measurements of the cosmic microwave background (CMB) (Spergel et al. (2006) where references to other cosmological measurements can be found also) and supernovae of type Ia we can fix the cosmological parameters of our universe pretty tightly today. The CMB is interpreted as the reminder of the Big Bang[1], while supernovae Ia are huge explosions in galaxies that can be used as a kind of standard candle (*i.e.*, they have, after a well defined simple correction, intrinsically the same brightness, see, *e.g.*, Riess et al. 2005). From this data follows not only that the universe has a flat, *i.e.*, of Euclidean geometry, but also that its expansion is accelerated. Its age is measured to be $13.73^{+0.13}_{-0.17}$ Ga and $H_0 = 74 \pm 3\,\mathrm{Mpc^{-1}\,km\,s^{-1}}$. These measurements also tell us that the energy density of the universe consists of about 72 % dark energy, 24 % dark matter and only 4 % ordinary matter also called baryonic matter. Up to now it is not clear what the dark energy is; and there is no consensus about what dark matter is, but we know that it is not baryonic, and it could be well explained by yet undetected heavy elementary particles.

General Relativity can also describe the objects that will be important in the next paragraph, *i.e.*, black holes (BHs). These are objects of extreme density such that not even light can escape their gravitational field. Their size is one Schwarzschild Radius

$$R_\mathrm{S} = \frac{2GM}{c^2} \approx 3\,\mathrm{km}\frac{M}{\mathrm{M}_\odot}, \tag{1.3}$$

where $G = 6.6742{\cdot}10^{-11}\,\mathrm{m^3\,kg^{-1}\,s^{-2}}$ is the gravitational constant, $\mathrm{M}_\odot = 1.99{\cdot}10^{30}$ kg is the solar mass, and M is the mass of the object. For non-rotating black holes, a sphere of radius R_S is the event horizon, *i.e.*, the surface beyond which nothing can escape the gravity of the BH. For rotating BHs, the event horizon becomes a prolate ellipsoid with R_s being its semi-major axis.

Quasars are point like sources, mainly of high redshift and as far as we know today, intrinsically extremely bright extra galactic objects. It is now a well accepted model that they are just the most powerful active galactic nuclei (AGN) known (see, *e.g.*, Antonucci, 1993) and as such harbor a supermassive black hole (SMBH), *i.e.*, a BH with a mass of more than $10^6\,\mathrm{M}_\odot$. AGNs are centers of galaxies with unusual spectral properties often containing strong radiation from different spectral regions like the radio, visible or X-rays. They often have a

[1]The Microwave Background is a relic of the recombination (combination rather) of the electrons with the protons to neutral hydrogen when the universe cooled down to about 3000 K at $z = 1100$, and thus it became transparent for electromagnetic radiation. Today the temperature of this radiation is about 2.7 K due to redshift.

bright core with jets coming out of it that sometimes lead to huge lobes of radio emission. The extreme luminosity of quasars of up to almost 10^{41} W (see, *e.g.*, Vestergaard, 2004) is thought to come about by accretion of matter onto the SMBH probably with a conversion factor of radiated energy to rest mass energy of around 0.1 (Frank et al., 2002). There are now quasars known with redshifts of $z > 6$, especially one of $z = 6.4$ corresponding to a time when the universe was only about 840 Ma old, having a SMBH mass of more than $10^9\,\mathrm{M}_\odot$ as inferred by Barth et al. (2003). More masses of high redshift SMBHs can be found in Vestergaard (2004) and are mostly of the same order of magnitude. The masses of SMBHs with low redshift can be inferred from line widths applying the virial theorem. The distance of the region where the emission lines are produced to the center can be estimated by the time difference of the variability in the continuum directly seen from the central source and the variability in the emission lines. From such measurements a heuristic relation is established between the size of the so called broad line region (a region from which the atomic lines have a large width) and the intrinsic luminosity of the AGN. This in turn is used to get masses of high redshift quasars. We also know from X-ray observation (Hasinger et al., 2005) that against naive expectations the large SMBHs formed much faster than the small ones. This is called anti-hierarchic growth. So how can these objects accrete so much mass in such a small period of time, and why is the growth anti-hierarchical? There are some models proposed to solve this puzzle, see, *e.g.* Duschl and Strittmatter (2006) or Begelman et al. (2006) for recent ones. Both models involve an accretion disk in some way.

1.2 Accretion disks

Accretion disks are very common in the universe. They are directly observed not only around AGNs like in Fathi et al. (2006), but also around other types of objects among which are forming stars (O'dell et al., 1993). They are indirectly inferred in the case of cataclysmic variables (CVs) (Frank et al., 2002), which are double star systems where one star is a white dwarf accreting material from its companion. Disks always seem to come about in the case of accretion. The reason is that the accreted material cannot get rid of all its angular momentum. The effective Newtonian potential in the two body system is given by (see, *e.g.*, Kuypers, 1997)

$$U_{\mathrm{eff}} = -\frac{Gm_1m_2}{r} + \frac{p_\varphi}{2mr^2}, \tag{1.4}$$

where r is the distance between the two bodies with masses m_1 and m_2, m is the reduced mass $m = m_1m_2 \cdot (m_1 + m_2)^{-1}$ (which is approximately the mass of the minor body) and p_φ is the conserved third component of the angular momentum. From Equation (1.4) it is obvious that the effective potential becomes positive infinity as $r \to 0$ which means that no particle with non-zero angular momentum can get to the center, and thus it must lose all its angular momentum to be accreted. This is not true in general if the potential falls off at least as steep as $\Phi \propto R^{-2}$ which is true for the General Relativistic potential very close to a black hole. In the direction parallel to the angular momentum vector, on the other

hand the material can collapse, which is the reason that the material forms a flat disk with the disk axis aligned with the angular momentum vector.

The theory of accretion disks can be found, *e.g.*, in Frank et al. (2002) or Pringle (1981). The main and still open question is the viscosity which gives rise to accretion by redistributing the angular momentum. What happens is that due to the viscosity some material loses its angular momentum and thus can be accreted. Some other material on the other hand takes up this angular momentum and gains distance to the center. But in the end most of the mass gets accreted and only a small fraction of the mass gains all the angular momentum and is lost for the accretion process. The usual molecular viscosity is far too small giving time scales longer than the age of the universe in almost all astrophysical situations. The standard viscosity in disks is the so called α-viscosity by Shakura and Sunyaev (1973) which is a heuristic ansatz. It is thought to come about by turbulence although at the time it was proposed there was no instability known in disks that could drive the turbulence. But in the meantime a magneto-hydrodynamic instability was found in the case of slightly ionized non-self-gravitating disks by the magneto rotational instability (MRI) of Balbus and Hawley (1991) that drives the turbulence and generates the α-viscosity. But as will be shown in the next section, this viscosity prescription might not fit all kinds of accretion disks.

1.3 A model for supermassive black hole formation

This model is described in Duschl and Strittmatter (2006). As we know from simulations, see, *e.g.*, Barnes and Hernquist (1996), Barnes and Hernquist (1998) and Barnes (2002), in a major merger of two gas rich galaxies a large fraction of the gas – which can be more than $10^9\,\mathrm{M}_\odot$ – is collected in the central few 100 pc of the merger and can form a disk. This takes place in a few hundred Ma. Similar massive disks are found around AGNs as in Scoville (1999), and there is observational evidence that there is a connection between galaxy interactions, indicated by the morphology of the galaxies, and AGNs (see *e.g.*, Veilleux et al. (2006) and references therein). The idea is now that the gas forms an accretion disk which transports the gas into the very center to form and then feed the black hole. The problem with this scenario is that the time scale of the α-viscosity is too large to do the job. Since in addition to the time scale problem Duschl et al. (2000) and independently Richard and Zahn (1999) found a principle problem to describe self-gravitating disks – *i.e.*, disks in which the gravitational potential of the disk is not negligible – using the α-viscosity, they proposed the so called β-viscosity which turns out to have the right time scale. It is also thought to be a turbulent viscosity. In addition the anti-hierarchic growth of the SMBHs comes about naturally in this model. There are still two major issues. One is that it is not clear whether star formation in a massive and thus probably gravitationally unstable disk is not effective enough to strongly deplete the gas in the disk and thus slow down accretion. The other one is that the nature of the instability driving the turbulence by which the viscosity comes about is still unclear. These two issues will be addressed in this work by linear stability analysis as well as by

two dimensional hydrodynamic simulations of a self-gravitating disk.

1.4 Layout of the thesis

After an introduction to the necessary theoretical basics in Chapter 2, Chapter 3 will deal with the gravitational instability of α- and β-disks using linear stability theory. This will lead to a new route to β-viscosity via turbulence driven by gravitational instability. In Chapter 4 the changes to the NIRVANA2.0 code that is used for this work are presented and tested. Then in Chapter 5 the code with the changes as a whole is tested for different numerical parameters. Chapter 6 then presents the simulations done and their results. We will see in this chapter that there is a strong accretion due to clump-clump interactions in the inner part of the disk while the same mechanism leads to a strong outflow at the outer part. In the discussion in Chapter 7 we show that this accretion takes place independently of all physical or numerical parameters tested and is well described by the β-viscosity that comes about by gravitational instability. The thesis closes with conclusions and outlook in Chapter 8.

Chapter 2

Theoretical basics

In this chapter the theoretical background necessary for this work will be presented. This includes the basics of fluid dynamics, also called hydrodynamics, the theory of accretion disks and its viscosities as well as theory and recent numerical work on the gravitational instability of accretion disks. Since cooling is important for the instability of disks, it will be discussed, too. The chapter closes with a section about numerics.

2.1 Hydrodynamics equations

An introduction to the theory of hydrodynamics can, *e.g.*, be found in Landau and Lifshitz (1959). The main equations of hydrodynamics are the conservation equations for mass (called the continuity equation), momentum (the Navier-Stokes equation) and the energy (conservation) equation. These are partial differential equations although they can be derived from an integral formulation that is more general as it circumvents the problem of discontinuities at which the differential equations become mathematically undefined. For brevity we will show here how the continuity equation is derived and only state the other equations since the way to derive these is then similar. Only the viscosity term will be examined more closely.

We start with the conservation of mass within any simply connected time independent volume V_0 with an oriented surface ∂V_0, where we postulate that there are no sources or sinks of mass

$$\frac{\mathrm{d}m}{\mathrm{d}t} = \frac{\partial m}{\partial t} = \oint\limits_{\partial V_0} (\rho\vec{v}) \cdot \mathrm{d}\vec{A}. \tag{2.1}$$

Here t is time, m is the mass in V_0, ρ is the mass density of the fluid and $\vec{v}$ is the velocity vector of the flow. $\vec{j} = \rho\vec{v}$ is the mass current density as well as the momentum density. Using the definition of the density we have $m = \int_{V_0} \rho \mathrm{d}V$ on the left hand side and use Gauss's law on the right hand side of Equation (2.1), so we get

$$\frac{\partial}{\partial t} \int\limits_{V_0} \rho \mathrm{d}V = \int\limits_{V_0} \vec{\nabla} \cdot (\rho\vec{v}) \mathrm{d}V, \tag{2.2}$$

or, since this must be true for all volumes V_0,

$$\frac{\partial \rho}{\partial t} = \vec{\nabla} \cdot (\rho \vec{v}). \tag{2.3}$$

This is the continuity equation. The Navier-Stokes equation then is

$$\frac{\partial \rho \vec{v}}{\partial t} = -\vec{\nabla} \cdot (\rho \vec{v} \vec{v}) - \vec{\nabla} P + \vec{\nabla} \cdot \tilde{\sigma} - \rho \vec{\nabla} \Phi, \tag{2.4}$$

which is, using Equation (2.3), equivalent to

$$\rho \frac{\partial \vec{v}}{\partial t} = -\rho (\vec{v} \cdot \vec{\nabla}) \vec{v} - \vec{\nabla} P + \vec{\nabla} \cdot \tilde{\sigma} - \rho \vec{\nabla} \Phi. \tag{2.5}$$

Here $\vec{v}\vec{v}$ is the dyadic product of the velocity with itself (which is in Cartesian coordinates defined as the tensor $v_i v_j$), P is the pressure, $\tilde{\sigma}$ is the viscous stress tensor and Φ is the gravitational potential. In Equation (2.4) the first term on the right hand side is the so called advection term that comes about simply due to the movement of the fluid. The second term is the pressure term and the third is the viscous term examined in more detail below. Without the viscous term Equation (2.4) or (2.5) is called the Euler equation. The last term is the gravitational acceleration. The energy equation reads

$$\frac{\partial \tilde{e}}{\partial t} = -\vec{\nabla} \cdot (\tilde{e} \vec{v}) - P \vec{\nabla} \cdot \vec{v} + \tilde{\sigma} : \vec{\nabla} \vec{v} + \vec{\nabla} \cdot (\tilde{\kappa} \vec{\nabla} T), \tag{2.6}$$

where $\tilde{e}$ is the internal energy density, the colon (:) denotes the tensor contraction (which in Cartesian coordinates is defined by $\mathcal{A} : \mathcal{B} := \mathcal{A}_{ij} \mathcal{B}_{ij}$), $\tilde{\kappa}$ is the thermal conductivity and T is the temperature. The last term, *i.e.*, the thermal conduction term, is not used in this work and is only stated for completeness. The first term on the right hand side is again the advection term, the second is the volume work $W = P \mathrm{d}V$ and the third is the heating term due to viscous dissipation. In addition to these terms there can be a sink term for radiative cooling as described later in Sections 2.6 and 4.6.1.

The viscous terms in Equation (2.4) and Equation (2.6) can only be inferred if we make some postulates about the nature of viscosity. Since we define viscosity to act only when there is a fluid element moving relative to a neighboring fluid element, $\tilde{\sigma}$ must be a function of the space derivatives of the velocity. We postulate that the viscosity is small, thus all higher-order derivatives and all non-linear terms must be zero. Constant terms (in $\frac{\partial v_i}{\partial x_k}$, where the indices indicate one of the three components) must also vanish to give $\tilde{\sigma} = 0$ for $\vec{v} =$ constant. Then we require the viscosity to be zero for rigid rotation. All this leads to the form of the viscous stress tensor in Cartesian coordinates

$$\tilde{\sigma}_{ij} = \tilde{\eta} \left(\frac{\partial v_i}{\partial x_k} + \frac{\partial v_k}{\partial x_i} - \frac{2}{3} \delta_{ik} \frac{\partial v_l}{\partial x_l} \right) + \tilde{\zeta} \delta_{ik} \frac{\partial v_l}{\partial x_l} \tag{2.7}$$

where δ_{ik} is the Kronecker delta. Here the Einstein sum convention has been used, *i.e.*, all indices of which happen to be more than one in the same product are summed over from 1 to the number of dimensions, *i.e.*, 3 in this case. $\tilde{\eta}$ and

$\tilde{\zeta}$ are scalars that can be shown to be positive. They are called first and second viscosity or shear and bulk viscosity, respectively. They are called the dynamic viscosities and the combinations

$$\nu = \frac{\tilde{\eta}}{\rho} \quad \text{and} \quad \xi = \frac{\tilde{\zeta}}{\rho} \tag{2.8}$$

are called the kinematic viscosities. The shear viscosity is well examined but the bulk viscosity, since it vanishes for incompressible fluids, is not known so well. Thus under many circumstances like in the accretion disk theory the bulk viscosity is neglected.

In our case the equations of motion will be used in cylindrical coordinates $\{R, \varphi, z\}$ in which the continuity equation becomes

$$\frac{\partial \rho}{\partial t} + \frac{1}{R}\frac{\partial}{\partial R}(\rho v_R R) + \frac{1}{R}\frac{\partial}{\partial \varphi}(\rho v_\varphi) + \frac{\partial}{\partial z}(\rho v_z) = 0. \tag{2.9}$$

The viscous stress tensor using only shear viscosity gets

$$\tilde{\sigma}_{RR} = 2\tilde{\eta}\left(\frac{2}{3}\frac{\partial v_R}{\partial R} - \frac{1}{3}\left(\frac{1}{R}\frac{\partial v_\varphi}{\partial \varphi} + \frac{\partial v_R}{\partial R} + \frac{\partial v_z}{\partial z}\right)\right), \tag{2.10}$$

$$\tilde{\sigma}_{\varphi\varphi} = 2\tilde{\eta}\left(\frac{2}{3}\left(\frac{1}{R}\frac{\partial v_\varphi}{\partial \varphi} + \frac{\partial v_R}{\partial R}\right) - \frac{1}{3}\left(\frac{\partial v_R}{\partial R} + \frac{\partial v_z}{\partial z}\right)\right), \tag{2.11}$$

$$\tilde{\sigma}_{zz} = 2\tilde{\eta}\left(\frac{2}{3}\frac{\partial v_z}{\partial z} - \frac{1}{3}\left(\frac{\partial v_R}{\partial R} + \frac{1}{R}\frac{\partial v_\varphi}{\partial \varphi} + \frac{\partial v_R}{\partial R}\right)\right), \tag{2.12}$$

$$\tilde{\sigma}_{R\varphi} = \tilde{\sigma}_{\varphi R} = \tilde{\eta}\left(\frac{\partial v_\varphi}{\partial R} - \frac{v_\varphi}{R} + \frac{1}{R}\frac{\partial v_R}{\partial \varphi}\right), \tag{2.13}$$

$$\tilde{\sigma}_{Rz} = \tilde{\sigma}_{zR} = \tilde{\eta}\left(\frac{\partial v_R}{\partial z} + \frac{\partial v_z}{\partial R}\right), \tag{2.14}$$

$$\tilde{\sigma}_{z\varphi} = \tilde{\sigma}_{\varphi z} = \tilde{\eta}\left(\frac{1}{R}\frac{\partial v_z}{\partial \varphi} + \frac{\partial v_\varphi}{\partial z}\right). \tag{2.15}$$

This as well as the following relations for the derivatives in cylindrical coordinates can be found, *e.g.*, in Spurk (1996). The gradient of a scalar Φ becomes

$$\vec{\nabla}\Phi = \frac{\partial \Phi}{\partial R}\vec{e}_R + \frac{1}{R}\frac{\partial \Phi}{\partial \varphi}\vec{e}_\varphi + \frac{\partial \Phi}{\partial z}\vec{e}_z, \tag{2.16}$$

where $\vec{e}_i$ is the unity vector in the i-direction. The divergence of a vector $\vec{v}$ becomes

$$\vec{\nabla} \cdot \vec{v} = \frac{1}{R}\left(\frac{\partial (v_R R)}{\partial R} + \frac{\partial v_\varphi}{\partial \varphi} + \frac{\partial (v_z R)}{\partial z}\right), \tag{2.17}$$

and the divergence of a tensor σ then is given by

$$\begin{aligned}\vec{\nabla} \cdot \sigma = &\left(\frac{1}{R}\frac{\partial (\sigma_{RR} R)}{\partial R} + \frac{1}{R}\frac{\partial \sigma_{\varphi R}}{\partial \varphi} + \frac{\partial \sigma_{zR}}{\partial z} - \frac{\sigma_{\varphi\varphi}}{R}\right)\vec{e}_R + \\ &+ \left(\frac{1}{R}\frac{\partial (\sigma_{R\varphi} R)}{\partial R} + \frac{1}{R}\frac{\partial \sigma_{\varphi\varphi}}{\partial \varphi} + \frac{\partial \sigma_{z\varphi}}{\partial z} + \frac{\sigma_{R\varphi}}{R}\right)\vec{e}_\varphi + \\ &+ \left(\frac{1}{R}\frac{\partial (\sigma_{Rz} R)}{\partial R} + \frac{1}{R}\frac{\partial \sigma_{\varphi z}}{\partial \varphi} + \frac{\partial \sigma_{zz}}{\partial z}\right)\vec{e}_z.\end{aligned} \tag{2.18}$$

There is still an equation missing that establishes the thermodynamics. We are using the ideal gas law

$$P = \frac{\rho \mathcal{R} T}{\mu}, \tag{2.19}$$

where $\mathcal{R} = 8.3145\,\mathrm{J\,mol^{-1}\,K^{-1}}$ is the universal gas constant and μ the mean molar mass. Using the formula for the kinetic energy per molecule

$$E = \frac{f}{2} k_\mathrm{B} T, \tag{2.20}$$

where $k_\mathrm{B} = N_\mathrm{A}\mathcal{R}$ is the Boltzmann constant, $N_\mathrm{A} = 6.0221{\cdot}10^{23}\,\mathrm{mol^{-1}}$ is the Avogadro number and f is the number of degrees of freedom of the molecules, we get to the relation

$$P = (\gamma - 1)\tilde{e}. \tag{2.21}$$

γ is the ratio of the specific heats that in this context comes about by the relation $\gamma = (f+2)\cdot f^{-1}$.

2.2 Accretion disk equations

Here the one dimensional accretion disk equations for thin disks in non-self-gravitating disks are presented. They are described, *e.g.*, in Frank et al. (2002) or Pringle (1981) although for their derivation we will proceed in a different way described in Illenseer (2002).

2.2.1 The time-dependent equations

The idea is to describe accretion in a thin disk using Equations (2.3) to (2.6) and only using the radial direction. This works only if the disk is azimuthally symmetric so all dependence on the φ-direction can be neglected, *i.e.*, $\frac{\partial \cdot}{\partial \varphi} = 0$. The equations are then all integrated over z from negative infinity to infinity and the height of the disk h, as defined later, is used where necessary. Derivatives with respect to z usually can be dropped since they become boundary terms under the integral, and we expect all variables to be zero at infinity. So we get

$$\Sigma := \int_{-\infty}^{+\infty} \rho(z)\mathrm{d}z \tag{2.22}$$

as the surface density. The velocities are usually thought not to change with z. Thus Equation (2.9) can be integrated over z and using the above mentioned simplifications, we get

$$\frac{\partial \Sigma}{\partial t} + \frac{1}{R}\frac{\partial}{\partial R}(\Sigma v_R R) = 0. \tag{2.23}$$

The angular momentum equation can be derived from the φ-component of Equation (2.4) using Equations (2.13) and (2.18) and using the above mentioned simplifications (including the skipping of terms that will become zero when integrating over z anyway). With the abbreviation $\mathcal{T}_{ij} = \sigma_{ij} - \rho v_i v_j$, we get

$$\frac{\partial(\rho v_\varphi)}{\partial t} = \frac{1}{R}\frac{\partial(\mathcal{T}_{R\varphi} R)}{\partial R} + \frac{\mathcal{T}_{R\varphi}}{R} = \frac{1}{R^2}\frac{\partial}{\partial R}(R^2 \mathcal{T}_{R\varphi}), \tag{2.24}$$

or after integration

$$\frac{\partial(\Sigma v_\varphi)}{\partial t} = -\frac{1}{R^2}\frac{\partial}{\partial R}\left(R^2\Sigma\Big(-\nu\Big(\frac{\partial v_\varphi}{\partial R} - \frac{v_\varphi}{R}\Big) + v_\varphi v_R\Big)\right) \tag{2.25}$$

or

$$R^2\frac{\partial}{\partial t}(\Sigma v_\varphi) + \frac{\partial}{\partial R}(R^2\Sigma v_\varphi v_R) = \frac{\partial}{\partial R}\left(\Sigma\nu\ R^3\frac{\partial}{\partial R}\Big(\frac{v_\varphi}{R}\Big)\right). \tag{2.26}$$

Next, under the assumption of a fixed gravitational potential, *i.e.*, that $\frac{\partial v_\varphi}{\partial t} = 0$, we write the left hand side as

$$R^2 v_\varphi\frac{\partial\Sigma}{\partial t} + Rv_\varphi\frac{\partial}{\partial R}(R\Sigma v_R) + R\Sigma v_R\frac{\partial}{\partial R}(Rv_\varphi) = R\Sigma v_R\frac{\partial}{\partial R}(Rv_\varphi) \tag{2.27}$$

using Equation (2.23). Differentiating Equation (2.26) with respect to R and again using (2.23) we get to

$$\frac{\partial\Sigma}{\partial t} = -\frac{1}{R}\frac{\partial}{\partial R}\left[\frac{1}{\frac{\partial}{\partial R}(Rv_\varphi)}\frac{\partial}{\partial R}\left(\Sigma\nu R^3\frac{\partial}{\partial R}\Big(\frac{v_\varphi}{R}\Big)\right)\right]. \tag{2.28}$$

This is the one dimensional time evolution equation for thin disks in fixed gravitational potentials. For completeness it shall be mentioned that this can be simplified more for non-self-gravitating disks by inserting the Keplerian velocity, neglecting pressure gradients in the centrifugal equilibrium,

$$v_\varphi \approx v_\mathrm{K} := \sqrt{\frac{GM_*}{R}}. \tag{2.29}$$

M_* is the mass of the central object.

For an order of magnitude estimate we set $\partial\Sigma \sim \Sigma$, $\partial t \sim t_\nu$ and $\partial R \sim R$, where t_ν is the viscous time scale, and get

$$\frac{\Sigma}{t_\nu} = \frac{\Sigma\nu}{R^2} \quad \Rightarrow \quad t_\nu = \frac{R^2}{\nu}, \tag{2.30}$$

from (2.28). The viscous time scale gives us an estimate on how fast the accretion takes place. Since (2.28) has the form of a diffusion equation the distance at which a perturbation has an influence is $\propto \sqrt{t}$, thus the R^2 dependence in (2.30).

2.2.2 The equations for stationary disks

We are now examining the time-independent disks, *i.e.*, we set all terms $\frac{\partial\cdot}{\partial t} = 0$. From Equation (2.23) we get directly

$$R\Sigma v_R = \text{constant} =: -\frac{\dot{M}}{2\pi}, \tag{2.31}$$

with the constant mass accretion rate $\dot{M}$ which is defined to be positive for accretion.

On the other hand integrating the angular momentum equation in the form of Equation (2.26) (without the time derivative), using an integration constant $\frac{C}{2\pi}$, and the angular velocity $\Omega := \frac{v_\varphi}{R}$, we get

$$\Sigma\nu R^3\frac{\partial\Omega}{\partial R} = \frac{C}{2\pi} - R^2\Sigma v_\varphi v_R \tag{2.32}$$

or

$$\nu\Sigma = \left(\frac{\partial\Omega}{\partial R}\right)^{-1}\left(\frac{C}{2\pi R^3} - \frac{\dot{M}\Omega}{2\pi R}\right), \tag{2.33}$$

where (2.31) has been used. The integration constant $\frac{C}{2\pi}$ is determined by the boundary conditions at the inner rim of the disk R_i since its influence vanishes for large R with respect to the other term. This term should be negligible for $R \gg R_\mathrm{i}$. In this case we can derive

$$v_R = \frac{R}{\Omega}\frac{\partial\Omega}{\partial R}\frac{\nu}{R} \tag{2.34}$$

from Equation (2.32), which is the missing equation for the radial velocity.

2.2.3 Vertical hydrostatic equilibrium of a non-self-gravitating disk

For the z-direction we use hydrostatic equilibrium, *i.e.*, the z-component of the Euler equation, setting $\frac{\partial\cdot}{\partial t}$ and all velocities to zero. For a non-self-gravitating disk this gives

$$\frac{1}{\rho}\frac{\partial P}{\partial z} = \frac{\partial}{\partial z}\left(\frac{GM_*}{\sqrt{R^2+z^2}}\right) \approx -\frac{GM_*z}{R^3}, \tag{2.35}$$

where the approximation is valid for thin disks, *i.e.*, $z \ll R$. For an isothermal equation of state this can be integrated to give, using the isothermal sound speed $c_\mathrm{s}^2 = \frac{P}{\rho}$,

$$\rho(R,z) = \rho_\mathrm{c}(R)\exp\left(\frac{-z^2}{2Rc_\mathrm{s}v_\varphi^{-1}}\right) =: \rho_\mathrm{c}(R)\exp\left(\frac{-z^2}{2h}\right), \tag{2.36}$$

where

$$h = \frac{c_\mathrm{s}}{\Omega_\mathrm{K}}R \tag{2.37}$$

is the scaleheight of a non-self-gravitating disk and $\rho_\mathrm{c}(R)$ is the density at $z = 0$. Equation (2.37) tells us that a thin disk needs to have an azimuthal velocity that is much higher than the speed of sound, which means that the pressure force is negligible with respect to the centrifugal force, and thus is consistent with the assumption $v_\varphi \approx v_\mathrm{K}$ in a non-self-gravitating disk. Calculating Σ from Equation (2.36) we get

$$\Sigma = \int_{-\infty}^{+\infty}\rho(z)\mathrm{d}z = 2h\sqrt{\frac{\pi}{2}}\rho_\mathrm{c}, \tag{2.38}$$

which is, regarding all the approximations and assumptions, usually approximated by setting

$$\Sigma = 2h\rho \tag{2.39}$$

where the index of ρ is skipped. Since the most important disk equations in the time-dependent (2.28) and in the time-independent case (2.33) are equations in Σ and not in ρ, we see that the height h of the disk is necessary to get the volume density. ρ in turn is needed for the equation of state.

2.2.4 Self-gravitating disks

Thin accretion disks can be divided into three groups according to the importance of self-gravity. First there is the group of the non-self-gravitating (NSG) disks which we encountered above. The most inner part of self-gravitating disks is of course such a disk.

Then there are the so called Keplerian self-gravitating (KSG) disks for which $v_\varphi \approx v_\mathrm{K}$ holds as shown below. The self-gravity in these disks does not change the radial behavior of the disk, but it does change the height profile. We need the solution of the Poisson equation for gravity

$$\Delta\Phi = 4\pi G\rho \quad \Leftrightarrow \quad -\vec{\nabla}\cdot\vec{g} = 4\pi G\rho, \tag{2.40}$$

where $\vec{g}$ is the gravitational acceleration, for the z-direction of the disk. For this we take the mass to be distributed in an infinite stratified sheet with constant surface density Σ. Using Gauss's Law it is easy to show that in such a case the acceleration (which has only a z-component) is

$$g_\mathrm{sg} = -2\pi G\Sigma_h \leq -2\pi G\Sigma \quad \text{where} \quad \Sigma_h = \int_{-h}^{h} \rho(z)\mathrm{d}z. \tag{2.41}$$

Thus using Equation (2.35), the gravitational acceleration due to the disk and due to the star become equal when

$$g_\mathrm{sg} \approx -\pi G\Sigma \approx -G\frac{M_\mathrm{d}(R)}{R^2} = -\frac{GM_*}{R^2}\frac{z}{R}, \tag{2.42}$$

where in the second equation $M_\mathrm{d}(R) \approx \pi\Sigma R^2$ has been used for an approximation of the mass of the disk inside R. This leads for $h = z$ to

$$M_\mathrm{d}(R) > \frac{h}{R}M_* \tag{2.43}$$

for the disk mass region of the KSG part of a disk.

The third group of self-gravitating disks, which of course have NSG and KSG regimes below certain radii, are the fully self-gravitating (FSG) disks. In these both the radial behavior and the height profile are dominated by self-gravity. We adopt here the monopole approximation by Mineshige and Umemura (1997), *i.e.*, the approximation where the Poisson equation for gravity is solved by neglecting material outside R (the radius at which we calculate $\vec{g}$) and take the material inside R to be spherically distributed, *i.e.*,

$$g_R = -\frac{G(M_* + M_d)}{R^2}. \tag{2.44}$$

Using this approximation we see immediately that $v_\varphi \neq v_\mathrm{K}$ for $M_\mathrm{d}(R) \gtrsim M_*$.

The height of a fully self-gravitating disk

Similar to the calculation of the height for a non-self-gravitating disk by using hydrostatic equilibrium (see Section 2.2.3), the same is possible for the fully self-gravitating case, as shown in Kippenhahn and Weigert (1990). Using $P = c_\mathrm{s}^2\rho$, they get a solution for the equations of the isothermal infinite self-gravitating sheet:

$$\frac{\partial^2\Phi}{\partial z^2} = 4\pi G\rho, \tag{2.45}$$

$$\frac{\partial P}{\partial z} = -\rho\frac{\partial\Phi}{\partial z}, \tag{2.46}$$

$$\Rightarrow c_\mathrm{s}^2\frac{\partial \ln\rho}{\partial z} = -\frac{\partial\Phi}{\partial z}, \tag{2.47}$$

$$\Rightarrow \frac{\partial^2 \ln\rho}{\partial z^2} = -\frac{4\pi G}{c_\mathrm{s}^2}\rho, \tag{2.48}$$

which is solved by

$$\rho(z) = \frac{\rho_\mathrm{c}}{(\cosh(\frac{z}{h}))^2}, \quad \rho(\pm\infty) = 0, \tag{2.49}$$

where

$$h = \sqrt{\frac{\mathcal{R}T}{2\pi\mu G\rho_\mathrm{c}}} = \frac{c_\mathrm{s}}{\sqrt{2\pi G\rho_\mathrm{c}}}. \tag{2.50}$$

We rewrite this equation using the result for isothermal disks by Paczyński (1978) for the same case:

$$\rho_\mathrm{c} = \frac{\pi G\Sigma^2\mu}{2\mathcal{R}T} \tag{2.51}$$

to get

$$h = \frac{c_\mathrm{s}^2}{\pi G\Sigma}. \tag{2.52}$$

This gives

$$\Sigma = \int_{-\infty}^{\infty} \frac{\rho_\mathrm{c}}{(\cosh(\frac{z}{h}))^2}dz = 2\rho_\mathrm{c}h, \tag{2.53}$$

$$\Sigma_h = \int_{-h}^{h} \frac{\rho_\mathrm{c}}{(\cosh(\frac{z}{h}))^2}dz = 2\rho_\mathrm{c}h\tanh(1) \approx 0.762\cdot 2\rho_\mathrm{c}h. \tag{2.54}$$

So the approximation $\Sigma = 2\rho h$ is again reasonable.

2.3 The heating of the disk

As we have seen in the last section, h depends on the temperature of the disk, so here we deal with the heating while in Section 2.6 we will deal with the cooling of the disk.

Using the energy equation (2.6), we get for heating by viscous dissipation[1]

$$\frac{\partial \tilde{e}}{\partial t} = \nu\rho\Big(R\frac{\partial\Omega}{\partial R}\Big)^2 \quad \Rightarrow \quad \frac{\partial e}{\partial t} = \nu\Sigma\Big(R\frac{\partial\Omega}{\partial R}\Big)^2, \tag{2.56}$$

where e is the internal energy per unit area.

In addition, the disk is heated by the $P\mathrm{d}V$ work and by shocks. These terms are usually very small and neglected for one dimensional disk equations, but they are included in our numerical setup for self-gravitating disks where the shocks are important. The numerical technique to deal with these terms involves an artificial kind of viscosity which is explained in Section 2.7.3.

2.4 Viscosity in disks

As stated above, the viscosity is very crucial on the one hand and on the other hand it is still not well understood. The most successful description of viscosity is the α-viscosity by Shakura and Sunyaev (1973). The ansatz for this turbulent viscosity is that the kinematic viscosity can be written as the product of a turbulent velocity v_t and a turbulent length scale l_t. To avoid extreme dissipation which would stop the viscosity if there is no energy source that can make up for the losses, the turbulence is thought to be subsonic, *i.e.*, $v_\mathrm{t} \lesssim c_\mathrm{s}$. On the other hand to have isotropic turbulence, we require $l_\mathrm{t} \lesssim h$ giving

$$\nu \propto v_\mathrm{t} l_\mathrm{t} \quad \Rightarrow \quad \nu = \alpha c_\mathrm{s} h, \tag{2.57}$$

where α is a parameter of value less than one and typically is of order $\alpha \sim \mathcal{O}(10^{-2} - 10^{-1})$.

For the reasons stated already in Section 1.3 Duschl et al. (2000), and independently by Richard and Zahn (1999), proposed the β-viscosity. It works in the same way as the α viscosity, but the isotropy of the turbulence is dropped and the limitation of the turbulent velocity by the speed of sound is handled differently. Here $v_\mathrm{t} \propto v_\varphi$ and $l_\mathrm{t} \propto R$ are the typical velocity and length scale in the disk. We also get this result from a different argument. Turbulence comes about at a high Reynolds number $\mathfrak{R} = \frac{v_\varphi R}{\nu}$ which is called the critical Reynolds number $\mathfrak{R}_\mathrm{crit}$. So this gives

$$\nu = \frac{1}{\mathfrak{R}_\mathrm{crit}} v_\varphi R =: \beta v_\varphi R, \tag{2.58}$$

which is the formula for the β-viscosity. Since from experience the typical critical Reynolds number is around $\mathfrak{R}_\mathrm{crit} \sim \mathcal{O}(10^2 - 10^3)$ this gives an estimate for the

[1] Here the gradient of a vector in cylindrical coordinates, which is not easy to find in textbooks, is needed. In order to avoid calculating it by ourselves, we see that the so called "Deformationsgeschwindigkeitstensor" $\mathcal{E} = \vec{\nabla}\vec{v} + (\vec{\nabla}\vec{v})^\mathrm{T}$ (where T indicates the transposed tensor) can be used from Spurk (1996) where its form in cylindrical coordinates is given. Here we state only the component we need, namely

$$\mathcal{E}_{R\varphi} = \mathcal{E}_{\varphi R} = \frac{1}{2}\Big(R\frac{\partial\Omega}{\partial R} + \frac{1}{R}\frac{\partial v_R}{\partial\varphi}\Big). \tag{2.55}$$

Since $\tilde{\sigma}$ is a symmetric tensor $\tilde{\sigma} : \vec{\nabla}\vec{v} = \frac{1}{2}\tilde{\sigma} : \mathcal{E}$.

value of β. From (2.58) it follows, using (2.30), that the time scale for the β-viscosity is

$$t_\nu = \frac{1}{\beta\Omega}. \tag{2.59}$$

Duschl et al. (2000) are also able show that in the limit where the turbulent velocity is limited by the speed of sound, called the dissipation limit, the β-viscosity leads to the α-viscosity with α being in the correct range of values.

It can even be inferred that

$$v_\mathrm{t} \approx \sqrt{\beta} v_\varphi, \quad l_\mathrm{t} \approx \sqrt{\beta} R. \tag{2.60}$$

This becomes evident if we look at the turbulent velocity as being also the typical change in velocity Δv_φ over the typical length scale ΔR which is the turbulent length scale. So we can write

$$\Delta v_\varphi = \left|\frac{\partial v_\varphi}{\partial R}\right| \Delta R \approx \frac{v_\varphi}{R} \Delta R. \tag{2.61}$$

Then putting (2.61) into the formula for the β-viscosity (Equation (2.58)), we get

$$\nu \approx l_\mathrm{t} v_\mathrm{t} = \Delta v_\varphi \Delta l \approx \Delta R \frac{v_\varphi}{R} \Delta R. \tag{2.62}$$

This leads to

$$\beta R v_\varphi \approx \frac{v_\varphi}{R} (\Delta R)^2 \quad \Leftrightarrow \quad \beta R^2 \approx (\Delta R)^2 \tag{2.63}$$

and thus

$$l_\mathrm{t} = \Delta R \approx \sqrt{\beta} R \quad \Rightarrow \quad v_\mathrm{t} \approx \sqrt{\beta} v_\varphi. \tag{2.64}$$

Hydrodynamic instability in a disk

In order to have turbulence in the disk that gives rise to viscosity, we need an instability which drives the turbulence. For partly ionized non-self-gravitating disks, this is the MRI as shown by Balbus and Hawley (1991). In contrast to this the β-viscosity was claimed by Duschl et al. (2000) and Richard and Zahn (1999) to arise from a purely hydrodynamic instability in the disk. This is mainly inspired by laboratory experiments of the Taylor-Couette flow which is the fluid flow between two rotating concentric cylinders (see, *e.g.*, Taylor, 1923, 1936; Wendt, 1933; Richard, 2001). In these experiments the flow became unstable at regimes where it was thought to be stable. The instability condition used for the linear stability of disks is the Rayleigh instability condition

$$\frac{\partial}{\partial R}\Big((R^2\Omega)^2\Big) < 0. \tag{2.65}$$

This is not fulfilled for $\Omega = \Omega_\mathrm{K}$. It can be rewritten as

$$\kappa^2 < 0 \quad \text{with} \quad \kappa^2 := \frac{1}{R^3} \frac{\mathrm{d}}{\mathrm{d}R}\Big((R^2\Omega)^2\Big), \tag{2.66}$$

where κ is the epicyclic frequency which is equal to the angular velocity for Keplerian orbits. κ is the frequency at which a mass oscillates around a circular

orbit when disturbed. This condition can be derived using a linear stability analysis in the R-direction as we will use later for viscous disks in Section 3.1. We are using the radial and azimuthal parts of the Euler equation (Equation (2.5) without the viscous term, in cylindrical coordinates) and set $\rho =$ constant for simplicity. Here we take the ansatz for each variable $X = v_R, v_\varphi$ (usually also for the variables Σ and Φ which is not necessary here)

$$X = X_0 + \delta X,\ \delta X = X_1 \exp i(\omega t + kR),\ \delta X \ll X_0, \tag{2.67}$$

omitting quadratic terms of small values (derivatives of small values are also assumed to be small) and terms of $\frac{\partial \cdot}{\partial \varphi}$. Since there is no viscosity, we can also set $v_{R0} = 0$. This leads to the two equations

$$\frac{\partial \delta v_R}{\partial t} = 2\frac{\delta v_R v_\varphi}{R}, \tag{2.68}$$

$$\frac{\partial \delta v_\varphi}{\partial t} = -\delta v_R \frac{\partial v_\varphi}{\partial R} - \frac{\delta v_R v_\varphi}{R} \tag{2.69}$$

and thus

$$i\omega \delta v_R = 2\frac{\delta v_R v_\varphi}{R}, \tag{2.70}$$

$$i\omega \delta v_\varphi = -\left(\frac{\partial v_\varphi}{\partial R} + \frac{v_\varphi}{R}\right)\delta v_R. \tag{2.71}$$

So we are searching for the eigenvalue $\lambda = i\omega$ of a matrix, *i.e.*,

$$\begin{vmatrix} -\lambda & 2\frac{v_\varphi}{R} \\ -\left(\frac{v_\varphi}{R} + \frac{\partial v_\varphi}{\partial R}\right) & -\lambda \end{vmatrix} = 0. \tag{2.72}$$

The solution is

$$\lambda = \pm\sqrt{-2\frac{v_\varphi}{R}\left(\frac{v_\varphi}{R} + \frac{\partial v_\varphi}{\partial R}\right)}. \tag{2.73}$$

This means we have instability for the case when δX grows exponentially with time which translates here to $\lambda = i\omega \in \mathbb{R}$ and $\lambda > 0$, *i.e.*,

$$\frac{v_\varphi}{R}\left(\frac{v_\varphi}{R} + \frac{\partial v_\varphi}{\partial R}\right) < 0 \quad \Leftrightarrow \quad \frac{\partial}{\partial R}\Big((R^2\Omega)^2\Big) < 0, \tag{2.74}$$

which had to be shown.

There is theoretical work like Grossmann (2000), Tevzadze et al. (2003) and Chagelishvili et al. (2003) showing the possibility of a non-linear instability in a Keplerian disk. On the other hand there are people trying to investigate this instability numerically, but they cannot find it for Keplerian flow in their simulations as shown in Balbus et al. (1996). They do find an instability in a different regime of linear stability though. In a recent paper by Lesur and Longaretti (2005) they are able to show that on the one hand today's computing power does not allow one to simulate the instability in the Keplerian flow correctly but that on the other hand by extrapolating their numerical simulations to this regime even with very favorable extrapolations, the critical Reynolds number becomes

very large. This would lead to a forbiddingly small value for α or β. This would even lead to laminar disks for less favorable extrapolations. The experiments are also not unproblematic. As stated by Richard (2001), it is possible that their experiments that showed an instability in the Keplerian regime suffer from pollution by the linearly stable regime which lies close by in parameter space. Therefore this is a highly controversial topic and is still undecided.

For self-gravitating disks an alternative to a hydrodynamic instability would be a gravitational instability as discussed in the next section.

2.5 Gravitational instability of disks

Toomre (1964), Goldreich and Lynden-Bell (1965) have shown that the criterion for the gravitational stability in a non-viscous gas disk is given by the condition

$$Q := \frac{c_\mathrm{s}\kappa}{\pi G\Sigma} > 1, \tag{2.75}$$

where Q is the Toomre parameter. Q can be interpreted as the ratio of the stabilizing forces of pressure and shear in the numerator and the destabilizing force of gravity in the denominator.

Using the Toomre parameter Q as defined in Equation (2.75), solving for c_s and substituting this into Equation (2.52), leads to

$$Q^2 = \frac{h\kappa^2}{\pi G\Sigma}. \tag{2.76}$$

Again using the monopole approximation in the form $\Omega = \sqrt{\frac{GM_d}{R^3}} = \sqrt{\frac{\pi G\Sigma}{R}}$, we get

$$\kappa^2 = 3\frac{\pi G\Sigma}{R} \Rightarrow \kappa = \sqrt{3}\,\Omega. \tag{2.77}$$

Using (2.77) and the monopole approximation in Equation (2.76), we get:

$$Q^2 = 3\frac{h}{R}. \tag{2.78}$$

This means that, neglecting viscosity, any really thin fully self-gravitating accretion disk is Toomre unstable. On the other hand disks not quite so thin can be stable as shown by Mestel (1963) for stellar disks and for gas disks by Bodo and Curir (1992) and Bertin and Lodato (1999) in which the marginally stable full self-gravitating disks are of height $h = \frac{1}{4}R$.

Most of the work done to answer the question of under what conditions disks become Toomre unstable and what happens if they do is done for inviscid KSG protoplanetary disks. Heating terms for $P\mathrm{d}V$ and shocks are usually included. The main question in this discussion turns out to be under what conditions the disk fragments and thus can possibly form a giant gas planet in relatively short time (see, *e.g.*, Boss (2000) and Durisen et al. (2006) and references therein). One answer is given by numerical simulations with a grid based code in a local approximation by Gammie (2001) and with global particle based code simulations

by Rice et al. (2003) and Lodato and Rice (2004), Lodato and Rice (2005). They all use a simplified cooling function of the form

$$\frac{\partial e}{\partial t} = -\frac{e}{t_{\rm cool}} \quad \text{where} \quad t_{\rm cool} = b\Omega^{-1} \tag{2.79}$$

with some constant b of order unity. As expected they find that fragmentation happens when the cooling is efficient enough. This is understood since in Equation (2.75) the cooling can easily control Q via $c_{\rm s}$. More accurately the result is that fragmentation always takes place if and only if

$$b < 3, \tag{2.80}$$

where the exact numerical value depends on γ as discussed below. In the case where $b \gtrsim 3$ the disk settles into a quasi steady state with $Q \approx 1$ in a wide radial range forming a transient spiral structure. This can be understood such that as the spirals are formed, gravitational energy gets transferred by shocks to heat which in turn prevents Q from dropping below one. As $Q = 1$ is reached, the heating stops, cooling is still efficient enough to keep a small value of Q. Rice et al. (2005) could show that the correct condition for fragmentation can be expressed by a constant $\alpha_{\rm max}$ (see also below) as

$$b < \frac{4}{9\gamma(\gamma-1)}\frac{1}{\alpha_{\rm max}}. \tag{2.81}$$

This quasi steady state was examined with regard to steady accretion due to the self-gravity by Gammie (2001) and in more detail by Lodato and Rice (2004), Lodato and Rice (2005), Rice et al. (2005). They find that accretion in these systems can be described by the α-viscosity with

$$\alpha = \frac{4}{9\gamma(\gamma-1)}\frac{1}{b} \tag{2.82}$$

and thus using Equation (2.81) there must be a maximal value of α which turns out to be $\alpha_{\rm max} \approx 0.06$. A similar formula can be derived when assuming that in a self-gravitating disk the energy freed by accretion is all radiated away as shown below.

The results above are amazing even though the cooling function seems rather artificial. Actually Duschl et al. (2000) found that self-gravitating steady α-disks must have an artificial cooling law that maintains isothermality throughout the whole disk in order to work, so it seems that the cooling law described above is quite special and maybe unphysical. Mejía et al. (2005) use a cooling function that is constant throughout the disk. Using this cooling function which is possibly more realistic, they show that the accretion, which is not steady in this case, cannot be described by α-viscosity using Equation (2.82). In a paper by Johnson and Gammie (2003) they use a more sophisticated cooling function very similar to the one used for the present work described in Section 4.6.1. They do not deal with the accretion but with fragmentation only, showing that with the more realistic cooling function in some temperature regimes Equation (2.80) is changed dramatically due to the change in the cooling time.

The behavior of a disk in a quasi steady state keeping $Q \approx 1$ and having a viscosity due to gravitational turbulence is already discussed by Paczyński (1978). Other authors like Lin and Pringle (1987) or Ebert (1994) describe a turbulent viscosity coming about by a gravitational instability in a KSG disk. A proposition for a viscosity from turbulence driven by gravitational instability in FSG disks can be found in Duschl and Britsch (2006) which is a short version of Chapter 3 of this work. At this point one might also pose the question of whether there can be thin self-gravitating disks at all. As shown above they are highly Toomre unstable, and should thus fragment into clumps in a short time. It is a well known problem for the outer parts of AGN disks since the cooling would make those disks thin (see, *e.g.*, Goodman, 2003). But in Scoville et al. (1997) the model of a thin, *i.e.*, unstable disk, fits the observed data well for a fully self-gravitating several 100 pc radius disk of Arp 220. And Kumar (1999) is able to show for an observed case of another AGN disk that if it is an α-disk, it has a higher mass than the BH in the center and has a very small value of $Q \sim 10^{-3}$. They conclude that the α-prescription breaks down. The disk fragments into clumps and those clumps interact to give rise to accretion. In this clumpy disk model the disk has a lower mass than the BH, but it is still self-gravitating and fragments. Their model gives an accretion rate of

$$\dot{M} = \eta \Omega M_R \left(\frac{M_R}{\pi M_\mathrm{t}} \right)^2, \tag{2.83}$$

where

$$\eta = \frac{R}{l_\mathrm{c}} \left(\frac{M_R}{\pi M_\mathrm{t}} \right)^{-1} \tag{2.84}$$

is a geometrical factor, including the size of the clumps l_c and is thought to be of order unity. M_R is the mass of the disk inside R and M_t is the axisymmetrically distributed mass inside R, *i.e.*, not including the clumps but including the star. The accretion timescale thus is determined to be

$$t_\mathrm{clump} = \frac{M_R}{\dot{M}} = \frac{1}{\eta \left(\frac{M_R}{\pi M_\mathrm{t}}\right)^2} \frac{1}{\Omega} \tag{2.85}$$

and thus has the same form as the time scale of the β-viscosity $t_\nu = \frac{1}{\beta\Omega}$ with $\beta = \eta \left(\frac{M_R}{\pi M_\mathrm{t}}\right)^2 = \frac{R}{l_\mathrm{c}} \left(\frac{M_R}{\pi M_\mathrm{t}}\right)$ which can be larger than one.

Let us now assume that in a disk where accretion is driven by a gravitational instability, the gravitational energy (per unit time) heating the disk due to accretion is dominating over the heating by fragmentation or spiral formation. Then we can equate the energy production rate by accretion in a small radial range ΔR which is

$$\Delta \frac{\Delta E}{\Delta t} = \frac{1}{\Delta t} \frac{\partial}{\partial R} \left(\frac{GM\Delta m}{R} \right) \Delta R = -\frac{1}{\Delta t} g_R \Delta m \Delta R, \tag{2.86}$$

where $M = M_* + M_d$, to the energy loss by cooling

$$\Delta \dot{E}_\mathrm{th} = \frac{e}{t_\mathrm{cool}} \Delta A = \frac{e}{t_\mathrm{cool}} 2\pi R \Delta R. \tag{2.87}$$

Using

$$\dot{M} = \frac{\Delta m}{\Delta t} = \delta \pi \Sigma \nu \tag{2.88}$$

from Equations (2.31) and (2.34) where $\delta = -2\frac{R}{\Omega}\frac{\partial \Omega}{\partial R}$ which is always of the order of unity and 3 in the case of Keplerian disks, we get

$$\nu = -\frac{2}{\delta}\frac{R^3}{GM}\frac{e}{\Sigma}\frac{1}{t_{\rm cool}} = -\frac{2}{\delta}\Omega^{-1}\varepsilon\frac{1}{\Omega t_{\rm cool}} \tag{2.89}$$

where ε is the internal energy per unit mass which is $\varepsilon = \frac{\frac{f}{2}\mathcal{R}T}{\mu}$. Using $\gamma = \frac{f+2}{f}$ and $c_{\rm s}^2 = \frac{\mathcal{R}T}{\mu}$, we get

$$\nu = \frac{2}{\delta}\frac{1}{\gamma - 1}\frac{1}{\Omega t_{\rm cool}}\frac{c_{\rm s}^2}{\Omega} \tag{2.90}$$

or with $\nu = \alpha\frac{c_{\rm s}^2}{\Omega}$ from Equations (2.57) and (2.37),

$$\alpha = \frac{2}{\delta}\frac{1}{\gamma - 1}\frac{1}{\Omega t_{\rm cool}}. \tag{2.91}$$

Equation (2.91) is very similar to Equation (2.82) and would be more similar if we had used the adiabatic instead of the isothermal speed of sound which was used for consistency reasons. This formula is not thought to give exact values, rather it is an approximation to the time averaged behavior; and as such is less exact but more general than Equation (2.82) in the sense that it might also hold for non-steady flows. It is also a local argument which might be its weakness as stated already for Equation (2.82) by Mejía et al. (2005).

The instability of viscous disks

As shown by many authors (*e.g.*, Mishurov et al. 1976, Kato and Kumar 1960, Kumar 1960, Stephenson 1961 and in more detail Hunter and Schweiker 1981, Hunter and Horak 1983) the infinite rotating viscous medium is Jeans unstable, which means that the Jeans criterion for instability

$$k < \frac{2\pi G\Sigma}{c_{\rm s}^2} =: k_{\rm J} \tag{2.92}$$

is valid, where k is the wave number. $k_{\rm J}$ is called the Jeans wave number, or $\lambda_{\rm J} := \frac{2\pi}{k_{\rm J}}$ the Jeans wavelength. This relation can also be shown for rigidly rotating viscous disks, see, *e.g.* Lynden-Bell and Pringle (1974). A more detailed discussion on viscous disks can be found in Gammie (1996) and Antonov and Kondratyev (1995). All of this implies that the Toomre criterion for the stability of an inviscous disk (see Equation (2.75)) is not a valid criterion for stability in viscous disks. Although in the above mentioned papers, in the Navier-Stokes equation the term $\frac{\partial \eta}{\partial R} = \frac{\partial \eta}{\partial \Sigma}\frac{\partial \Sigma}{\partial R}$, where $\eta := \nu\Sigma$, is missing, which can be of importance (see, *e.g.* Schmit and Tscharnuter (1995), Fridman and Polyachenko (1984) and Section 3.2).

2.6 The cooling mechanism

As we saw in the last section, cooling is crucial for the question of stability and fragmentation in a disk. The energy equation (2.6) can be completed with a cooling term using some cooling function Λ (in the z-integrated form), such that

$$\frac{\partial e}{\partial t} = -\Lambda. \tag{2.93}$$

To get a handle on this cooling function it is necessary to know how the radiation gets influenced by the disk material when it tries to escape. An introduction to basic radiation theory can, *e.g.*, be found in Unsöld and Baschek (2002). Here we need the transport equation for radiation neglecting emission and scattering

$$\frac{\mathrm{d}I_\nu}{\mathrm{d}s} = -\kappa_\nu \rho I_\nu, \tag{2.94}$$

where I_ν is the frequency dependent intensity, s is the length of the light-path and κ_ν is the opacity which is a property of the material. This equation can be integrated to give

$$I_\nu = I_{\nu 0}\mathrm{e}^{-\tau_\nu} \quad \text{with} \quad \tau_\nu = \int_0^s \rho\kappa_\nu \mathrm{d}s', \tag{2.95}$$

where τ_ν is called the optical depth. Especially for the disk of height h we get

$$\tau_\nu = \int_0^h \rho\kappa_\nu \mathrm{d}s = \frac{1}{2}\Sigma\kappa_\nu. \tag{2.96}$$

There are two limiting cases of Equation (2.96). The first is the optically thin case where $\tau_\nu \ll 1$ and the second is the optically thick case where $\tau_\nu \gg 1$. In these cases a mean frequency weighted opacity can be found which are the Planck mean opacity in the optically thin and the Rosseland mean opacity in the thick case. These opacities are tabled for different temperatures, densities and element contents. Bell and Lin (1994) found that using such tables and applying theoretical ansatzes, interpolation formulae for the Rosseland mean opacity of the form

$$\kappa_i = \kappa_{i,0}\rho^{a_i}T^{b_i}, \tag{2.97}$$

for 8 regions i with different exponents a_i and b_i, can be used. These formulae were used by Gail (2003) for a single interpolation formula

$$\frac{1}{\kappa_\mathrm{R}} = \sqrt[4]{\frac{1}{\kappa_1^4} + \frac{T_0^{10}}{T_0^{10}+T^{10}}\frac{1}{\kappa_2^4+\kappa_3^4}} + \sqrt[4]{\frac{1}{\kappa_4^4+\kappa_5^4+\kappa_6^4} + \frac{1}{\kappa_7^4+\kappa_8^4}}, \tag{2.98}$$

where $T_0 = 3000\,\mathrm{K}$ and the κs are set according to Equation (2.97) and Table 2.1. This formula is meant to be a simple formula used to reproduce the experimental values as well as possible. It might not be perfectly physical especially in the transition regions between the power laws.

Region	$\kappa_{i,0}$	a_i	b_i
Ice grains	$2{\cdot}10^{-4}$	0	2
Evaporation of ice grains	$2{\cdot}10^{16}$	0	-7
Metal grains	0.1	0	$\frac{1}{2}$
Evaporation of metal grains	$2{\cdot}10^{81}$	1	-24
Molecules	$1{\cdot}10^{-8}$	$\frac{2}{3}$	3
H-scattering	$1{\cdot}10^{-36}$	$\frac{1}{3}$	10
Bound-free and free-free	$1.5{\cdot}10^{20}$	1	$-\frac{5}{2}$
Electron scattering	0.348	0	0

Table 2.1: Base opacities and exponents for the use of Equation (2.97), taken from Bell and Lin (1994). In the first column the material or physical processes dominating the opacity are listed.

2.7 Numerics

Here the most important numerical background is presented. An introduction to numerical methods in general can be found in Press et al. (1992). An introduction to numerical fluid dynamics can be found, *e.g.*, in Hirsch (1988) and Hirsch (1990).

2.7.1 Finite difference and finite volume schemes

The code used for this thesis is a grid-based code, *i.e.*, the calculation domain is divided into grid cells to do the discretization that is necessary for the numerical approximation. The most simple grid-based method to solve differential equations is the so called finite difference method where derivatives are approximated using differences. The most simple finite difference method is the Euler method which is first order, *i.e.*, its uncertainty is of the order $\mathcal{O}(\Delta x^2)$ where the Δx is the spacing of the grid or the time step size if x is the time. The idea is to start at the cell number one, solve the discetized equation for that cell, go on to the next cell and so on. If we have the one dimensional differential equation

$$\frac{\mathrm{d}f}{\mathrm{d}x} = F(f(x), x) \tag{2.99}$$

the corresponding discretization of the derivative is

$$\frac{\Delta f}{\Delta x} = \frac{f(x_{i+1}) - f(x_i)}{x_{i+1} - x_i}. \tag{2.100}$$

The x in F on the right hand side of Equation (2.99) can be either be x_i or x_{i+1} (or any combination of them which would lead to other methods). x_i means the value of x of the ith cell and f_i means $f(x_i)$. This leads to the two possibilities

$$f(x_{i+1}) = F(f_i, x_i) f_i \Delta x \tag{2.101}$$

or

$$f(x_{i+1}) = F(f_{i+1}, x_{i+1}) f_i \Delta x. \tag{2.102}$$

The first equation is the explicit Euler method because f_i is given explicitly while in the second one, the implicit Euler, f_{i+1} is given implicitly since according to our stepping method f_{i+1} is not calculated yet and must be obtained by solving Equation (2.102) numerically. This becomes more obvious if x represents the time. Of course implicit methods are more demanding to implement, but they have the important advantage that they are unconditionally stable, *i.e.*, no matter how large the grid size or more important the time step (if x is time) is taken, the errors do not blow up. Explicit methods on the other hand need to choose the grid or time step size according to a formula like the Courant condition presented below.

As stated in Section 2.1 the differential form of the hydrodynamics equations are not the most physical one but rather the volume integrated forms are. Thus using this form of the equation to get a discretization is better than the simple finite difference method and is called the finite volume method. Actually this can be seen as a special type of finite difference method. Since the understanding of how the finite volume method works in detail is not essential for this work, we do not describe it in detail here but ask the interested reader to refer to the above cited literature.

2.7.2 The Courant condition

The condition for the stability of an explicit numerical scheme mentioned above is called the Courant or Courant-Friedrichs-Levy (CFL) condition in the case of an advection equation for any conserved scalar or vector quantity u

$$\frac{\partial u}{\partial t} = \vec{\nabla} \cdot (u\vec{v}). \tag{2.103}$$

The Courant condition for the time step size Δt for a first order scheme is

$$\Delta t = C_{\mathrm{CFL}} \min_i \left(\frac{\Delta x}{|v_i| + c_\mathrm{s}} \right) \tag{2.104}$$

where the i is the dimension and the constant $C_{\mathrm{CFL}} < 1$ is the CFL number. This constraint can be interpreted, such that the maximal speed at which information can travel in the direction $\vec{n}$, *i.e.*, $v_{\max}(\vec{n}) = c_\mathrm{s} \pm \vec{v} \cdot \vec{n}$ where the sign is chosen to get the maximal value, must not be limited by numerics. Therefore the sound cone (in the case of $\vec{v} = 0$) must lie within the cone of $\frac{\Delta x}{\Delta t}$ as depicted in Figure 2.1. To put it another way the numerical speed with which information can travel must hold

$$\frac{\Delta x}{\Delta t} \geq C_{\mathrm{CFL}}^{-1}(|v_i| + c_\mathrm{s}). \tag{2.105}$$

A similar argument leads to a CFL-like condition for the viscous term of the form

$$\Delta t \geq \frac{C_\nu}{4} \min_i \left(\frac{(\Delta x)^2}{\nu} \right), \tag{2.106}$$

where C_ν is again a CFL-like number. This formula includes $(\Delta x)^2$ since the viscous term is a diffusion term with a spread that increases like $\sqrt{t}$.

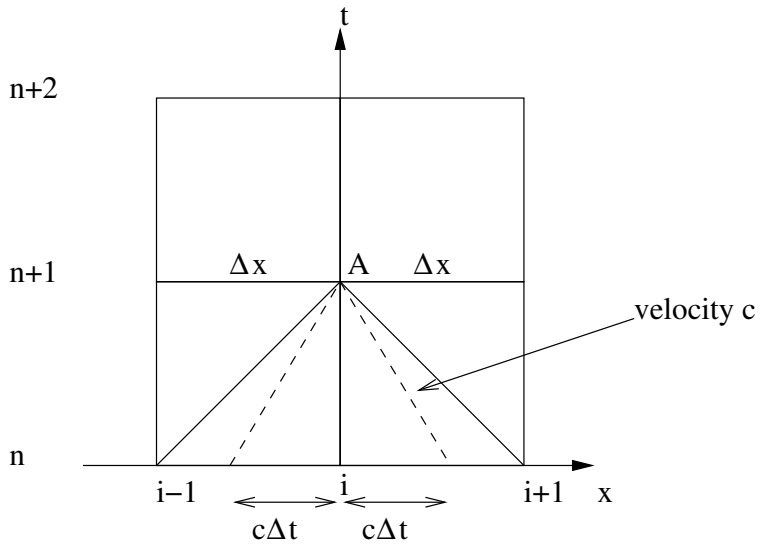

Figure 2.1: The Courant condition demands that the domain from which information travels to point A at x_i, t_{n+1} (*i.e.*, the region at time t_n from x_{i-1} to x_{i+1}) must include the region from which, by physical processes, information travelling with the maximal wave speed (and thus the maximal speed at which information can travel) c can reach point A (which is $x_i - c\Delta t$ to $x_i + c\Delta t$).

2.7.3 Artificial viscosity

When using first-order advection schemes for hydrodynamics there is a problem with shocks since they get smeared strongly. In second-order schemes on the other hand, shocks lead to strong oscillations. Von Neumann and Richtmyr (1950) found a solution for this problem with second-order schemes, which does not require the knowledge of the position of the shock. The way this is done is by introduction of an artificial viscosity which becomes very low in regions outside of shocks. Tscharnuter and Winkler (1979) introduce a similar method which can treat especially accretion processes very well. In the code used for this work the artificial viscous tensor is split into two parts, one is the part described in von Neumann and Richtmyr (1950) called the anisotropic artificial viscosity and the other part is the viscosity described by Tscharnuter and Winkler (1979) called the tensor artificial viscosity of which the diagonal elements are taken only to inhibit artificial momentum transport. As a formula this gives for the artificial viscosity tensor (given in Cartesian coordinates here)

$$\bar{\sigma}_{ij} = -l_{\mathrm{T}}^2(\Delta x_i)^2\rho\min(0,\vec{\nabla}\cdot\vec{v})\cdot\Big((\vec{\nabla}\vec{v})_{ii} - \frac{1}{3}\vec{\nabla}\cdot\vec{v}\Big)\delta_{ij} + \\ + l_{\mathrm{A}}^2\rho\big(\Delta x_i\cdot\min(0,(\vec{\nabla}\vec{v})_{ii})\big)^2\delta_{ij}, \quad (2.107)$$

where l_{T} is the shock smearing length for the tensor viscosity in units of the grid spacing Δx_i and l_{A} is the same for the anisotropic part. These expressions are of order unity. The terms $\min(0,\vec{\nabla}\cdot\vec{v})$ and $\min(0,(\vec{\nabla}\vec{v})_{ii})$ help ensure that the artificial viscosity only acts where it is needed. This tensor is included in the momentum and energy equation as well as in the calculation of the CFL condition.

Chapter 3

Gravitational instability of a viscous disk

In this chapter we perform a linear stability analysis for thin viscous disks including self-gravity. First we apply this analysis to non-self-gravitation α-disks to show that not all of these disks are stable without introducing a second viscosity. Then we examine self-gravitating β-disks to show not only that they are unstable but in addition our calculation leads to the proposition of an instability-driven turbulence that can give rise to the β-viscosity.

3.1 The dispersion relation

In this section, we derive the full dispersion relation for axisymmetric waves in a thin viscous disk for wavelengths $\lambda \ll R$. The continuity equation and the R- and φ-dimensions of the Navier-Stokes equation in cylindrical coordinates are Equation (2.9) and

$$\frac{\partial v_R}{\partial t} + v_R\frac{\partial v_R}{\partial R} + \frac{v_R}{R}\frac{\partial v_R}{\partial \varphi} - \frac{v_\varphi^2}{R} = \\ -\frac{1}{\Sigma}\frac{\partial}{\partial R}(c_s^2\Sigma) - \frac{\partial \Phi}{\partial R} + \nu\Big(\frac{\partial^2 v_R}{\partial R^2} + \frac{1}{R}\frac{\partial v_R}{\partial R} - \frac{v_R}{R^2}\Big) + \frac{\nu}{3}\frac{\partial}{\partial R}\Big(\frac{1}{R}\frac{\partial v_R R}{\partial R}\Big), \quad (3.1)$$

$$\frac{\partial v_\varphi}{\partial t} + v_R\frac{\partial v_\varphi}{\partial R} + \frac{v_\varphi}{R}\frac{\partial v_\varphi}{\partial \varphi} + \frac{v_\varphi v_R}{R} = \\ -\frac{1}{\Sigma R}\frac{\partial}{\partial \varphi}(c_s^2\Sigma) - \frac{1}{R}\frac{\partial \Phi}{\partial \varphi} + \nu\Big(\frac{\partial^2 v_\varphi}{\partial R^2} + \frac{1}{R}\frac{\partial v_\varphi}{\partial R} - \frac{v_\varphi}{R^2}\Big), \quad (3.2)$$

where terms of $\frac{\partial \tilde{\eta}}{\partial R}$ and $\frac{\partial \tilde{\eta}}{\partial \varphi}$ have been omitted for clarity but will be taken care of separately as follows. After some minor algebra using Equations (2.10) to (2.15) and (2.18) where again $\frac{\partial \cdot}{\partial \varphi} = \frac{\partial \cdot}{\partial z} = v_z = 0$ is used, we get

$$\vec{\nabla}\cdot\sigma = \Big\{\nu\Sigma\frac{4}{3}\Big(\frac{\partial^2 v_R}{\partial R^2} + \frac{1}{R}\frac{\partial v_R}{\partial R} - \frac{v_R}{R^2}\Big) + \frac{\partial \nu\Sigma}{\partial R}\Big(\frac{4}{3}\frac{\partial v_R}{\partial R} - \frac{2}{3}\frac{v_R}{R}\Big)\Big\}\vec{e}_R \\ + \Big\{\nu\Sigma\Big(\frac{\partial^2 v_\varphi}{\partial R^2} + \frac{1}{R}\frac{\partial v_\varphi}{\partial R} - \frac{v_\varphi}{R^2}\Big) + \frac{\partial \nu\Sigma}{\partial R}\Big(\frac{\partial v_\varphi}{\partial R} - \frac{v_\varphi}{R}\Big)\Big\}\vec{e}_\varphi. \quad (3.3)$$

The first term in the radial and azimuthal components respectively are the terms for $\frac{\partial\tilde{\eta}}{\partial R} = 0$.

Using the ansatz as in Section 2.4 for each variable $X = \Sigma, v_R, v_\varphi, \Phi$ and with the same omissions, we arrive at

$$i\omega\delta\Sigma + \frac{1}{R}\frac{\partial}{\partial R}(R\Sigma_0)\delta v_R + \Sigma_0 ik\delta v_R + \frac{1}{R}\frac{\partial}{\partial R}(\Sigma v_{R0})\delta\Sigma + v_{R0}ik\delta\Sigma = 0, \tag{3.4}$$

$$i\omega\delta v_R + \delta v_R\frac{\partial v_{R0}}{\partial R} + ikv_{R0}\delta v_R - \frac{2v_{\varphi 0}}{R}\delta v_\varphi = - \frac{c_s^2}{\Sigma_0}ik\delta\Sigma + \frac{c_s^2}{\Sigma_0^2}\frac{\partial\Sigma_0}{\partial R}\delta\Sigma - ik\delta\Phi - \frac{4}{3}\nu\chi^2\delta v_R, \tag{3.5}$$

$$i\omega\delta v_\varphi + \delta v_R\frac{\partial v_{\varphi 0}}{\partial R} + ikv_{R0}\delta v_\varphi + \frac{v_{\varphi 0}}{R}\delta v_R + \frac{v_{R0}}{R}\delta v_\varphi = -\nu\chi^2\delta v_R, \tag{3.6}$$

where $\chi^2 := k^2 - i\frac{k}{R} + \frac{1}{R}$. The solution for the Poisson equation $\Delta\delta\Phi = 4\pi G\Sigma\delta(z)$, where $\delta(z)$ is Dirac's delta function, is given by

$$\delta\Phi = -2\pi G\frac{\delta\Sigma}{|k|} \tag{3.7}$$

for $k \gg \frac{1}{R}$ (see, *e.g.*, Binney and Tremaine, 1987). For the additional terms in Equation (3.3), we get $A\delta v_R + B\delta\Sigma$ for the radial and $C\delta v_\varphi + D\delta\Sigma$ for the azimuthal part, with

$$A := \frac{4}{3}\Big(\frac{\partial\nu}{\partial R} + \frac{\nu}{\Sigma_0}\frac{\partial\Sigma_0}{\partial R}\Big)ik - \frac{2}{3}\Big(\frac{\partial\nu}{\partial R}\frac{1}{R} + \frac{\nu}{\Sigma_0}\frac{1}{R}\frac{\partial\Sigma_0}{\partial R}\Big), \tag{3.8}$$

$$B := \Big(\frac{4}{3}\frac{\nu}{\Sigma_0}\frac{\partial v_{R0}}{\partial R} - \frac{2}{3}\frac{\nu}{\Sigma_0}\frac{v_{R0}}{R}\Big)ik - \Big(\frac{4}{3}\frac{\nu}{\Sigma_0^2}\frac{\partial v_{R0}}{\partial R}\frac{\partial\Sigma_0}{\partial R} - \frac{2}{3}\frac{\nu}{\Sigma_0^2}\frac{v_{R0}}{R}\frac{\partial\Sigma_0}{\partial R}\Big), \tag{3.9}$$

$$C := \Big(\frac{\partial\nu}{\partial R} + \frac{\nu}{\Sigma_0}\frac{\partial\Sigma_0}{\partial R}\Big)ik - \Big(\frac{\partial\nu}{\partial R}\frac{1}{R} + \frac{\nu}{\Sigma_0}\frac{1}{R}\frac{\partial\Sigma_0}{\partial R}\Big), \tag{3.10}$$

$$D := \Big(\frac{1}{2}\frac{\kappa^2}{\Omega} - 2\Omega\Big)\frac{\nu}{\Sigma_0}ik - \Big(\frac{1}{2}\frac{\kappa^2}{\Omega} - 2\Omega\Big)\frac{\nu}{\Sigma_0^2}\frac{\partial\Sigma_0}{\partial R}, \tag{3.11}$$

where $\frac{\partial v_{\varphi 0}}{\partial R} + \frac{v_{\varphi 0}}{R} = -2\tilde{B} = \frac{1}{2}\frac{\kappa^2}{\Omega}$ ($\tilde{B}$ is Oort's second constant and Ω is the angular frequency, see *e.g.*, Binney and Tremaine 1987). Calculating the determinant of the combined system, we get for $k > 0$

$$\begin{aligned}
&(i\omega + ikv_{R0} + \frac{1}{R}\frac{\partial}{\partial R}(v_{R0}R))(i\omega + ikv_{R0} + \frac{4}{3}\nu\chi^2 - A)(i\omega + \frac{v_{R0}}{R} + ikv_{R0} + \nu\chi^2 - C)\\
&\quad + \kappa^2(i\omega + ikv_{R0} + \frac{1}{R}\frac{\partial}{\partial R}(v_{R0}R))\\
&\quad - (i\omega + ikv_{R0} + \frac{v_{R0}}{R} + \nu\chi^2 - C)(\frac{c_s^2}{\Sigma_0}ik - \frac{c_s^2}{\Sigma_0^2}\frac{\partial\Sigma_0}{\partial R} - 2\pi Gi - B)\\
&\qquad \cdot (\frac{\partial\Sigma_0}{\partial R} + \frac{\Sigma_0}{R} + ik\Sigma_0) + 2\Omega D\Big(\frac{1}{R}\frac{\partial}{\partial R}\big(R\Sigma_0\big) + \Sigma_0 ik\Big) = 0,
\end{aligned} \tag{3.12}$$

or using

$$\bar{\omega} := \omega + kv_{R0}, \tag{3.13}$$

$$a := \frac{\partial v_{R0}}{\partial R} + \frac{4}{3}\nu\chi^2 - A, \tag{3.14}$$

$$b := \frac{v_{R0}}{R} + \nu\chi^2 - C, \tag{3.15}$$

$$c := \frac{c_s^2}{\Sigma_0}ik - \frac{c_s^2}{\Sigma_0^2}\frac{\partial \Sigma_0}{\partial R} - B, \tag{3.16}$$

$$d := \frac{\partial \Sigma_0}{\partial R} + \frac{\Sigma_0}{R} + ik\Sigma_0, \tag{3.17}$$

$$V := \frac{1}{R}\frac{\partial}{\partial R}(v_{R0}R)) = \frac{\partial v_{R0}}{\partial R} + \frac{v_{R0}}{R}, \tag{3.18}$$

the result is

$$\begin{aligned} -i\bar{\omega}^3 - (b+a+V)\bar{\omega}^2 + (i(ab+\kappa^2 - cd + Vb + Va) - 2\pi G d)\bar{\omega} \\ - bcd + 2\pi i G bd + \kappa^2 V + abV + 2\Omega dD = 0. \end{aligned} \tag{3.19}$$

Since the stability depends only on the imaginary part of ω and since $\Im(\bar{\omega}) = \Im(\omega)$, linear stability is given if $\Im(\bar{\omega}) > 0$.

When we set (now omitting the index 0 and the bar over the ω) $\nu \equiv 0, v_R \equiv 0, \frac{\partial \Sigma}{\partial R} \equiv 0, \chi^2 = k^2, \frac{\partial \tilde{\eta}}{\partial R} \equiv 0$ and neglect the geometric term involving $\frac{\Sigma}{R}$, we get the usual Toomre stability criterion via the dispersion relation of Binney and Tremaine (1987) p. 362.

When we set $v_R \equiv 0, \frac{\partial \Sigma}{\partial R} \equiv 0, \chi^2 = k^2, \frac{\partial \tilde{\eta}}{\partial R} \equiv 0$ and omit the term involving $\frac{\Sigma}{R}$, which is not present in Cartesian coordinates, the result is Equation (16) of Gammie (1996) (calculated in the local Cartesian coordinate system) with $s = i\omega$.

3.2 A thin non-self-gravitating α-disk

Here we consider the case of a thin non-self-gravitating α-disk, *i.e.*, $\nu = \alpha h c_s = \alpha \frac{c_s^2}{\Omega}$, $\frac{h}{R} \ll 1$ and $M_d \approx \Sigma R^2 \pi < \frac{h}{R} M_* \Rightarrow \pi G \Sigma < \frac{h}{R^3} M_* G = c_s \Omega$ (see also Section 2.2.4) where in the last relation the monopole approximation was used. Although the disk is non-self-gravitating in the sense discussed above, we will not disregard the self-gravitating term right from the beginning since it can have an effect on the result as we will see. Neglecting boundary terms, using the first equation above and $\kappa = \Omega \propto R^{-\frac{3}{2}}$ for Keplerian rotation this leads to $\nu \propto R^{\frac{3}{2}}$ and thus

$$\frac{\partial \nu}{\partial R} = \frac{3}{2}\frac{\nu}{R}. \tag{3.20}$$

Since $\Sigma\nu = \frac{\dot{M}}{3\pi}$ from Equation (2.33)

$$\Rightarrow \Sigma \propto R^{-\frac{3}{2}} \Rightarrow \frac{\partial \Sigma}{\partial R} = -\frac{3}{2}\frac{\Sigma}{R} \tag{3.21}$$

for $\dot{M} =$ constant and using Equation (2.34)

$$v_R = -\frac{3}{2}\frac{\nu}{R} \Rightarrow \frac{\partial v_R}{\partial R} = -\frac{v_R}{R}. \tag{3.22}$$

With these relations, we get $A = 0$, $B = 0$ and $C = 0$, whereas

$$D = -\frac{3}{2}\Omega\frac{\nu}{\Sigma}ik - \frac{9}{4}\Omega\frac{\nu}{\Sigma}\frac{1}{R}. \tag{3.23}$$

Substituting this into Equation (3.19), and neglecting terms of higher order in Rk with regard to terms of lower order, we get

$$s^3 + \frac{7}{3}\nu k^2 s^2 + \Big(\frac{4}{3}\nu^2 k^4 + \Omega^2 + c_s^2 k^2 - 2\pi G\Sigma k\Big)s + \nu k^2\big(c_s^2 k^2 + 3\Omega^2 - 2\pi G\Sigma k - 3\frac{\nu^2}{R^2}k^2\big) = 0, \tag{3.24}$$

where $s := i\bar{\omega}$. Thus we have linear stability, if $\Re(s) < 0$.

Using the Routh-Hurwitz theorem (see, *e.g.*, Gradshteyn and Ryzhik, 2000, p. 1076), one can determine the sign of the (real) root. If a_1, a_2 and a_3 are the coefficients of s^2, s and the constant term respectively, then the root is *negative* if

$$a_1 > 0, \tag{3.25}$$

$$\begin{vmatrix} a_1 & 1 \\ a_3 & a_2 \end{vmatrix} > 0. \tag{3.26}$$

and

$$\begin{vmatrix} a_1 & 1 & 0 \\ a_3 & a_2 & 1 \\ 0 & 0 & a_3 \end{vmatrix} = \begin{vmatrix} a_1 & 1 \\ a_3 & a_2 \end{vmatrix} \cdot a_3 > 0. \tag{3.27}$$

The first condition holds trivially since $\frac{7}{3}\nu k^2 s^2 > 0$. The second condition leads – after neglecting higher order terms – to

$$\frac{28}{9}\nu^2 k^4 - \frac{2}{3}\Omega^2 + \frac{4}{3}c_s^2 k^2 - \frac{8}{3}\pi G\Sigma k > 0 \tag{3.28}$$

for stability. If we neglect the third term in Equation (3.28), *i.e.*, the self-gravity term which should be negligible for non-self-gravitating disks, we can prove stability for a wide range of accretion disks. Please note that this would not be the case if we had set $\frac{\partial\tilde{\eta}}{\partial R} \equiv 0$. In that case we would come to the same conclusions as the authors mentioned in Section 2.5, namely that the Jeans criterion holds and thus any disk with a radius above the Jeans length is unstable. On the other hand please mind that the above mentioned authors were examining self-gravitating disks while this section is about a non-self-gravitating disk.

Coming back to the calculation, we get

$$\frac{28}{9}\nu^2 k^4 + \frac{4}{3}c_s^2 k^2 > \frac{2}{3}\Omega^2 \tag{3.29}$$

for stability. With $y = k^2$ and replacing the greater than sign with an equals sign, we get the positive solution

$$y = \frac{3}{14}\frac{c_s^2}{\nu^2}\left(\sqrt{1 + \frac{14}{3}\frac{\nu^2\Omega^2}{c_s^4}} - 1\right). \tag{3.30}$$

Using Equations (2.57) and (2.37), we get $\frac{\nu^2\Omega^2}{c_s^4} = \alpha^2 \ll 1$ and thus (with $\sqrt{1+\varepsilon} \approx 1 + \frac{1}{2}\varepsilon$ for $\varepsilon \ll 1$)

$$k_{\min}^2 = y \approx \frac{1}{2}\frac{c_s^2\alpha^2}{\nu^2} = \frac{1}{2}h^2, \tag{3.31}$$

leading to a minimum wavelength for instability of

$$\lambda_{\min} = \frac{2\pi}{k_{\min}} = \sqrt{2}2\pi h \approx 8.9h. \tag{3.32}$$

Or – since $\lambda \ll 2\pi R$ – we have stability *at least* for $R < \sqrt{2}2\pi h$, or

$$\frac{h}{R} = \frac{c_s}{v_\varphi} > \frac{1}{2\sqrt{2}\pi} \approx 0.11, \tag{3.33}$$

which would mean stability for a wide range of disks, especially since $\lambda < 2\pi R$ was used instead of $\lambda \ll 2\pi R$, meaning that 0.11 is a very conservative limit. This still implies instability for some non-self-gravitating disks while we have even neglected (the small) self-gravity.

But first, the third condition (3.27) must be fulfilled which is the case if $a_3 > 0$, *i.e.*,

$$f := c_s^2k^2 + 3\Omega^2 - 2\pi G\Sigma k - 3\frac{\nu^2}{R^2}k^2 > 0. \tag{3.34}$$

Setting $\frac{\partial f}{\partial k} = 0$ to find a minimum ($\frac{\partial^2 f}{\partial k^2} > 0$, since $c_s^2 > 3\frac{\nu^2}{R^2} = 3\alpha^2\frac{h^2}{R^2}c_s^2$) at k_0, we get

$$k_0 = \frac{\pi G\Sigma}{c_s^2 - 3\frac{\nu^2}{R^2}}. \tag{3.35}$$

Inserting this into Equation (3.34) after some algebra we get as an equivalent condition

$$\frac{c_s^2\Omega^2}{(\pi G\Sigma)^2}\Big(1 - 3\frac{h^2}{R^2}\alpha^2\Big) \approx Q^2 > 1. \tag{3.36}$$

This is always fulfilled for thin NSG α-disks, since $Q = \frac{\Omega c_s}{\pi G\Sigma} > \frac{\Omega c_s}{\Omega c_s} = 1$ (see the conditions at the beginning of this section).

All of this can change, if we implement a second kinematic viscosity ξ as introduced in Section 2.1, of the same order of magnitude as the first viscosity as is believed to exist due to turbulence in the same way as the first viscosity (see, *e.g.*, Papaloizou and Pringle, 1977). Equation (3.24) becomes

$$\begin{aligned} s^3 + \big(\xi + \frac{7}{3}\nu\big)k^2s^2 + \Big(\big(\xi + \frac{4}{3}\nu\big)\nu k^4 + \Omega^2 + c_s^2k^2 - 2\pi G\Sigma k\Big)s \\ + \nu k^2\big(c_s^2k^2 + 3\Omega^2 - 2\pi G\Sigma k - 3\frac{\nu^2}{R^2}k^2\big) = 0. \end{aligned} \tag{3.37}$$

Using $\xi = x\nu$, after some algebra and neglecting higher-order terms, we find

$$\Big(x + \frac{7}{3}\Big)\Big(x + \frac{4}{3}\Big)\nu^2k^4 + \Big(x - \frac{2}{3}\Big)\Omega^2 + \Big(x + \frac{4}{3}\Big)c_s^2k^2 - \Big(x + \frac{4}{3}\Big)2\pi G\Sigma > 0 \tag{3.38}$$

for the second condition (Equation (3.26)). Even by neglecting the third term in finding the minimum of this expression (which makes the expression smaller, since

the third term is a positive one), we get after a lot of algebra the conservative condition

$$\frac{1}{q}\frac{1}{2\left(x+\frac{7}{3}\right)^{\frac{1}{3}}}\alpha^{-\frac{2}{3}} > 1, \tag{3.39}$$

(where $q = \frac{8}{3}\left(\frac{3}{14}\right)^{\frac{1}{3}} - \frac{28}{9}\left(\frac{3}{14}\right)^{\frac{4}{3}} \approx 1.2$) which for $x = 1$ comes to about

$$0.28\alpha^{-\frac{2}{3}} \approx 1.3 > 1 \quad \text{for } \alpha = 0.1 \tag{3.40}$$

for stability. The third condition (3.27) does not change and is thus met. So for $x = 1$ and $\alpha < 0.15$ all thin NSG α-disks are linearly stable even using this conservative condition. Unfortunately the second viscosity is hardly discussed in the accretion disk literature, as a rare exception, see Papaloizou and Pringle (1977).

3.3 A thin self-gravitating β-disk

To get disk parameters to probe the dispersion relation of a thin self-gravitating β-disk, we take the equations of a thin stationary accretion disk (see Section 2.2.2), neglecting the boundary terms

$$\nu\Sigma = -\frac{\dot{M}}{2\pi R}\Omega\left(\frac{\partial\Omega}{\partial R}\right)^{-1}, \tag{3.41}$$

$$\dot{M} = -2\pi R\Sigma v_R. \tag{3.42}$$

Using the monopole approximation for the potential with a negligible central mass $v_\varphi = \sqrt{\frac{M_d G}{R}} = \sqrt{\pi G\Sigma R}$ and the β-parameterization of the viscosity (2.57), we get after some algebra

$$\Sigma = \left(\frac{\dot{M}}{2\pi\beta}\frac{1}{\sqrt{G\pi}}\right)^{\frac{2}{3}} R^{-1}, \tag{3.43}$$

$$\frac{\partial\Sigma}{\partial R} = -\left(\frac{\dot{M}}{2\pi\beta}\frac{1}{\sqrt{G\pi}}\right)^{\frac{2}{3}} R^{-2}, \tag{3.44}$$

$$\nu = \left(\frac{G\dot{M}}{2}\right)^{\frac{1}{3}}\beta^{\frac{2}{3}}R, \tag{3.45}$$

$$v_R = -\left(\frac{G\dot{M}}{2}\right)^{\frac{1}{3}}\beta^{\frac{2}{3}}, \tag{3.46}$$

$$\kappa = \sqrt{3}\left(\frac{G\dot{M}}{2\beta}\right)^{\frac{1}{3}} R^{-1}, \tag{3.47}$$

$$c_s = \text{constant } (= 1000\frac{\text{m}}{\text{s}} \text{ typically}), \tag{3.48}$$

$$\dot{M} = (2\pi)^{\frac{3}{2}}\sqrt{\frac{G}{2}}\beta R_{\text{O}}^{\frac{3}{2}}\Sigma_{\text{O}}^{\frac{3}{2}} \tag{3.49}$$

with Σ_{O} being the surface density at the outer rim of the disk. A similar analysis as in Section 3.2 can be carried out for a fully self-gravitating β-disk. Using

Equations (3.43) to (3.49) and $\kappa^2 = 3\Omega^2$ (see Equation (2.77)), we get $A = C = 0$ and

$$B = \frac{\nu^2}{\Sigma R^2} ik + \frac{\nu^2}{\Sigma R^3}, \tag{3.50}$$

$$D = -\frac{1}{2}\Omega\frac{\nu}{\Sigma} ik - \frac{1}{3}\Omega\frac{\nu}{\Sigma R}. \tag{3.51}$$

This leads – after neglecting higher-order terms – to

$$s^3 + \frac{7}{3}\nu k^2 s^2 + \Big(\frac{4}{3}\nu^2 k^4 + 3\Omega^2 + c_s^2 k^2 - 2\pi G\Sigma k\Big)s + \nu k^2\big(c_s^2 k^2 + \Omega^2 - 2\pi G\Sigma k - 3\frac{\nu^2}{R^2}k^2\big) = 0. \tag{3.52}$$

The first condition for stability (Equation (3.25)) again is met trivially. From condition (3.27) we investigate

$$a_3(k) = c_s^2 k^2 + \Omega^2 - 3\frac{\nu^2}{R^2}k^2 - 2\pi G\Sigma k > 0 \tag{3.53}$$

for stability. Actually this is necessary for stability since, if $a_3 < 0$ by (3.27), $(a_1 a_2 - a_3) < 0$ must hold for stability which in turn would violate condition (3.26). Thus $a_3 > 0$ is necessary for stability. Searching for an extremum k_0, we find

$$k_0 = \frac{\pi G\Sigma}{c_s^2 - 3\frac{\nu^2}{R^2}}. \tag{3.54}$$

There are two possible cases:

$$\frac{\partial^2 a_3}{\partial k^2} = 2c_s^2 - 6\frac{\nu^2}{R^2} = 2(c_s^2 - 3\beta^2 v_\varphi^2) > 0 \Rightarrow c_s > 3\beta v_\varphi \tag{3.55}$$

and

$$\frac{\partial^2 a_3}{\partial k^2} < 0 \Rightarrow c_s < 3\beta v_\varphi. \tag{3.56}$$

If Equation (3.55) holds k_0 is a minimum and by some algebra the condition for stability can be rewritten as

$$\frac{1}{3}Q^2 - \frac{\frac{\nu^2\Omega^2}{R^2}}{(\pi G\Sigma)^2} > 1, \tag{3.57}$$

which cannot be fulfilled, since the second term is negative and $\frac{1}{3}Q^2 \ll 1$ by Equation (2.78). On the other hand if Equation (3.56) holds, then obviously $a_3(k \to \infty) < 0$, and all large k, *i.e.*, small λ, are unstable. Thus all thin FSG β-disks are unstable. But please note the comments at the end of this section.

In Figures 3.1 and 3.2 the imaginary part of ω is shown for the parameters $R = 1{\cdot}10^{18}$, $R_\mathrm{O} = 3 \cdot 10^{18}\,\mathrm{m}$, $\Sigma_\mathrm{O} = 30\frac{\mathrm{kg}}{\mathrm{m}^2}$ and $c_s = 1000\frac{\mathrm{m}}{\mathrm{s}}$ using Mathematica (Wolfram Research, 2005). In Figure 3.1 the imaginary part of solution two is plotted with $\beta = 5{\cdot}10^{-3}$, while in the other graph $\beta = 5{\cdot}10^{-4}$. Solutions one and three seems to be stable always, *i.e.*, $\Im(\omega) > 0$. Please mind that Equations (3.43) to (3.49) are not self-consistent, since in the monopole approximation $\Sigma =$ constant was used. Thus these equations must be seen as a simple approximation. Since the disk is probably not stationary, a better approximation would not be of use here.

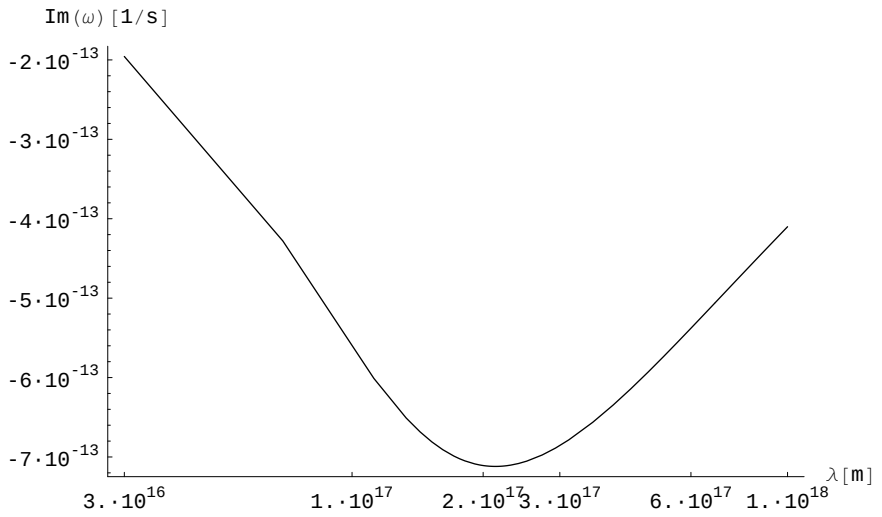

Figure 3.1: $\Im(\omega)$ for $\beta = 5{\cdot}10^{-3}$. Parameters are: $R = 1 \cdot 10^{18}\,\mathrm{m}, R_\mathrm{O} = 3{\cdot}10^{18}, \Sigma_\mathrm{O} = 30\frac{\mathrm{kg}}{\mathrm{m}^2}$ and $c_s = 1000\frac{\mathrm{m}}{\mathrm{s}}$.

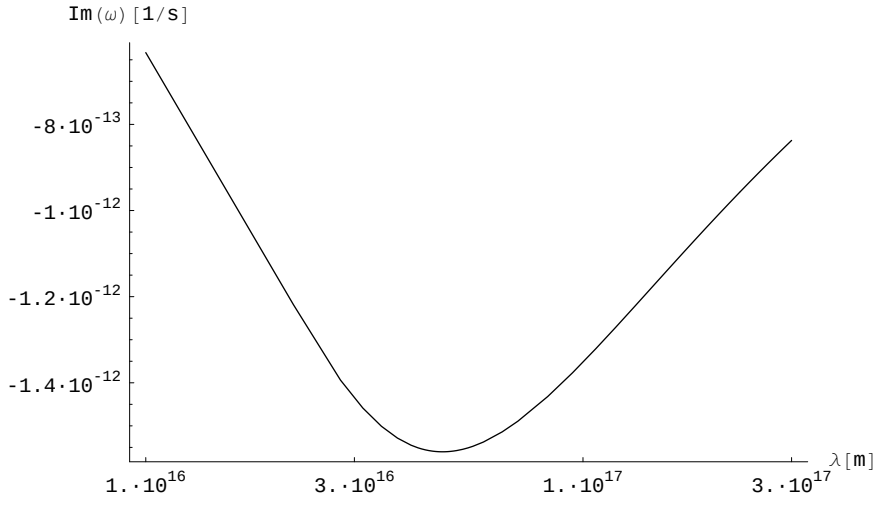

Figure 3.2: $\Im(\omega)$ for $\beta = 5{\cdot}10^{-4}$, $R = 1 \cdot 10^{18}\,\mathrm{m}, R_\mathrm{O} = 3{\cdot}10^{18}, \Sigma_\mathrm{O} = 30\frac{\mathrm{kg}}{\mathrm{m}^2}$ and $c_s = 1000\frac{\mathrm{m}}{\mathrm{s}}$.

3.4 A new route to β-viscosity

The original idea presented in Section 2.4 was that a hydrodynamic instability drives the turbulence and thus $\beta = \frac{1}{\mathfrak{R}_{\rm crit}}$. The new idea is that the gravitational instability is the main driver of the turbulence. So we look for a characteristic length in the self-gravitating viscous disk. Neglecting pressure and shear, a characteristic length is the wavelength where the time scale of viscosity equals the time scale of gravity, *i.e.*, the corresponding term in Equation (3.52) which can be interpreted as being approximately the dynamical time scale for a clump with surface density Σ at distance λ. So we require that $\nu k^2 = \sqrt{2\pi G \Sigma k}$. This leads, using again the monopole approximation and neglecting a possible central source to

$$\lambda_{\rm min} = (4\pi^3)^{\frac{1}{3}} \beta^{\frac{2}{3}} R \tag{3.58}$$

which evaluates to $1.5{\cdot}10^{17}$ m for the conditions of Figure 3.1 and $3.1{\cdot}10^{16}$ m for the conditions of Figure 3.2. Obviously our calculated characteristic wavelength corresponds, up to a factor of 1.5, to the minimum of the imaginary part of ω – which is rather independent of all the other parameters – and thus is the predominant size of structure in the system.

This ansatz leads to

$$l_{\rm t} = \sqrt{\beta} R = \lambda_{\rm min} = (4\pi^3)^{\frac{1}{3}} \beta^{\frac{2}{3}} R \tag{3.59}$$

which gives the number

$$\beta = \frac{1}{16\pi^6} = 6.5{\cdot}10^{-5} \tag{3.60}$$

close to the expected order of magnitude (see Section 2.4). Due to the approximations used, the correspondence cannot be expected to be very good considering that any error in the most unstable wavelength enters to the $6^{\rm th}$ power. This calculation changes a little bit, if we include a non-negligible central mass, giving

$$\beta = \frac{1}{16\pi^6} \left(1 + \frac{M_*}{\pi \Sigma R^2} \right)^{-2} = 6.5{\cdot}10^{-5} \left(1 + \frac{M_*}{\pi \Sigma R^2} \right)^{-2} \tag{3.61}$$

altering the value of β at the rim to the Kepler self-gravitating regime to $\beta = \frac{1}{4} \frac{1}{16\pi^6}$ at the radius where the central mass $M_* = \pi \Sigma R^2$.

So if a thin self-gravitating disk is thought to be laminar in the beginning, we would have no turbulent viscosity, but (see Equation (2.76)) we would have gravitational instability. If this instability leads to a turbulence and hence a viscosity, using the β-parameterization of the viscosity, for consistency the β-value has to lie in the above mentioned order of magnitude and thus is about as large as expected.

It is expected that the self-gravity that drives the turbulence has enough potential energy to drive a supersonic turbulence. Thus for such a viscosity the dissipation limit would not hold.

Chapter 4

Simulation techniques

In this chapter the program NIRVANA2.0 and the necessary further developments to it for our special purposes are described. In Section 4.1 the program and some changes to the hydrodynamics are described. Section 4.2 discusses the changes to the self-gravitation algorithm which are evaluated in Section 4.3. Section 4.4 analyzes the convergence and the time behavior which show a major problem with the used CPU time. Thus in Section 4.5 we introduce the multi-grid method that was implemented to increase the speed of the gravity solver. We describe the implementation of the cooling function in the last section of this chapter.

4.1 Using NIRVANA2.0 to simulate an accretion disk

4.1.1 NIRVANA2.0

NIRVANA2.0 is described in Ziegler (1998) and Ziegler (1999) and can be downloaded from Ziegler (2003) including more detailed descriptions. It is a non-relativistic computational fluid dynamics code including MHD (magneto hydro dynamics), viscosity, thermodynamics, heat conduction and self-gravity written in C. Cartesian, cylindrical and spherical coordinates are implemented in three and partly in two dimensions. In NIRVANA2.0 an AMR (adaptive mesh refinement) algorithm is implemented. This is a method where the computational grid can be made finer where necessary, *e.g.*, in regions where clumps are found, and coarser where the resolution is not needed (*e.g.*, in low-density regions). MHD, AMR and heat conduction are not used in the present work.

The algorithm is a finite difference with a finite volume scheme using operator splitting on a staggered grid, where scalar values and diagonal elements of tensors are defined in the center of a cell, vectors are defined face-centered and off-diagonal elements of tensors are defined edge-centered (see Figure 4.1). The operators can be switched on or off using an input file. The time integration is an explicit Euler scheme.

After some initialization the different functions for the differential operators are called at every time step in the following ordering:

- `gravity.c` computes the gravitational potential

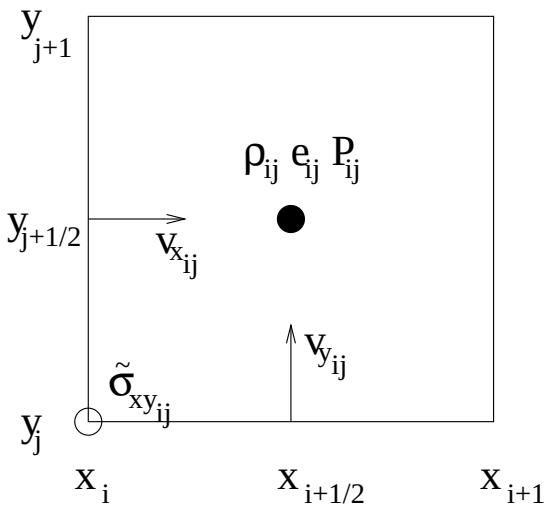

Figure 4.1: The staggered grid of NIRVANA2.0 in 2D for simplification. Depicted is the cell at position i, j. Scalars like ρ, e or P but also diagonal elements of tensors are defined in the cell center. Vector components like v_x and v_y are defined on the face-centers and off-diagonal elements of tensors like $\tilde{\sigma}_{xy}$ are defined at the centers of the edges.

- `sourceMomentum.c` is the momentum source operator
- `viscosity.c` contains the physical and artificial viscosity
- `sourceEnergy.c` includes the sinks and sources of heat apart from the heat by viscous dissipation which is done in `viscosity.c`
- `advection.c` performs the advection for all variables.

The gravitational force due to the central point mass is included in `sourceMomentum.c`.

Hydrodynamics and energy equation

The advection is a second-order accurate finite-volume scheme by van Leer. The code is conservative for mass and angular momentum, though for the disk it is important to rotate it in the negative direction; otherwise angular momentum conservation might not be perfect at the boundary $\varphi = 0, 360°$. The problem is that the advection scheme used needs three ρ values, *i.e.*, three cells, upstream of the point where the velocity is calculated. The boundary conditions give only two such cells. This third upstream ρ value gives only a minor contribution to the advection and is negligible for small gradients in ρ in the φ-direction. Since the azimuthal velocity at $\varphi = 0$ is included in the calculation domain (instead of v_φ at $\varphi = 360°$), the transport is not perfect in the positive rotation direction at this boundary.

The energy equation is used in the thermal energy density form. The source terms are implemented as central differences and are thus second order in space. Apart from the physical viscosity which is implemented as a finite difference

scheme there is also the possibility to use a tensor or an anisotropic artificial viscosity in the case of shocks as described in Section 2.7.3.

The self-gravity algorithm

The self-gravity algorithm of NIRVANA2.0 is a recursive ADI (Alternative Direction Implicit) method, described in Douglas, Jr. (1962). It consists of the source files `gravity.c`, `sourceGravity.c` and `adiLevel.c`. From the first file `adiLevel.c` is called, which implements the ADI solver every pseudo-time step. In the second file the source function is defined. An ADI solver for parabolic partial differential equations works by calculating an intermediate result at each (pseudo-)time step, using a finite difference scheme, where only the differential operator in one direction (say the x-direction) is handled implicitly. The differential operators in the other directions are handled explicitly. In the next intermediate step a similar thing is done for the y- and eventually for the z-direction (for a detailed description see *e.g.*, Smith 1970 or Douglas, Jr. 1962). The ADI solver of NIRVANA2.0, which can also handle the heat conduction equation, solves the equation

$$\vec{\nabla} \cdot (f \vec{\nabla}(hu)) = \frac{du}{dt} + s, \tag{4.1}$$

where f, h, u and s are some functions. In the case of self-gravity $s = 4\pi G\rho$, $u = \Phi$, $h \equiv f \equiv 1$. It is solved recursively with a special method of choosing the pseudo-time steps dt. This way a solution for the Poisson equation $\Delta\Phi(\vec{x}) = 4\pi G\rho$ is obtained.

The boundary conditions for the ADI solver are taken from the boundary condition files of NIRVANA2.0, but they are also partly implemented directly in the ADI solver. Please note that in NIRVANA2.0 the cylindrical coordinates are $\{x, y, z\} \hat{=} \{z, R, \varphi\}$, *i.e.*, the z-direction is the first direction in the ADI solver. Since the z-direction is of special interest for us, here are the relevant equations (in Cartesian notation for simplification):

$$\Delta_x(f_{n+\frac{1}{2}} \Delta_x(hu^*_{n+1})) - \frac{2}{\Delta t} u^*_{n+1} = d_x, \tag{4.2}$$

$$d_x := - \left[\Delta_x(f_{n+\frac{1}{2}} \Delta_x hu_n) + 2\Delta_y(f_{n+\frac{1}{2}} \Delta_y hu_n) + 2\Delta_z(f_{n+\frac{1}{2}} \Delta_z hu_n) + \frac{2}{\Delta t} u_n - 2s_n \right], \tag{4.3}$$

where

$$\Delta_x(f_{n+\frac{1}{2}} \Delta_x hu_n) := \frac{f_{i+\frac{1}{2},j,k,n+\frac{1}{2}}(hu_{i+1,j,k,n} - hu_{i,j,k,n}) - f_{i-\frac{1}{2},j,k,n+\frac{1}{2}}(hu_{i,j,k,n} - hu_{i-1,j,k,n})}{(\Delta x)^2}. \tag{4.4}$$

The equations for the y- and z-directions look similar. Here i, j and k are the space indexes and n is the time index. The asterisk indicates the value at the next intermediate step, *i.e.*, after the intermediate step in the x-direction is done.

Boundary conditions

The boundary conditions of density, velocity, thermal energy density and gravitational potential are set in `bcrho.c`, `bcv.c`, `bce.c` and `bcphi.c` respectively. For the potential, there is also the file `bcphiMultipol.c` for calculating the multipole expansion of the potential. The boundary conditions are implemented by ghost cells, *i.e.*, the grid has two additional cells at each boundary, called ghost cells. In these cells the boundary values are set. The numbering of the cells starts at zero, so cell number two is the first of the computational grid and numbers zero and one are ghost cells.

4.1.2 Modifications of NIRVANA2.0

Modifications of the hydrodynamics

NIRVANA2.0 does not support a polar grid. To have such a grid for the hydrodynamics, the code has been changed to use only one layer of cells in the z-direction of the calculation. Any flow through the z = constant-planes of the cells is set to zero by the boundary conditions. The φ-boundary conditions are straightforwardly set by copying the values.

The calculation of the centrifugal term was changed, such that four instead of two values of v_φ in the radial direction were taken to calculate an average by Lagrange polynomial interpolation (see, *e.g.*, Press et al., 1992). This change was necessary for stabilization in this version. When using self-gravity, this could not be used and thus leads to radial velocity oscillations as discussed later in Section 7.1.1.

This was the state of the program mainly used in this chapter. Later two dimensional hydrodynamics using a surface density Σ and a scaleheight h was implemented. That process also leads to changes in the self-gravity algorithm, described below.

To do this, the equations of continuity, internal energy and the Navier-Stokes equations were integrated over the z-direction as in Section 2.2.1. The one-zone approximation is used, *i.e.*,

$$\frac{\partial \cdot}{\partial z} \equiv 0, \tag{4.5}$$

$$\int_{-\infty}^{\infty} X dz = 2hX, \quad \text{where } X \text{ is any simple variable,} \tag{4.6}$$

$$v_z \equiv 0. \tag{4.7}$$

Thus the continuity equation takes the form

$$\frac{\partial \Sigma}{\partial t} = \vec{\nabla} \cdot (\vec{v}\Sigma) \tag{4.8}$$

and so the only change in the code is to replace ρ with Σ. The Navier-Stokes equation is split into the advection, the source term and the viscosity part (operator splitting). The advection and source terms do not change (setting $\rho = \frac{\Sigma}{2h}$

where necessary):

$$\Sigma\frac{\partial\vec{v}}{\partial t}+\Sigma(\vec{v}\cdot\vec{\nabla})\vec{v}=-2h\vec{\nabla}(P+\Phi)+\int\vec{\nabla}\cdot\tilde{\sigma}dz. \tag{4.9}$$

For advection and source terms, we get

$$\Rightarrow\frac{\partial\vec{v}}{\partial t}+(\vec{v}\cdot\vec{\nabla})\vec{v}=-\frac{2h}{\Sigma}\vec{\nabla}(P+\Phi). \tag{4.10}$$

In the viscosity case, we have, using $\tilde{\sigma}_{ij}=\nu\rho\big((\vec{\nabla}\vec{v})_{ij}+(\vec{\nabla}\vec{v})_{ji}-\frac{2}{3}\vec{\nabla}\cdot\vec{v}\delta_{ij}\big)$,

$$\begin{aligned}\Sigma\frac{\partial\vec{v}}{\partial t}&=\int\vec{\nabla}\cdot\Big(\nu\rho\big((\vec{\nabla}\vec{v})_{ij}+(\vec{\nabla}\vec{v})_{ji}-\frac{2}{3}\vec{\nabla}\cdot\vec{v}\delta_{ij}\big)\Big)dz\\&=\vec{\nabla}\cdot\Big(\nu\Sigma\big((\vec{\nabla}\vec{v})_{ij}+(\vec{\nabla}\vec{v})_{ji}-\frac{2}{3}\vec{\nabla}\cdot\vec{v}\delta_{ij}\big)\Big)\end{aligned} \tag{4.11}$$

$$\Rightarrow\frac{\partial\vec{v}}{\partial t}=\frac{1}{\Sigma}\vec{\nabla}\cdot\sigma, \tag{4.12}$$

where σ is the viscosity tensor with $\tilde{\eta}=\nu\rho$ exchanged with $\eta:=\nu\Sigma$.

Similarly the internal energy equation is expressed in the internal energy per unit area $e=2h\tilde{e}$.

Modifications of the self-gravity algorithm

The self-gravity is handled in 3D, *i.e.*, a small odd number of cells are used in the z-direction.

The file `bcphiMultipol.c` was rewritten completely to allow for the boundary conditions described in Section 4.2.

Since the idea for the boundary conditions for the potential in the z-direction is to give the derivative with respect to z (which can be non-zero), some changes to the original code were necessary. Firstly the von Neumann boundary conditions as implemented in `adiLevel.c` work only for vanishing gradients. If we set the derivative of the potential with respect to x at the x-boundary: $\left(\frac{\partial u}{\partial x}\right)_{x=0}=a$, *i.e.*, $u_1=-a\Delta x+u_2$, we get for the first cell in the computational domain (*i.e.*, the cell number 2) in x (*i.e.*, z), using equations (4.2) and (4.4):

$$\frac{f_{\frac{5}{2}}h_3\frac{1}{\Delta x^2}}{-(f_{\frac{5}{2}}h_2+f_{\frac{3}{2}}(h_2-h_1))\frac{1}{\Delta x^2}-\frac{2}{\Delta t}}u_3^*+u_2^*=\frac{d_x+a\Delta x f_1h_1\frac{1}{\Delta x^2}}{-(f_{\frac{5}{2}}h_2+f_{\frac{3}{2}}(h_2-h_1))\frac{1}{\Delta x^2}-\frac{2}{\Delta t}}, \tag{4.13}$$

where d_x also contains boundary conditions. While the denominator has already been implemented in NIRVANA2.0, the second part of the numerator had to be added to allow for non-zero gradients for von Neumann boundary conditions.

Secondly, the boundary conditions had to be set by calling `bcphi.c` in `gravity.c` every pseudo-time step to make the von Neumann boundary conditions in the z-direction work properly, otherwise the boundary values do not change and are thus effectively Dirichlet boundary conditions.

In addition, it was necessary to multiply the pseudo-time step by a large number, depending on the grid in use, to get it to converge reasonably fast. For

the grid mentioned below (see Section 4.3.1), this number is 200,000 as obtained by trial and error. The reason is probably that the grid is spaced very differently in the (R, φ) and z-directions.

At the start-up of NIRVANA2.0 some additional initializing steps are done, see, *e.g.*, Section 4.2.4.

Later, a multi-grid algorithm for the ADI-solver was implemented as described in Section 4.5.

Modifications of the self-gravity algorithm due to 2D hydrodynamics

To adapt the self-gravity algorithm to the two-dimensional hydrodynamics, the following has been done. The ADI-solver needs the mean density in every grid cell. For the ith cell in the z-direction (where the central layer of cells is counted as $i = 1$) and grid spacing in the same direction of $h_g = \frac{\Delta z}{2}$, we get using Equation (2.49)

$$\bar{\rho}_i = \frac{\int_{(2i-3)h_g}^{(2i-1)h_g} \rho \mathrm{d}z}{2h_g} = \frac{\rho_c h(\tanh \frac{(2i-1)h_g}{h} - \tanh \frac{(2i-3)h_g}{h})}{2h_g}. \tag{4.14}$$

It can happen, especially where the surface density is very low and thus the height h is large, that $h > z_{\max}$ ($z_{\max}$ being the upper boundary of the calculation domain) and thus the main part of the mass is not included in the self-gravity calculations. This is circumvented by setting $\rho_{\mathrm{grav}} = \frac{\Sigma}{z_{\max}}$ in that case. Please note that only the density used in the self-gravity algorithm is changed; ρ for thermodynamics does not change.

Using Equation (2.52) to calculate the height of the disk at some position assumes that the disk is locally self-gravitating meaning that the height is mainly determined by the surface density and temperature at that location. If the disk becomes inhomogeneous this may not be the case since a location of low surface density may be gravitationally dominated by a near region of high surface density. As long as the height is much smaller than the resolution of the grid, a wrong density profile might not be critical. But if the height is in the range of the resolution or higher this might pose a problem. To overcome this problem, the height, if it is not too small, can be approximated by using the gravitational acceleration in the z-direction, g_z, at the top of the calculation domain. This calculation only holds near this point since g_z is assumed to be constant. This procedure is practical since for the boundary conditions, g_z is calculated anyway. So we have using $P = c_s^2 \rho$:

$$\frac{dP}{dz} = c_s^2 \frac{d\rho}{dz} = -\rho g_z, \tag{4.15}$$

$$\Rightarrow \ln \rho = -\frac{g_z}{c_s^2} + C, \tag{4.16}$$

$$\Rightarrow \rho = \rho_0 \exp\left(-\frac{g_z}{c_s^2}|z|\right) \quad \text{with} \quad h = \frac{c_s^2}{g_z}, \tag{4.17}$$

where C is a constant and Δz is the grid spacing in the z-direction. To prevent a jump in the height when it changes from one form to the other, a factor of two was inserted, so we set $h = 2 \cdot \frac{c_s^2}{g_z}$ when the disk is not locally self-gravitating at

this point which should not be too bad regarding all of the approximations. The z-profile (Equation (2.49)) is kept the same since a better solution is not known and hardly necessary for low z-resolution. To decide which height shall be used, the criteria are that this alternative height is used whenever

$$\frac{c_s^2}{\pi G\Sigma} > \Delta z \quad \text{and} \quad 2\pi G\Sigma < g_z. \tag{4.18}$$

The first guarantees the approximate validity of this alternative height since g_z is calculated at a point some Δz above the disk, while the other guarantees that local self-gravity (Σ is the local value) is not a good approximation here.

4.2 Using NIRVANA2.0's self-gravity algorithm

The self-gravity algorithm of NIRVANA2.0 is described in Section 4.1.1.

The boundary conditions for the potential as implemented in NIRVANA2.0 which uses Cartesian multipoles to the fourth order, are not adequate in the case of a disk, where the boundaries are close to the disk. Consequently boundary conditions had to be found. As stated above, the basic idea is to use $\frac{\partial\Phi}{\partial z}$ as boundary conditions in the z-direction.

To exclude non-convergence by extremely low ρ-values above and below the central plane, a ρ-value of $10^{-4}\rho_c$ is added to these cells, where ρ_c is the density in the central-plane cell. For the following we first need some formulae.

4.2.1 The potential of a cylinder

From Jackson (1967), we get for a cylindrical symmetric mass distribution:

$$\frac{1}{|\vec{x}-\vec{x}'|} = \frac{4}{\pi}\int_0^\infty \cos[k(z-z')]\cdot \\ \cdot\left\{\frac{1}{2}I_0(kR_<)K_0(kR_>) + \sum_{m=1}^{\infty}\cos[m(\varphi-\varphi')]I_m(kR_<)K_m(kR_>)\right\}dk. \tag{4.19}$$

Here I_m and K_m are modified Bessel functions and $R_<$ ($R_>$) is the smaller (larger) value of $\{R, R'\}$ ($\vec{x} = (R, \varphi, z)$). For $\varphi = 0$ and a homogeneous cylinder ring of inner and outer radii R_i and R_a and height h the potential

$$\Phi(\vec{x}) = \int_{R_i}^{R_a}\int_0^{2\pi}\int_{-\frac{h}{2}}^{\frac{h}{2}} \frac{G\rho(\vec{x}')}{|\vec{x}-\vec{x}'|}dz'd\varphi'dR'$$

leads to:

$$\Phi(\vec{x}) = 8G\rho_0\int_{R_i}^{R_a}\int_0^\infty \cos(kz)\frac{1}{k}\sin\left(\frac{kh}{2}\right)I_0(kR_<)K_0(kR_>)R'dkdR'. \tag{4.20}$$

4.2.2 Evaluating the integral for the potential of a cylinder

For comparison it is practical to evaluate the integral in Equation (4.20), or its derivative with respect to z. This has been done numerically to get the potential $\Phi(\vec{x})$ in the mid-plane of the disk ($z = 0$) in the following way.

As algorithms, the numerical recipes Press et al. (1992)[1] function `midpnt.c` and `midinf.c` were used in a simple adaptive way. These functions use the extended midpoint rule, *i.e.*,

$$\int_{x_1}^{x_N} f(x)\mathrm{d}x \approx \Delta x\Big(f\Big(\frac{1}{2}(x_2{+}x_1)\Big){+}f\Big(\frac{1}{2}(x_3{+}x_2)\Big){+}\cdots{+}f\Big(\frac{1}{2}(x_N{+}x_{N-1})\Big)\Big) \quad (4.21)$$

(where $\Delta x = x_{i+1} - x_i$ has to be equal for all i) to evaluate integrals and thus can be used to compute improper integrals where `midinf.c` is for the case when one integral boundary is infinite. The integral over k is improper at the lower and upper limits. It is improper at the lower limit, since $K_0(x) \to \infty$ for $x \to 0$. The integral over k had to be split into two parts, one from $k = 0$ to a point $k = k_{\mathrm{mid}}$ and one from $k = k_{\mathrm{mid}}$ to $k = \infty$, where the first was computed using the `midpnt.c` program and the second using the `midinf.c` program. In the second part, the modified Bessel functions had to be exchanged by their asymptotic behavior for large arguments (see, *e.g.*, Jackson, 1967):

$$\begin{aligned} I_n(x) &\to \frac{1}{\sqrt{2\pi x}}\, e^{x}, \\ K_n(x) &\to \sqrt{\frac{\pi}{2x}}\, e^{-x}. \end{aligned} \quad (4.22)$$

The splitting point $k_{\mathrm{mid}} = 1 \cdot 10^{-16}\,\mathrm{m}^{-1}$ is reasonable and practical, making the argument of the modified Bessel functions $kR \sim \mathcal{O}(10^2)$ (for $x = 100$ the error when using the asymptotic values instead of the correct ones is about 0.01% for the product $I_0(x)K_0(x)$). $R_i = 7.5{\cdot}10^{17}\,\mathrm{m}$ and $R_a = 4.05{\cdot}10^{18}\,\mathrm{m}$ were used. The result can be seen in Figure 4.3 as the dashed line.

The z-derivative of the potential (at a height $z \neq 0$) makes a $\sin(kz)$ from the $\frac{1}{k}\cos(kz)$. Unfortunately, this makes it impossible for the numerical recipes routines to evaluate the integral in the case of $R_i \lesssim R \lesssim R_a$. Nevertheless, it can be used to calculate the appropriate derivative. $g_z = -\frac{\partial \Phi}{\partial z}$ can be evaluated for an infinite plane parallel matter distribution which is constant in each plane, as in Section 2.2.4 to give

$$g_z = -\frac{\partial \Phi}{\partial z} = -2\pi G \Sigma_h. \quad (4.23)$$

Now it is possible to compute the above integral in the case of a cylinder of radius R_i and a cylinder of very large radius ($R \gg R_a$), where a cylinder of radius R_a is cut out of the middle. The correction for the infinite case can be calculated in the case of a constant density in a cylinder ring and no density elsewhere. This correction is of the order $\mathcal{O}(10^{-5})$ relative only, but not correcting the boundary

[1]The precision of all numerical recipes functions has been changed from single to double.

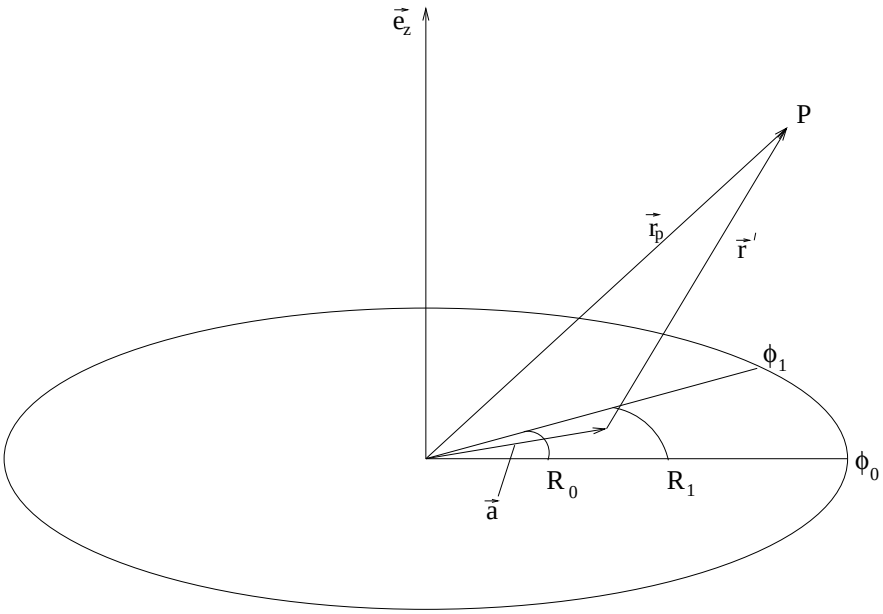

Figure 4.2: The integration to get the solid angle of a cell on the polar grid, bounded by R_0, R_1, φ_0 and φ_1, as seen from point P.

conditions in this way leads to an incorrect shape for the potential as we will see below. Using another method, assuming the mass distribution is a thin sheet, it can be done very quickly. The difference between the corrections calculated according to these two methods are typically of the order 0.1% and always smaller than about 2%. This method is the solid angle method of Section 4.2.3. As we will see later in Section 4.3, using Equation (4.23) with corrections – let's call it the 2π-method with corrections – does not give adequate results in the case of non-constant surface densities in the disk.

4.2.3 The solid angle method

As described in MacMillan (1958), the acceleration in the z-direction (*i.e.*, normal to the plane) due to a plane of constant surface mass density Σ_h, can be written as

$$g_z = -\Omega G \Sigma_h, \tag{4.24}$$

where Ω is the solid angle covered by the surface as seen from the point where g_z is evaluated. Assuming the mass density is a thin sheet and by calculating the solid angle of a grid cell of NIRVANA2.0 as seen from the point above another cell, g_z above this other cell can be calculated.

4.2.4 Calculating the solid angle

The solid angle of an infinitesimal surface element seen from a point P is

$$\mathrm{d}\Omega = \frac{\mathrm{d}A \cos\alpha}{\vec{r}^2}, \tag{4.25}$$

where $\mathrm{d}A$ is the surface element, $\cos\alpha = \frac{\vec{r}\vec{n}}{|\vec{r}|}$, $\vec{r}$ is the difference vector of the two points, $\vec{n}$ is the surface normal and α is obviously the angle between the two vectors. Using Figure 4.2 and Equation (4.25), we get

$$\mathrm{d}\Omega = \frac{\mathrm{d}A\frac{\vec{r}'\vec{e}_z}{|\vec{r}'|}}{\vec{r}'^2} = \frac{R_a \mathrm{d}\varphi_a \mathrm{d}R_a \vec{r}'\vec{e}_z}{|\vec{r}'|^3}. \tag{4.26}$$

After some algebra, and applying $\varphi_\mathrm{P} = 0$, we get

$$\Omega = \int_{R_0}^{R_1}\int_{\varphi_0}^{\varphi_1} \frac{z_\mathrm{P} R_a \mathrm{d}R_a \mathrm{d}\varphi_a}{(R_\mathrm{P}^2 + R_a^2 - 2R_\mathrm{P}R_a\cos\varphi_a + z_\mathrm{P}^2)^{\frac{3}{2}}} \tag{4.27}$$

for the solid angle of a cell on the polar coordinates grid. Using Mathematica (Wolfram Research, 2005), this can be evaluated partly to yield

$$\Omega = \int_{\varphi_0}^{\varphi_1} \left[\frac{2z_p(R_p^2 + z_p^2 - R_a R_\mathrm{P}\cos\varphi_a)}{\sqrt{R_\mathrm{P}^2 + R_a^2 - 2R_\mathrm{P}R_a\cos\varphi_a + z_\mathrm{P}^2)(-R_\mathrm{P}^2 - 2z_\mathrm{P}^2 + R_\mathrm{P}^2\cos(2\varphi_a))}} \right]_{R_a=R_0}^{R_a=R_1} \mathrm{d}\varphi_a. \tag{4.28}$$

These integrals in turn are evaluated numerically at the start of NIRVANA2.0 using the numerical recipes Press et al. (1992) function `qromb.c` for which the maximal error has been set to 10^{-10}. `qromb.c` is an integral solver that is based on the Romberg integration which is a special adaptive way to use the trapezoidal rule $\int_a^b f(x)\mathrm{d}x \approx \frac{1}{2}(a-b)(f(b)+f(a))$. In addition to this, an integral for the solid angle of the inner disk, *i.e.*, the disk which is supposed to be inside the inner boundary of the simulated disk, is calculated for every radius. This is used in an additional term for the influence of the inner disk on the simulated disk using the supposed mean surface density of the inner disk.

4.2.5 The boundary condition in the R-direction

The boundary conditions for the potential in the R-direction are implemented by direct summation of the point mass potentials of all cells in the 2D grid. The monopole approximation of the potential of the inner disk is added.

4.3 Evaluating the methods

In this section we evaluate the different implementations of the boundary conditions for self-gravity. In Chapter 5 test runs to check the entire code with different parameters are done. Some of the problems discussed here will appear again in Chapter 5.

4.3.1 The setup

To evaluate the methods, the following setup has been chosen. The disk is a cylinder of constant density $\rho_0 = 2{\cdot}10^{-8}\,\frac{\mathrm{kg}}{\mathrm{m}^3}$ of which a cylinder of equal height

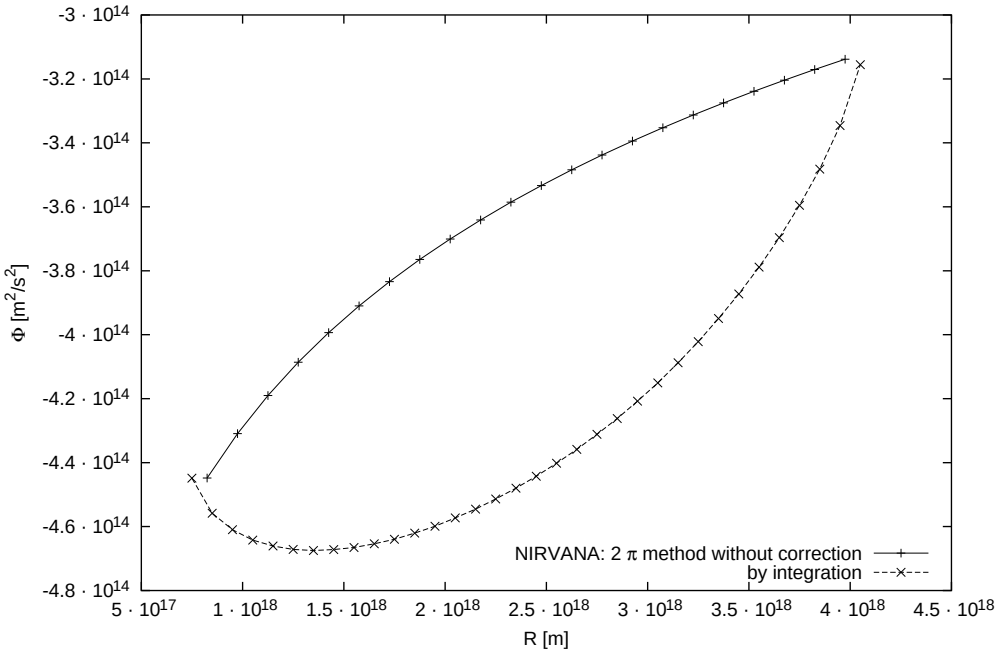

Figure 4.3: Potential for constant density in a cylinder ring with NIRVANA2.0 using the 2π-method, *i.e.*, Equation (4.23), without correction (see Section 4.2.2, solid line with +-symbols) in comparison to the result of the integration of Equation (4.20) (see Section 4.2.2, dashed lines with $\times$-symbols).

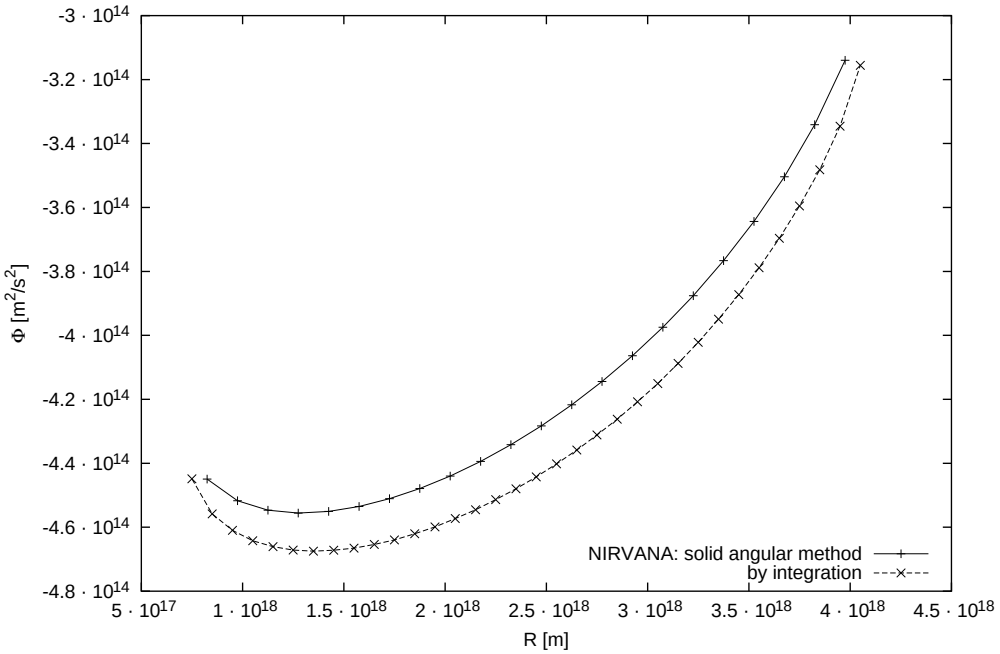

Figure 4.4: Potential for constant density in a cylinder ring with NIRVANA2.0 using the solid angle method (see Section 4.2.3, solid line with +-symbols) in comparison to the result of the integration of Equation (4.20) (see Section 4.2.2, dashed lines with $\times$-symbols).

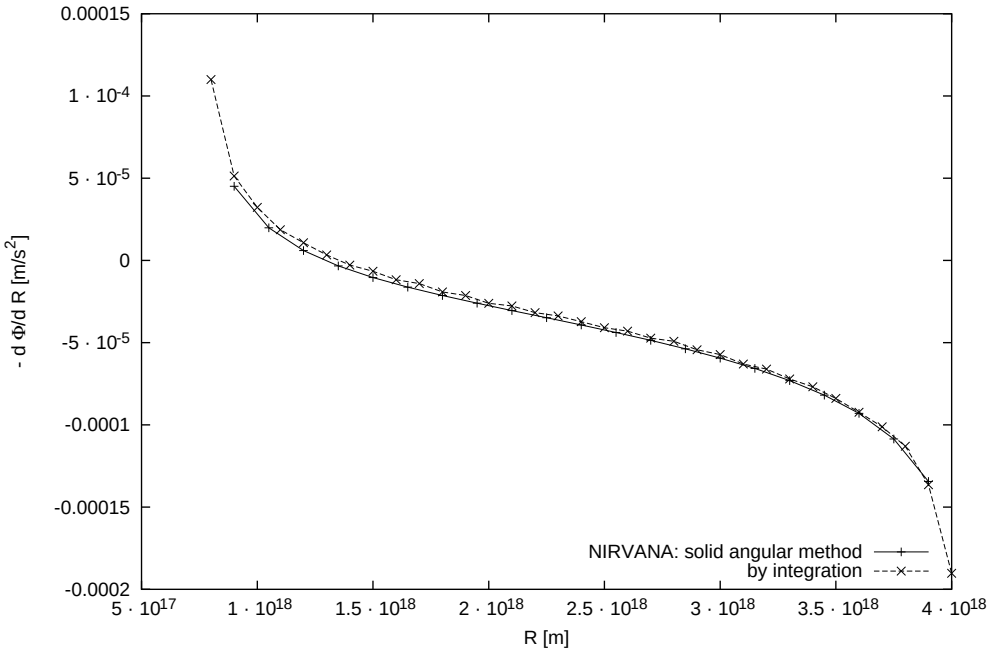

Figure 4.5: Same as Figure 4.4, but for the derivative of the potential. The agreement is acceptable.

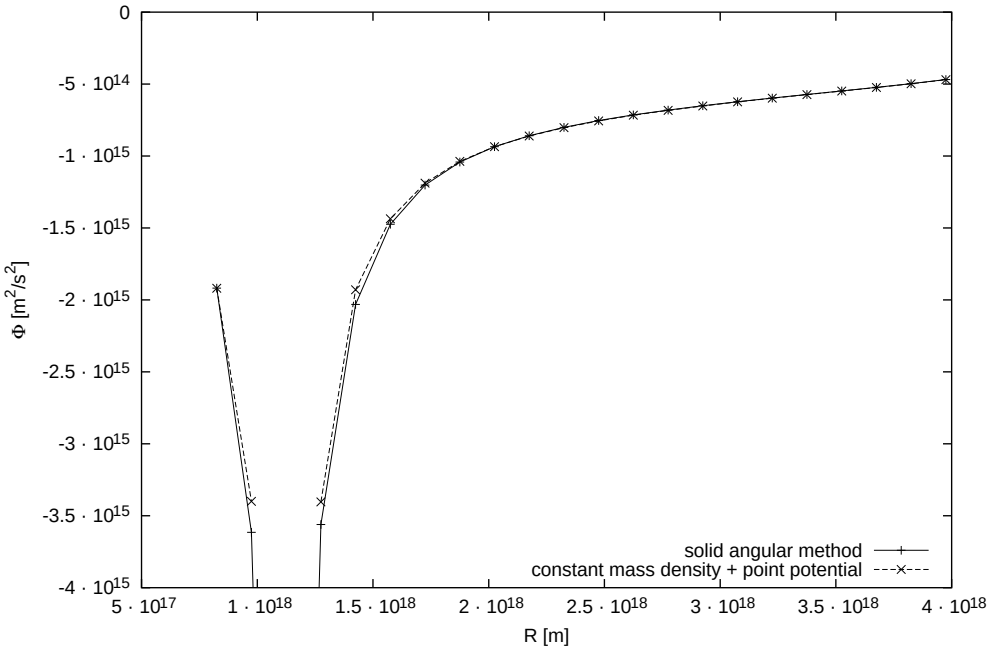

Figure 4.6: Same as Figure 4.4, but with raised density in one cell only (by a factor of 10^3). The dashed line with $\times$-symbols marks the potential of Figure 4.4 from NIRVANA2.0 plus a point mass potential.

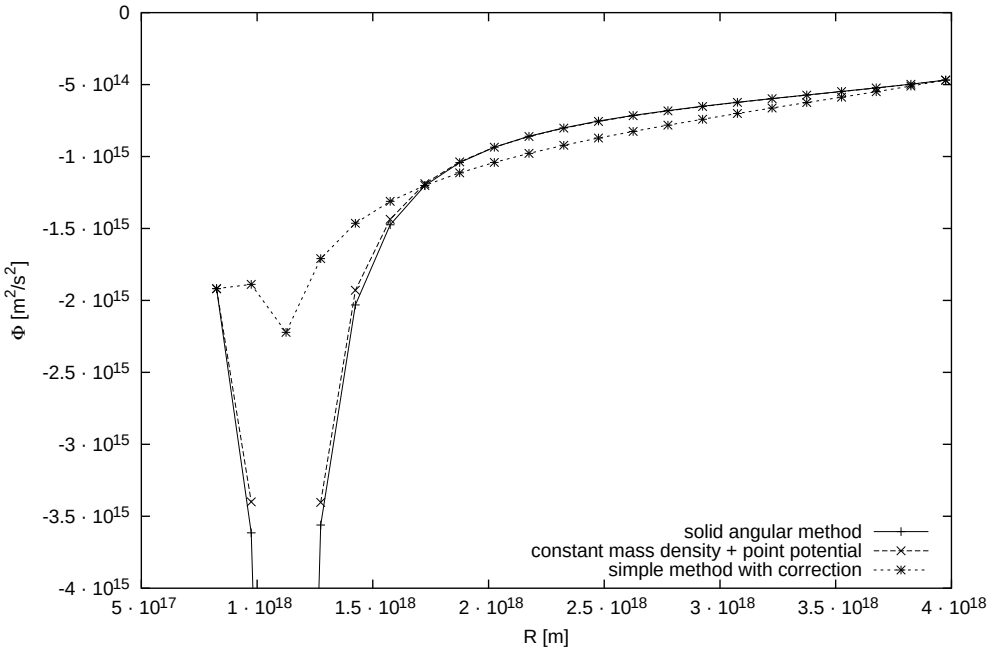

Figure 4.7: Same as Figure 4.6, but in addition, the result for the 2π-method with corrections shown (see Section 4.2.2, short dashed line with $*$-symbols) which gives a significantly different result.

but smaller radius is cut out of the middle to make a cylinder ring. The inner radius is $R_i = 7.5{\cdot}10^{17}$ m, the outer radius is $R_a = 4.05{\cdot}10^{18}$ m, the height is $h = 1.5{\cdot}10^{13}$ m which is the height of one cell. The dimensions of the equidistant grid in NIRVANA2.0 are $n_R \times n_\varphi \times n_z = 20 \times 48 \times 7$ (where the disk is one cell wider at each boundary in the radial direction). In this first setup the influence of the inner disk is obviously neglected.

In a second slightly different setup, the density of one cell has been raised by a factor of 10^3 to check the behavior of non-constant density.

In a third setup, the first setup was changed such that the cylinder was a full one and thus the inner disk, inside the inner radius of the numerical domain, was taken into account.

4.3.2 Comparison of the methods

In Figure 4.3, the result of NIRVANA2.0 using Equation (4.23) for the boundary condition of the potential can be seen at $z = 0$ as the solid line with $+$-symbols, also shown is the potential by integrating Equation (4.20) (see Section 4.2.2, dashed line with $\times$-symbols). Obviously, the correction, as described in Section 4.2.2, is necessary. The solid angle method to calculate the boundary conditions of Section 4.2.3 gives, for constant mass distributions in the disk, results so similar to the 2π-method with correction that the two curves could not be distinguished in a plot like Figure 4.4. Using NIRVANA2.0 with the solid angle method gives a result as shown in Figures 4.4 and 4.5 as the solid line with $+$-symbols in comparison to the results of integrating Equation (4.20) as described in Section

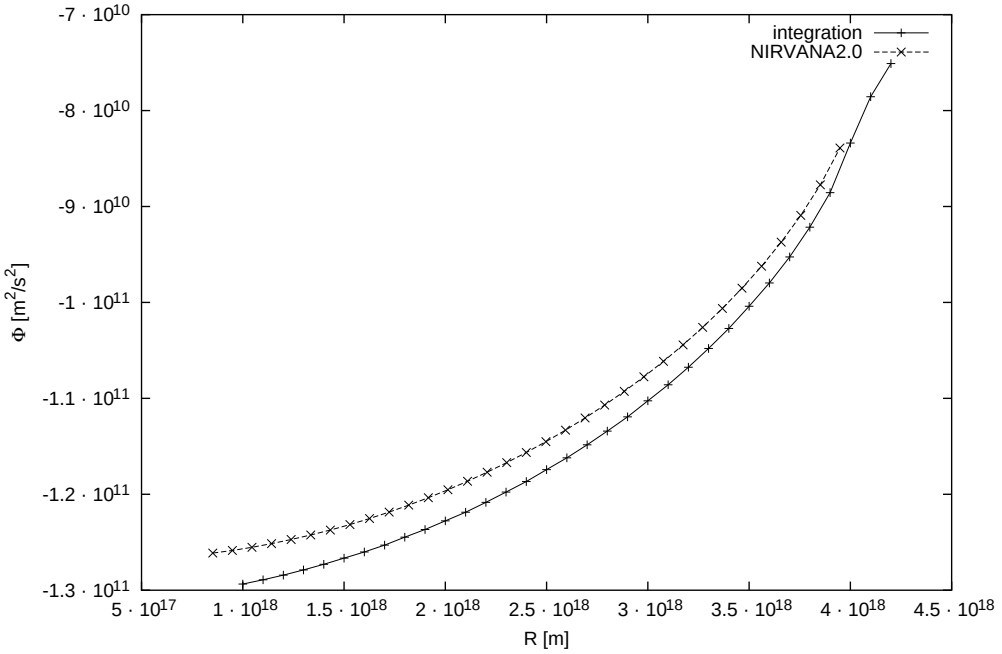

Figure 4.8: Potential for a cylinder with constant density with NIRVANA2.0 using the solid angle method (see Section 4.2.3, dashed line with ×-symbols) in comparison to the result of the integration of Equation (4.20) (see Section 4.2.2, solid line with +-symbols).

4.2.2 shown as the dashed line with ×-symbols. In Figure 4.6, the same is done for the solid angle method, though in one cell the density has been raised by a factor of 10^3. The comparison is the result of NIRVANA2.0 as shown in Figure 4.4 plus a point mass potential. In Figure 4.7, the same is shown and in addition the result of NIRVANA2.0 using the 2π-method with corrections (see Section 4.2.2, short dashed line with $*$-symbols). So the corrected 2π-method gives a potential that is not acceptable.

In Figures 4.8 (potential) and 4.9 (negative acceleration) the result of the integration and the solid angle method using NIRVANA2.0 is shown for the full cylinder again. The two curves agree acceptably well. The small fluctuations in the acceleration for the integration is due to the high precision needed and the fact that the calculations took a lot of CPU-time for this double integral. We demanded an error of less than 10^{-4} and 10^{-6} for the R- and k-integration respectively.

4.3.3 Using different heights

We also allow a Gaussian profile for the mass distribution in the z-direction. If this is done using the solid angle method and a scaleheight of $h = 3{\cdot}10^{12}\,\mathrm{m}$, the potential at $z = 0$ does not change. Even if the height is changed in the middle of the disk from $h = 3{\cdot}10^{13}\,\mathrm{m}$ to filling the mid-plane cells only (not changing the surface density), this does not affect the potential. Although for a higher

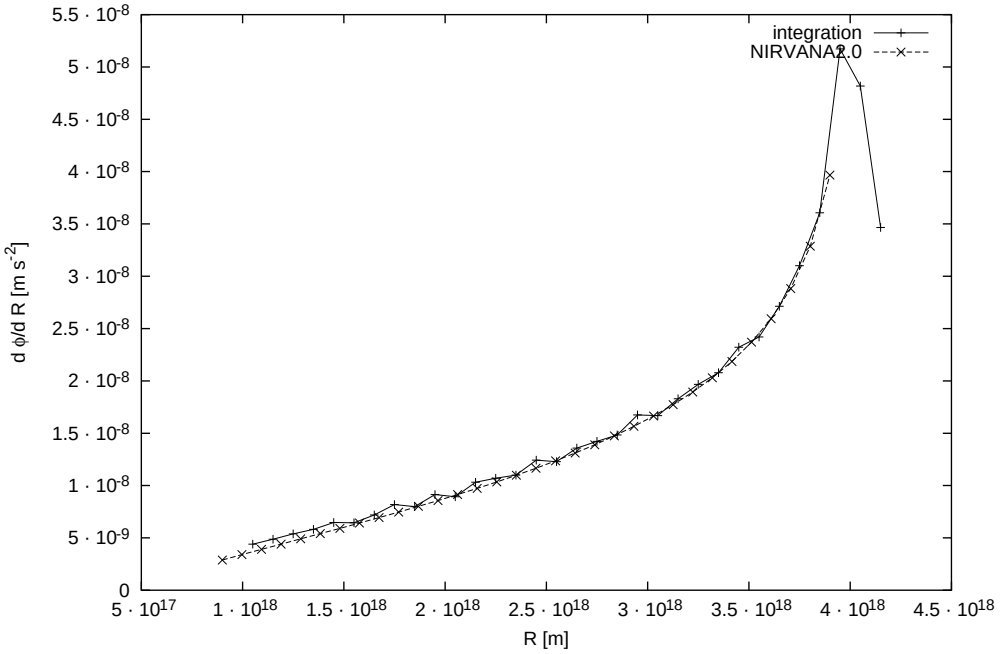

Figure 4.9: Same as Figure 4.8, but for the derivative of the potential.

resolution[2] of $n_R \times n_\varphi \times n_z = 40 \times 100 \times 7$, the potential changes completely for a Gaussian profile[3], as shown in Figure 4.10. With 23 instead of 7 cells of the same size in the z-direction, this effect vanishes and results in the usual potential. This is an indication that the method is not good in the case that a large mass is distributed over the whole height of the calculation domain.

4.3.4 The case $h > z_{\max}$

To verify that the alternative height calculation in Section 4.1.2 does not introduce a large error, we calculated the potential of a cylinder of radius $R = 5{\cdot}10^{16}\,\mathrm{m}$, density $\rho_1 = 1{\cdot}10^{-17}\frac{\mathrm{kg}}{\mathrm{m}^3}$ and height of $h_1 = 1{\cdot}10^{16}\,\mathrm{m}$, using the program introduced in Section 4.2.2. The radius roughly corresponds to half the radial extent of a cell in NIRVANA2.0 for the resolution $n_R \times n_\varphi = 31 \times 63$, an inner radius of $R_i = 9{\cdot}10^{18}\,\mathrm{m}$ and an outer radius of $R_a = 3.9{\cdot}10^{18}\,\mathrm{m}$, *i.e.*, we use a cylinder as a simple model for the complex geometry of a cell in a cylindrical grid. Then the same is done for a cylinder of the same radius but with a height $h_2 = 1.2{\cdot}10^{14}\,\mathrm{m}$ and density $\rho_2 = \frac{h_2}{h_1}\rho_1 = 83.3\frac{\mathrm{kg}}{\mathrm{m}^3}$, *i.e.*, with the same mass but different height, as would happen in NIRVANA2.0 if the calculated height h in a cell is $1{\cdot}10^{16}\,\mathrm{m}$ but $z_{\max} = 1.2{\cdot}10^{14}\,\mathrm{m}$. The relative deviation between the two potentials can be seen in Figure 4.11. Obviously the error is very small. But what about the z-derivative of the potential at $z_{\max}$ that is used for the boundary condition? This is plotted in Figure 4.12 at $z = z_{\max} = 6{\cdot}10^{13}\,\mathrm{m}$. It is the relative deviation for a cylinder of $h_1 = 1{\cdot}10^{16}\,\mathrm{m}$ and for one with $h_2 = 1.5{\cdot}10^{13}\,\mathrm{m}$ and the corresponding ρ. Again

[2]The pseudo-time step size had to be multiplied by 2000 in this case (see Section 4.1.2)

[3]This happens for the solid angle method as well as for the corrected 2π-method (where the solid angle method was used for corrections) the same way.

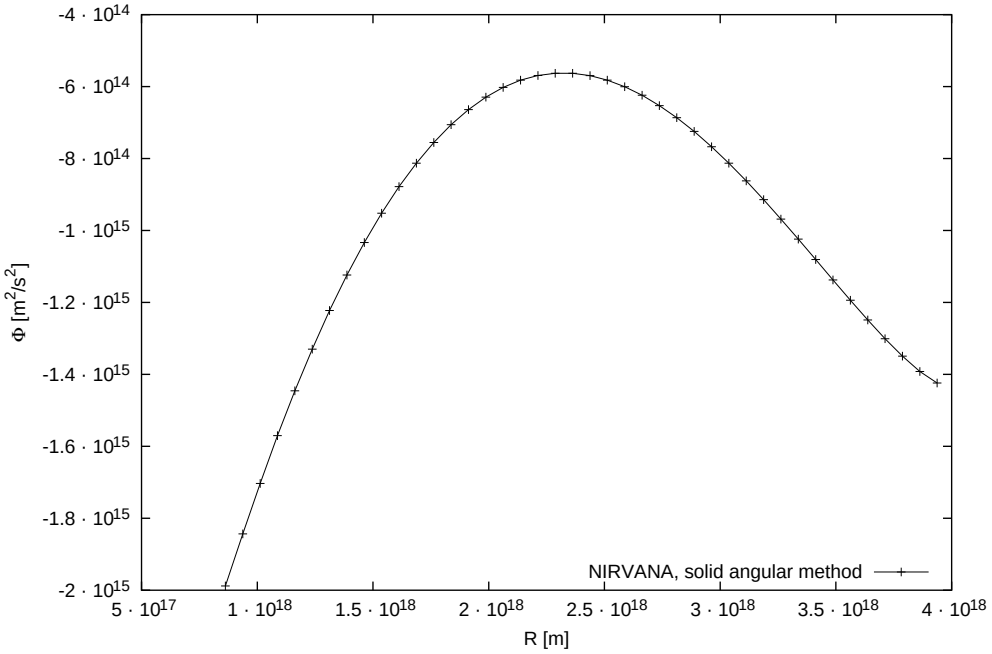

Figure 4.10: Potential for constant density in NIRVANA2.0 using the solid angle method and a higher resolution of $n_R \times n_\varphi \times n_z = 40$ x 100 x 7 (see text).

the error is small. Running NIRVANA2.0 two times with an isothermal equation of state, once with the correction described here and the second time without the correction, showed no qualitative differences. The reason is that $h > z_{\max}$ happens only for very small Σ and thus for cells that do not have strong gravity and no influence on the dynamics in the disk.

4.4 Behavior of the method

4.4.1 Convergence

For the resolution as used in Section 4.3.1, the convergence to a residual[4] smaller than 10^{-4} takes about 700 pseudo-time steps and a CPU-time on a 2 GHz PC for each time step of about 12 s. For a higher resolution of $n_R \times n_\varphi \times n_z = 40 \times 100 \times 7$, a time step takes about 23,000 pseudo-time steps and 30 minutes. Of course, it is possible that the pseudo-time step size is not chosen optimally in spite of many trials.

As a comparison, for a cube-like grid, it only takes about $\mathcal{O}(10)$ pseudo-time steps and the default maximal number of pseudo-time steps in NIRVANA2.0 is 300. The reason for the bad convergence seems to be the high aspect ratios of the grid cells.

[4]The residual is defined by $\max_{\vec{x}} \left| \frac{\Delta\Phi}{4\pi G\rho(\vec{x})} - 1 \right|$.

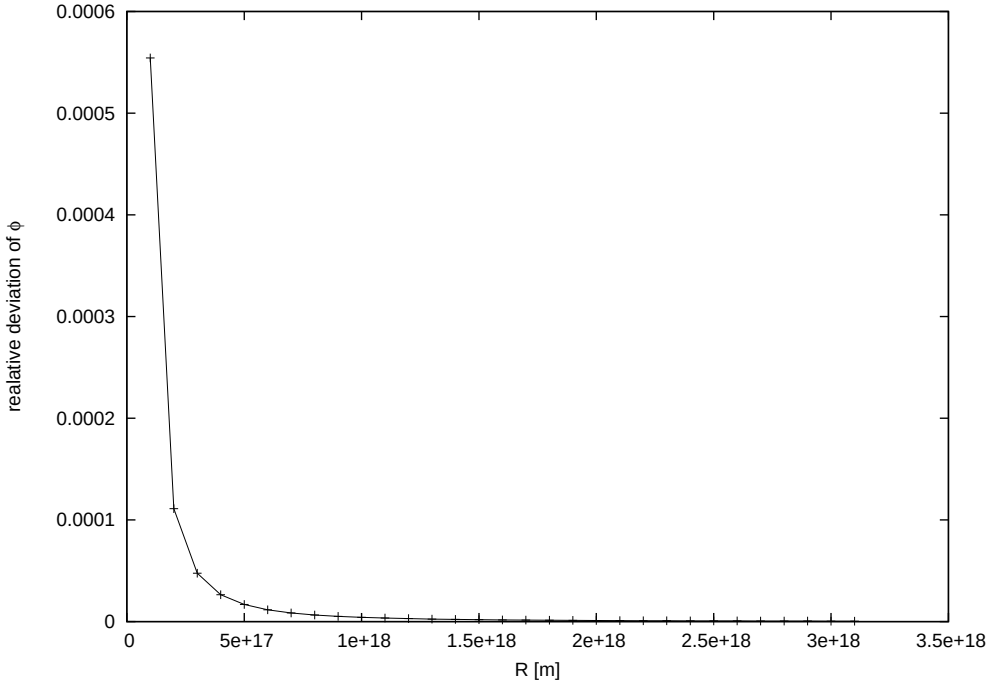

Figure 4.11: The relative deviation for the potential of two different cylinders. One with height $h_1 = 1{\cdot}10^{16}\,\mathrm{m}$ the other with $h_2 = 1.2{\cdot}10^{14}\,\mathrm{m}$. Both have the same mass.

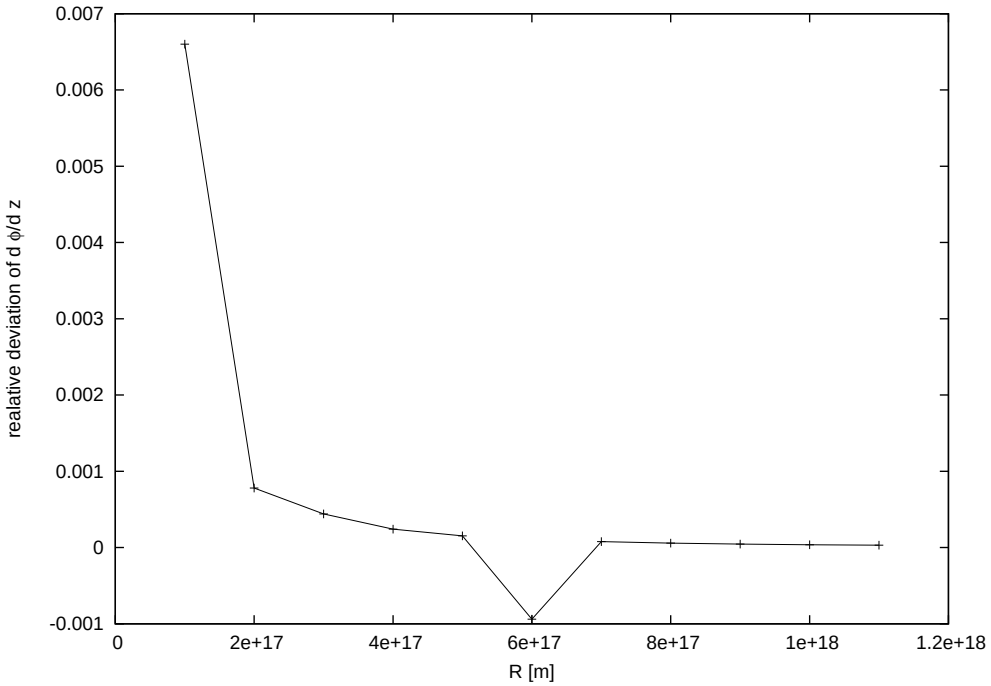

Figure 4.12: The relative deviation of the z-derivative for the potential of two different cylinders at $z = z_{\max} = 6{\cdot}10^{13}\,\mathrm{m}$, one with height $h_1 = 1{\cdot}10^{16}\,\mathrm{m}$ and the other with $h_2 = 1.5{\cdot}10^{13}\,\mathrm{m}$. Both have the same mass.

4.4.2 Time complexity and a faster computation of the z-boundary condition

Obviously, the time complexity for calculating the radial boundary conditions for the potential is $\mathcal{O}(n_R n_\varphi^2 n_z)$, whereas for the z-boundary conditions using the corrected 2π-method, it is $\mathcal{O}(n_R n_\varphi n_z)$ and $\mathcal{O}(n_R^2 n_\varphi^2 n_z)$ for the solid angle method. Each recursive pseudo-time step of the ADI solver has the complexity $\mathcal{O}(n_R n_\varphi n_z)$. Thus as long as the convergence is good, using the solid angle method, the z-boundary conditions calculation is the limiting algorithm for time. With the grid as described in Section 4.3.1, the time difference between the corrected 2π-method and the solid angle method is smaller than 1%. The reason is that the convergence is not good (see Section 4.4.1), such that the ADI solver takes much more time than the calculation of the boundary conditions.

For higher resolutions, the time performance of the solid angle method may become too slow. To circumvent this, the z-boundary condition has been altered in a way that the summation in the φ-direction was done by the convolutions theorem and a fast Fourier transform (FFT) (see, *e.g.*, Press et al., 1992). Unfortunately, the usual FFT needs to have the number of elements $N = 2^n, n \in \mathbb{N}$, while the multi-grid method of Section 4.5 needs $N = 2^n - 1, n \in \mathbb{N}$. Here, a C-subroutine taken from Engeln-Müllges and Reutter (1996) is used that uses the convolution theorem to be able to use any number of elements N for an FFT. Since this method has to perform three instead of one convolution and one has additional calculational costs, it was measured to need about three to four times as much time as a simple convolution. Nevertheless, it reduces the time complexity for calculating the z-boundary conditions to $\mathcal{O}(n_R^2 n_\varphi \log(n_\varphi) n_z)$ which pays off for higher resolutions.

4.5 A multi-grid algorithm for the ADI-solver

To overcome the problems described in Section 4.4.1, a multi-grid algorithm for the ADI-solver in NIRVANA2.0 has been implemented.

4.5.1 The multi-grid method

An introduction to the multi-grid method can be found, *e.g.*, in Hackbusch (1985). It is a theoretically understood observation that most grid methods for the solution of differential equations converge faster on small scales (compared to the grid size) than on large scales. For this reason the idea is to perform a step with a known grid method (which in our case is the ADI method) first. Then we perform a step using the same method on a coarser grid. This is done for every (pseudo-)time step. It helps to reduce the error on larger scales, *i.e.*, for lower frequencies. It can be iterated to coarser and coarser grids until the calculation domain consists of a single cell only.

May the discretized equation to solve be

$$L_l u_l - f_l = 0 \tag{4.29}$$

as defined on the fine grid labeled l, where L_l is the discretized differentiation operator and u_l is the searched solution. Writing the error as

$$v_l = \bar{u}_l - u_l \tag{4.30}$$

($\bar{u}_l$ being the approximate solution of the iteration step on the fine grid), exchanging u_l by $\bar{u}_l$ in Equation (4.29) we define the so called defect

$$d_l := L_l \bar{u}_l - f_l. \tag{4.31}$$

It is a measure for the error. Since $L_l v_l = L_l \bar{u}_l - L_l u_l = L_l \bar{u}_l - f_l = d_l$, we get

$$L_l v_l = d_l. \tag{4.32}$$

This has the same form as (4.29) and can thus be solved with the same method. The problem is mapped on to the coarser grid to be solved there. This is done since the error is known to contain more low than high frequencies (after the iteration on the fine grid), and the low frequencies converge better on a coarser grid, as stated before. This mapping is called *restriction* or just r and results in

$$L_{l-1} v_{l-1} = d_{l-1} \quad \text{with} \quad d_{l-1} = r d_l. \tag{4.33}$$

After solving this equation, the result has to be interpolated on the finer grid again. This is called *prolongation* or just p:

$$\tilde{v}_l = p v_{l-1}, \tag{4.34}$$

giving us a new approximate solution for the next (pseudo-)time step

$$u_l^{\text{new}} = \bar{u}_l - \tilde{v}_l. \tag{4.35}$$

Using recursive functions, a multi-grid algorithm in pseudocode could look like this (taken from Hackbusch, 1985):

multi-grid iteration $MGM^{(\nu_1,\nu_2)}$ for solving $L_l u_l = f_l$

procedure $MGM(l, u, f)$**; integer** l**; array** u, f**;**
if $l = 0$ **then** $u := L_0^{-1} * f$ **else**
begin array d, v**; integer** j**;**
  $u := \mathcal{S}_l^{(\nu_1)}(u, f)$**;**
  $d := r * (L_l * u - f)$**;**
  $v := 0$**;**
  for $j := 1$ **step** 1 **until** γ **do** $MGM(l-1, v, d)$**;**
  $u := u - p * v$**;**
  $u := \mathcal{S}_l^{(\nu_2)}(u, f)$**;**
end;

Here $\mathcal{S}_l^{(\nu)}$ is the solver on the l-grid, performing ν steps and L_0^{-1} is the inverse differential operator on the grid consisting of a single cell. Thus on each grid, ν_1 steps are performed, and then the procedure is called recursively γ times for the coarser grid and after that ν_2 steps are performed.

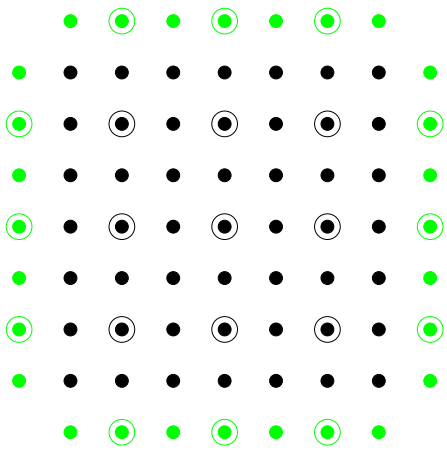

Figure 4.13: Two grids of a multi-grid method. The finer grid is depicted as the full circles and the coarser grid as the open ones. The green circles are the boundary cells.

4.5.2 Implementation for the NIRVANA2.0 ADI-solver

The simplest way to implement such a scheme as done here is to use a grid of $2^l - 1$, $l \in \mathbb{N}$, number of cells in each direction. Figure 4.13 shows how this looks in two dimensions. If the grid has different numbers of cells in each direction the lowest l may not be zero.

Since in the present case the z-direction has only a minor number of cells and in addition it is very small, it was observed that the coarsening in this direction did not help to improve convergence. Thus only in the R- and φ-directions the multi-grid method is used. For this a file `multigrid.c` was written with the main, recursive function `multigrid`, called from the `gravity` function. As restriction the nine-point formula was used. It is a weighted average of the next and next-to-next neighbors, written in the matrix form like this:

$$\frac{1}{16}\begin{bmatrix} 1 & 2 & 1 \\ 2 & 4 & 2 \\ 1 & 2 & 1 \end{bmatrix}, \tag{4.36}$$

i.e., the center cell is weighted by $\frac{1}{16} \cdot 4$, the next neighbors are weighted by $\frac{1}{16} \cdot 2$ and the next-to-next neighbors are weighted by $\frac{1}{16} \cdot 1$. A very similar method is used for the prolongation, the so called nine-point prolongation. Let the points (0,0), (0,2h), (2h,0), (2h, 2h) be on the coarse grid, where h is the mesh size of the finer grid. On the mentioned points, $v_l = v_{l-1}$ is set trivially. For the other

points, we set:

$$v_l(0,h) = \frac{1}{2}v_{l-1}(0,0) + \frac{1}{2}v_{l-1}(0,2h), \tag{4.37}$$

$$v_l(h,0) = \frac{1}{2}v_{l-1}(0,0) + \frac{1}{2}v_{l-1}(2h,0), \tag{4.38}$$

$$v_l(2h,h) = \frac{1}{2}v_{l-1}(2h,0) + \frac{1}{2}v_{l-1}(2h,2h), \tag{4.39}$$

$$v_l(h,2h) = \frac{1}{2}v_{l-1}(0,2h) + \frac{1}{2}v_{l-1}(2h,2h), \tag{4.40}$$

$$v_l(h,h) = \frac{1}{4}v_{l-1}(0,0) + \frac{1}{4}v_{l-1}(0,2h) + \frac{1}{4}v_{l-1}(2h,0) + \frac{1}{4}v_{l-1}(2h,2h). \tag{4.41}$$

Symbolized by a stencil this is

$$\begin{bmatrix} \frac{1}{4} & \frac{1}{2} & \frac{1}{4} \\ \frac{1}{2} & 1 & \frac{1}{2} \\ \frac{1}{4} & \frac{1}{2} & \frac{1}{4} \end{bmatrix}. \tag{4.42}$$

This represents a linear interpolation.

4.5.3 Parameters and performance

For resolutions of, *e.g.*, $n_R \times n_\varphi \times n_z = 31 \times 63 \times 7$ and $n_R \times n_\varphi \times n_z = 63 \times 127 \times 7$, the typical number of iteration steps needed to reach a residual of 10^{-4} was around 10 to 40, which is up to three orders of magnitude better than described in Section 4.4.1 although the chosen parameters in that section where not optimal. Actually finding the best parameters is still a problem and the parameters depend greatly on the resolution and size of the grid.

When performing a run of the simulation, the number of iterations necessary can temporarily grow significantly above the cited level and even become larger than the maximum set to 1000 steps in which case the program stops. The reason is related to strong density gradients leading to differences of many orders of magnitude ($\sim$ 6 to 10) between neighboring cells.

4.6 The cooling function and its implementation

4.6.1 The used cooling function

The energy Equation (2.6) is solved in NIRVANA2.0 by first-order finite difference, where a predictor-corrector method is used for the compressional heat part. A cooling part as in Equation (2.93) is not implemented in NIRVANA2.0.

Here a radiative cooling part is implemented following Hubeny (1990) using a total effective optical depth τ_{eff} where

$$\Lambda = \frac{16}{3}\sigma T_{\text{eff}}^4, \; T_{\text{eff}}^4 = \frac{T^4}{\tau_{\text{eff}}} \tag{4.43}$$

with

$$\tau_{\rm eff} := \tau_{\rm R} + \frac{2}{\sqrt{3}} + \frac{2}{3\tau_{\rm P}},\ \tau_{\rm R/P} = \frac{1}{2}\Sigma\kappa_{\rm R/P}, \tag{4.44}$$

where σ is the Stefan-Boltzmann constant, $T_{\rm eff}$ is the effective temperature, T is the central temperature, $\tau_{\rm R/P}$ is an optical depth with $\kappa_{\rm R/P}$ being its corresponding opacity. $\tau_{\rm R}$ and $\tau_{\rm P}$ are the Rosseland and Planck mean optical depths as described in Section 2.6. An effective optical depth description is chosen here to describe the transition from optically thin to thick. There are also other effective optical depths in use, *e.g.*, one from Artemova et al. (1996), that can be written as $\tau_{\rm eff} = \tau_{\rm R} + \frac{4}{3} + \frac{2}{3\tau_{\rm P}}$ (see Mayer, 2004). The two descriptions are not identical although the difference is never larger than about 6%, and the difference vanishes in the optically thick and thin regimes. For this work the main question concerning cooling is whether a clump, which usually is optically thick, can cool efficiently enough to collapse. Thus the choice of the effective optical depth does not affect the main point of this thesis.

For the opacities, an interpolation formula for Rosseland opacities by Gail (2003) is used. This is also used for the optically thin case which is not a bad approximation for temperatures below a few 100 K (Biermann, 2001).

4.6.2 The numerical implementation

Unfortunately, the cooling times turn out to be much smaller than the typical time step size calculated from the CFL condition (see Section 2.7.2). Thus a simple explicit Euler method does not work and can even give negative values for the temperature. Only first-order implicit methods can guarantee positivity for arbitrary step sizes (Sandu 2001 and references therein), but here the implicit Euler method does not give results accurate enough. Thus an implicit Euler scheme (as described in Section 2.7.1) with an adaptive step size has been implemented, *i.e.*, during one NIRVANA2.0 time step the cooling subroutine can carry out several time steps to calculate the cooling for that NIRVANA2.0 time step. The implicit Euler scheme is implemented by the method of bisection (see below) to guarantee convergence even if opacity tables, and therefore non-continuous opacities, would be used. An adaptive step size method taken from Engeln-Müllges and Reutter (1996) is used as follows. The a-posteriori error of a finite difference scheme solving the equation $\dot{y}(t) = f(y,t)$, where the dot indicates the time derivative, with the numerical solution $Y_h(t)$ for the step size h, can be approximated by

$$e_h := y(t) - Y_h(t) \approx \frac{Y_h(t) - Y_{\tilde{h}}(t)}{\left(\frac{\tilde{h}}{h}\right)^q - 1}, \tag{4.45}$$

where q is the order of the method. This can be used in the following way. Carry out two time steps with $\Delta t = h$ and one (starting at the same point in time) of $\Delta t = \tilde{h} = 2h$ using the implicit Euler rule. Then calculate the error using Equation (4.45) giving $e_h \approx Y_h(t) - Y_{2h}(t)$. If the relative error is smaller than the demanded one, go to the next time step. Otherwise repeat this time step with half the time step size. In addition we allowed the time step size to grow by a factor of two if the relative error was an order of magnitude smaller than

demanded. In this program a relative error of 10^{-2} was demanded. Due to CPU-time restrictions this was not set to be smaller. The first step size chosen is the current time step size of NIRVANA2.0.

Using this setup, where the cooling is due to the operator splitting calculated in a different function (namely `sourceEnergy.c`) than the heating by artificial and physical viscosity – which is the dominating part of the heating – there turned out to be some problems due to operator splitting. Following LeVeque (1997), if we have an operator splitting method for the equation

$$\frac{\partial y}{\partial t} = (\mathcal{A} + \mathcal{B})y, \tag{4.46}$$

where the equation is split into the equations $\dot{y} = \mathcal{A}y$ and $\dot{y} = \mathcal{B}y$, it can be shown that the splitting error, *i.e.*, the error introduced by the splitting method alone, is

$$y(\Delta t) - Y(\Delta t) = \frac{1}{2}\Delta t^2 [\mathcal{A}, \mathcal{B}]_- y(0) + \mathcal{O}(\Delta t^3), \tag{4.47}$$

after one time step of size Δt, where $[\mathcal{A}, \mathcal{B}]_- := \mathcal{A}\mathcal{B} - \mathcal{B}\mathcal{A}$ is the commutator, y is the solution of Equation (4.47) and Y is the approximate solution when the operators are split. In our case, we have $y = e$, $e \propto T$ and $\mathcal{A} \propto -\frac{T^3}{\tau_{\text{eff}}}$, $\mathcal{B} \propto \frac{C}{T}$, where C is the heating calculated for the artificial and physical viscosity in `viscosity.c`. Since the two operators both change and use T, they do not commute. It turns out that this would reduce the possible time step in addition to the CFL conditions. For some opacity regions this would restrict the time step size extremely even if the relative error was allowed to be as much as 10%.

Thus in the case of heating by viscosity and cooling, the above mentioned implicit adaptive step-size method was used instead of the operator splitting, *i.e.*, the equation

$$\frac{\partial e}{\partial t} = -\Lambda + C \tag{4.48}$$

is solved instead of the equation of cooling alone.

Bisection (see, *e.g.*, Press et al., 1992) is the simplest root finding algorithm. For the equation $f(x) = 0$, if for an interval $\left[a, b\right]$ in x, $f(x)$ is known to have different signs at the boundaries, the middle of this interval $\frac{a+b}{2}$ is used as a new boundary. Then the new interval is $\left[a, \frac{a+b}{2}\right]$ or $\left[\frac{a+b}{2}, b\right]$ such that $f(x)$ again changes sign in the interval. This can be iterated as far as necessary every time which decreases the error by a factor of two in each iteration. This method is guaranteed to converge to one solution when starting with different signs at the interval boundaries. As starting points $e_1 = 1{\cdot}10^{-37}$ and $e_2 = 10 \cdot e$ are used. The factor of 10 in the second boundary is used to allow e to rise. The bisection is iterated 20 times, guaranteeing an accuracy of 2^{-20}, *i.e.*, 6 digits. Expecting e not to change its order of magnitude in one time step, this gives a relative error of $\mathcal{O}(10^{-5})$ (due to the above additional factor of 10).

Chapter 5

Testing the setup

The goal of this chapter is to show that the main outcome of the simulations does not depend critically on the chosen numerical parameters. It will be shown that the details do change with the parameters but the main points remain, *i.e.*, clumps form of the same order of magnitude in size and after a short period of quiescence a fast accretion at the inner boundary of the calculation domain and a strong outflow at the outer range is established. This happens due to the interaction between the clumps. The mass accretion and outflow is roughly the same in all runs. As we have seen in Chapter 3, the system is linearly unstable. Thus we cannot expect the details of different runs to be the same even if the parameters are changed only slightly.

5.1 Changing the resolution

As a check of the influence of resolution on the simulation results we made two runs with different resolutions but exactly the same parameters otherwise. The higher resolution is also used for the main simulation (see Section 6.1), *i.e.*, $n_R \times n_\varphi = 63 \times 127$. The lower resolution run has $n_R \times n_\varphi = 31 \times 63$. The number of cells in the z-direction, n_z, stayed the same, *i.e.*, 7. In Figure 5.1 (a) we show the integrated accreted mass at the inner radial boundary for the high (solid line) and low (dashed line) resolution runs. In Figure 5.1 (b) the same is shown for the integrated mass that passed the outer radial boundary of the calculation domain. Both graphs show that there is a difference but also that the curves agree qualitatively.

On the other hand, Figure 5.2 shows the surface density distribution of both runs after $9.4{\cdot}10^5$ years when the turbulence has fully developed, and there is still a lot of mass in the disk. Differences are obvious when comparing the two graphs. The clumps in the high-resolution run are more compact, have higher density and they are more numerous. This indicates that the resolution is not high enough to follow the fragmentation in detail. Truelove et al. (1997) have shown that to follow the fragmentation, a resolution of $\frac{\Delta x}{\lambda_\mathrm{J}} = 0.25$ is needed. This resolution is not reasonable using this code without AMR since $\lambda_\mathrm{J} = \mathcal{O}(10^{13})\,\mathrm{m} = \mathcal{O}(10^{-4})\,\mathrm{pc} \ll \Delta R = 4.76{\cdot}10^{16}\,\mathrm{m} = 1.54\,\mathrm{pc}$ here. Therefore our aim in this work cannot be to follow the fragmentation. On the other hand the qualitative appearance is similar

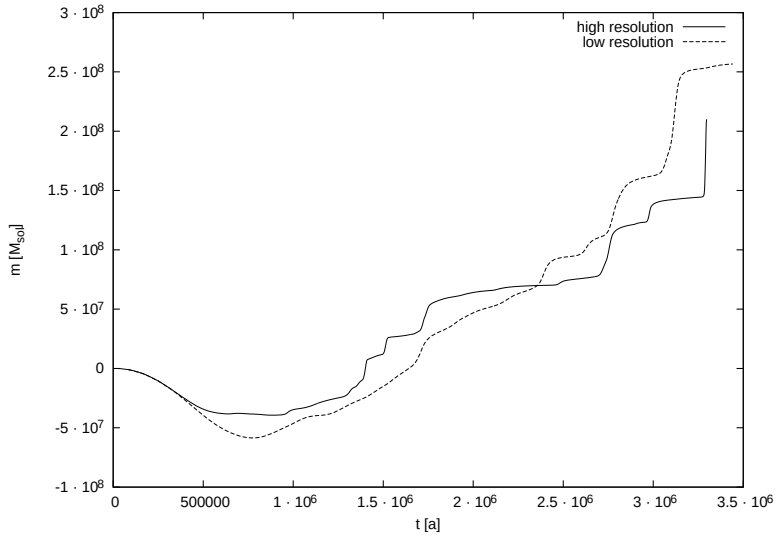

(a) Accreted mass

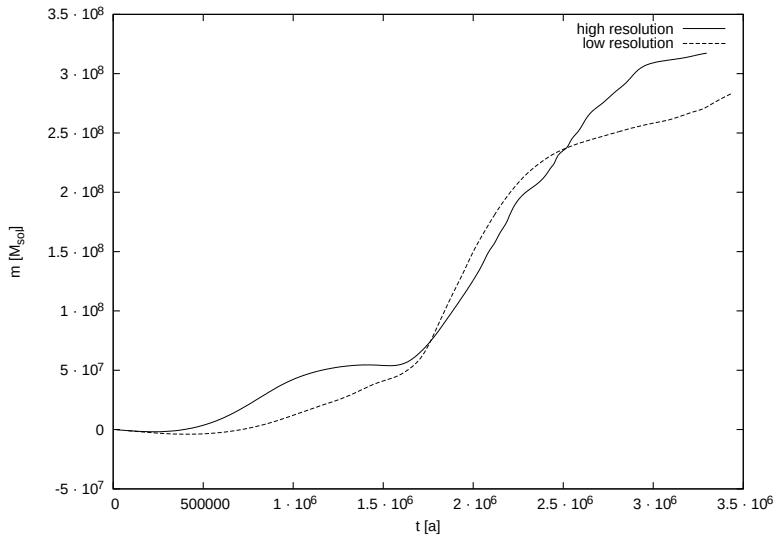

(b) Lost mass due to outflow at the outer radial boundary

Figure 5.1: The integrated accreted mass in solar masses at the inner boundary of the calculation domain (a) and the integrated outflow mass of the calculation domain at the outer radial boundary (b) versus time in years. The solid line is for the high-resolution run with 63×127 grid points, the broken line is for the low-resolution run with 31×63 grid points.

and the accretion rates do not differ too much.

5.2 Using different heights for the calculation domain

In this section we compare the low-resolution run of the last section with two runs that have a height for the calculation domain which is higher by a factor of three and lower by a factor of five, *i.e.*, $9{\cdot}10^{13}\,\mathrm{m} = 2.9{\cdot}10^{-3}\,\mathrm{pc}$ and $6{\cdot}10^{12}\,\mathrm{m} = 5.8{\cdot}10^{-3}\,\mathrm{pc}$, respectively. It is expected that heights of the calculation domain that are too low do not give good results since even for the cells that include high masses (which have small heights and contribute most to the potential) a large part of the height profile of the density is cut off. This gives an incorrect profile and introduces the problems for the numerical method described in Section 4.3.3. In Figure 5.3 (a) again the integrated accreted mass that passed the inner boundary inwards is plotted, where the solid line is for the thin calculation domain, the long dashed line is for the normal case and the short dashed line is for the thick case. In Figure 5.3 (b) with the line styles corresponding to the same cases as before, the integrated mass that passed the outer boundary outwards is shown. The differences between the three curves are small in both graphs.

Looking at Figure 5.4 where the surface density distributions at $t = 9.4{\cdot}10^5\,\mathrm{a}$ is shown for the thick and thin case, we see that they do not match well. But comparing the thick case with the normal case in Figure 5.2 (b), it is obvious that their match is good. This indicates that the results do not depend on the height of the calculation domain as long as it is much larger than $6{\cdot}10^{12}\,\mathrm{m}$.

5.3 Changing the parameters of the artificial viscosity

For these tests two high-resolution runs were performed with changed artificial viscosity parameters for the tensor viscosity and the anisotropic viscosity (see Section 2.7.3). These parameters, *i.e.*, the smearing lengths in units of the grid spacing l_A and l_T, are typically set to $l_\mathrm{T}^2 = 1.5$ and $l_\mathrm{A}^2 = 2$ respectively as done in all the other runs. We compare the runs of this section with the high-resolution run in Section 5.1 which differ only by their artificial viscosity parameters. In Figure 5.5 again the integrated accreted mass (a) and the integrated outflow mass (b) are shown. The solid line is for the run with artificial viscosity parameters of $l_\mathrm{T}^2 = 3$ and $l_\mathrm{A}^2 = 4$, the long dashed line is for the normal run and the short dashed line is for artificial viscosity parameters of $l_\mathrm{T}^2 = 0.75$ and $l_\mathrm{A}^2 = 1$. Again the three curves do not differ much. The curve for the lower parameters stops at around $1.7{\cdot}10^6\,\mathrm{a}$ due to non-convergence of the gravity solver. This in turn most likely has to do with the unphysically high velocities in this run as shown in Figure 5.6 where the radial velocity at $t = 9.4{\cdot}10^5\,\mathrm{a}$ is plotted. The velocities become larger than $10^8\,\mathrm{m\,s^{-1}}$ while in the other runs it stays mainly below $10^6\,\mathrm{m\,s^{-1}}$. When looking at Figure 5.7 (b), we see that the position of the extreme velocities is close to a point with a strong density gradient. Thus we conclude that the

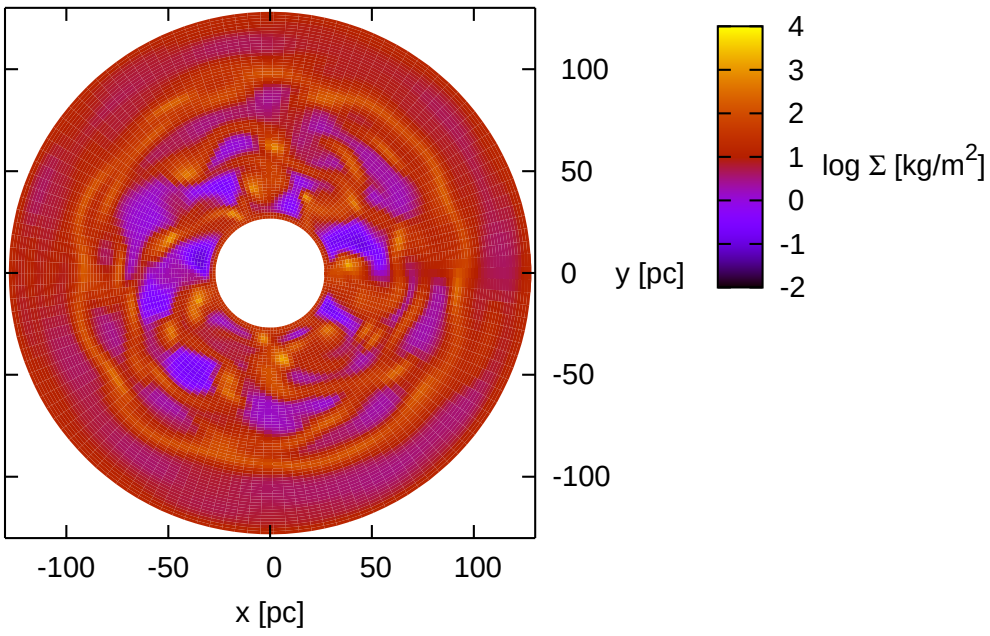

(a) Higher resolution

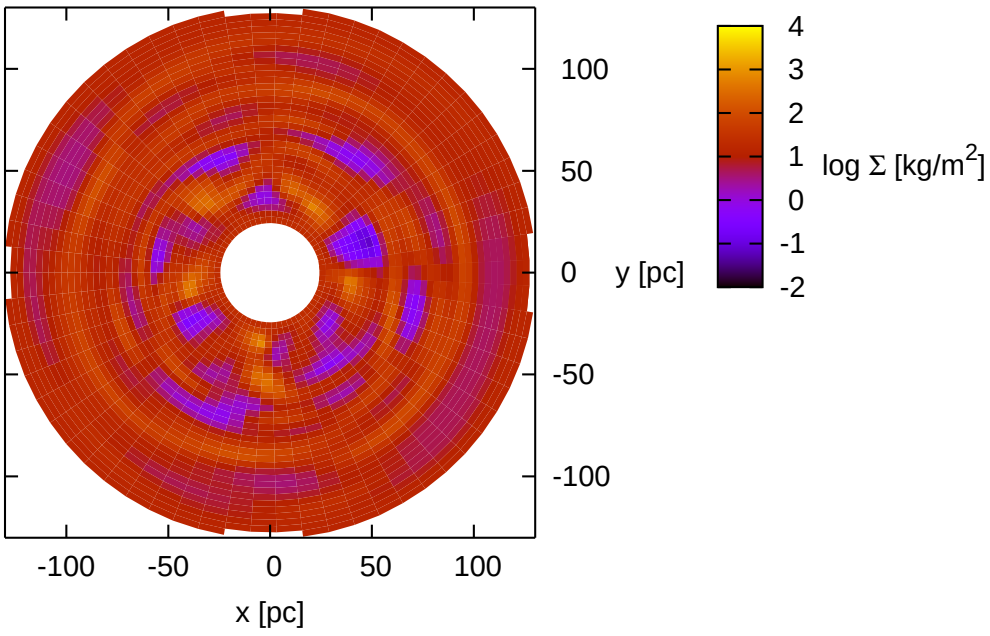

(b) Lower resolution

Figure 5.2: The decadic logarithm of the surface density in units of $\mathrm{kg\,m^{-2}}$ at t = $9.4{\cdot}10^5$ a for the higher resolution of 63×127 (a) and the lower resolution of 31×63 grid points (b). The clumps are more numerous and more compact in the higher-resolution case.

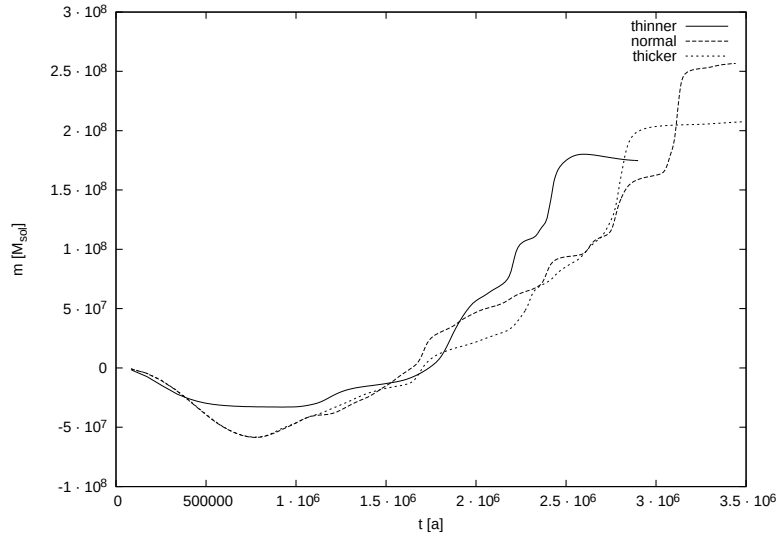

(a) Accreted mass

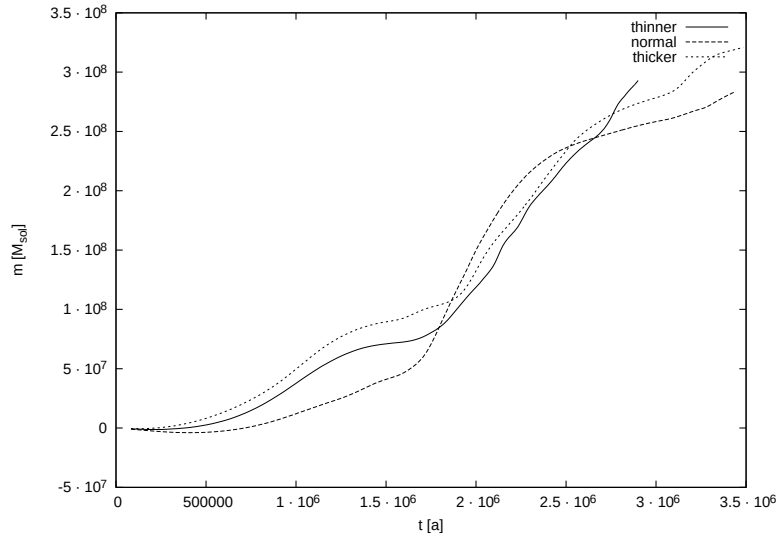

(b) Lost mass due to outflow

Figure 5.3: The integrated accreted mass at the inner boundary of the calculation domain (a) and the integrated outflow mass of the calculation domain at the outer boundary (b) versus time in years. The solid line is for the smaller height of the calculation domain of $6{\cdot}10^{12}$ m, the long dashed line is for the run with $1.5{\cdot}10^{13}$ m height, and the short dashed line is for the run with a larger height of the calculation domain of $9{\cdot}10^{13}$ m. The long dashed line in this graph is the same as the dashed line in Figure 5.1.

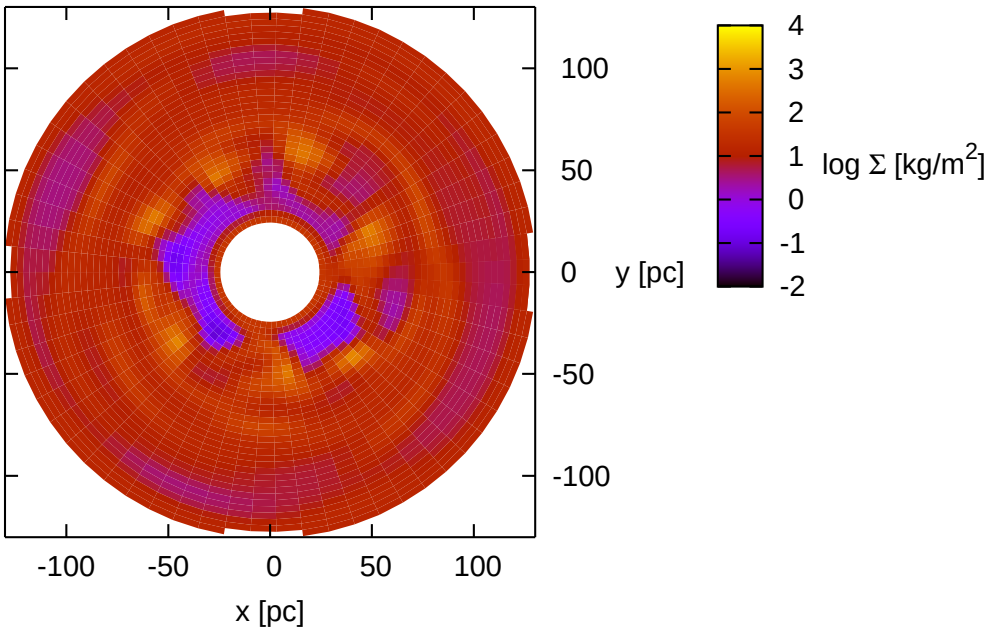

(a) Smaller calculation domain height

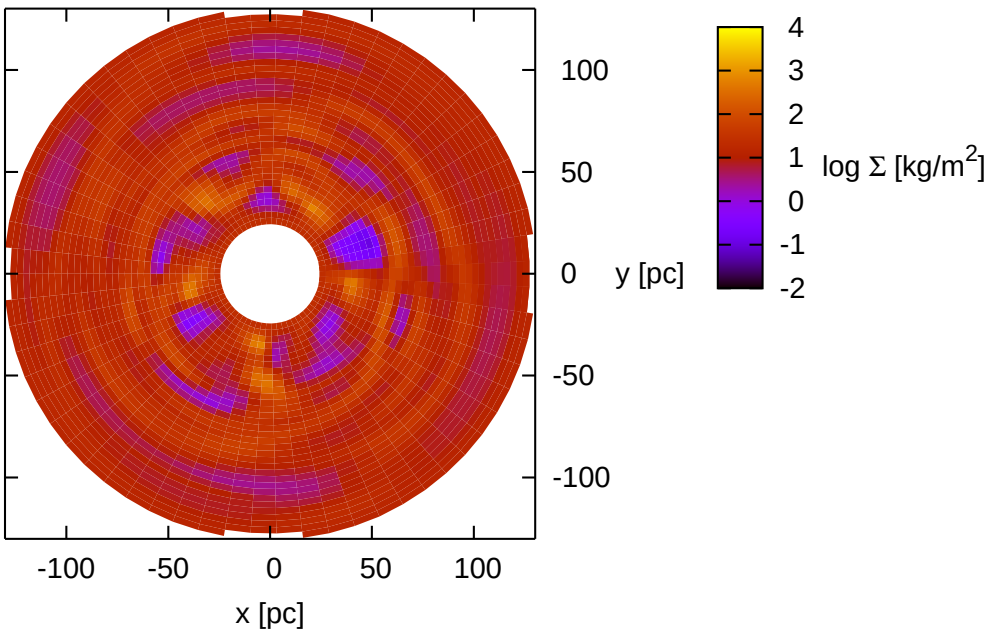

(b) Larger calculation domain height

Figure 5.4: The decadic logarithm of the surface density at t = $9.4 \cdot 10^5$ a for the run with a smaller height of the calculation domain of $6 \cdot 10^{12}$ m (a) and with a larger height of the calculation domain of $9 \cdot 10^{13}$ m (b). The corresponding graph for the run with a height of $3 \cdot 10^{13}$ m is shown in Figure 5.2 (b).

extreme velocities are due to the artificial viscosity parameters chosen to be too low.

In Figure 5.7 we show the surface density distributions for the two runs which agree qualitatively with each other, while the graph for normal artificial viscosity parameters is shown in Figure 5.2 (a).

5.4 Testing the commutability of the advection and the energy sources/sinks

As pointed out in Section 4.6.2 the operator splitting method can introduce an error when the operators do not commute. This is easily shown for the heating term which is an ordinary differential equation but the energy advection equation is a partial differential equation. This makes it much harder to calculate the commutator and thus the error. The energy advection equation is

$$\frac{\partial e}{\partial t} = -\vec{\nabla} \cdot (e\vec{v}) = -e\vec{\nabla} \cdot \vec{v} - \vec{v} \cdot (\vec{\nabla} e). \tag{5.1}$$

The first term of the last expression is proportional to e and thus T. This means that this part of the operator would keep $\mathcal{A}$ constant as used in Section 4.6.2, *i.e.*, if the temperature is independent of the position in the disk, $\mathcal{A}$ commutes with any other operator and the error vanishes. But it might not commute in the case that a temperature gradient exists. Fortunately, the strongest temperature gradients are expected and observed where the clumps form, *i.e.*, where $\vec{\nabla} \cdot \vec{v}$ is large. Thus we can hope that the first term in the last expression of Equation (5.1) dominates and the error stays small. Actually it is sufficient that the temperature changes by the same factor due to heating and cooling everywhere in the vicinity of the position where equation (5.1) is evaluated, which means that $\vec{\nabla} e$ is proportional to T and thus $\mathcal{A} =$ constant again.

We see that we have reason to believe that the error due to the operator splitting method is small. To double check this, we take a more phenomenological approach here. Two runs have been performed where the order in which the two operators are evaluated, *i.e.*, the heat source/sink and the advection, is reversed. In Figure 5.8 the integrated accretion rate at the inner boundary (a) and the integrated outflow mass at the outer boundary are plotted for the two runs. There is no difference visible. Also the surface densities (see Figure 5.9) and the temperatures (see Figure 5.10) match extremely well even at time $t = 2.3{\cdot}10^6$ a. This time was chosen to be later than for the figures of the other sections in this chapter in order to show the agreement even at such a late time. This confirms the above reasoning that the error due to the operator splitting in this case stays small. This is of course not a proof but a strong indication justifying our approach.

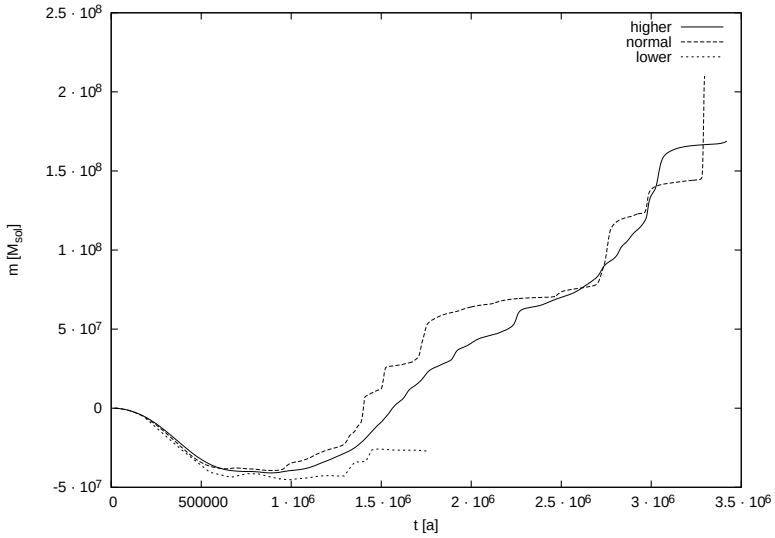

(a) Accreted mass

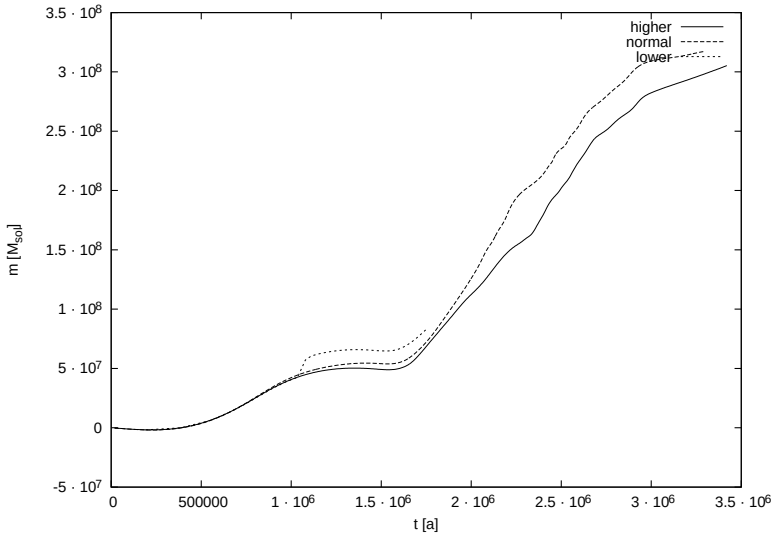

(b) Lost mass due to outflow

Figure 5.5: The integrated accreted mass in solar masses at the inner boundary of the calculation domain (a) and the integrated outflow mass of the calculation domain at the outer boundary (b) versus time in years. The solid line is for the run with higher artificial viscosity parameters of $l_{\mathrm{T}}^2 = 3$ and $l_{\mathrm{A}}^2 = 4$, the long dashed line is for the run with normal parameters of $l_{\mathrm{T}}^2 = 1.5$ and $l_{\mathrm{A}}^2 = 2$ and the short dashed line is for the run with lower parameters of $l_{\mathrm{T}}^2 = 0.75$ and $l_{\mathrm{A}}^2 = 1$. This last run stops early due to non-convergence of the gravity solver (see text). The long dashed line in this graph is the same as the solid line in Figure 5.1.

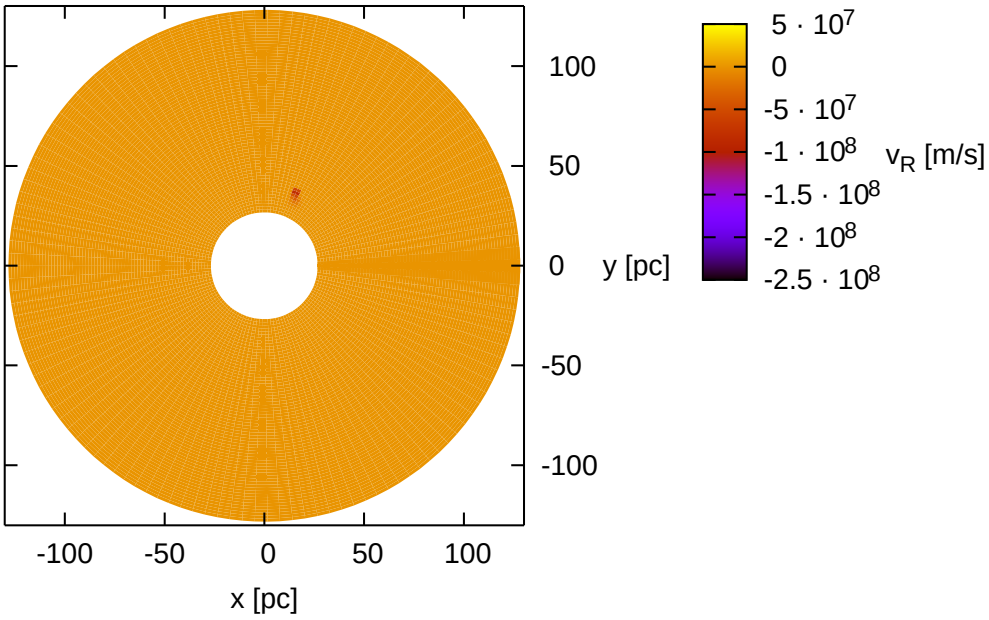

Figure 5.6: The radial velocity in $\mathrm{m\,s^{-1}}$ at $t = 9.4{\cdot}10^5\,\mathrm{a}$ for the run with lower artificial viscosity parameters of $l_\mathrm{T}^2 = 0.75$ and $l_\mathrm{A}^2 = 1$. Please refer to the text for a discussion.

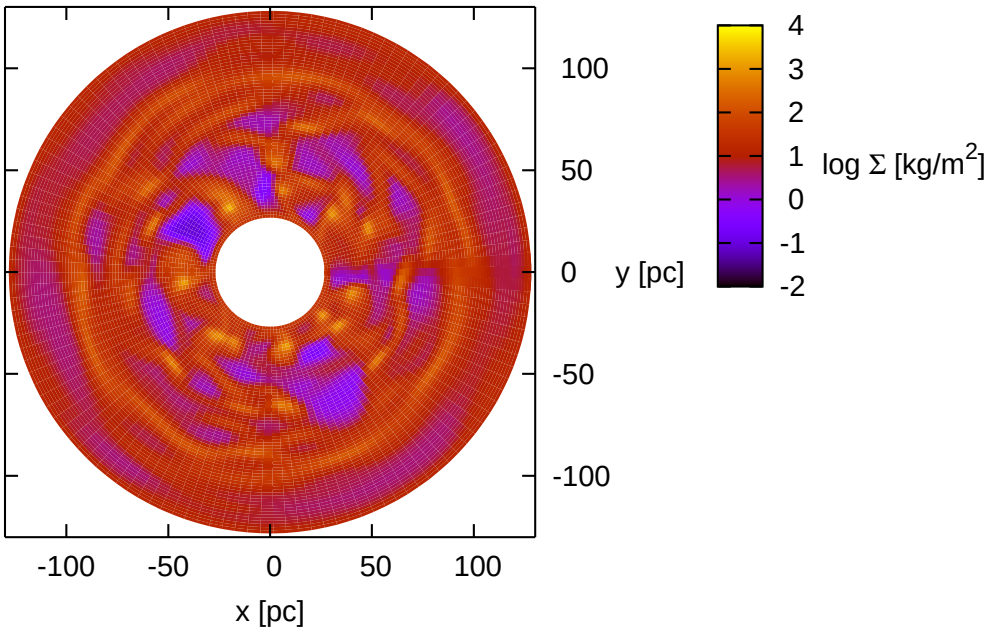

(a) Factor 2 higher artificial viscosity parameters

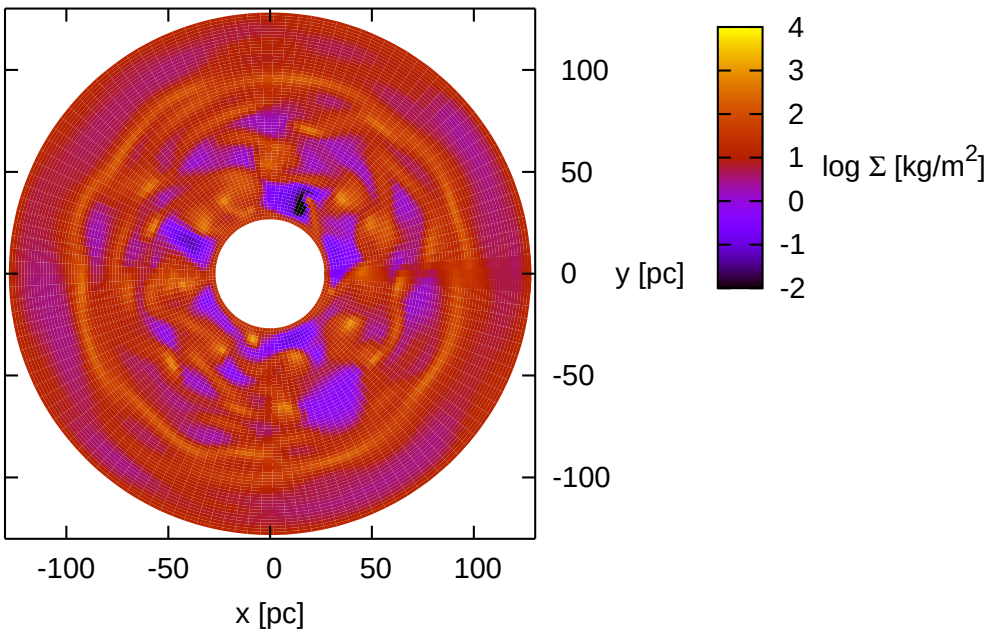

(b) Factor 2 lower artificial viscosity parameters

Figure 5.7: The decadic logarithm of the surface density in $\mathrm{kg\,m^{-2}}$ at $t = 9.4{\cdot}10^5$ a for the run with artificial viscosity parameters of $l_\mathrm{T}^2 = 3$ and $l_\mathrm{A}^2 = 4$ (a) and the run with those of $l_\mathrm{T}^2 = 0.75$ and $l_\mathrm{A}^2 = 1$ (b). The corresponding graph for the normal run with parameters of $l_\mathrm{T}^2 = 1.5$ and $l_\mathrm{A}^2 = 2$ is shown in Figure 5.2 (a).

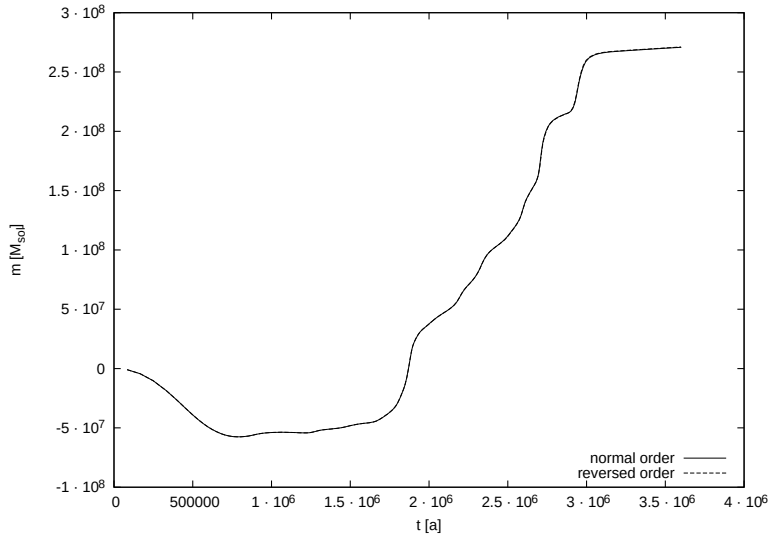

(a) Accreted mass

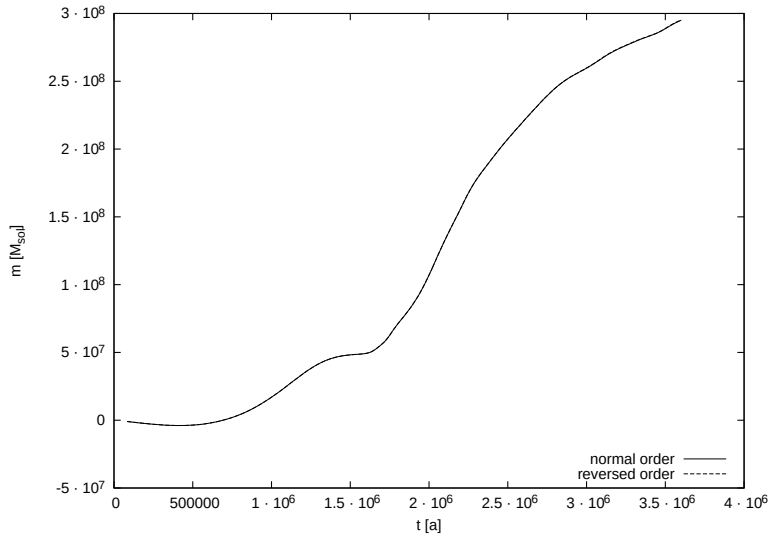

(b) Lost mass due to outflow

Figure 5.8: The integrated accreted mass in solar masses at the inner boundary of the calculation domain (a) and the integrated outflow mass of the calculation domain at the outer boundary (b) versus time in years. The solid line is for the normal order of evaluating heat sink/sources and advection, *i.e.*, heat sources/sinks first. The dashed line is for the run with reversed evaluation order.

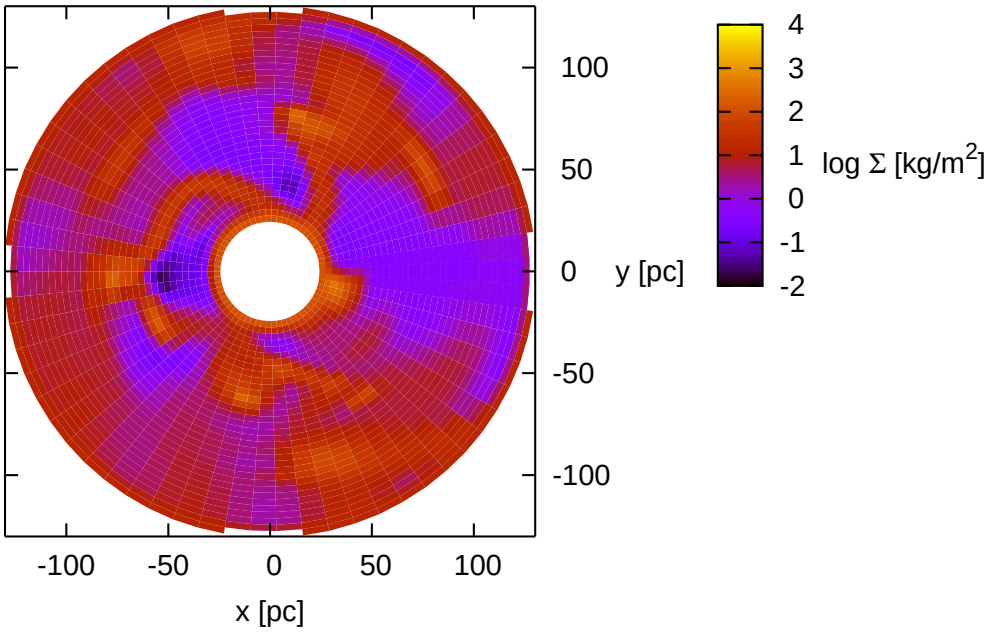

(a) Normal order

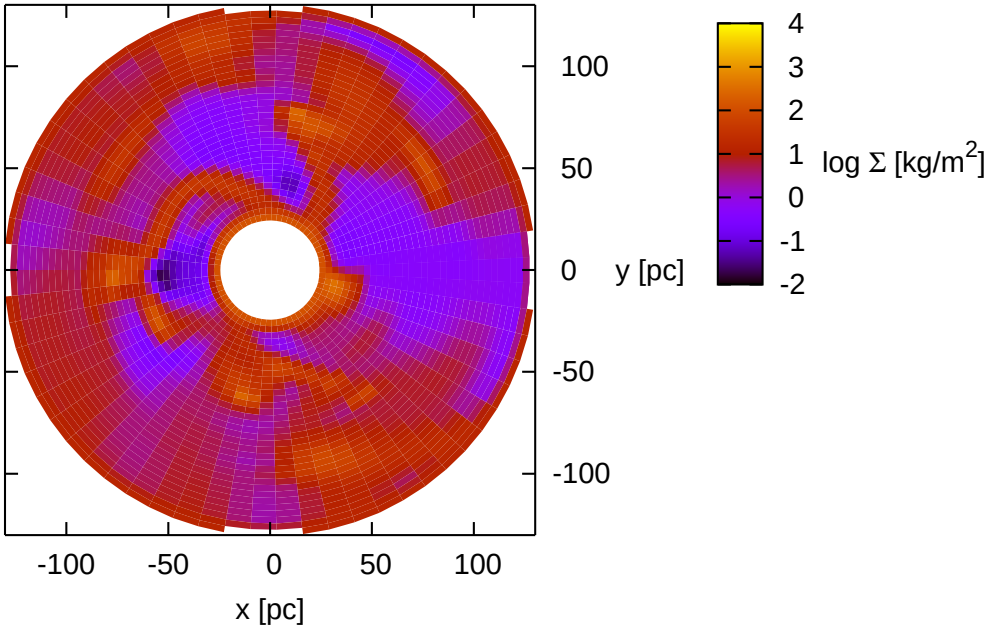

(b) Reversed order

Figure 5.9: The decadic logarithm of the surface density in $\mathrm{kg\,s^{-2}}$ at $t = 2.3{\cdot}10^6$ a. In (a) the heat sources and cooling is evaluated in the code before the advection is done. In (b) it is vice versa.

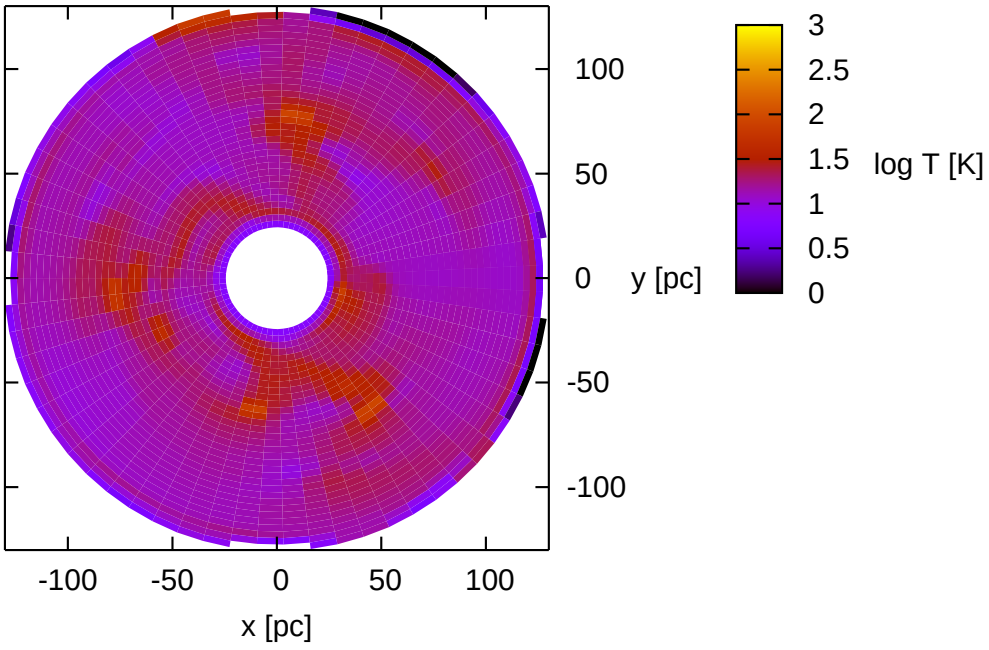

(a) Normal order

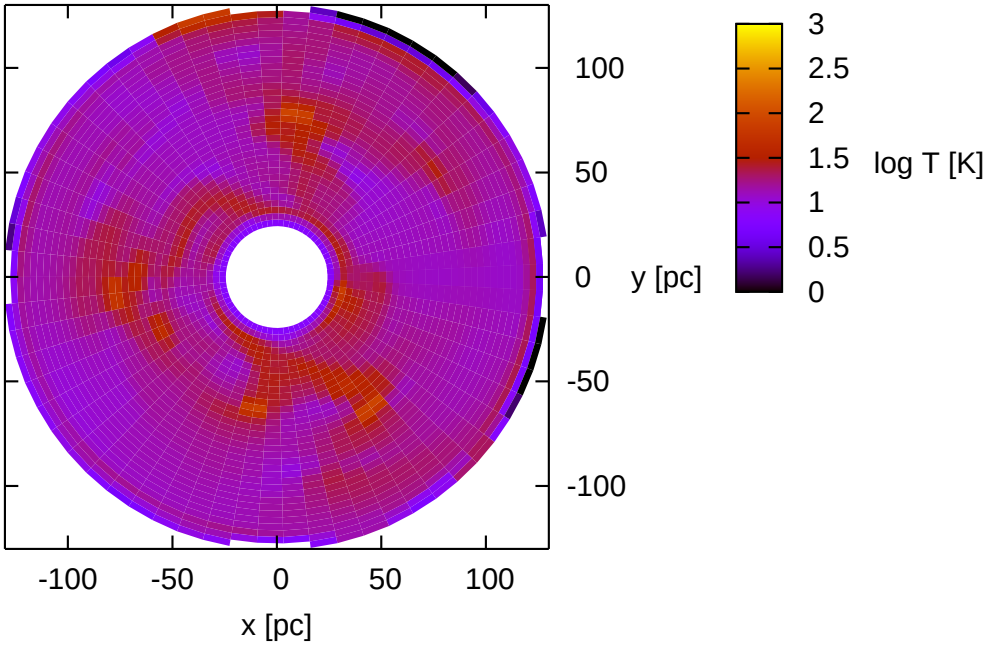

(b) Reversed order

Figure 5.10: The decadic logarithm of the temperature in Kelvin at $t = 2.3{\cdot}10^6$ a. In (a) the heat sources and cooling is evaluated in the code before the advection is done. In (b) it is vice versa.

Chapter 6

Simulations

In this chapter the simulations done for this work are described starting in Sections 6.1 and 6.2. The physical and numerical conditions of the standard simulation are described first and then the results are presented. In Section 6.3 the additional simulations which all differ significantly from the standard simulation by only one parameter are described and their results are compared with those of the standard one. A CD with movies of the different variables for all the runs can be found in Appendix A.

6.1 Description of the standard simulation

6.1.1 Physical and numerical conditions

Here the physical and numerical conditions for the standard simulation are described. The simulations are done with NIRVANA2.0 with the changes described in Chapter 4 using the β-viscosity description. The simulated disk is an FSG disk with a mass in the calculation domain $M_\mathrm{d} = 6{\cdot}10^8 M_\odot$ around an SMBH of $M_* = 7.5{\cdot}10^7 M_\odot$. At the beginning the disk inside the inner boundary of the calculation domain at radius R_i, called the inner disk, has a mass of $M_\mathrm{d,i} = 7.9{\cdot}10^7 M_\odot$. The computational domain stretches from $R_\mathrm{i} = 9{\cdot}10^{17}\,\mathrm{m} = 29\,\mathrm{pc}$ to $R_\mathrm{a} = 3.9{\cdot}10^{18}\,\mathrm{m} = 126\,\mathrm{pc}$ with a half height of $z_\mathrm{max} = 1.04{\cdot}10^{14}\,\mathrm{m} = 3.5{\cdot}10^{-3}\,\mathrm{pc}$. The resolution is $n_R{\times}n_\varphi{\times}n_z = 63{\times}127{\times}7$. The viscosity parameter is $\beta = 0.005$. The ratio of specific heats and the molar mass are set differently in two temperature regimes. They are $\gamma = \frac{7}{5}$ and $\mu = 0.002\,\mathrm{kg\,mol^{-1}}$ where $T < 2000\,\mathrm{K}$ to represent a molecular gas, and $\gamma = \frac{5}{3}$ and $\mu = 0.001\,\mathrm{kg\,mol^{-1}}$ for larger temperatures to represent an atomic gas. Since γ and μ are used to compute the temperature itself, the mean of the two temperatures is taken, in the case that the temperature using the atomic values (giving a lower temperature) is lower than 2000 K and it is above 2000 K using the molecular temperature. The same is done for the pressure which is the only other value affected directly by γ and μ. These values and how the are handled are only crude approximations to the very complex physics of formation and destruction of molecules in the interstellar gas which cannot be taken into account here. Later it must be checked that the results do not depend crucially on these choices. The simulation took about one week of CPU time on a PC and reached a physical time of $9.8{\cdot}10^{13}\,\mathrm{s} = 3.1{\cdot}10^6\,\mathrm{a}$

with 56,200 time steps. The time corresponds to 5.9 outer dynamical time scales of $1.7{\cdot}10^{13}\,\mathrm{s} = 5.3{\cdot}10^{5}\,\mathrm{a}$. An outer dynamical time scale is the inverse angular velocity at the outer boundary here taken at the beginning of the run.

6.1.2 Initial conditions

At the start of a simulation the variables are initialized using the following values. Σ as inspired by the model in Section 3.3 is set to be proportional to R^{-1} with random white noise of a maximal amplitude of $6\,\mathrm{kg\,m^{-2}}$ corresponding to about 10 to 30 %. The azimuthal and radial velocities are set after the first calculation of the potential. v_φ is set to balance gravity and the centrifugal forces while v_R is set by using Equation (2.34). The internal energy per unit area is set to a constant value of $e_{\mathrm{start}} = 10^7\,\mathrm{J\,m^{-2}}$ giving temperatures of 15 to 55 K which are in the order of magnitude reached (independent of e_{start}) within the first few time steps of the simulation.

6.1.3 Boundary Conditions

Due to self-gravity, it is quite difficult to find boundary conditions for which the material neither crowds nor evacuates the regions close to the boundaries, especially at R_{i}. Working boundary conditions have been found by trial and error and they are set as follows. The mass of the inner disk which can increase and decrease due to the flow at the inner boundary is thought to be evenly distributed in its domain and this way the inner boundary value for Σ is set. This mass also influences the z-boundary conditions for the potential as explained in Section 4.3.1. In Section 4.2 the boundary conditions for Φ are described already. At the outer boundary the surface density is set to a constant value of $14.4\,\mathrm{kg\,m^{-2}}$, so at the beginning Σ is smooth at the outer boundary.

e is set at the inner boundary to its initial value of $e_{\mathrm{start}} = 10^7\,\mathrm{J\,m^{-2}}$ and set to have a vanishing gradient at the outer boundary, *i.e.*, the value at the outermost computation cell is copied into the first ghost cell and the value of the second but last outer cell is copied into the second most outer ghost cell. The azimuthal velocity at the inner boundary is set to balance gravity where the monopole approximation is used. At the outer boundary the same is done but the derivative of the potential is used. In the rare case that the derivative is negative, v_φ is set to zero at the outer boundary. v_R at the last most outer computation cell is simply copied to the ghost cells of the outer boundary. The radial velocity at the inner boundary is treated in a very special way which is necessary since it can give rise to a self-enhancing flow otherwise. As soon as material flows into the calculation domain at the inner boundary at one point there will be an enhancement of material close to it. Thus due to self-gravity the velocity of the flow increases. Since the density in the ghost cell does not drop this process is self-enhanced and leads to unwanted velocities and clumps or even a to ring around the inner boundary. To understand how this is prevented we have to remember the staggered grid as described in Section 4.1. From that section, and from Figure 6.1, it is obvious that v_R has three instead of two boundary values at the R-boundaries. This is purely due to using ghost cells and the

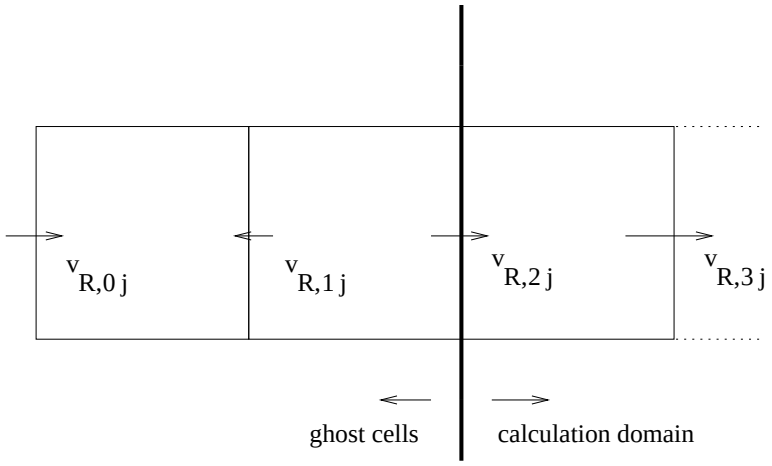

Figure 6.1: The two ghost cells and the first cell in the computational domain at the inner boundary for the jth cell in the φ-direction. Obviously v_R has three boundary values $v_{R,0j}$, $v_{R,1j}$ and $v_{R,2j}$.

staggered grid. A third boundary condition is in principle not needed for solving the equations. The trick is now that $v_{R,0j}$ and $v_{R,1j}$ (where the first index is the index for R and the second one is for φ) are set to zero while $v_{R,2j}$ is not set by the boundary conditions but defined to be included in the calculation domain and thus computed like all other non-boundary variables. This way in the case of a flow into the computational domain the velocity $v_{R,2j}$ is diminished by advection from the boundary.

6.2 Results of the standard Simulation

6.2.1 Fragmentation and dynamics

After one outer dynamical time scale

In Figures 6.2 to 6.7 the azimuthal average of the most interesting dynamic variables, the surface density and the height of the disk are plotted versus radius at $t = 1.7{\cdot}10^{13}\,\mathrm{s} = 5.3{\cdot}10^{5}\,\mathrm{a}$, $n = 3200$, where n is the number of time steps. This time corresponds to the outer dynamical time scale Ω_{O}^{-1} of the disk. From the start of the simulation until shortly after the time for which Figure 6.2 is done, the shape of Ω stays similar, except for the most inner part. v_φ is slowly rising with R as can be seen in Figure 6.3. In Figure 6.4 the azimuthal average of the Mach number in the azimuthal velocity, $M_{\mathrm{a}\varphi} := \frac{v_\varphi}{c_{\mathrm{s}}}$, is plotted which shows that the flow is highly supersonic in the φ-direction. At this early time the absolute value of the radial velocity is already much higher than at the beginning when it was of the order of 1000 m s^{-1}. The azimuthal average of v_R is plotted in Figure 6.5. This already tells us that the accretion due to the hydrodynamical viscosity (which has not changed much since the start of the run) does not play a role here. Knowing Ω_{O} we can also estimate the viscous time scale from Equation (2.59) to be $t_\nu \sim 3.3{\cdot}10^{15}\,\mathrm{s} = 1.1{\cdot}10^{8}\,\mathrm{a}$ which is much longer than the time of the whole simulation. In Figure 6.6, Σ is plotted azimuthally averaged which shows strong

signs of fragmentation. The plot of the height of the disk in Figure 6.7 verifies that our choice for the height of the calculation domain is – up to that point in time – appropriate.

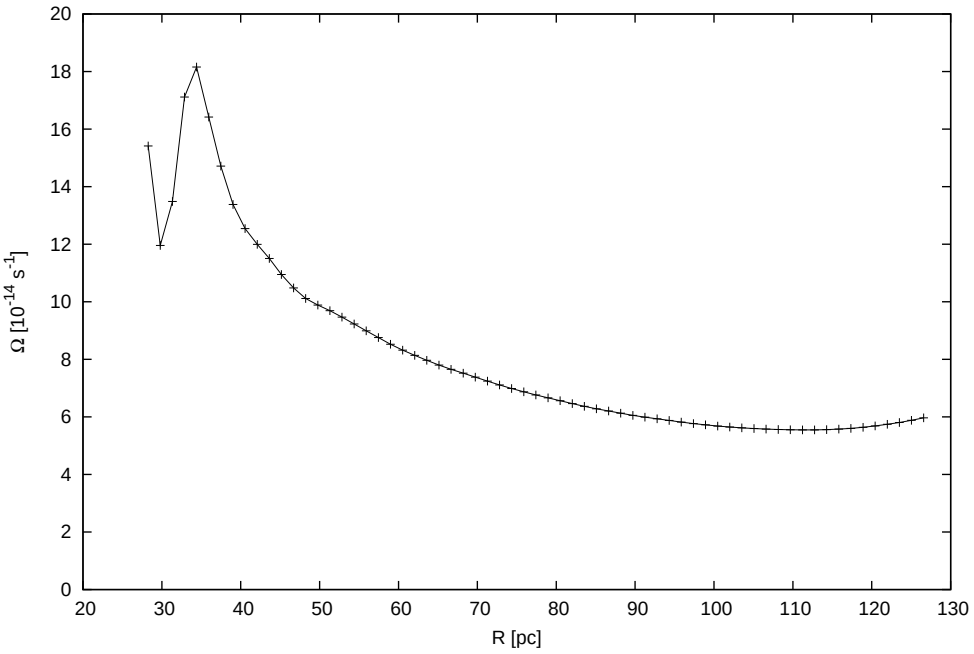

Figure 6.2: The azimuthal average of the angular velocity in the standard simulation at $t = 1.7{\cdot}10^{13}\,\mathrm{s} = 5.3{\cdot}10^{5}\,\mathrm{a}$, versus the radius in pc. The values are given in units of $10^{-14}\,\mathrm{s}^{-1}$.

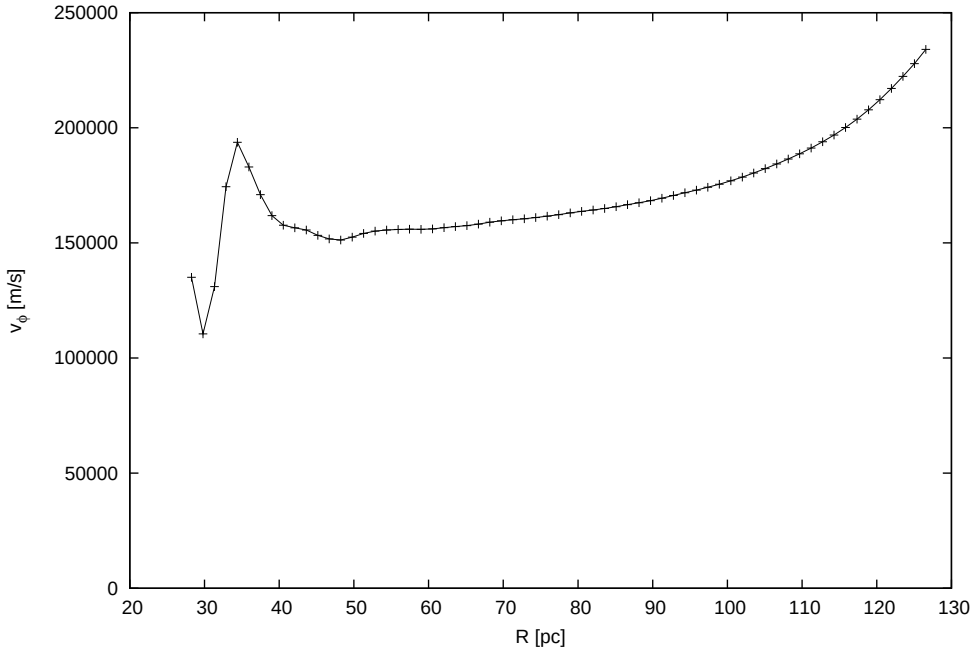

Figure 6.3: Same as Figure 6.2 but for the azimuthal velocity in m s^{-1}. Although the gas rotates in the mathematically negative direction, it is plotted positively for convenience.

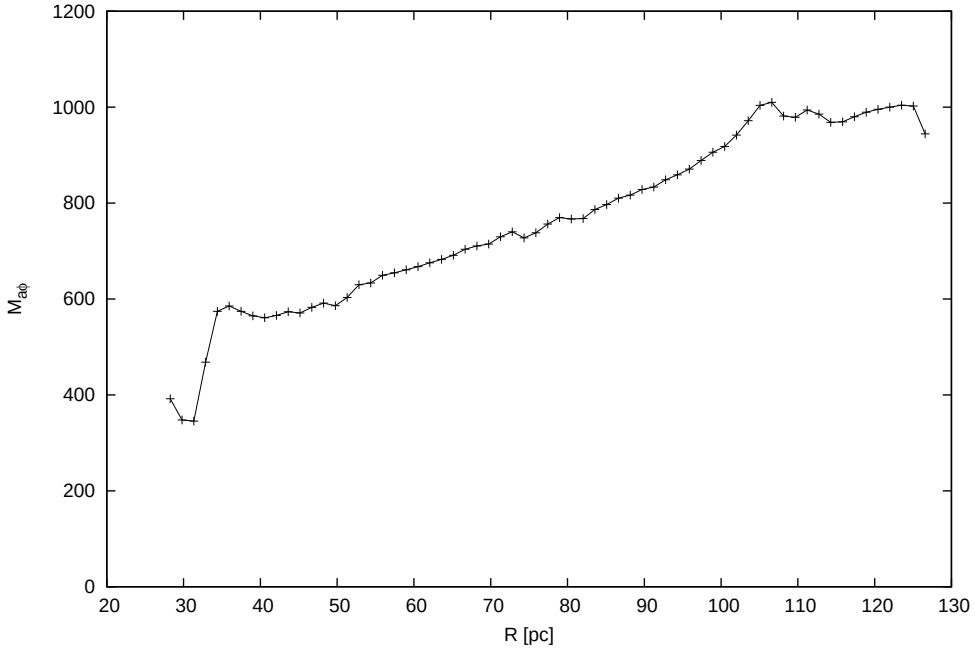

Figure 6.4: Same as Figure 6.2 but for the Mach number in the φ-direction $M_{a\varphi}$. As in Figure 6.3, it is plotted positively. This shows that the flow is highly supersonic in the azimuthal direction.

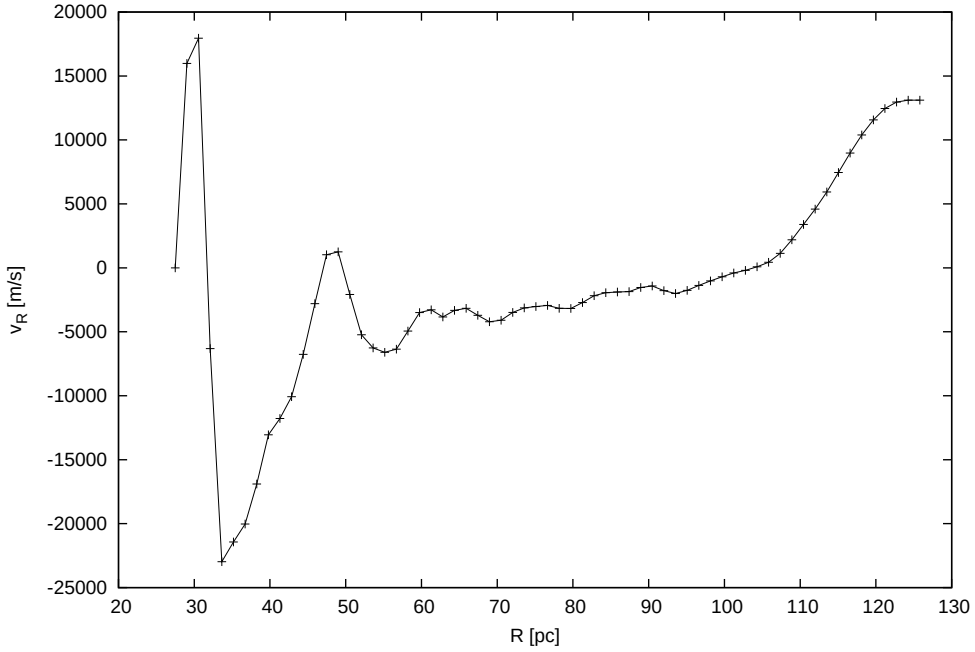

Figure 6.5: Same as Figure 6.2 but for the radial velocity in m s^{-1}. The absolute values of v_R are already much higher than at the beginning of the run indicating that the hydrodynamic viscosity (which has hardly changed by that time) does not drive this flow. The strong oscillations at the inner boundary are still due to the initial conditions.

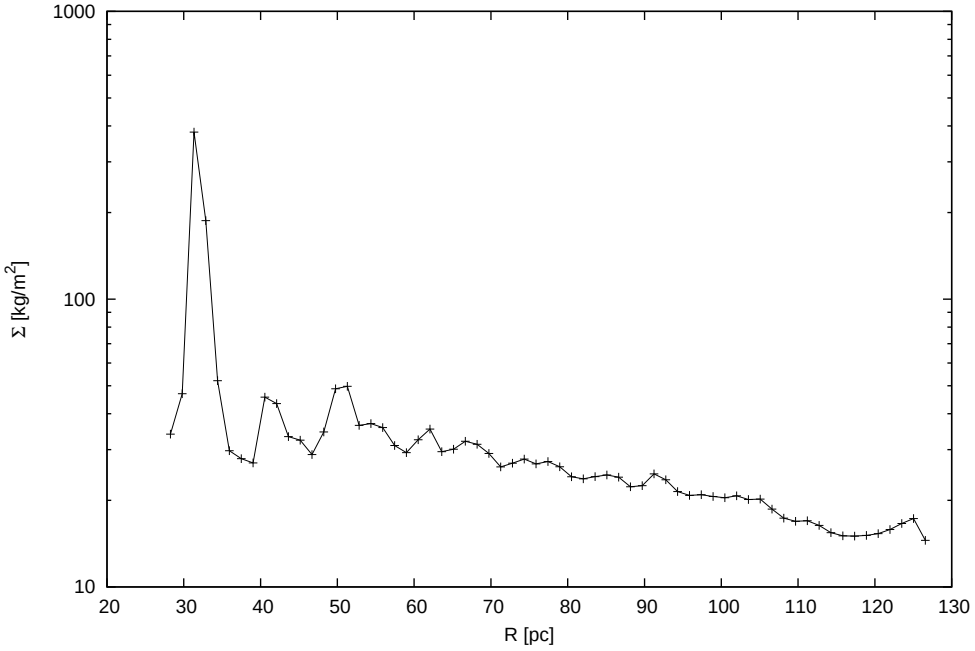

Figure 6.6: Same as Figure 6.2 but for the surface density in kg m^{-2}. It shows signs of fragmentation.

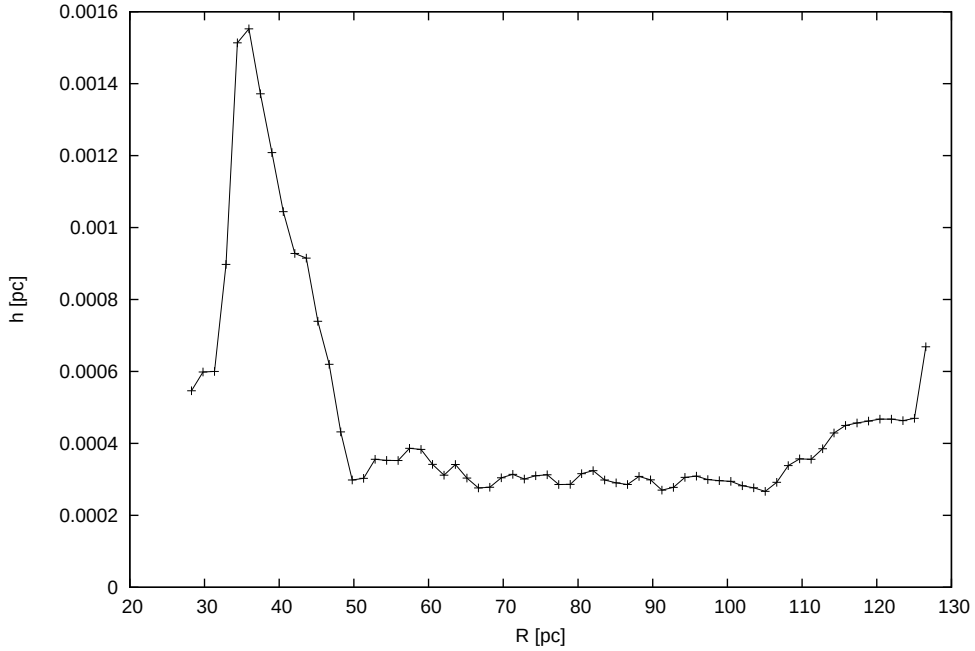

Figure 6.7: Same as Figure 6.2 but for the height of the disk in pc. The height is still smaller than the half height of the calculation domain of $3.5{\cdot}10^{-3}$ pc.

From Figure 6.8 which shows the distribution of the surface density in the disk at the same time as in Figure 6.6, it is obvious that at one dynamical outer time scale the disk already fragments at the inner boundary. Of course the same can be concluded looking at Figure 6.9 where the volume density is plotted. The gradients in the volume density are much steeper since regions of high Σ are much thinner than regions of low surface density which follows from Equation (2.52). Figure 6.10, where v_R is plotted, shows that the flow at this time is already turbulent. In Figure 6.11 the Toomre parameter Q is plotted in 2D. First of all we see that the disk is unstable everywhere with $0.3 < Q < 10^{-3}$. The white spaces are cells with $Q \notin \mathbb{R}$, *i.e.*, $\kappa^2 < 0$ which is the condition for Rayleigh instability (see Equation (2.66)). This means that in these regions the disk is not only gravitationally unstable but in addition linearly dynamically unstable.

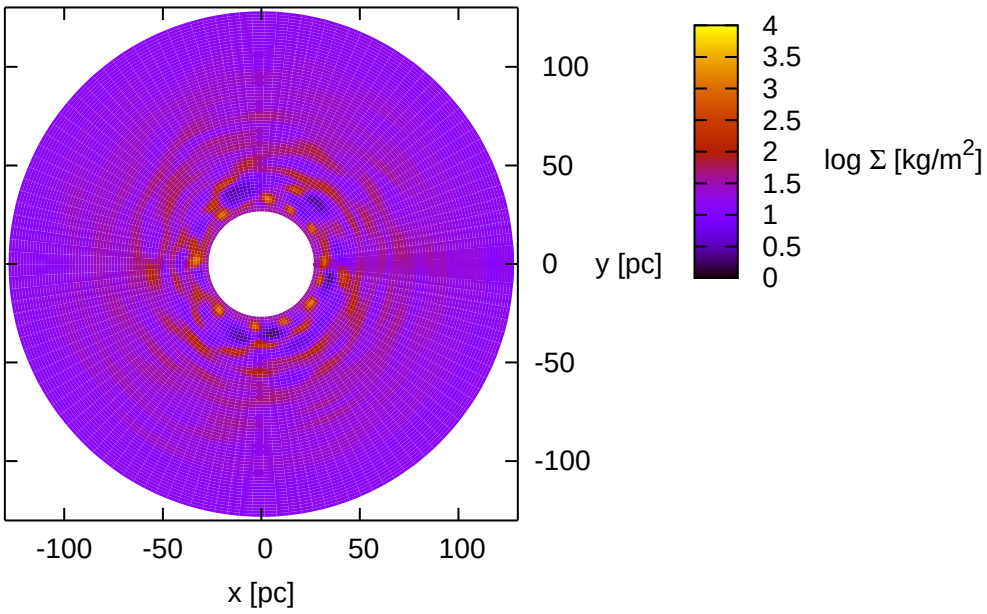

Figure 6.8: The decadic logarithm of the surface density in $\mathrm{kg\,m^{-2}}$ at $t = 1.7{\cdot}10^{13}\,\mathrm{s} = 5.3{\cdot}10^{5}\,\mathrm{a}$. There is already fragmentation occurring at the inner rim.

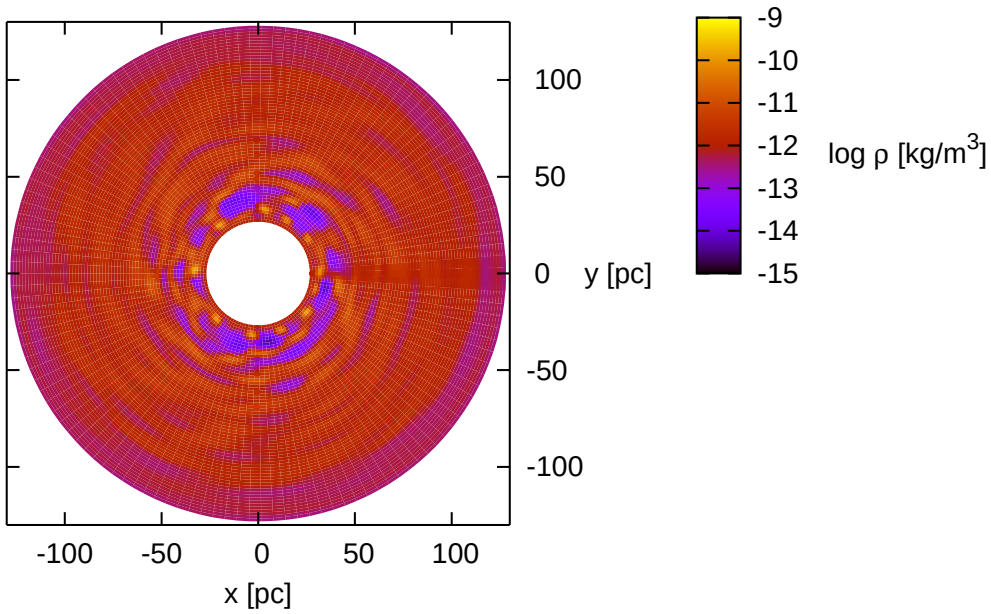

Figure 6.9: Same as Figure 6.8 but the for decadic logarithm of ρ in $\mathrm{kg\,m^{-3}}$. The gradients are much steeper than in Σ since the height is smaller for large Σ (see Equation (2.52)).

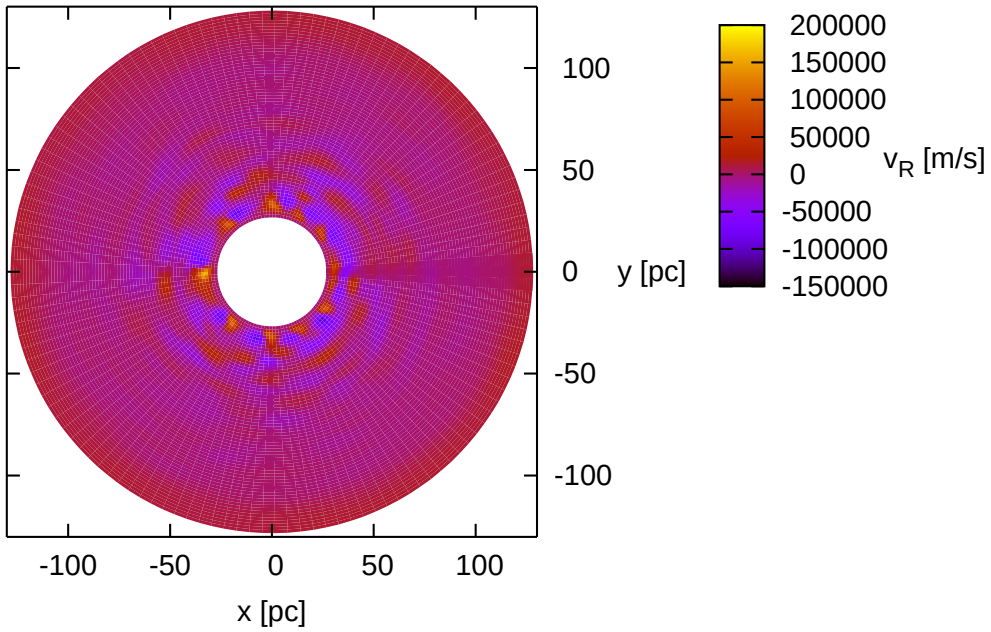

Figure 6.10: The radial velocity in $\mathrm{m\,s^{-1}}$ at $t = 1.7{\cdot}10^{13}\,\mathrm{s} = 5.3{\cdot}10^{5}\,\mathrm{a}$. There are already signs of turbulence at the inner rim.

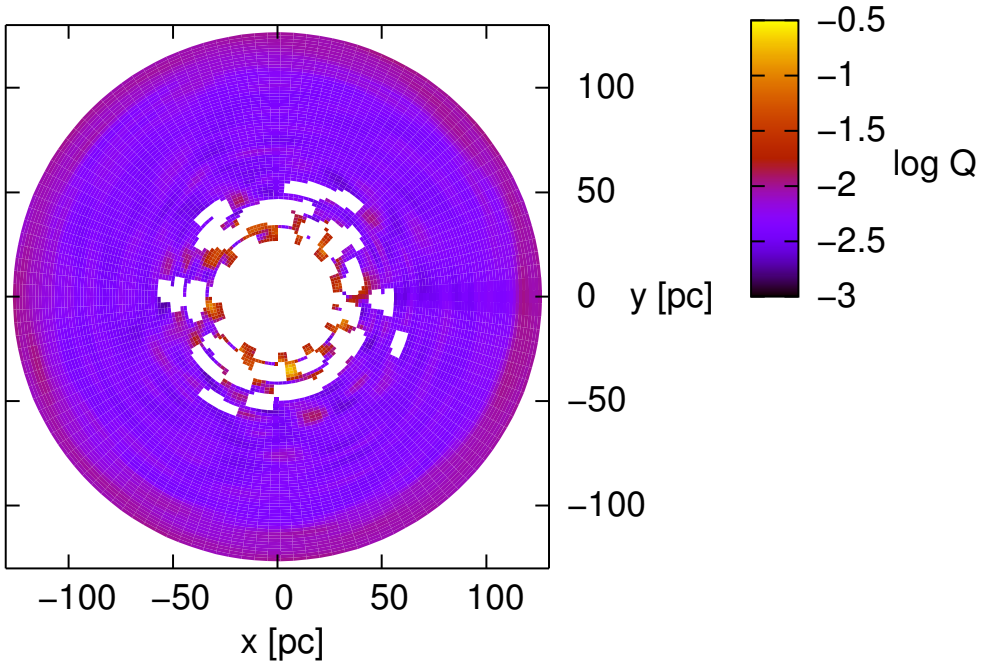

Figure 6.11: The decadic logarithm of the Toomre parameter at time $t = 1.7{\cdot}10^{13}\,\mathrm{s} = 5.3{\cdot}10^{5}\,\mathrm{a}$. The white spaces are cells where $Q \notin \mathbb{R}$, *i.e.*, $\kappa^2 < 0$. This means that the whole disk is either Toomre unstable ($Q < 1$) or dynamically unstable ($\kappa^2 < 0$), see text for more explanations.

After a few outer dynamical time scales

Later the disk fragments more and the flow becomes more violent. As long as the mass in the calculation domain dominates over the mass in the inner disk and the central point mass the details change but the overall picture stays the same, so here we show plots at $t = 5.6{\cdot}10^{13}\,\mathrm{s} = 1.8{\cdot}10^{6}\,\mathrm{a} \approx 3.3\Omega_{\mathrm{O}}^{-1}$ and $n = 24000$ except where stated otherwise. This time is more or less representative for this phase, *i.e.*, starting from about $t = 10^{6}\,\mathrm{a}$ away from the very end when the disk has lost almost all of its mass.

In Figure 6.12 where the azimuthal average over v_R is plotted we see that there are high negative radial velocities inside of $R = 60\,\mathrm{pc}$ while beyond this radius the velocities point outwards in the mean. This radius of 60 pc moves to larger radii with time. We will see in the next section that material is really accreted at the inner boundary and that it is lost at the outer boundary. In Figure 6.13 the azimuthal average of the surface density is plotted. Apart from strong variations, it seems to be constant over the radius in the mean.

While the surface density profile stays roughly constant with R which is different from the model used in Section 3.3, the angular velocity and thus also the azimuthal velocity profile changes with time. As we see from Figure 6.14(a) where the Ω profile is shown in a double logarithmic plot the angular velocity is roughly proportional to $R^{-\frac{1}{2}}$ at $t = 1.6{\cdot}10^{6}\,\mathrm{a}$ (and actually most of the time before also) which is what the monopole approximation predicts for a constant Σ profile. But later on at $t = 1.8{\cdot}10^{6}\,\mathrm{a}$ already, the profile steepens for smaller radii as shown in Figure 6.14(b). In Figure 6.14(c) the same is plotted for $t = 2.3{\cdot}10^{6}\,\mathrm{a}$ from which we see that the inner parts of the disk have become Keplerian. This happens since the disk loses mass and the inner disk, the influence of which is included using the monopole approximation, gains mass. So at some point in time around $t = 2{\cdot}10^{6}\,\mathrm{a}$ the gravitational influence of the inner disk is the main dynamic driver at the inner edge of the calculation domain giving the disk a Keplerian rotational profile at small radii.

An observable for turbulence is the root mean square (RMS) over the radial velocity (corrected by the mean radial velocity at the corresponding radius) which is a measure for the turbulent velocity. This divided by the azimuthal velocity is plotted in Figure 6.15. It fluctuates between 0.1 and 0.4.

Now in Figures 6.16 and 6.17 the surface and the volume density distribution is plotted and shows strong fragmentation. If we compare this with Figure 6.18 where the height distribution is shown with the $\Sigma = 10\,\mathrm{kg\,m^{-2}}$ contour as the white dashed line, we see that the height in the higher-density regions stays below the height of the calculation domain. From Figure 6.19 where again the v_R distribution over the disk is plotted, we can estimate the vortex size which is another observable for the turbulence. Roughly the vortices are 0.1 to 0.3 times their radial coordinate R.

In Figure 6.20 Q is plotted. Now there are some regions that are gravitationally stable but still most parts are either gravitationally or dynamically unstable.

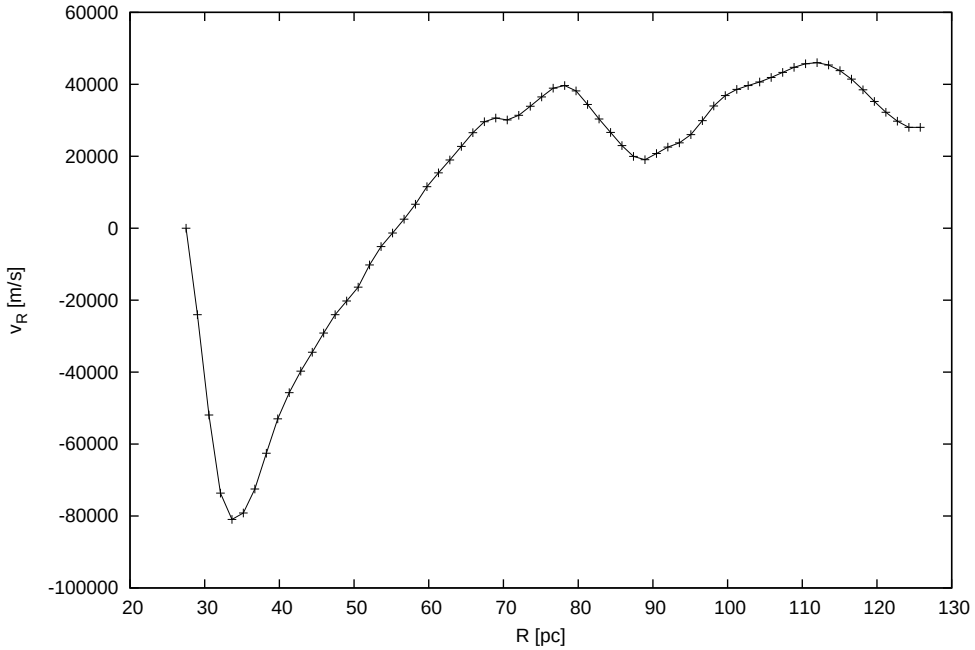

Figure 6.12: Similar to Figure 6.5 but at time $t = 5.6{\cdot}10^{13}\,\mathrm{s} = 1.8{\cdot}10^{6}\,\mathrm{a}$. Within $\sim 60\,\mathrm{pc}$ the velocity points inwards, beyond that radius it points outwards.

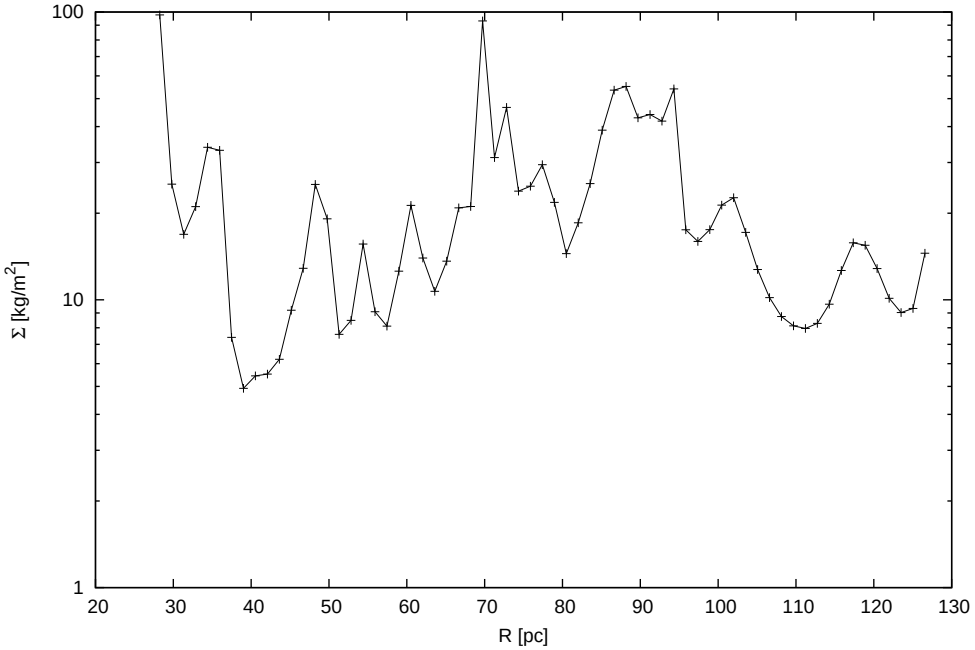

Figure 6.13: Similar to Figure 6.6 but at time $t = 5.6{\cdot}10^{13}\,\mathrm{s} = 1.8{\cdot}10^{6}\,\mathrm{a}$. Apart from fluctuations Σ stays constant with radius.

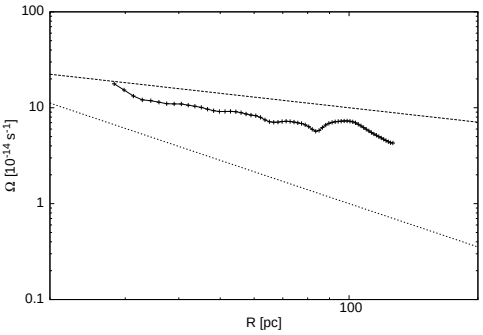

(a) $t = 5.0{\cdot}10^{13}\,\mathrm{s} = 1.6{\cdot}10^{6}\,\mathrm{a}$

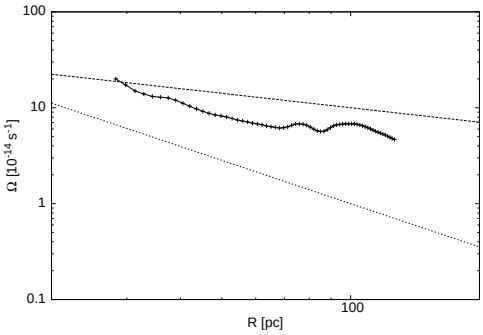

(b) $t = 5.6{\cdot}10^{13}\,\mathrm{s} = 1.8{\cdot}10^{6}\,\mathrm{a}$

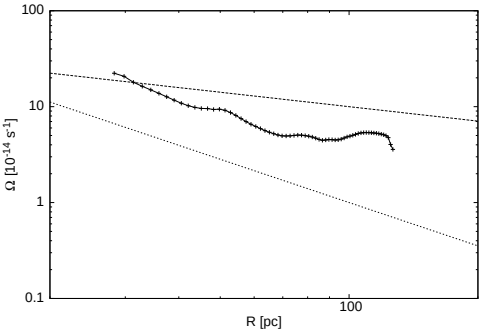

(c) $t = 7.1{\cdot}10^{13}\,\mathrm{s} = 2.3{\cdot}10^{6}\,\mathrm{a}$

Figure 6.14: Similar to Figure 6.2 but at different times t. The long dashed line is $\propto R^{-\frac{1}{2}}$ and the short dashed line is $\propto R^{-\frac{3}{2}}$. In (a) Ω is roughly fit by proportionality to $R^{-\frac{1}{2}}$. In (b) the radial profile already starts to deviate from $R^{-\frac{1}{2}}$ proportionality. In (c) the inner part of the calculation domain is roughly fit by $\Omega \propto R^{-\frac{3}{2}}$.

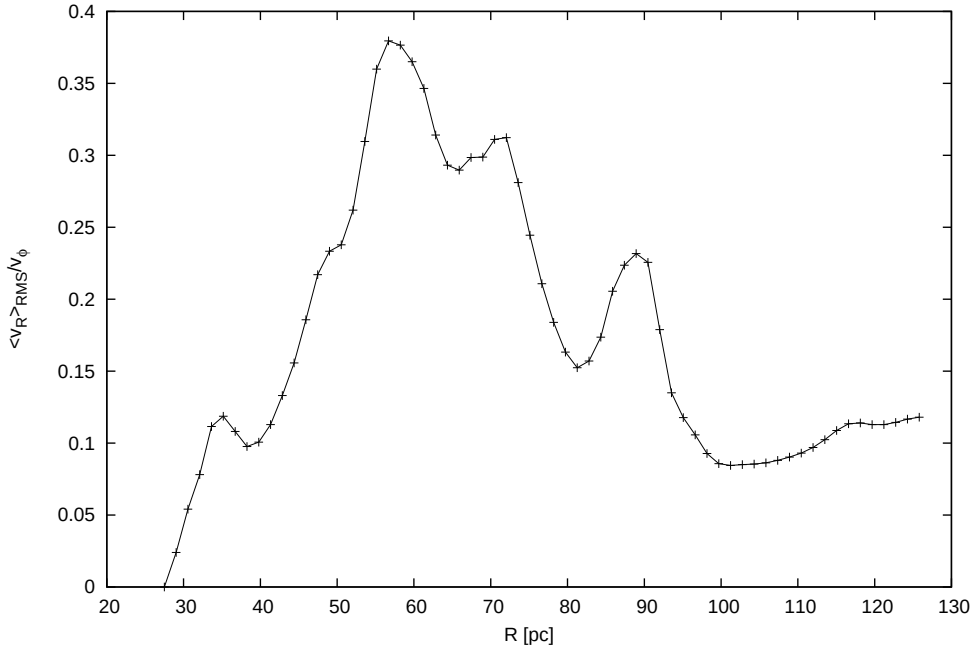

Figure 6.15: $\frac{\langle v_R \rangle_{\mathrm{RMS}}}{v_\varphi}$ versus radius in pc. $\langle v_R \rangle_{\mathrm{RMS}}$ is the RMS of the radial velocity minus the mean radial velocity at the corresponding radius.

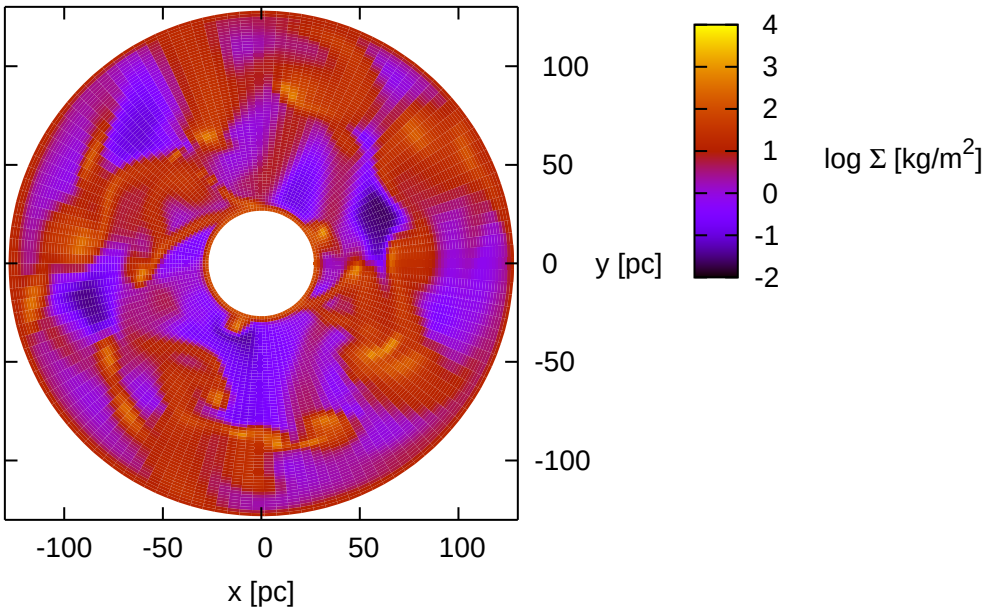

Figure 6.16: Similar to Figure 6.8 but at time $t = 5.6{\cdot}10^{13}\,\mathrm{s} = 1.8{\cdot}10^{6}\,\mathrm{a}$. The fragmentation is now obvious in the whole disk.

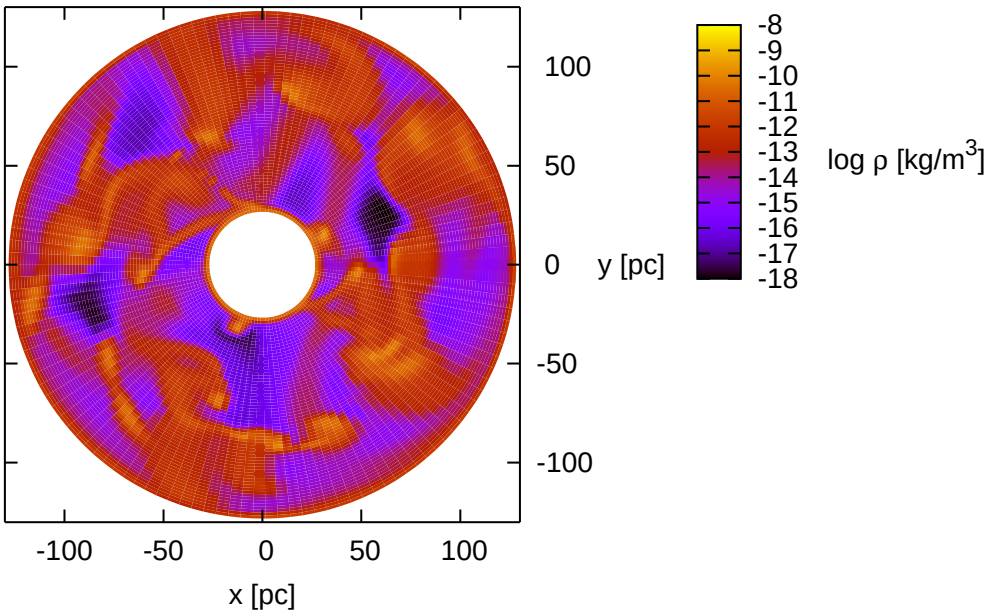

Figure 6.17: Similar to Figure 6.8 but the decadic logarithm of the volume density in $\mathrm{kg\,m^{-3}}$ at time $t = 5.6{\cdot}10^{13}\,\mathrm{s} = 1.8{\cdot}10^{6}\,\mathrm{a}$. Again the gradients are much steeper than in Σ.

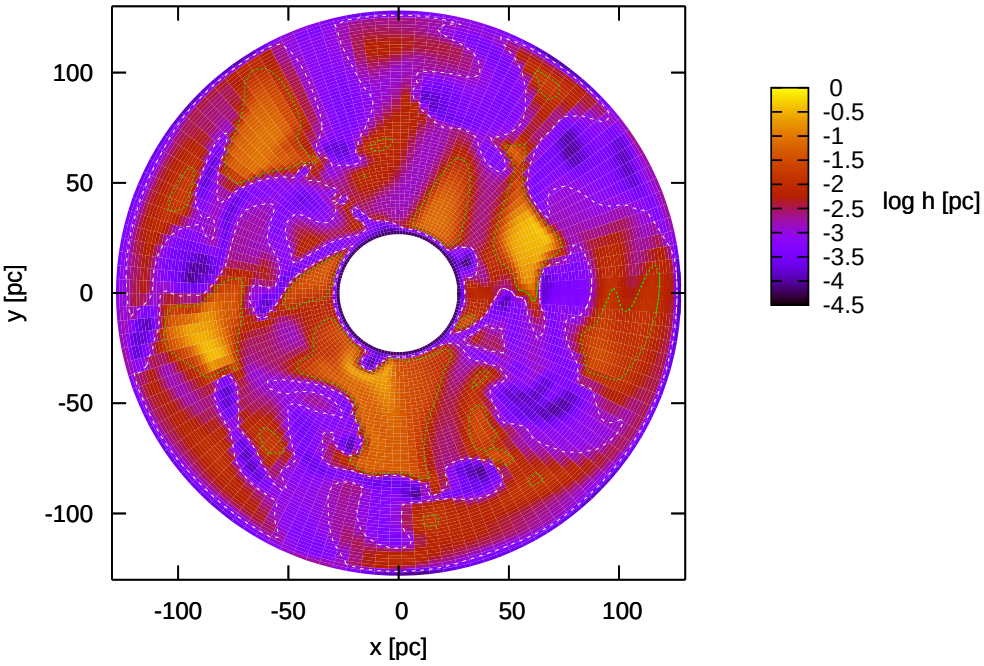

Figure 6.18: Similar to Figure 6.8 but the decadic logarithm of the height of the disk in pc at time $t = 5.6{\cdot}10^{13}\,\mathrm{s} = 1.8{\cdot}10^{6}\,\mathrm{a}$. The green dotted line is the contour of $\Sigma = 1\,\mathrm{kg\,m^{-2}}$, the white dashed line is the contour of $\Sigma = 10\,\mathrm{kg\,m^{-2}}$. From this figure it is evident that in low-density regions the height becomes much larger than the half height of the computational domain of $1.05{\cdot}10^{14}\,\mathrm{m} = 3.5{\cdot}10^{-3}\,\mathrm{pc}$; but in high-density regions, the height stays smaller.

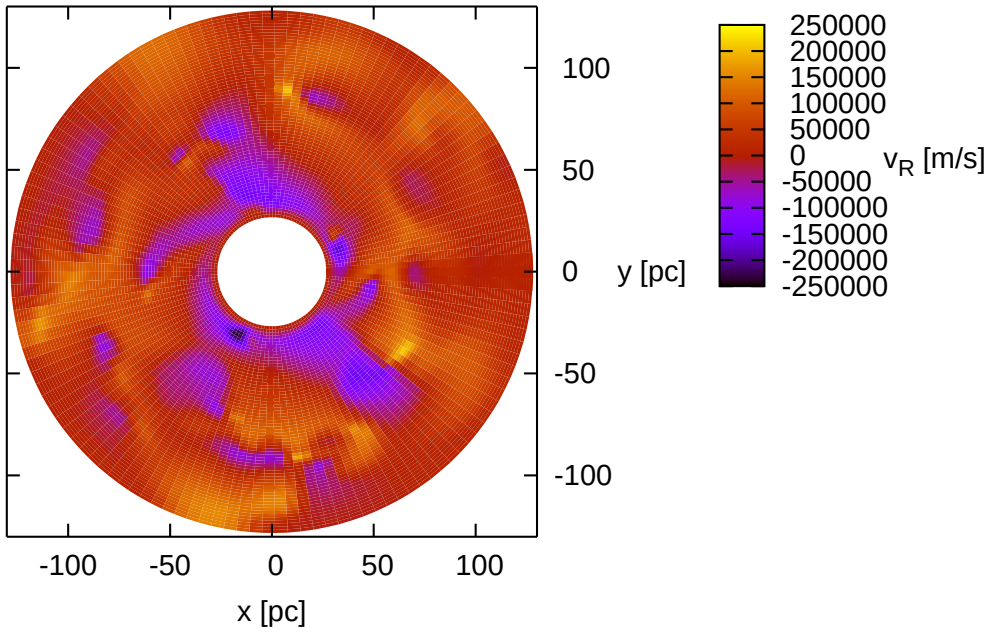

Figure 6.19: Similar to Figure 6.10 but at time $t = 5.6{\cdot}10^{13}\,\mathrm{s} = 1.8{\cdot}10^{6}\,\mathrm{a}$. The flow looks turbulent and the size of the eddies is around 0.1 to 0.3 R.

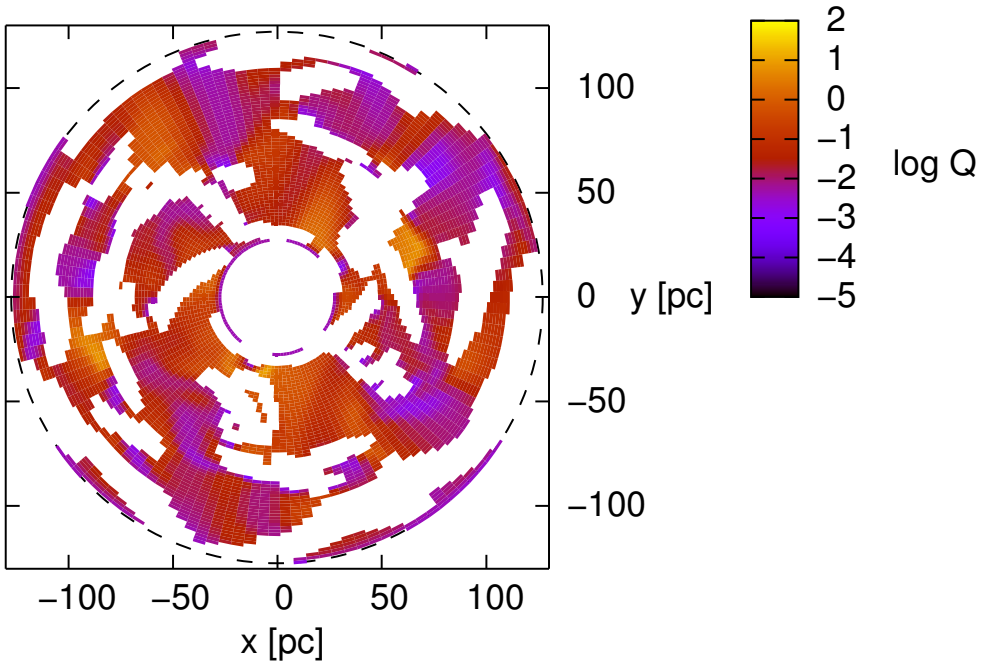

Figure 6.20: Similar to Figure 6.11 but at time $t = 5.6{\cdot}10^{13}\,\mathrm{s} = 1.8{\cdot}10^{6}\,\mathrm{a}$. Although some regions have become stable, most of the disk is still unstable. The dashed circle marks the outer calculation domain boundary.

6.2.2 Thermodynamics and cooling

As can be seen from Figure 6.21, where the azimuthal average of the temperature versus radius for the times $t = 1.6{\cdot}10^6$ a, $t = 1.8{\cdot}10^6$ a and $t = 2.3{\cdot}10^6$ a are plotted, the temperature profile is constant in radius and time at ~ 20 K despite some fluctuations. The same is then of course true for the azimuthal average of the speed of sound which is plotted versus the radius in Figure 6.22 for $t = 1.8{\cdot}10^6$ a from which we see that $c_\mathrm{s} \approx 260 - 340\,\mathrm{m\,s^{-1}}$. The temperature itself actually varies quite a bit as can be seen in Figure 6.23 where the temperature is plotted in 2D. From this plot we see that the temperature range is roughly from 1 K to 3000 K where the main part of the disk is at ~ 10 K while the clumps (if compared with the surface density in Figure 6.16) have temperatures around 1000 K.

Since the optical depth (which is the Rosseland mean taken to be equal to the Planck mean, see Section 4.6.1) strongly depends on the temperature, it behaves similarly. In Figure 6.24 the azimuthal average of the optical depth is plotted versus the radius at $t = 1.8{\cdot}10^6$ a which shows that it is fluctuating but constant in the mean at $\tau \approx 0.02 - 5$. Without averaging, we see in Figure 6.25 where the optical depth is shown in 2D that the main part of the disk is optically thin. In the clumps in the other hand where the densities and the temperatures are higher, the material becomes optically thick. The whole range is $10^{-5} < \tau < 10^3$.

Except for the surface density, the temperature and the optical depth are the variables determining the cooling time $t_\mathrm{cool} = \frac{e}{\Lambda}$ with Λ from Equation (4.43) giving

$$t_\mathrm{cool} = \frac{1}{\gamma - 1} \frac{16\mathcal{R}\Sigma}{3\mu\sigma} \frac{\tau_\mathrm{eff}}{T^3}, \tag{6.1}$$

where the relation $T = (\gamma - 1)\frac{\mu e}{\mathcal{R}\Sigma}$ is used. In Figure 6.26 the azimuthal average of t_cool is plotted versus the radius for the times $t = 1.6{\cdot}10^6$ a, $t = 1.8{\cdot}10^6$ a and $t = 2.3{\cdot}10^6$ a, respectively. In Figures 6.26(a) and 6.26(b) it seems to be constant with radius except for a small break at around $R = 60 - 70$ pc. In Figure 6.26(c) at later times, the constancy is not very clear anymore. As we have seen in Section 2.5, the interpretation of the accretion as an α-disk predicts the value of $t_\mathrm{cool}\Omega$ to be constant which cannot be true if t_cool is constant and Ω is not. In Figure 6.27 the azimuthal average of $t_\mathrm{cool}\Omega$ is plotted versus radius for $t = 1.8{\cdot}10^6$ a. This is indeed not too far from being constant but this is mainly due to the fact that Ω is almost constant from $R = 70$ pc upwards for that instant (see Figure 6.14(b)). Below $R = 70$ pc, a constant function does not fit $t_\mathrm{cool}\Omega$ well. This plot again shows that the cooling time is much smaller than the dynamical time scale. In Figure 6.28 the cooling time is plotted in 2D. This Obviously shows strongly varying values again, mainly of $10^8\,\mathrm{s} = 3.2\,\mathrm{a} < t_\mathrm{cool} < 3.2{\cdot}10^4\,\mathrm{a} = 10^{12}\,\mathrm{s}$ which are well below the dynamical time scale of $t = 1.7{\cdot}10^{13}\,\mathrm{s} = 5.3{\cdot}10^5$ a. Figure 6.28 also shows that the regions of clumps have cooling times in the lower range if compared with Figure 6.16.

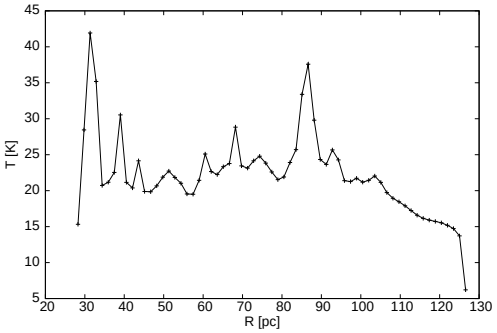

(a) $t = 5.0{\cdot}10^{13}\,\mathrm{s} = 1.6{\cdot}10^{6}\,\mathrm{a}$

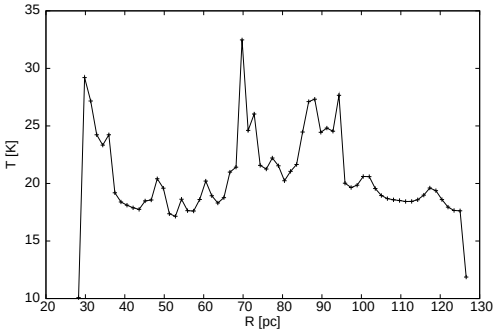

(b) $t = 5.6{\cdot}10^{13}\,\mathrm{s} = 1.8{\cdot}10^{6}\,\mathrm{a}$

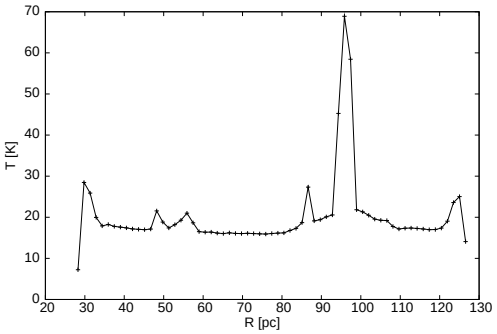

(c) $t = 7.1{\cdot}10^{13}\,\mathrm{s} = 2.3{\cdot}10^{6}\,\mathrm{a}$

Figure 6.21: Azimuthal average of the temperature in Kelvin versus radius in pc at different times t. The temperature seems to stay constant with radius despite some fluctuations .

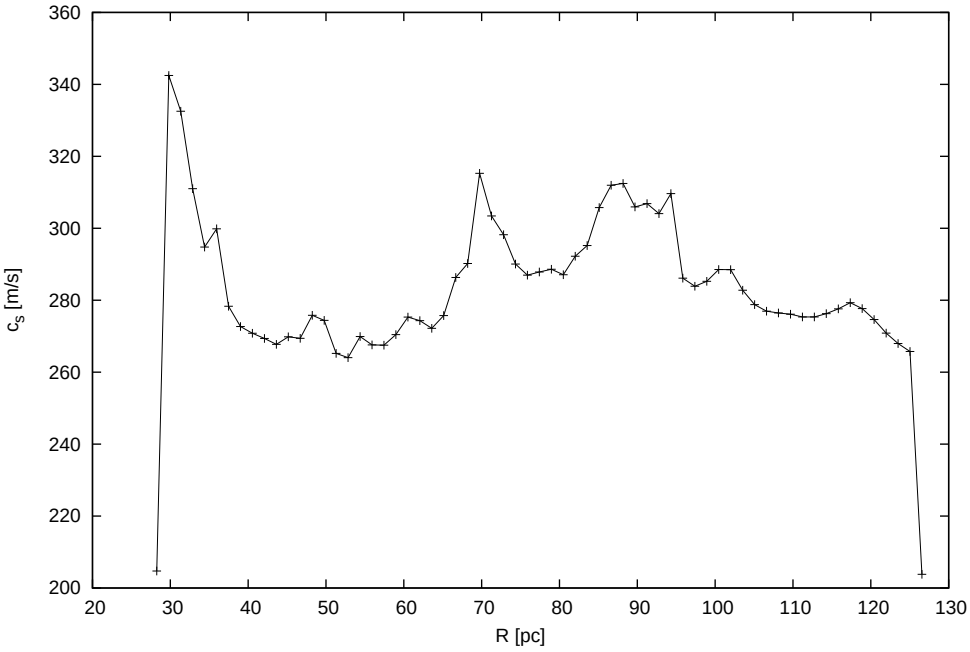

Figure 6.22: The azimuthal average of the speed of sound in $\mathrm{m\,s^{-1}}$ versus radius in pc at time $t = 5.6{\cdot}10^{13}\,\mathrm{s} = 1.8{\cdot}10^{6}\,\mathrm{a}$. It stays roughly constant at values of $260 - 340\,\mathrm{m\,s^{-1}}$.

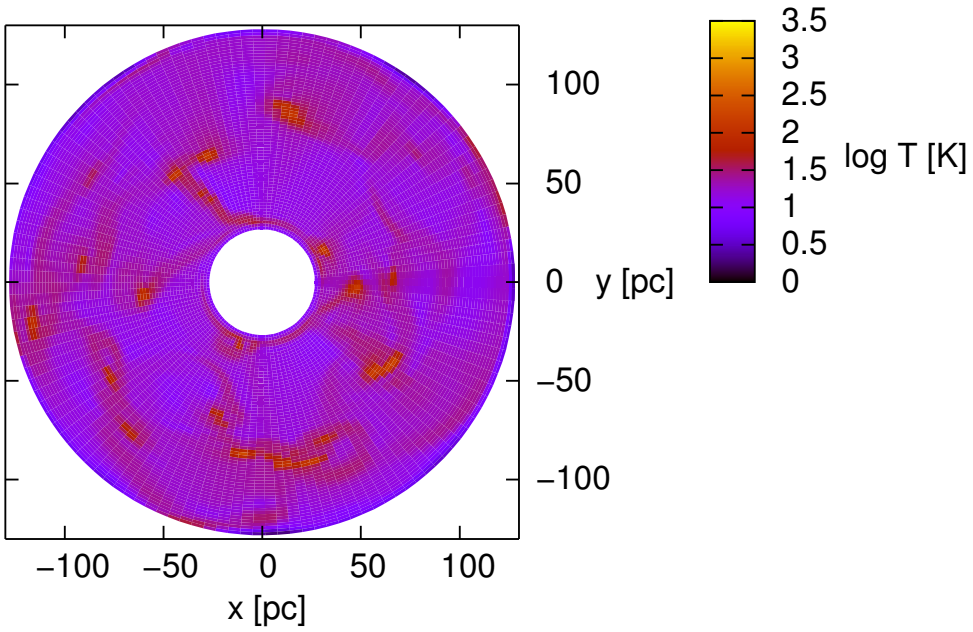

Figure 6.23: The decadic logarithm of the temperature in Kelvin at $t = 5.6{\cdot}10^{13}\,\mathrm{s} = 1.8{\cdot}10^{6}\,\mathrm{a}$. T stays between 1 K and 3000 K where most of the disk is cool at ~ 10 K, and the clumps heat up to 1000 K and above.

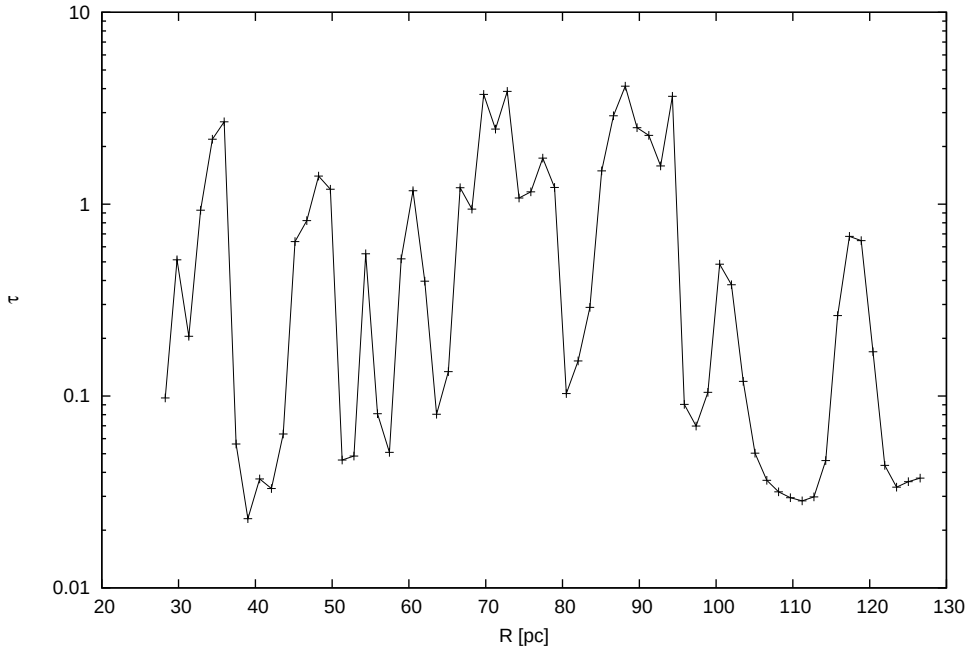

Figure 6.24: Same as Figure 6.22 but for the azimuthal average of the (Rosseland mean) optical depth. Despite some fluctuations, is remains constant around 0.02 to 5.

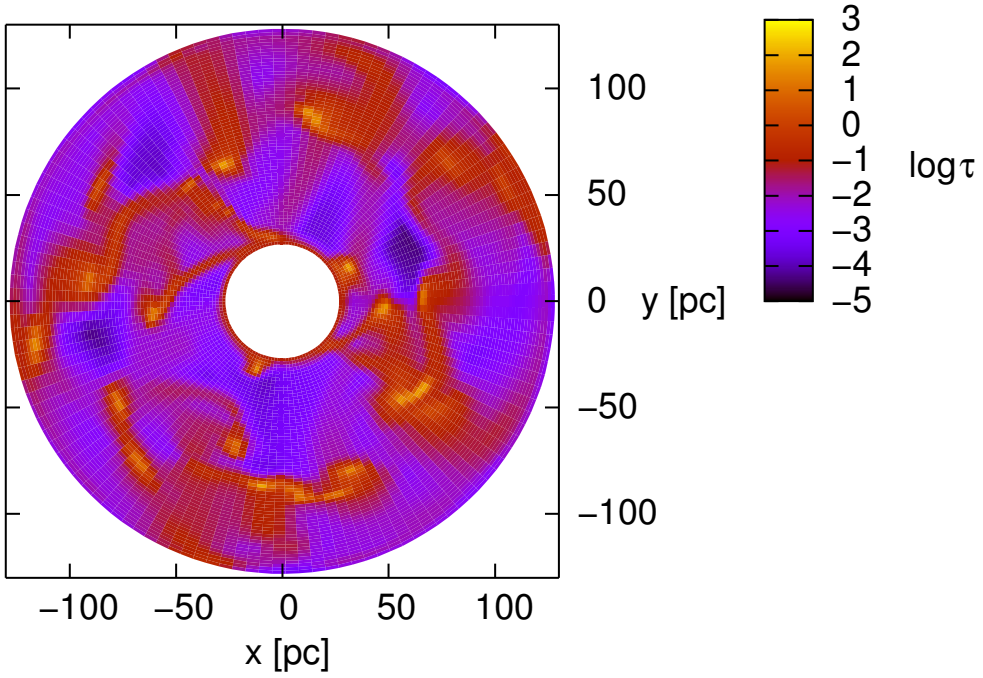

Figure 6.25: Same as Figure 6.23 but for the decadic logarithm of the (Rosseland mean) optical depth. It stays at $10^{-5} < \tau < 10^{3}$. The disk material is optically thick in the clumps and optically thin elsewhere.

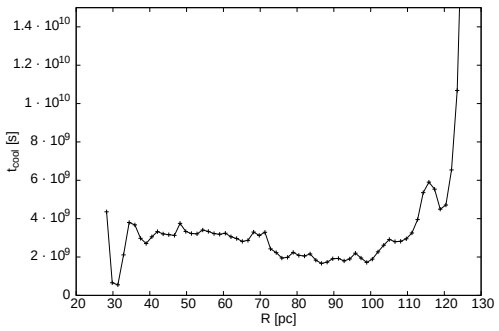

(a) $t = 5.0{\cdot}10^{13}\,\mathrm{s} = 1.6{\cdot}10^{6}\,\mathrm{a}$

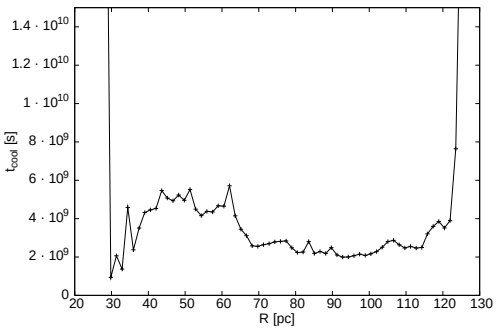

(b) $t = 5.6{\cdot}10^{13}\,\mathrm{s} = 1.8{\cdot}10^{6}\,\mathrm{a}$

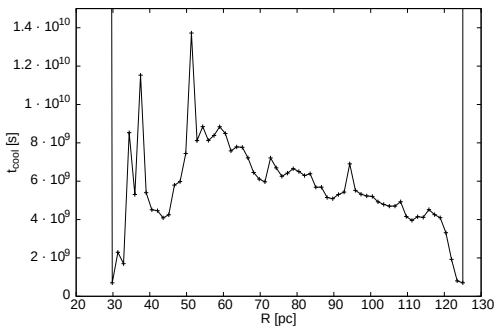

(c) $t = 7.1{\cdot}10^{13}\,\mathrm{s} = 2.3{\cdot}10^{6}\,\mathrm{a}$

Figure 6.26: Azimuthal average of the cooling time in seconds versus radius in pc at different times. In (a) and (b) it is roughly constant with R except for a break at $R \approx 70\,\mathrm{pc}$ where it drops from $4{\cdot}10^{9}\,\mathrm{s}$ to $2{\cdot}10^{9}\,\mathrm{s}$. This is not true for (c).

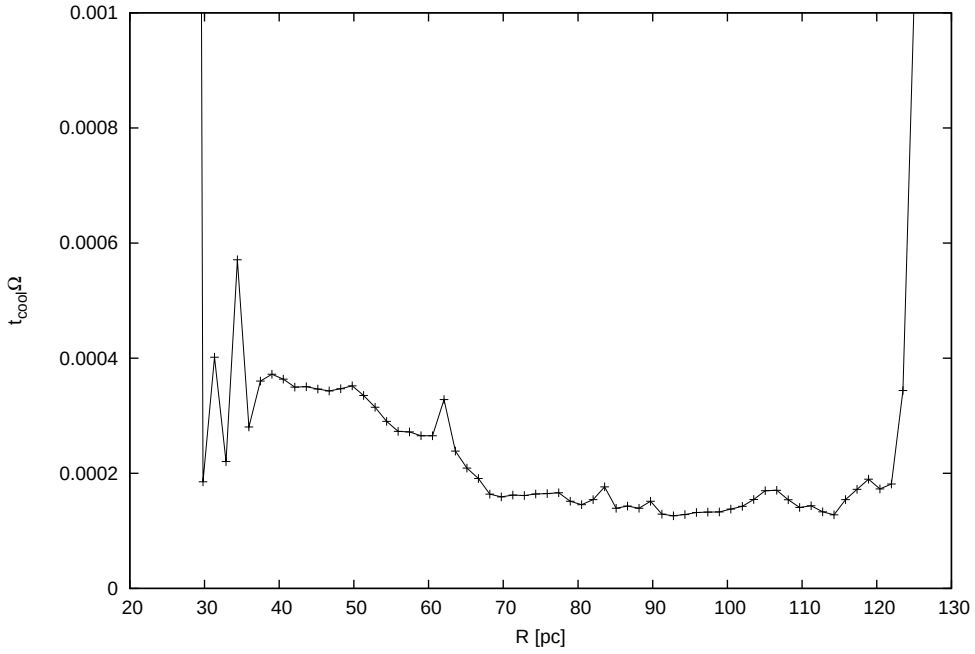

Figure 6.27: Same as Figure 6.22 but for the cooling time divided by the local dynamical time scale Ω^{-1}. This again shows that the cooling time is much shorter than the dynamical time scale. $t_{\rm cool}\Omega$ is not quite constant but the deviations are small, see also the remark in the text.

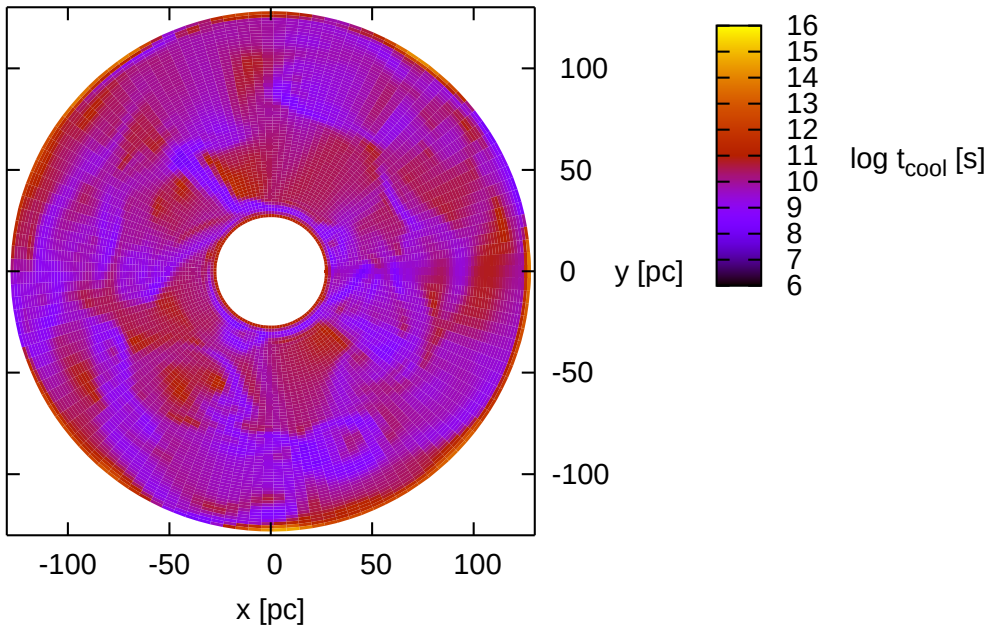

Figure 6.28: Same as Figure 6.23 but for the decadic logarithm of the cooling time in seconds. It is very small compared to the dynamical time scale of $t = 1.7{\cdot}10^{13}\,\mathrm{s} = 5.3{\cdot}10^{5}\,\mathrm{a}$ and smallest ($10^8 - 10^9\,\mathrm{s}$) in the clumps.

6.2.3 Accretion

The solid line in Figure 6.29 is the mass that has passed the inner boundary of the calculation domain inwards, *i.e.*, accreted to the inner disk. This is plotted versus time. Except for the first $5{\cdot}10^5$ a, the slope is mainly positive indicating accretion. At the end of the run at about only $3{\cdot}10^6$ a, almost $1.5{\cdot}10^8\,\mathrm{M}_\odot$ have been accreted to the inner disk giving a mean accretion rate of $\dot{M} = 50\frac{\mathrm{M}_\odot}{\mathrm{a}}$. From this we get an estimate for the accretion time scale of

$$t_{\mathrm{acc}} \approx \frac{M_{\mathrm{d}}}{\dot{M}} \approx 1.2{\cdot}10^7\,\mathrm{a}. \tag{6.2}$$

This accretion happens mainly in steps indicating that clumps fall into the inner disk. We will see below that this is what actually occurs. The dashed line in Figure 6.29 on the other hand is the mass that has passed the outer calculation boundary outwards plotted versus time. At the end of the run this is by a factor of about two more than what is accreted. In contrast to the accretion, this line is much smoother. From Figure 6.30, where the mass of the gas in the calculation domain is plotted versus time as the solid line, we see that at the end of the run more than 70 % of the disk is lost. The dashed line shows the mass of the inner disk versus time which becomes equal to the disk mass at around $t = 2.7{\cdot}10^3$ a. This means that from that time on, the dynamics is dominated by the influence of the inner disk. We have seen above that at $t = 2.3{\cdot}10^6$ a already about half of the disk is Keplerian. Following the same reasoning, at some instant the whole disk must become Keplerian. The gravitational influence of the inner disk is not perfectly modeled especially because it does not contain clumps. Thus the simulation was stopped shortly after $t = 2.7{\cdot}10^3$ a.

In Figure 6.31, which is a time sequence of the surface density from $t = 1.4{\cdot}10^6$ a to $t = 2.1{\cdot}10^6$ a with slightly varying time steps of about $1.5{\cdot}10^5$ a, we can follow the interaction between two clumps that formed due to gravitational instability. The clumps are marked by arrows. In Figure 6.31(a) they approach each other where one of the clumps is in the process of merging with another clump. In Figure 6.31(b) the two clumps get closer and then collide in Figure 6.31(c). Then in Figures 6.31(d) to 6.31(f) one of the clumps is flung inwards while some diffuse gas is blown outward. The inward moving clump eventually passes the inner calculation domain. In the other parts of the disk similar interactions, mostly including more than two clumps, can be seen. This explains the accretion, especially the steps in the accretion, and the absence of such steps in the mass that passes the outer rim in Figure 6.29.

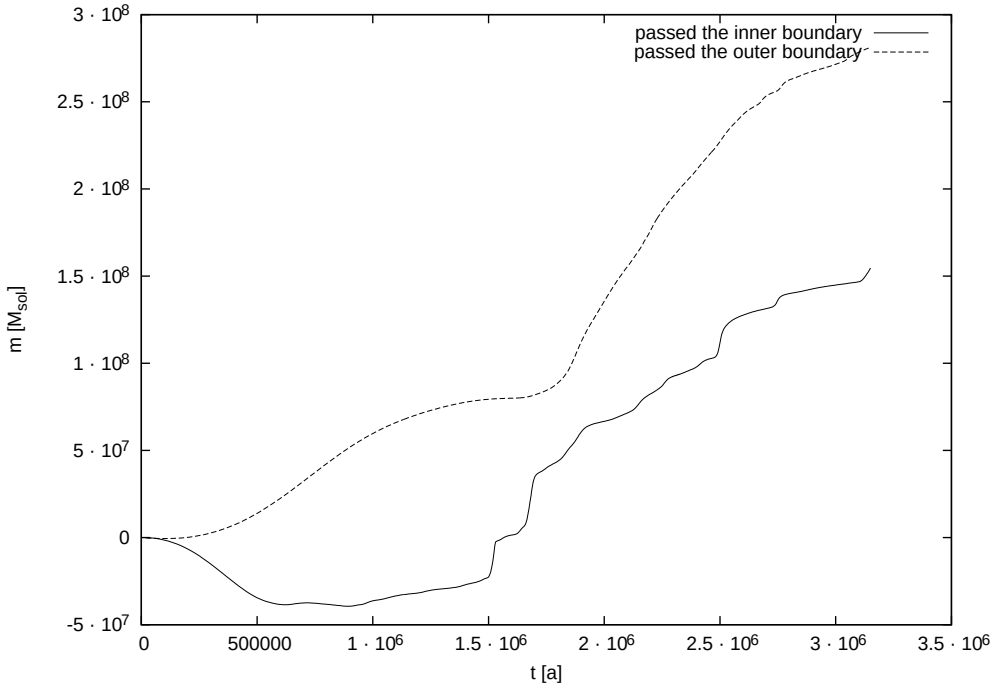

Figure 6.29: The mass that passed the inner rim inwards (solid line) and the outer rim outwards (dashed line) in solar masses versus time in years for the standard run. The solid line shows strong accretion at the inner rim while the dashed line shows even stronger decretion at the outer rim.

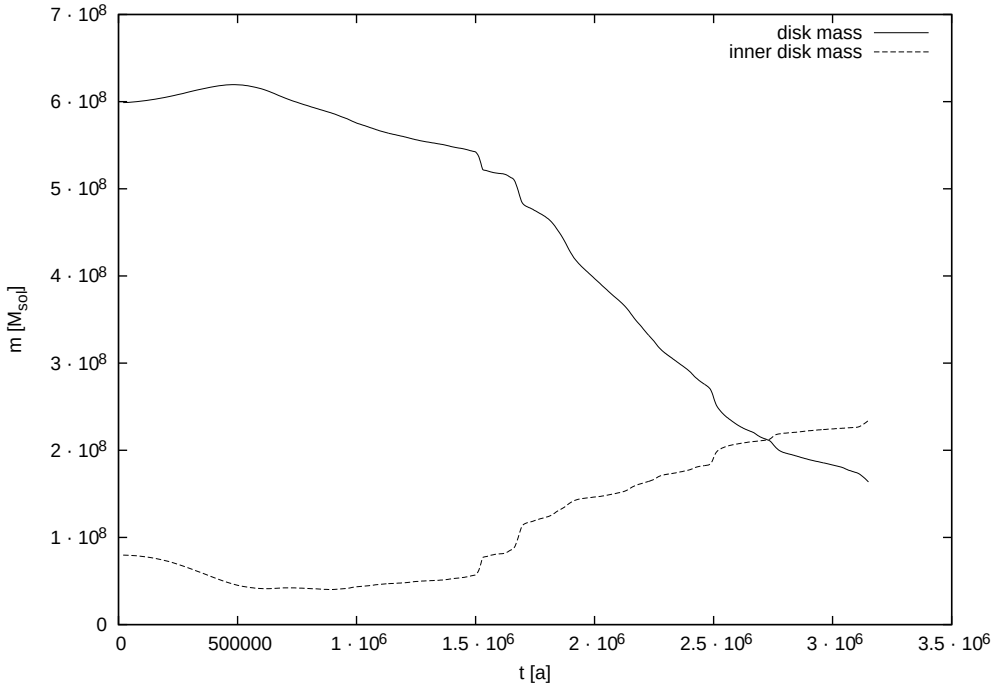

Figure 6.30: The mass in the calculation domain (solid line) and the mass of the inner disk (dashed line) in solar masses versus time in years for the standard run. At the end of the run, the disk has lost more than 70 % of its mass, partly to the inner disk as seen by the rise of the dashed line. At about $2.7{\cdot}10^6$ a, the mass of the disk (in the calculation domain) equals that of the inner disk.

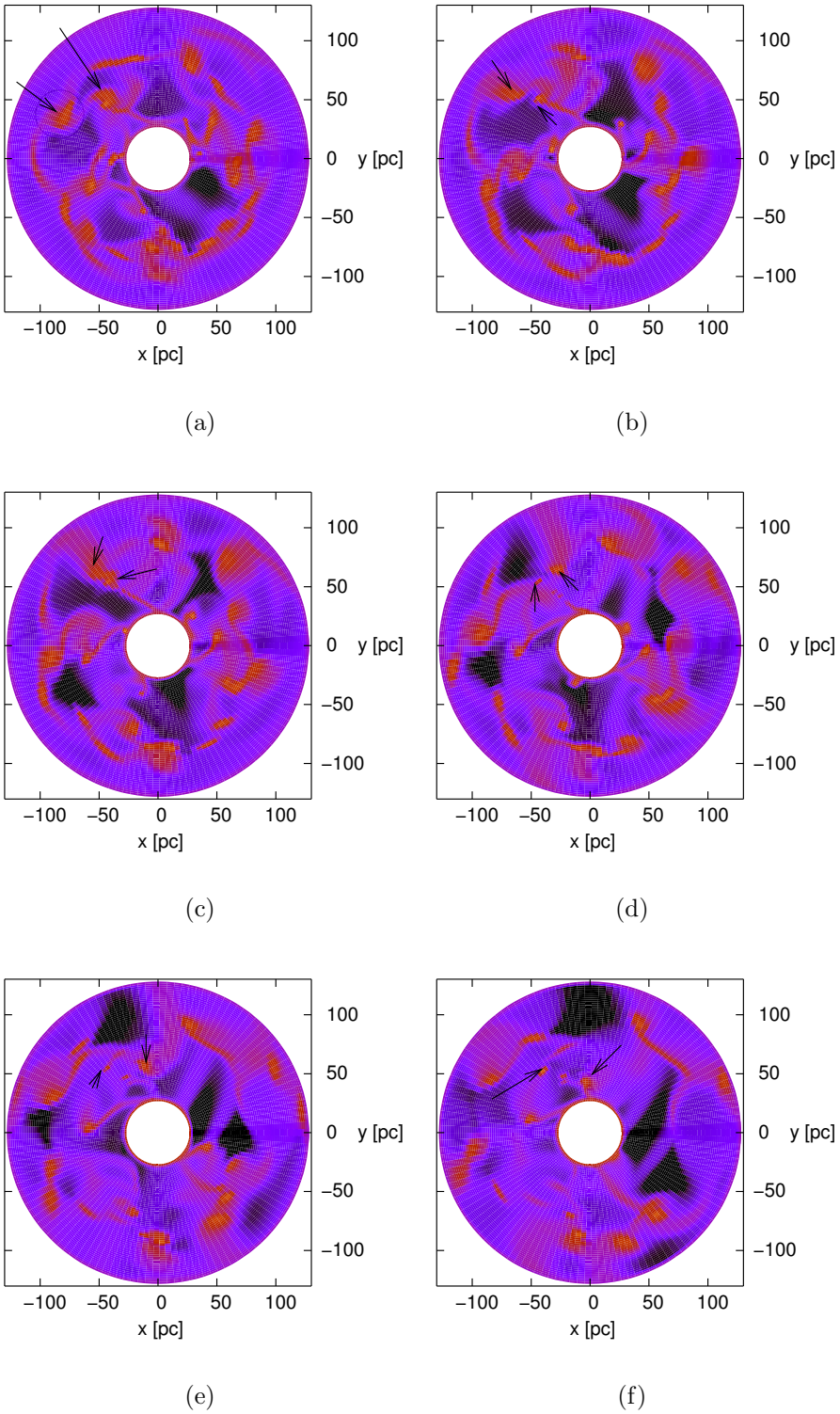

Figure 6.31: The decadic logarithm of the surface density in $\mathrm{kg\,m^{-2}}$ ranging from -1 to 5. Shown are the time steps $n = 15000$ to $n = 30000$ with a step size of 3000 from the upper left to the lower right. These correspond to the times $t = 1.4{\cdot}10^6$ a, $t = 1.5{\cdot}10^6$ a, $t = 1.6{\cdot}10^6$ a, $t = 1.8{\cdot}10^6$ a, $t = 2.0{\cdot}10^6$ a, $t = 2.1{\cdot}10^6$ a. In the upper left of the disk a collision of two clumps which are marked with arrows can be seen. While one of the clumps is sent to the inner disk, diffuse material gets blown outwards.

Comparison with predictions

If we interpret the accretion to be due to the β-like viscosity that comes about by the turbulence driven by gravitational instability, we can estimate the resulting β_{grav} (where the subscript is used to distinguish it from the hydrodynamic viscosity used in the simulation) using the accretion time scale from Equation (6.2) to get $\beta_{\text{grav}} = \frac{1}{t_{\text{acc}}\Omega_{\text{O}}} \approx 0.04$. On the other hand, if the β-viscosity can really describe the accretion, then the turbulent velocity and the turbulent length scale must follow the relations of (2.60). In Section 6.2.1 we found that $v_{\text{t}} \sim (0.1 - 0.3)v_{\varphi}$ and $l_{\text{t}} \sim (0.1 - 0.4)R$ agreeing well with each other and giving $\beta_{\text{grav}} \sim 0.01 - 0.16$ which agrees with the value above from the accretion time scale. Of course there is a large discrepancy with the value predicted by the linear stability analysis in Section 3.4.

If we assumed instead that the gravitational instability leads to some kind of α-disk like accretion as discussed in Section 2.5, we would get for $R = R_{\text{O}}$ using (2.88) (with $\delta \approx 1$ for $\Omega \propto R^{-\frac{1}{2}}$) and $\nu = \alpha\frac{c_{\text{s}}^2}{\Omega}$ from (2.57) and (2.37)

$$\alpha = \frac{\dot{M}\Omega_{\text{O}}}{\Sigma\delta\pi c_{\text{s}}^2} = 7.5{\cdot}10^3, \tag{6.3}$$

where $\Sigma = 20\,\text{kg}\,\text{m}^{-2}$ and $c_{\text{s}} = 300\,\text{m}\,\text{s}^{-1}$ were used (see Figures 6.13 and 6.22). But if we take a value for $t_{\text{cool}}\Omega$ from Figure 6.27 of $2{\cdot}10^{-4}$ (which hardly changes with time), we get

$$\alpha \approx \frac{1}{t_{\text{cool}}\Omega_{\text{O}}} \approx 5{\cdot}10^3, \tag{6.4}$$

which is of the same order of magnitude. If we had used $\nu = \alpha h c_{\text{s}}$ with the real height of the disk, we would have a much larger α in Equation (6.3) since the height of the disk is much smaller than $\frac{c_{\text{s}}}{\Omega}$, leading to a much more serious disagreement.

To compare the accretion time scale of our simulation to the predictions for the clumpy disk model in 2.5, we arrive at the question what the axisymmetrically distributed mass in our model is. From Figure 6.16, we see that the minimal surface density is $\Sigma_{\text{min}} \sim 10^{-2}\,\text{kg}\,\text{m}^2$ which is three orders of magnitude smaller than the mean surface density. Thus M_{t} is dominated by the star. This would mean that $M_{\text{R}} \approx 10M_{\text{t}}$. With this value and an estimated $\frac{l_{\text{c}}}{R} \sim \frac{1}{10}$, we get using Equation (2.85)

$$t_{\text{clump}} = \frac{l_{\text{c}}}{R}\frac{1}{\left(\frac{M_{\text{R}}}{\pi M_{\text{t}}}\right)}\frac{1}{\Omega} \sim \frac{1}{25\Omega}, \tag{6.5}$$

which is orders of magnitude different compared to $t_{\text{acc}} \approx \frac{1}{0.04\Omega}$ the result from our simulation in Section 6.2.3. The disagreement becomes even worse for the case of no central object which approximately the same accretion time scale (see Section 6.3.5).

number	β	$\Sigma \propto$	$M_\mathrm{d}[\mathrm{M}_\odot]$	$\frac{M_\mathrm{d}}{M_*}$	other
1	0.005	$\frac{1}{R}$	$6{\cdot}10^8$	8	—
2	0.001	·	·	·	—
3	0.01	·	·	·	—
4	$5{\cdot}10^{-4}$	·	·	·	—
5	·	·	$6{\cdot}10^9$	·	—
6	·	·	$6{\cdot}10^7$	·	—
7	·	const.	$3.5{\cdot}10^8$	4.7	—
8	·	·	·	∞	—
9	·	·	·	·	factor 10 in cooling
10	·	·	·	·	CMB heating
11	·	·	·	·	$\gamma = \frac{5}{3}$, $\mu = 0.001\,\mathrm{kg\,mol^{-1}}$

Table 6.1: This table lists the parameters used for the different simulations. The first column gives the simulation a reference number. The second column lists the β-viscosity parameter is listed, and the third column lists the radial dependence of the surface density at the beginning of the simulation. Columns four and five show the mass of the disk in the calculation domain and the ratio of the SMBH mass to the disk mass, respectively. The last column lists any other changes made to the simulation. A dot ($\cdot$) means that the parameter is the same as in the standard simulation (simulation 1). In simulation 9, τ_eff was divided by 10 to reduce the cooling time by a factor of 10 for the same temperature and surface density. Simulation 10 restricted the temperature to values larger then 30 K which is the temperature of the cosmic microwave background at $z = 10$. In simulation 11, $\gamma = \frac{5}{3}$ and $\mu = 0.001\,\mathrm{kg\,mol^{-1}}$ were set for all temperatures.

6.3 Comparison with the additional simulations

6.3.1 Description of the additional simulations

As stated above, the additional simulations differ from the standard simulation mainly by one parameter each. A listing of all the simulations with their parameters can be found in Table 6.1. Simulation 1 is the standard run described in Section 6.1. The other simulations are described in more detail in the sections below.

6.3.2 Different viscosity parameters β

There are four different viscosity parameters used: $\beta = 0.01$ (run number 3), $\beta = 0.005$ (run number 1), $\beta = 0.001$ (run number 2) and $\beta = 5{\cdot}10^{-4}$ (run number 4). In Figure 6.32, the surface density is plotted for the extreme runs (3 and 4) at the same point of time as Figure 6.8 ($t = 1.7{\cdot}10^{13}\,\mathrm{s} = 5.3{\cdot}10^5\,\mathrm{a}$). Obviously the three plots look differently, especially because the clumps are more compact for lower viscosity. This effect is predicted by the linear theory for the typical scale length (see Equation (3.58)) although the dynamics at this time are

probably not linear anymore.

Even at later times, *e.g.*, $t = 5.6{\cdot}10^{13}\,\mathrm{s} = 1.8{\cdot}10^{6}\,\mathrm{a}$, the simulations with different viscosity parameters look different from each other. In Figure 6.33 the surface densities of simulation 3 and 4 are plotted for that time and can be compared with Figure 6.16 for the standard run. Still the gradients in the densities are much more pronounced for the less viscous case. This causes numerical problems in solving the Poisson equation, as mentioned before, and prohibits a simulation with very low or no physical viscosity.

In Figure 6.34 the mass accreted into the inner disk is plotted versus time for all the runs with different viscosities. In Figure 6.35 on the other hand the mass that was lost at the outer calculation domain is plotted versus time for the same runs. From these plots, it is obvious that in spite of the different surface densities seen above, their accretion and decretion behavior is very similar.

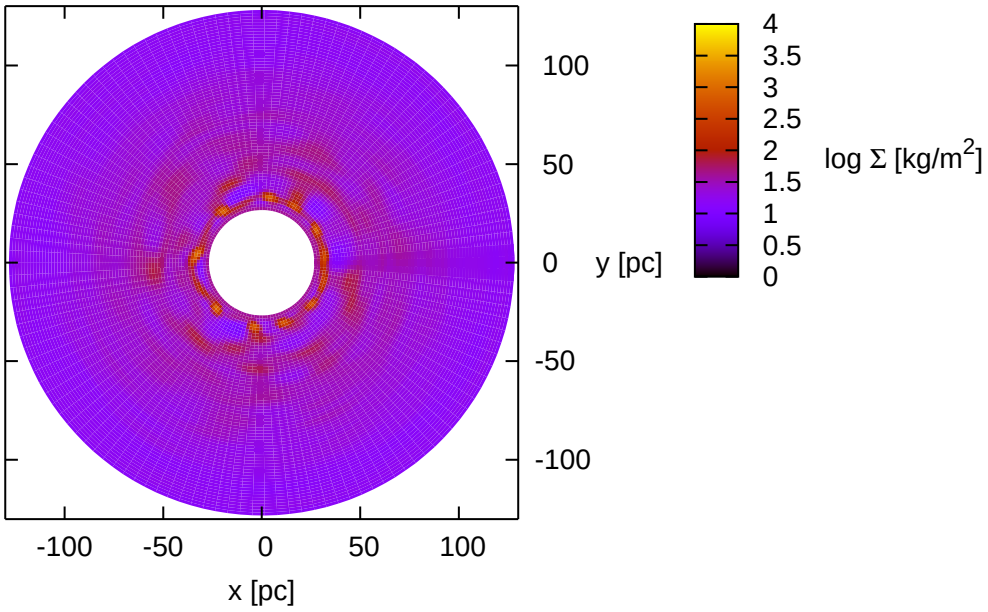

(a)

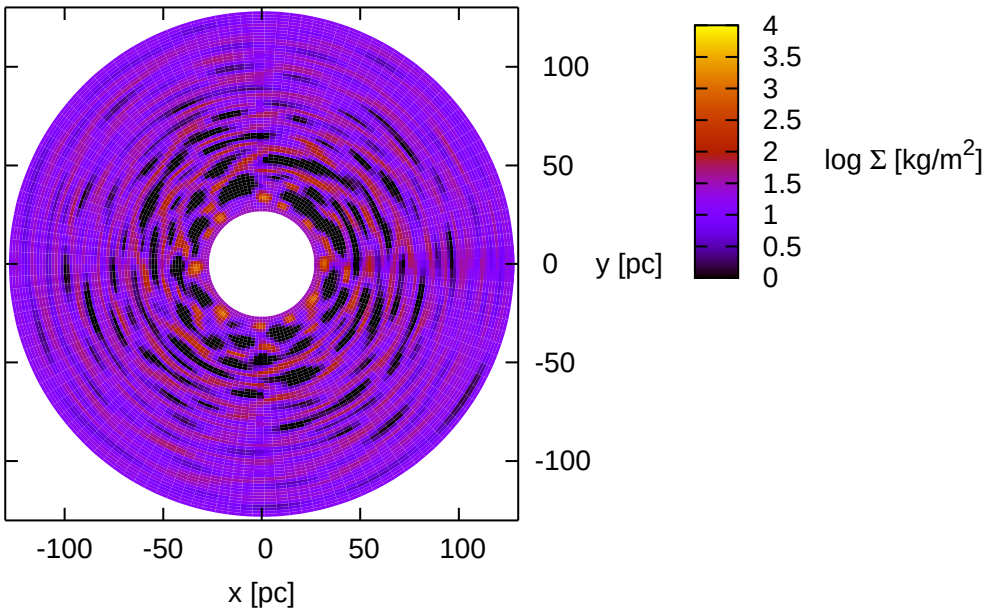

(b)

Figure 6.32: The decadic logarithm of the surface density in $\mathrm{kg\,m^{-2}}$ for simulation 3, where $\beta = 0.01$ (a) and for simulation 4, where $\beta = 5{\cdot}10^{-4}$ (b), at $t = 1.7{\cdot}10^{13}\,\mathrm{s} = 5.3{\cdot}10^{5}\,\mathrm{a}$. Figure 6.8 shows the same for the standard run. There are obvious differences, see text for the details.

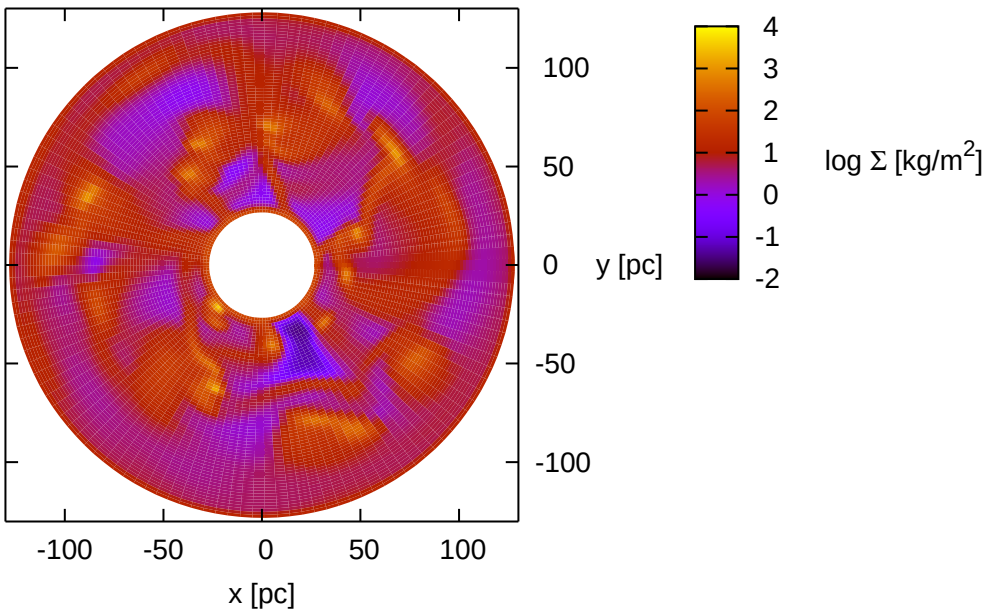

(a)

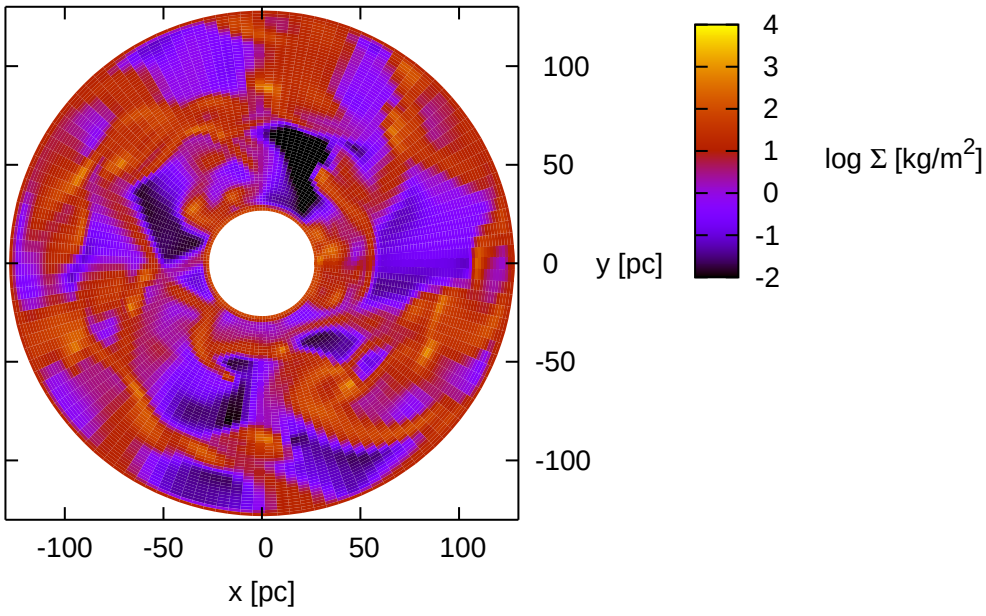

(b)

Figure 6.33: The same as Figure 6.32 but at time $t = 1.7{\cdot}10^{13}\,\mathrm{s} = 5.3{\cdot}10^{5}\,\mathrm{a}$. Figure 6.16 shows the same for the standard run. There are obvious differences, see text for the details.

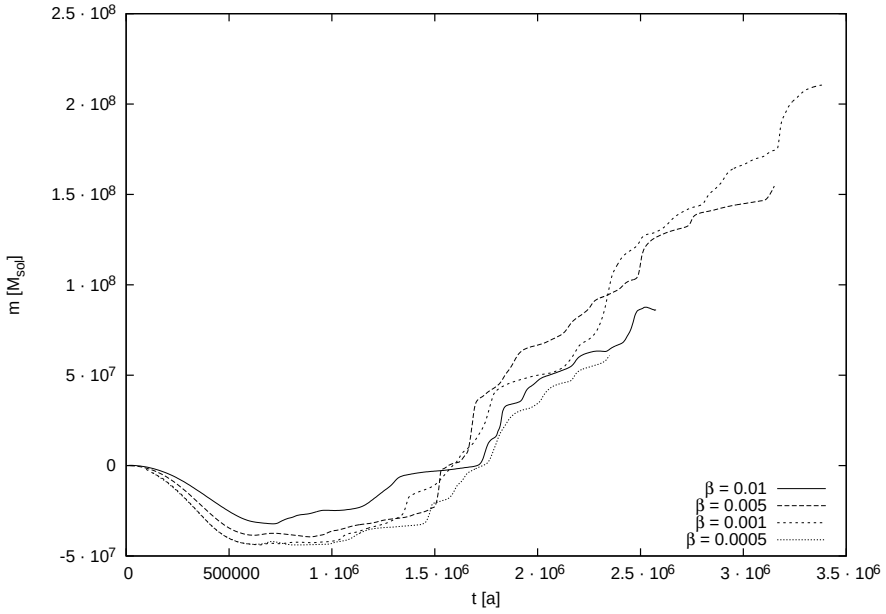

Figure 6.34: The mass in solar masses that passed the inner rim inwards versus time in years for the runs with different viscosity parameters.

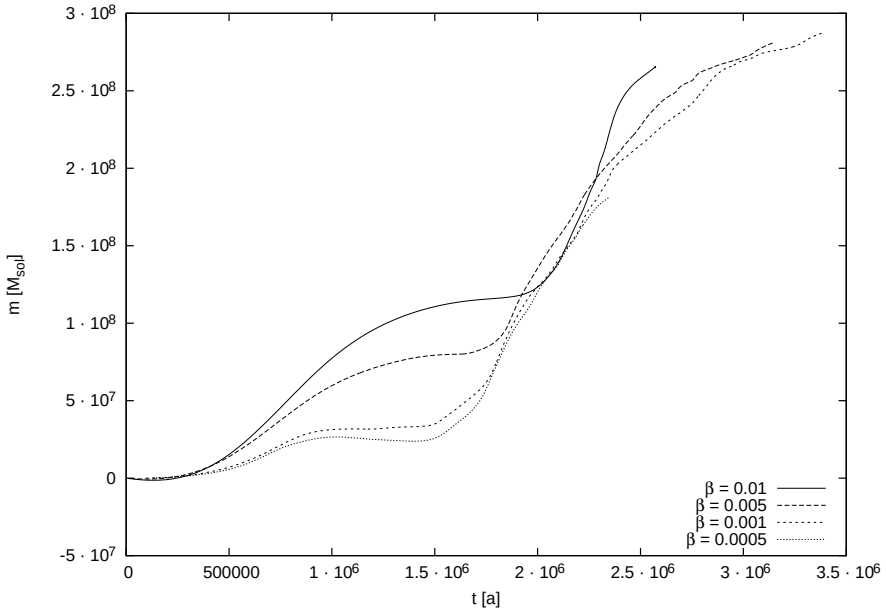

Figure 6.35: The mass in solar masses that passed the outer rim outwards versus time in years for the runs with different viscosity parameters.

6.3.3 Changing the mass

There are three runs with significantly different disk masses: run number 6 with $M_\mathrm{d} = 6{\cdot}10^7\,\mathrm{M}_\odot$, run number 1 with $M_\mathrm{d} = 6{\cdot}10^8\,\mathrm{M}_\odot$ and run number 5 with $M_\mathrm{d} = 6{\cdot}10^9\,\mathrm{M}_\odot$. The initial mass of the inner disk, the amplitude of the noise in Σ, as well as the boundary condition for Σ at the outer boundary had to be changed accordingly in order to produce white noise with the same relative amplitude and smooth transitions at the boundaries. Since the disk in run number 5 gets relatively warm e_start (which is used as initial and boundary value) was set to $10^8\,\mathrm{J\,m^{-2}}$. In Figure 6.36 the mass accreted into the inner disk is plotted versus time for these runs. In Figure 6.37 the same is done for the mass that was lost from the calculation domain at the outer boundary. As expected, the three simulations show very different mass and time scales. To compare them with each other in Figures 6.38 and 6.39, they are plotted again but this time the line for the $M_\mathrm{d} = 6{\cdot}10^9\,\mathrm{M}_\odot$ simulation and the line for the $M_\mathrm{d} = 6{\cdot}10^7\,\mathrm{M}_\odot$ simulation are scaled as follows. We scale the mass $m_\mathrm{higher} \to \frac{1}{10} m_\mathrm{higher}$ in the higher mass case and $m_\mathrm{lower} \to 10 m_\mathrm{lower}$ in the lower mass case to account for the mass difference. The time is scaled $t_\mathrm{higher} \to 3 t_\mathrm{higher}$ in the higher mass case and $t_\mathrm{lower} \to \frac{1}{3} t_\mathrm{lower}$ in the lower mass case to account for the difference of the dynamical time scale with respect to the standard run (which is $\Omega^{-1} \approx \sqrt{\frac{R}{\pi G \Sigma}}$ in the monopole approximation giving a factor $\sqrt{10}^{-1} \approx \frac{1}{3}$ for Σ a factor of ten higher). The angular velocities indeed differ by a factor of about three each and can be seen in Figure 6.40 where they are plotted versus radius for the three runs. From these plots we see that the scaled accretion and decretion behave very similarly except for the start of simulation 5 with $M_\mathrm{d} = 6{\cdot}10^9\,\mathrm{M}_\odot$ that starts accreting at the inner boundary and decreting at the outer boundary earlier than in the other simulations. The slope is again similar to the others. It follows that the accretion and evolution time scales of these disks are roughly proportional to the dynamical time scale as predicted by the β-viscosity (see Equation (2.59)).

In Figure 6.41, the azimuthal average of the temperature in the $M_\mathrm{d} = 6{\cdot}10^9\,\mathrm{M}_\odot$ simulation (short dashed line with $*$-symbols), that of the standard run with $M_\mathrm{d} = 6{\cdot}10^8\,\mathrm{M}_\odot$ (long dashed line with $\times$-symbols) and that of the simulation with $M_\mathrm{d} = 6{\cdot}10^7\,\mathrm{M}_\odot$ (solid line with $+$-symbols) is shown at $t = 5.9{\cdot}10^5\,\mathrm{a} = \frac{1}{3} \cdot 1.8{\cdot}10^6\,\mathrm{a}$, $t = 1.8{\cdot}10^6\,\mathrm{a}$ and $t = 5.3{\cdot}10^6\,\mathrm{a} = 3 \cdot 1.8{\cdot}10^6\,\mathrm{a}$ respectively versus radius. $t = 1.8{\cdot}10^6\,\mathrm{a}$ is the time for Figure 6.21(b) where the same is plotted for the standard run. The temperature in the high mass disk run is about a factor of five higher than in the standard run and roughly by a factor of two lower in the low mass disk run.

In Figure 6.42, the azimuthal average of the cooling time for the $M_\mathrm{d} = 6{\cdot}10^9\,\mathrm{M}_\odot$ simulation (short dashed line with $*$-symbols) and the $M_\mathrm{d} = 6{\cdot}10^7\,\mathrm{M}_\odot$ simulation (solid line with $+$-symbols) is plotted versus radius at the corresponding times as it was done in Figure 6.26(b) (again shown here as the long dashed line with $\times$-symbols) for the standard run. Analogously the cooling time divided by the dynamical time scale in Figure 6.43 can be compared with Figure 6.27. In the higher mass disk, the cooling time is by a factor of three lower than in the standard run and divided by the dynamical time scale there is no consistent

difference over all radii. The cooling time in the lower mass run is about a factor of larger than ten higher and $t_{\rm cool}\Omega$ is about a factor of five higher.

At the same radius, the viscous time scale is proportional to the inverse of the viscosity (see Equation (2.30)). For the α-viscosity interpretation described in Section 2.5 this means that

$$t_\nu \propto \frac{\Omega}{\alpha c_{\rm s}^2} \propto t_{\rm cool}\Omega\frac{\Omega}{T}. \tag{6.6}$$

From Figure 6.38 we see that the accretion time was approximately three times shorter than for the standard run for a disk mass 10 times higher. While the accretion time was a factor of three longer for a disk mass ten times lower. If we put in the numbers from above for the factors by which Ω, T and $t_{\rm cool}\Omega$ have changed, we see that the α-viscosity interpretation predicts the viscous and thus the accretion time scale to be a factor 1.7 instead of 3 shorter in the high mass disk and a factor of 7.5 instead of 3 longer in the low mass disk, each compared with the standard disk.

In Figure 6.44 the azimuthal average of the root mean square of the radial velocity is plotted for the higher mass (short dashed line with $*$-symbols), lower mass (solid line with $+$-symbols) and the standard mass (long dashed line with $\times$-symbols) simulations. It can be seen that like in the standard run (already shown in Figure 6.15), the turbulent velocity is about the same in all three simulations with around $0.1 - 0.5\ v_\varphi$. From Figures 6.45 and 6.46, where the radial velocities are plotted for the higher and lower mass simulations, we can again conclude as in Section 6.2.1 from Figure 6.19 that the turbulent length scale is about the same in all three simulations with about $0.1 - 0.3\ R$. This is necessary for the β-viscosity interpretation.

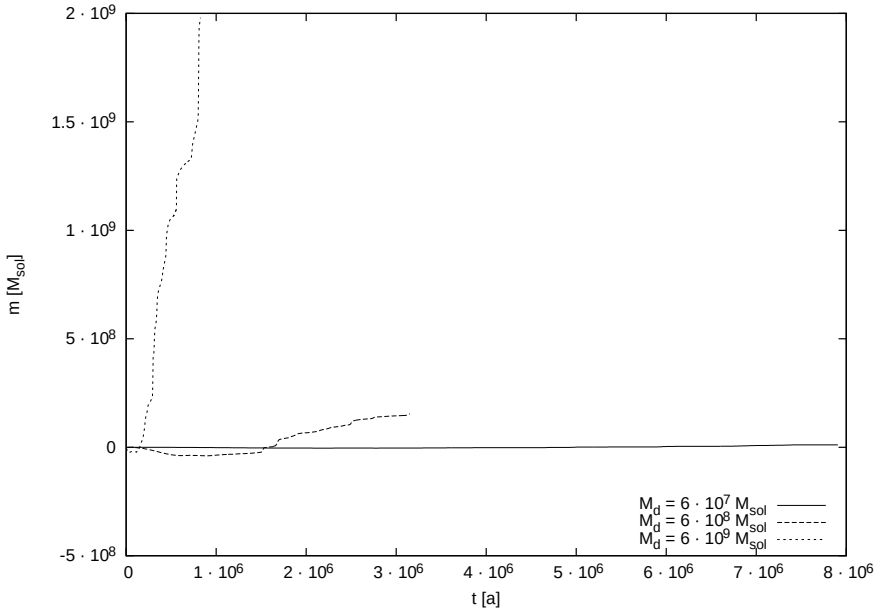

Figure 6.36: The mass in solar masses that passed the inner rim inwards versus time in years for the runs with different disk masses.

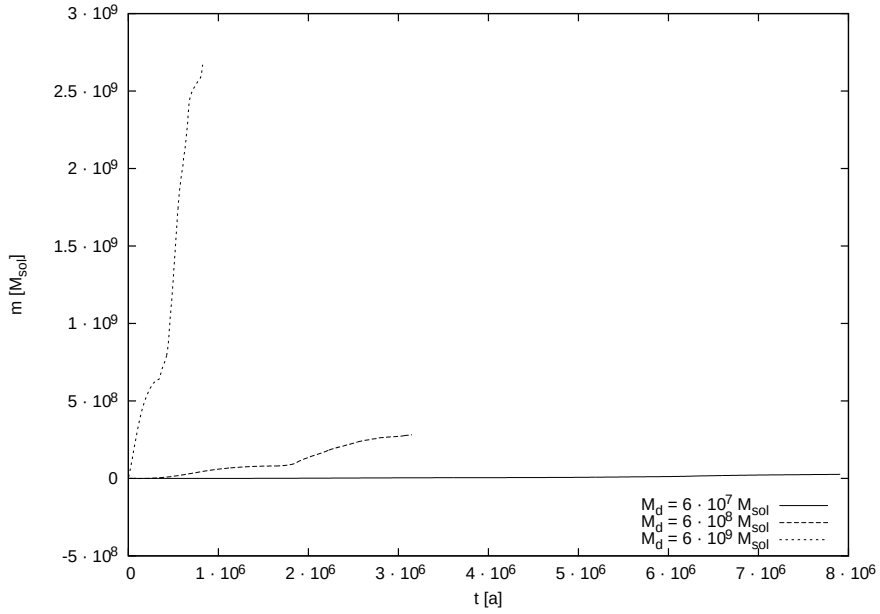

Figure 6.37: The mass in solar masses that passed the outer rim outwards versus time in years for the runs with different disk masses.

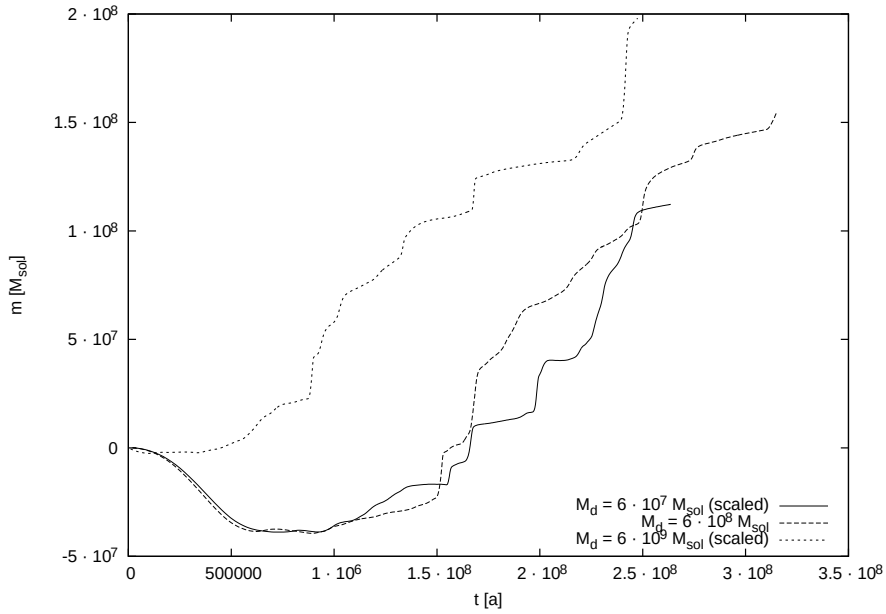

Figure 6.38: Same as Figure 6.36 but for the line for $M_\mathrm{d} = 6{\cdot}10^7\,\mathrm{M}_\odot$ is scaled by a factor of $\frac{1}{3}$ in time and a factor of ten in mass and the line for $M_\mathrm{d} = 6{\cdot}10^9\,\mathrm{M}_\odot$ is scaled by a factor of three in time and a factor of $\frac{1}{10}$ in mass. The line for $M_\mathrm{d} = 6{\cdot}10^8\,\mathrm{M}_\odot$ was not scaled. The three curves agree qualitatively except that the simulation with $M_\mathrm{d} = 6{\cdot}10^9\,\mathrm{M}_\odot$ starts the accretion phase early.

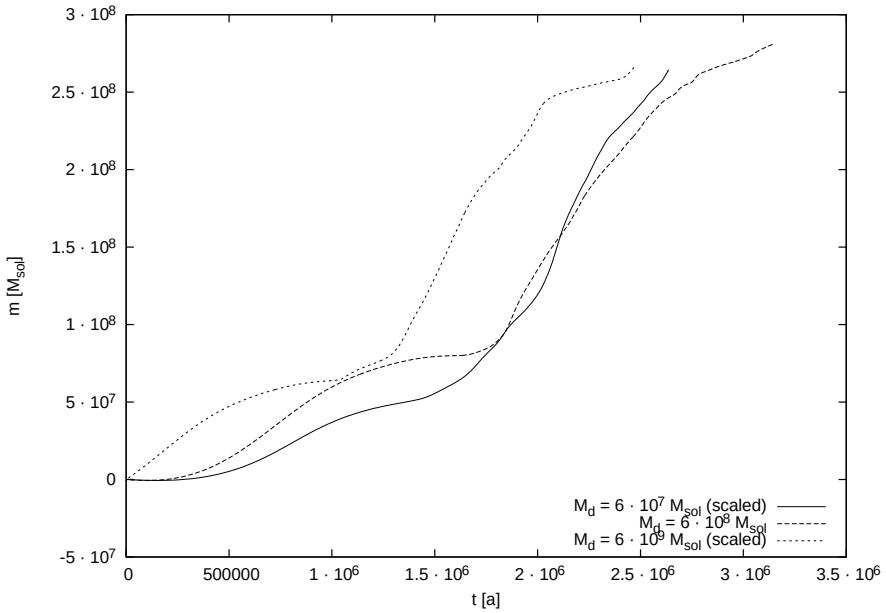

Figure 6.39: Same as Figure 6.37 but for the line for $M_\mathrm{d} = 6{\cdot}10^7\,\mathrm{M}_\odot$ is scaled by a factor of $\frac{1}{3}$ in time and a factor of ten in mass and the line for $M_\mathrm{d} = 6{\cdot}10^9\,\mathrm{M}_\odot$ is scaled by a factor of three in time and a factor of $\frac{1}{10}$ in mass. The line for $M_\mathrm{d} = 6{\cdot}10^8\,\mathrm{M}_\odot$ was not scaled. They behave similarly but again the curve for $M_\mathrm{d} = 6{\cdot}10^9\,\mathrm{M}_\odot$ starts early.

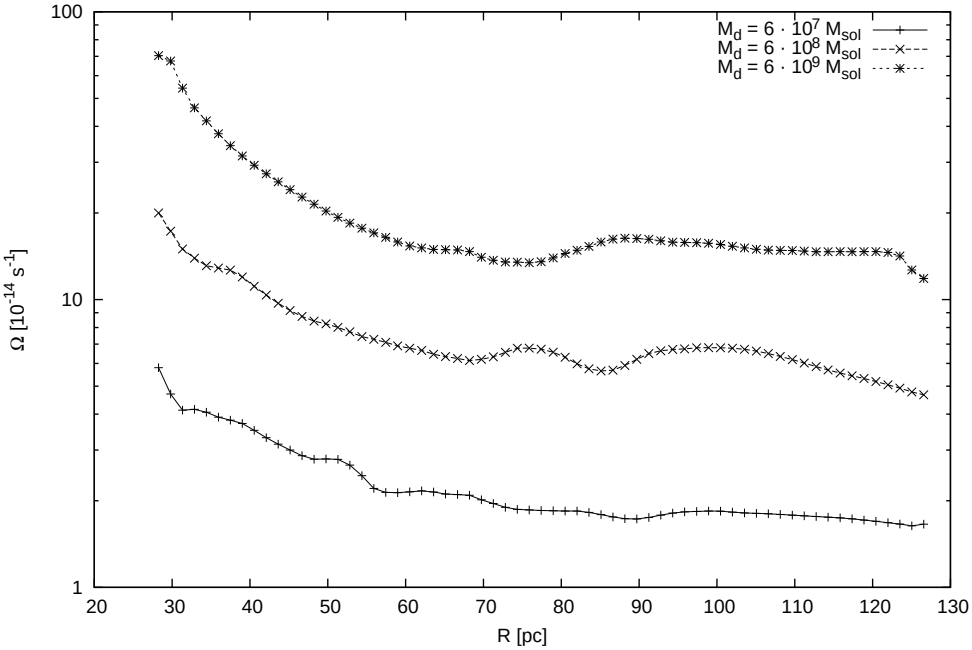

Figure 6.40: The azimuthal average of Ω in $10^{-14}\,\mathrm{s}$ plotted versus radius in pc for the run with $M_\mathrm{d} = 6{\cdot}10^9\,\mathrm{M}_\odot$ at $t = 5.9{\cdot}10^5\,\mathrm{a} = \frac{1}{3} \cdot 1.8{\cdot}10^6\,\mathrm{a}$, the standard run with $M_\mathrm{d} = 6{\cdot}10^8\,\mathrm{M}_\odot$ at $t = 1.8{\cdot}10^6\,\mathrm{a}$ and the run with $M_\mathrm{d} = 6{\cdot}10^7\,\mathrm{M}_\odot$ at $t = 5.3{\cdot}10^6\,\mathrm{a} = 3 \cdot 1.8{\cdot}10^6\,\mathrm{a}$.

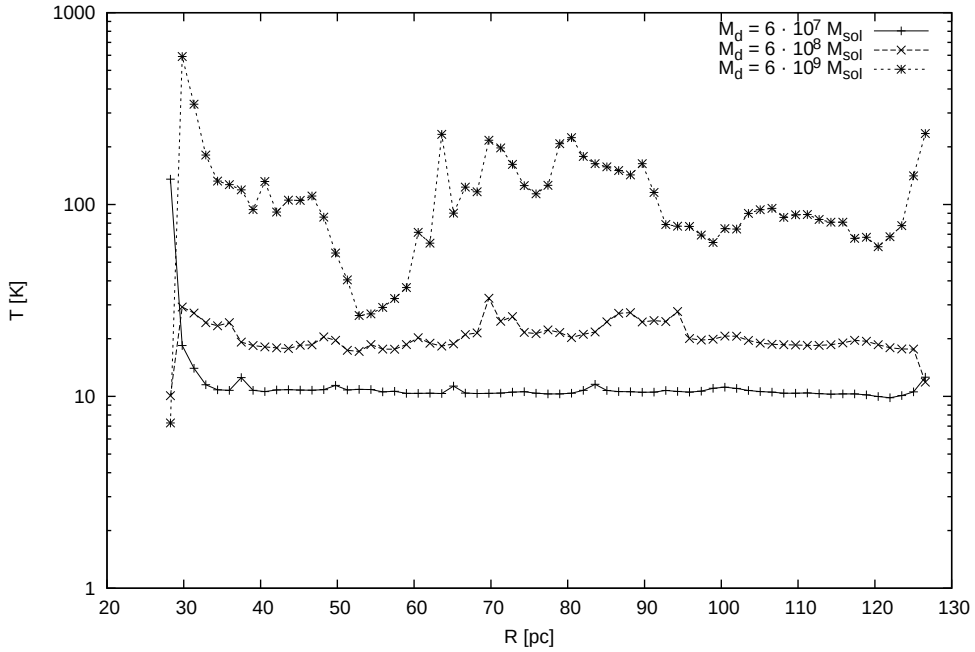

Figure 6.41: The azimuthal average of T in Kelvin plotted versus radius in pc for the run with $M_\mathrm{d} = 6{\cdot}10^9\,\mathrm{M}_\odot$ at $t = 5.9{\cdot}10^5\,\mathrm{a} = \frac{1}{3} \cdot 1.8{\cdot}10^6\,\mathrm{a}$, the standard run with $M_\mathrm{d} = 6{\cdot}10^8\,\mathrm{M}_\odot$ at $t = 1.8{\cdot}10^6\,\mathrm{a}$ and the run with $M_\mathrm{d} = 6{\cdot}10^7\,\mathrm{M}_\odot$ at $t = 5.3{\cdot}10^6\,\mathrm{a} = 3 \cdot 1.8{\cdot}10^6\,\mathrm{a}$. See text for more details and interpretation.

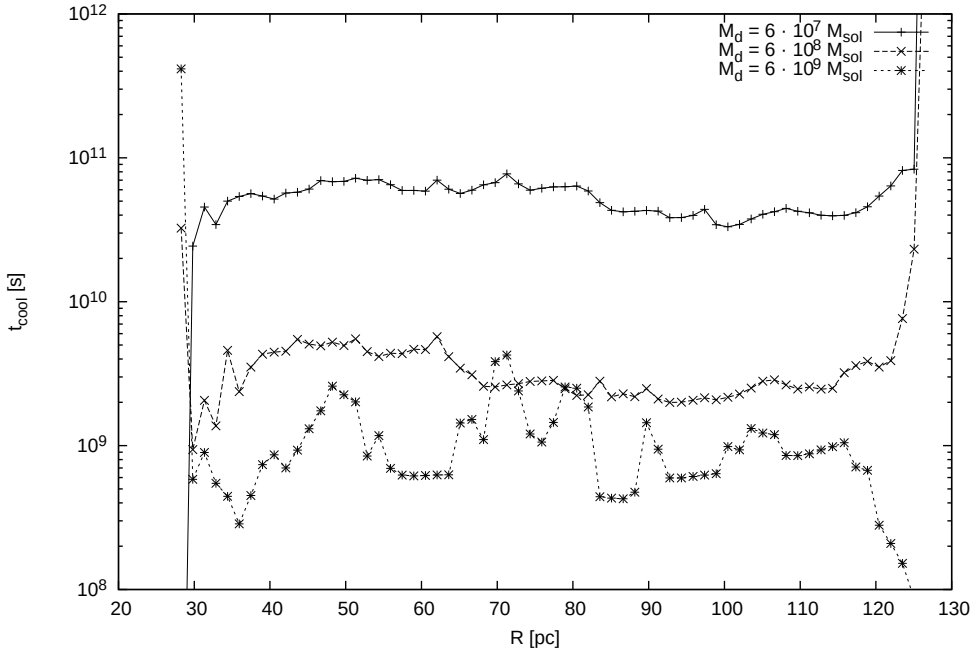

Figure 6.42: Same as Figure 6.41 but for the azimuthal average of the cooling time in seconds.

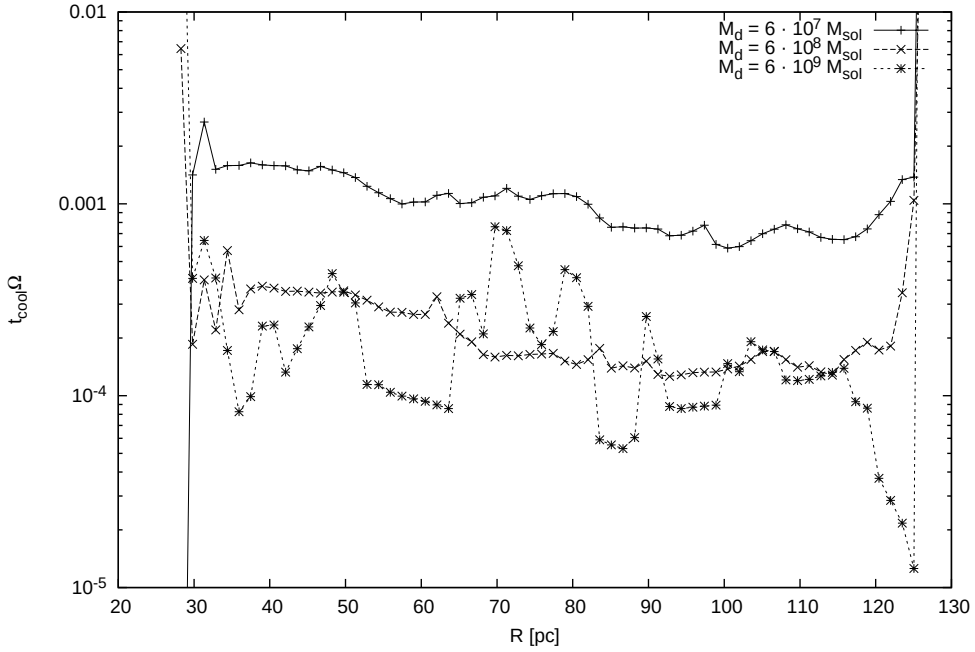

Figure 6.43: Same as Figure 6.41 but for the azimuthal average of the cooling time times the angular velocity.

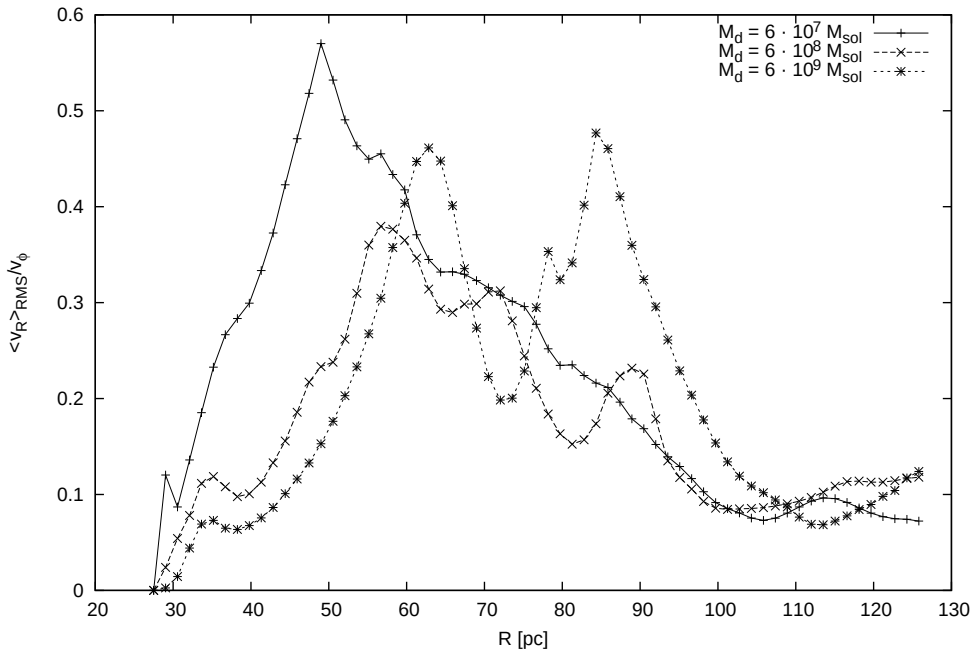

Figure 6.44: Same as Figure 6.41 but for the azimuthal average of $\frac{\langle v_R \rangle_{\rm RMS}}{v_\varphi}$ corrected by the mean radial velocity at each radius. $\frac{\langle v_R \rangle_{\rm RMS}}{v_\varphi}$ is a measure of the turbulent velocity. See text for more details and interpretation.

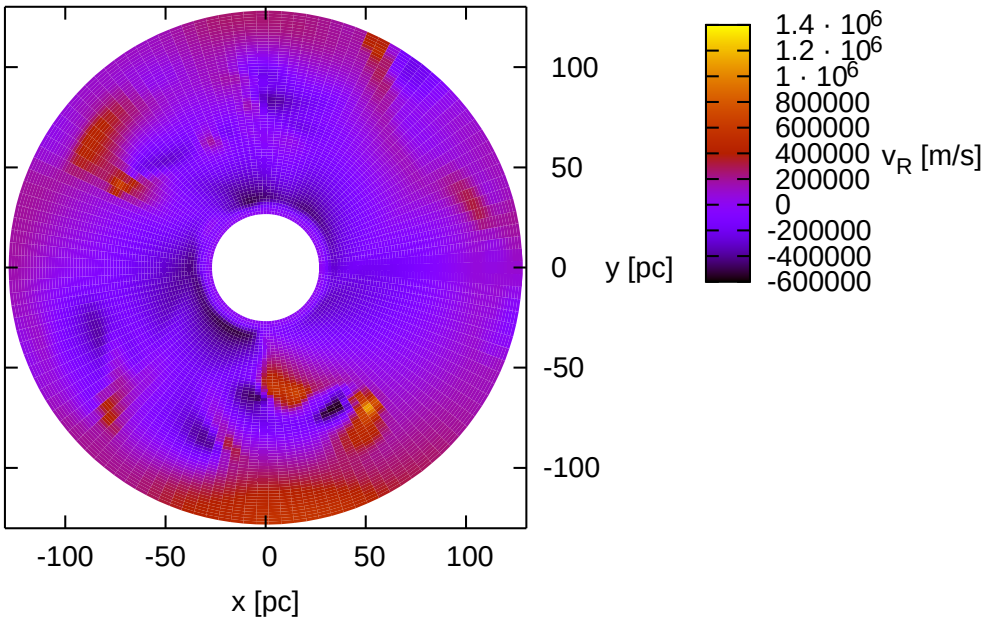

Figure 6.45: The radial velocity in $\mathrm{m\,s^{-1}}$ for run number 5 with $M_\mathrm{d} = 6{\cdot}10^9\,\mathrm{M}_\odot$ at $t = 1.9{\cdot}10^{13}\,\mathrm{s} = 5.9{\cdot}10^5\,\mathrm{a} = \frac{1}{3}\cdot 1.8{\cdot}10^6\,\mathrm{a}$ which is the time of Figure 6.19 where the same is plotted for the standard run with $M_\mathrm{d} = 6{\cdot}10^8\,\mathrm{M}_\odot$. From this plot the turbulent length scale can be estimated as done in Section 6.2.1 for the standard run.

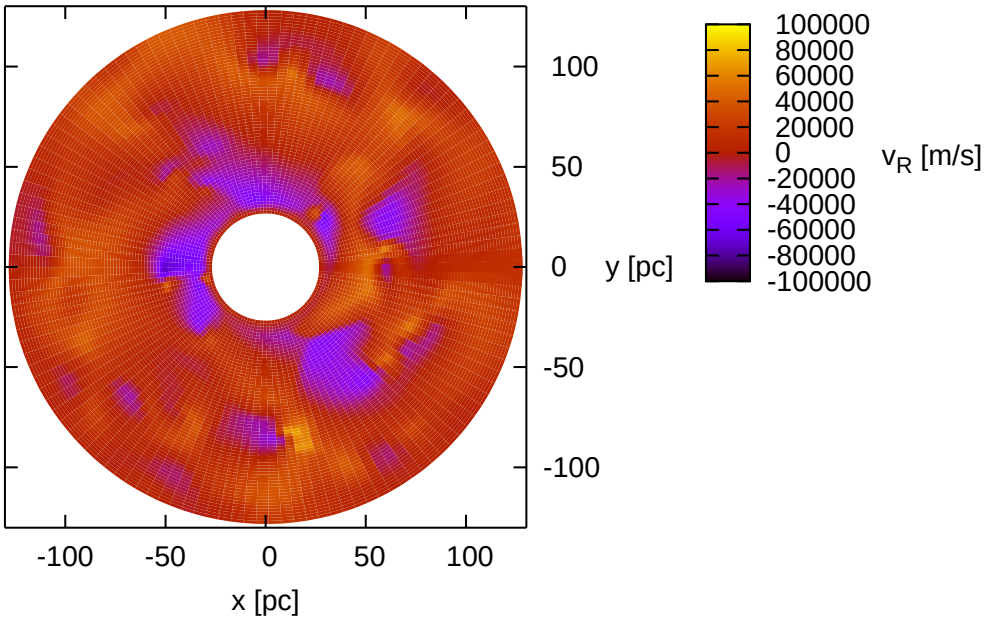

Figure 6.46: The same as in Figure 6.45 but for simulation 6 with $M_\mathrm{d} = 6{\cdot}10^7\,\mathrm{M}_\odot$ at time $t = 1.7{\cdot}10^{14}\,\mathrm{s} = 5.3{\cdot}10^6\,\mathrm{a} = 3\cdot 1.8{\cdot}10^6\,\mathrm{a}$.

6.3.4 A different initial condition

In Simulation 7 the radial Σ-profile at the beginning of the simulation is set to be constant instead of proportional to the inverse radius as in the standard run. The value of the boundary condition for Σ at the outer boundary had to be changed for a smooth transition. The mass of the disk changed to $M_{\mathrm{d}} = 3.5{\cdot}10^{8}\,\mathrm{M}_{\odot}$ but stayed in the same order of magnitude while the mass of the central object was the same as in the standard run. Again the mass of the inner disk at the beginning had to be adapted in this case to $M_{\mathrm{d,i}} = 2.1{\cdot}10^{7}\,\mathrm{M}_{\odot}$. In Figures 6.47 and 6.48 the accretion at the inner rim and decretion at the outer rim is shown in comparison to the standard run. This comparison shows that the behavior is still very similar despite the fact that at the first $1.5{\cdot}10^{8}$ a the flow *into* the calculation domain at the inner boundary is much smaller and the outflow at the outer boundary is smaller overall. Please note that the mass in the disk is about a factor of 1.7 different in the two simulations (see Table 6.1).

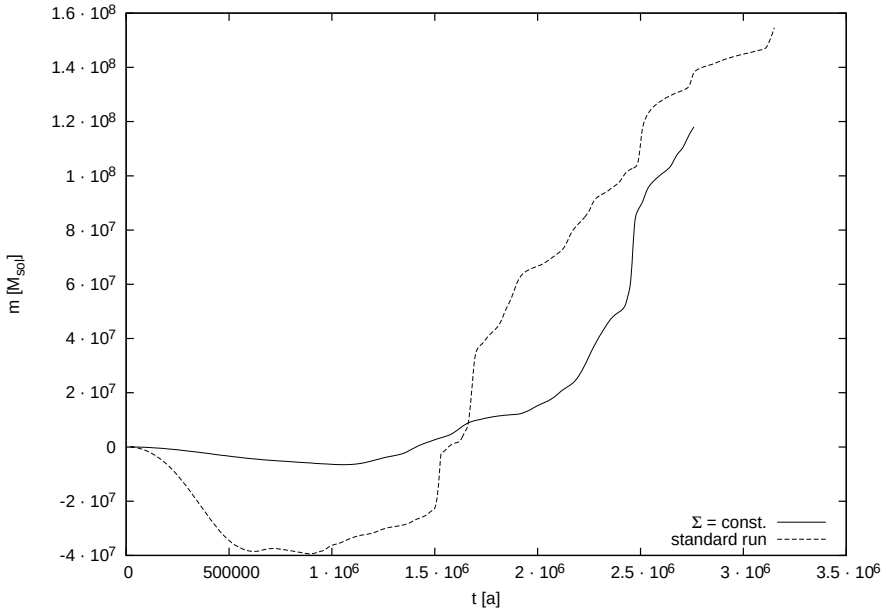

Figure 6.47: The mass in solar masses that passed the inner rim inwards versus time in years for run number 7 where Σ was initialized to be constant compared to the standard run where initially $\Sigma \propto R^{-1}$. Except for the very slow decretion at the first $1.5{\cdot}10^{6}$ a the two curves are not very different.

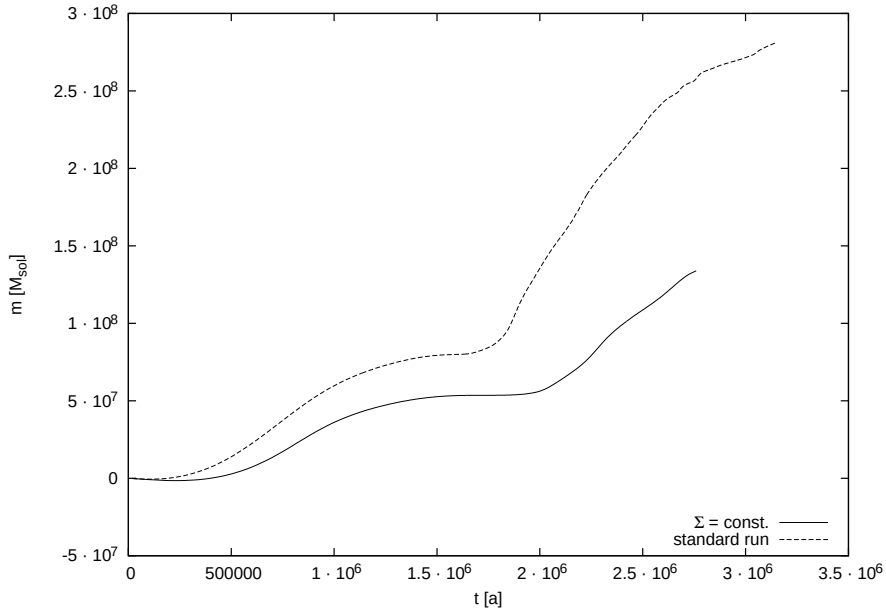

Figure 6.48: The mass in solar masses that passed the outer rim outwards versus time in years for run number 7 where Σ was initialized to be constant compared to the standard run where initially $\Sigma \propto R^{-1}$. They agree qualitatively, but the solid line lies significantly lower. Note that M_{d} is also slightly different.

6.3.5 A simulation with $M_* = 0$

In this section we compare simulation 8 where the central mass is set to zero to the standard run where $M_* = 7.5{\cdot}10^7\,\mathrm{M}_\odot$. In Figures 6.49 and 6.50 the accretion at the inner rim and decretion at the outer rim are shown for run number 8 in comparison with the standard run. From Figure 6.50 we see that the behavior at the outer rim is almost the same in both simulations whereas in Figure 6.49 we see that at the inner edge the evolution of the simulation without a central mass is the same at first but then slower up to $t \approx 2.3{\cdot}10^6$ a. At this point it becomes similarly as fast as the evolution of the standard run and maybe even faster. This behavior can be understood as the disk mass dominating the dynamics at the outer boundary while at the inner boundary the dynamics are dominated by the central mass and inner disk mass. At the beginning the inner disk has about the same mass as the central mass in the standard run and thus the dominating masses at small radii differ by a factor of two in the two runs.

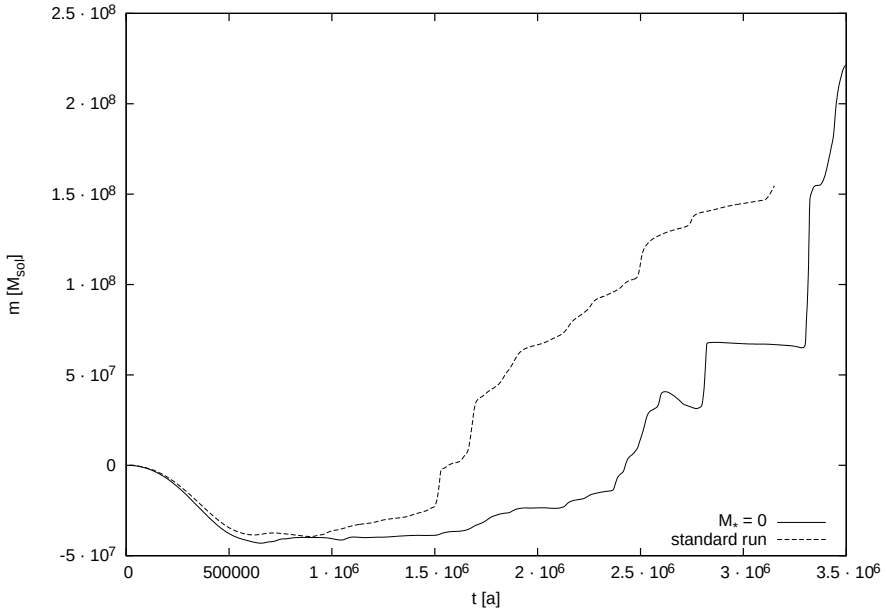

Figure 6.49: The mass in solar masses that passed the inner rim inwards versus time in years for run number 8 where $M_* = 0$ compared to the standard run where $M_* = 7.5{\cdot}10^7\,\mathrm{M}_\odot$. The two curves behave similarly, see text for the explanation of the difference.

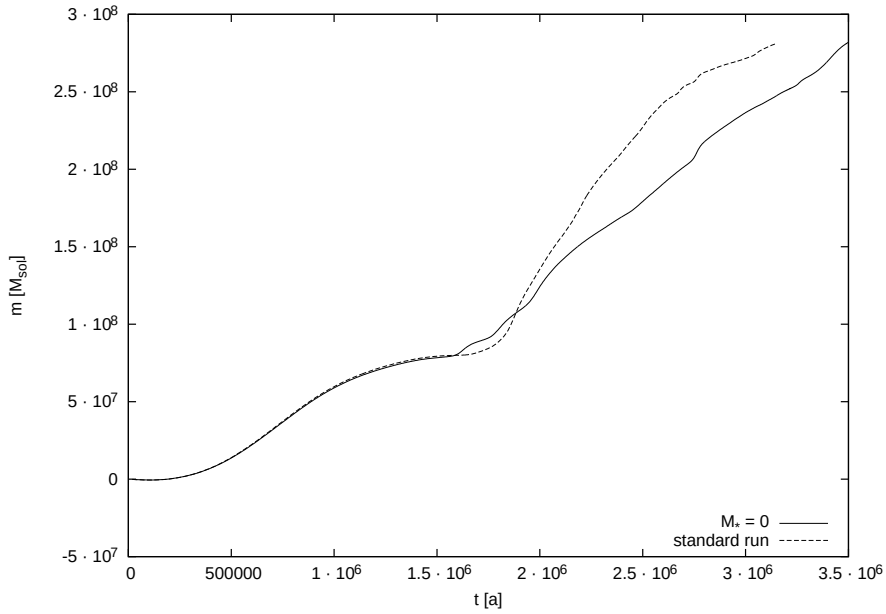

Figure 6.50: The mass in solar masses that passed the outer rim outwards versus time in years for run number 8 where $M_* = 0$ compared to the standard run where $M_* = 7.5{\cdot}10^7\,\mathrm{M}_\odot$.

6.3.6 Changing the cooling time

In simulation 9, the cooling time for the same conditions, mainly the same temperature and surface density, was reduced artificially by a factor of ten by dividing the effective optical depth by ten. The accretion at the inner boundary and the decretion at the outer boundary are plotted in Figures 6.51 and 6.52 with comparison to the standard run. From these plots we see that the accretion at the inner rim and the outflow at the outer rim do not change significantly. The only obvious difference is the stronger steps in the accretion in Figure 6.51.

In Figure 6.53 the temperature at $t = 1.8{\cdot}10^6$ a in run number 9 is plotted versus the radius as the solid line. The dashed line is the same for the standard run as in Figure 6.21(b). We see that the temperature is hardly different for the two runs; maybe it is a small factor (say 1.2) lower in run number 9. The cooling time as well as the cooling time per dynamical time scale is depicted in Figures 6.54 and 6.55, the solid line for run number 9 and the dashed line for the standard run. Both values seem to be about a factor of five lower in the run with the reduced cooling time.

As in Section 6.3.3 using Equation (6.6), we can estimate the prediction for the viscous time scale for the α-disk interpretation. The accretion time scale does not change when changing the cooling time (see Figure 6.51). From the above estimates for the changes in T and $t_{\mathrm{cool}}\Omega$, we see that the α-viscosity in this form predicts the accretion time scale to change by a factor of four.

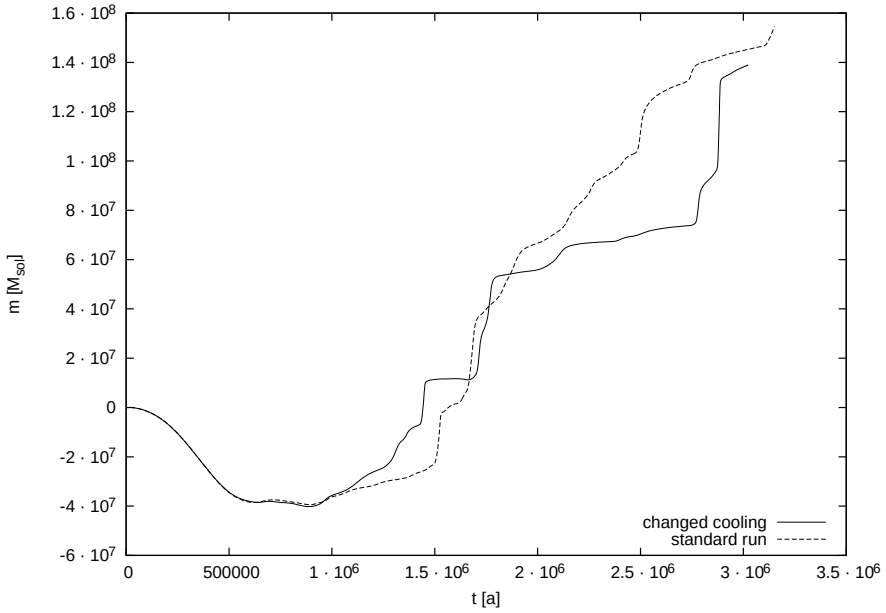

Figure 6.51: The mass in solar masses that passed the inner rim inwards versus time in years for run number 9 with changed cooling and the standard run. The two curves behave very similarly except for the steps which are much more pronounced in the case of stronger cooling.

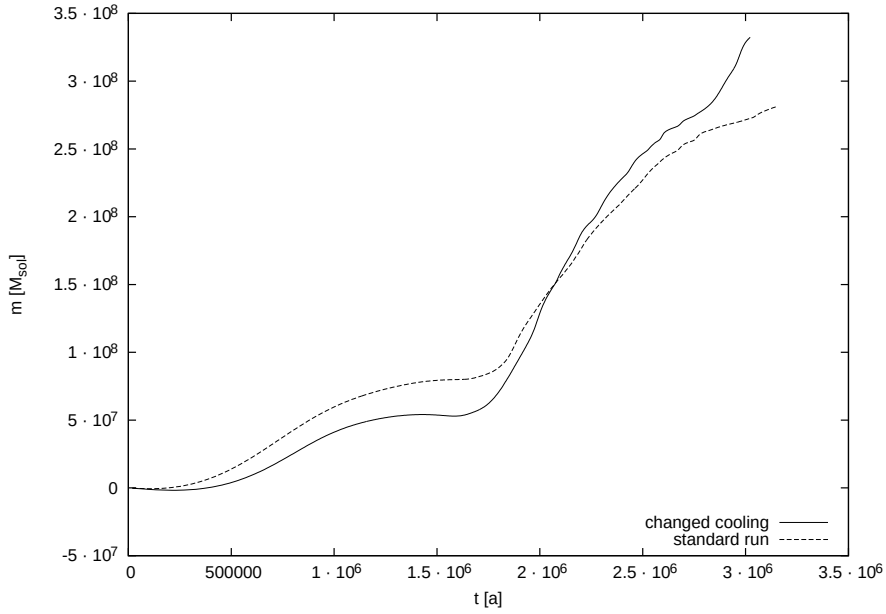

Figure 6.52: The mass in solar masses that passed the outer rim outwards versus time in years for run number 9 with changed cooling and the standard run.

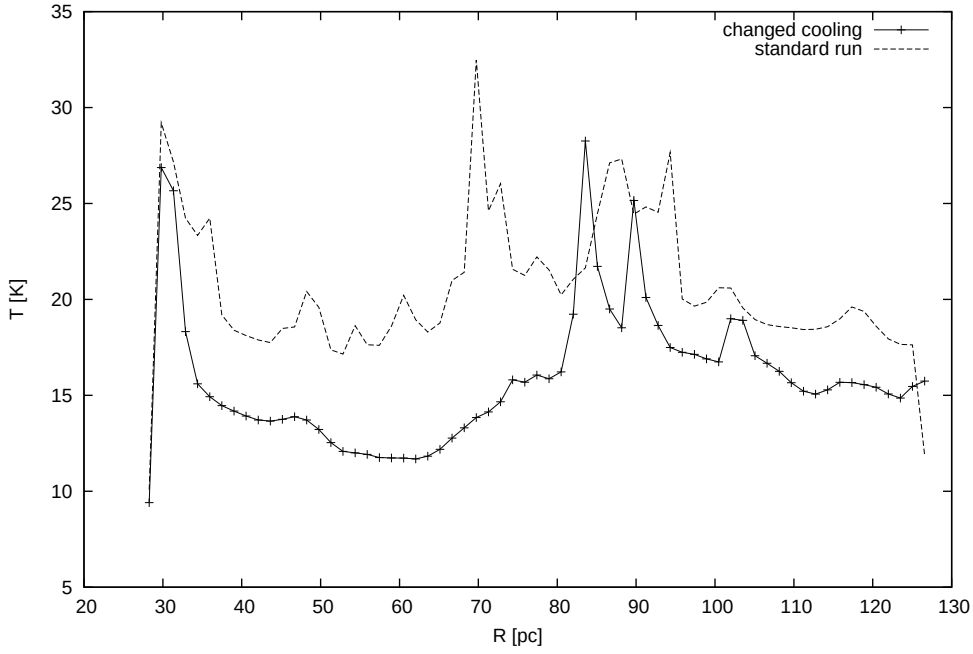

Figure 6.53: The azimuthal average of T in Kelvin versus radius in pc for the run number 9 with changed cooling at $t = 5.8{\cdot}10^{13}\,\mathrm{s} = 1.8{\cdot}10^{6}\,\mathrm{a}$. The dashed line corresponds to Figure 6.21(b).

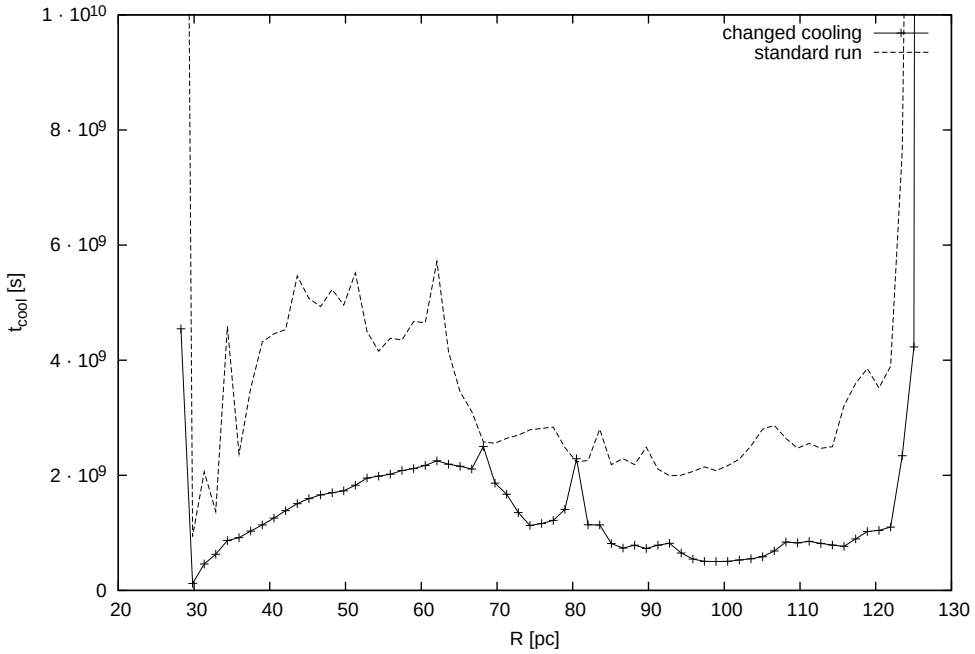

Figure 6.54: The same as in Figure 6.53 but the azimuthal average of the cooling time in seconds. The dashed line is the same as in Figure 6.26(b).

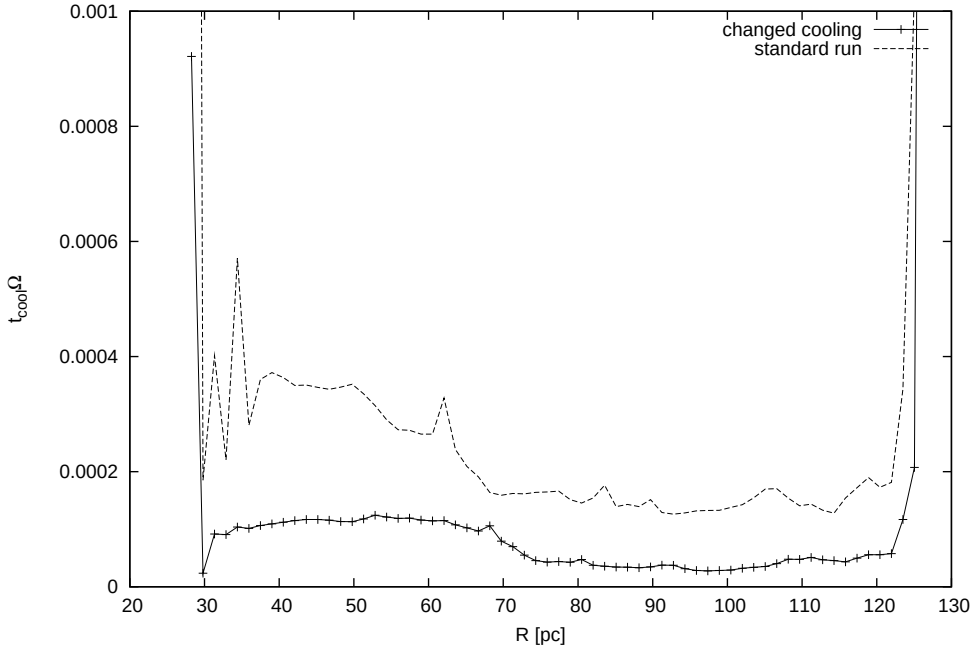

Figure 6.55: Same as Figure 6.53 but for the azimuthal average of the cooling time multiplied by the angular velocity. The dashed line is the same as in Figure 6.27.

6.3.7 Including heating by the CMB

In run number 10 the minimal temperature was set to the temperature of the CMB at $z = 10$, *i.e.*, $(z + 1)T_{\rm CMB} = 30\,{\rm K}$ (where $T_{\rm CMB}$ is today's value). In Figures 6.56 and 6.57, the accretion at the inner boundary and the decretion at the outer boundary of the calculation domain is plotted where the solid line is run number 10 and the broken line is the standard run. The differences are very small. The curve for run number 10 ends early due to CPU-time restrictions.

Figures 6.58 to 6.60 show the azimuthal average of the temperature, the cooling time and the cooling time per dynamical time scale for this run (solid line with +-symbols) in comparison to the standard run (dashed line with ×-symbols). We see that the temperature is about a factor of 1.5 higher when including the CMB and the cooling time and the cooling time per dynamical time scale is about a factor of 15 lower. This means, using the same reasoning as in Sections 6.3.3 and 6.3.6, that the accretion time scale should be by a factor of more than 20 different in the α-viscosity interpretation. We have just seen above that the accretion time scale is the same as in the standard run.

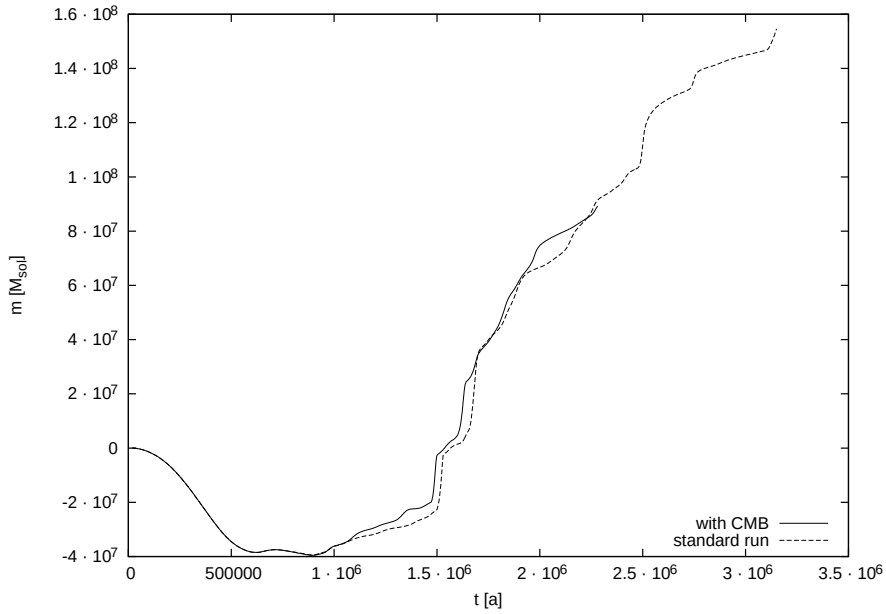

Figure 6.56: The mass in solar masses that passed the inner rim inwards versus time in years for run number 10 where a minimal temperature of 30 K was set compared to the standard run.

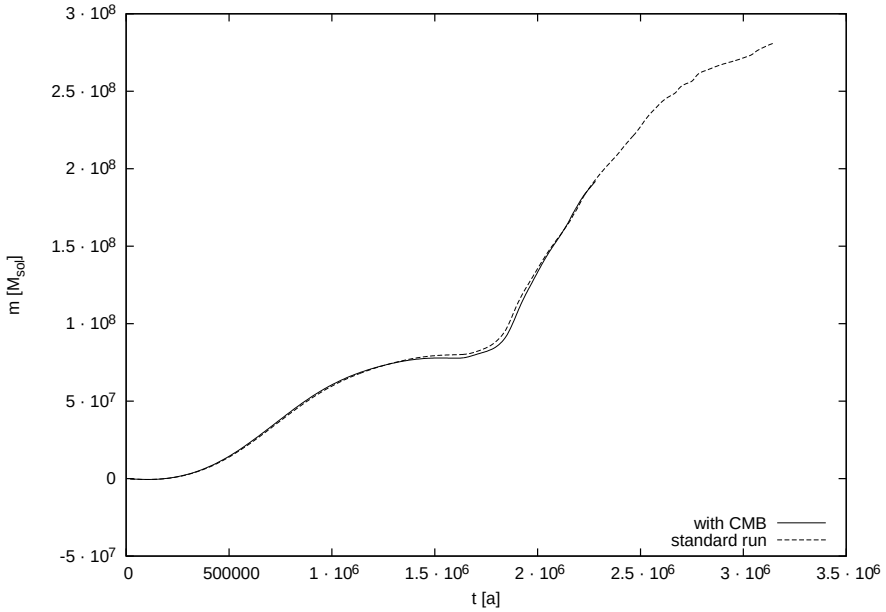

Figure 6.57: The mass in solar masses that passed the outer rim outwards versus time in years for run number 10 where a minimal temperature of 30 K was set compared to the standard run.

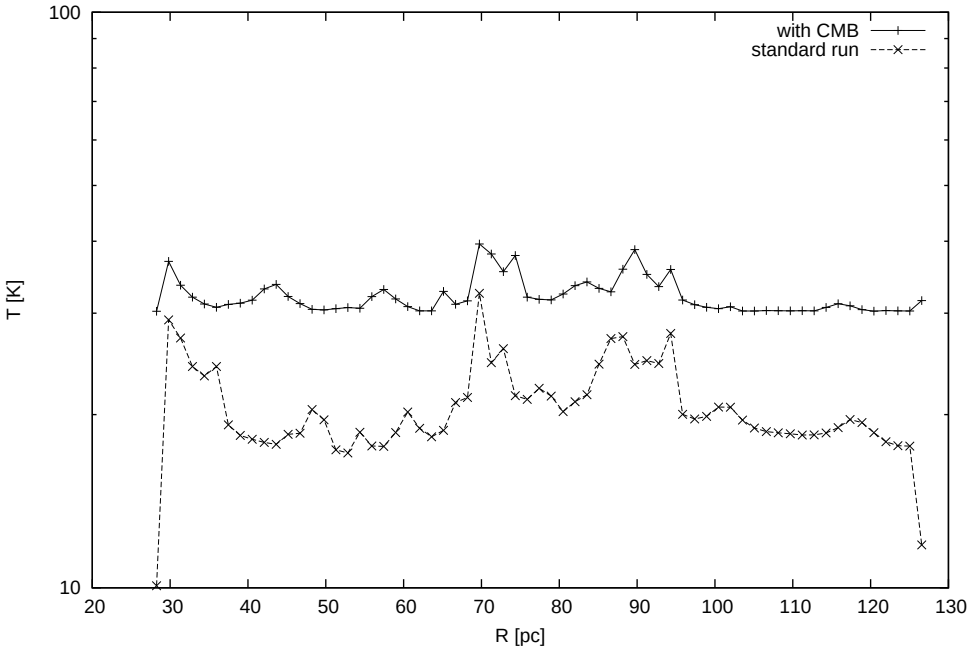

Figure 6.58: The azimuthal average of T in Kelvin plotted versus radius in pc for run number 10 with a minimal temperature of 30 K at $t = 5.8{\cdot}10^{13}\,\mathrm{s} = 1.8{\cdot}10^{6}\,\mathrm{a}$. The dashed line corresponds to Figure 6.21(b).

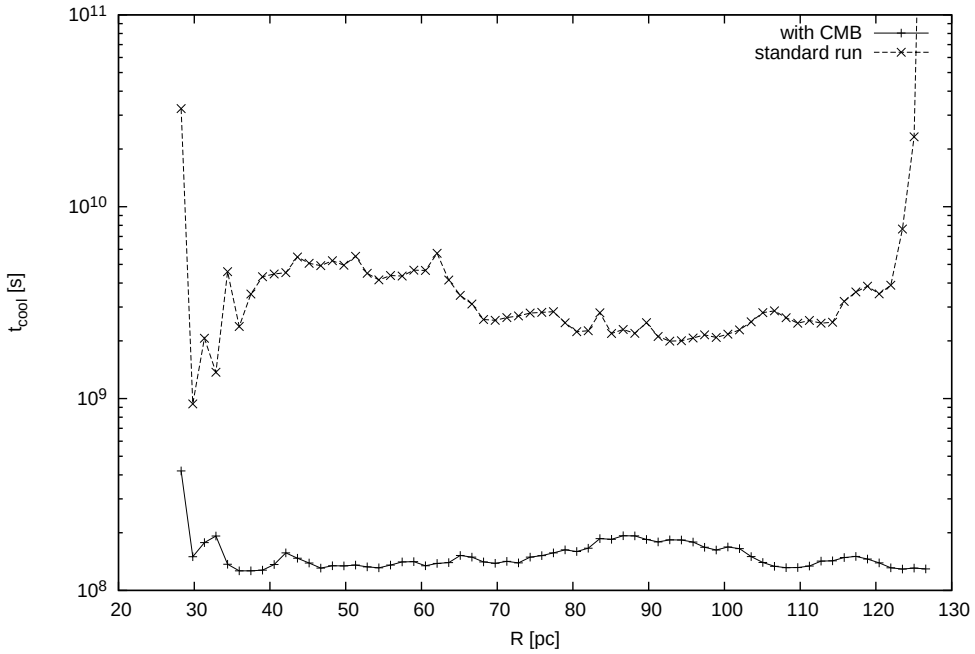

Figure 6.59: Same as Figure 6.58 but for the azimuthal average of the cooling time in seconds. The dashed line is the same as in Figure 6.26(b).

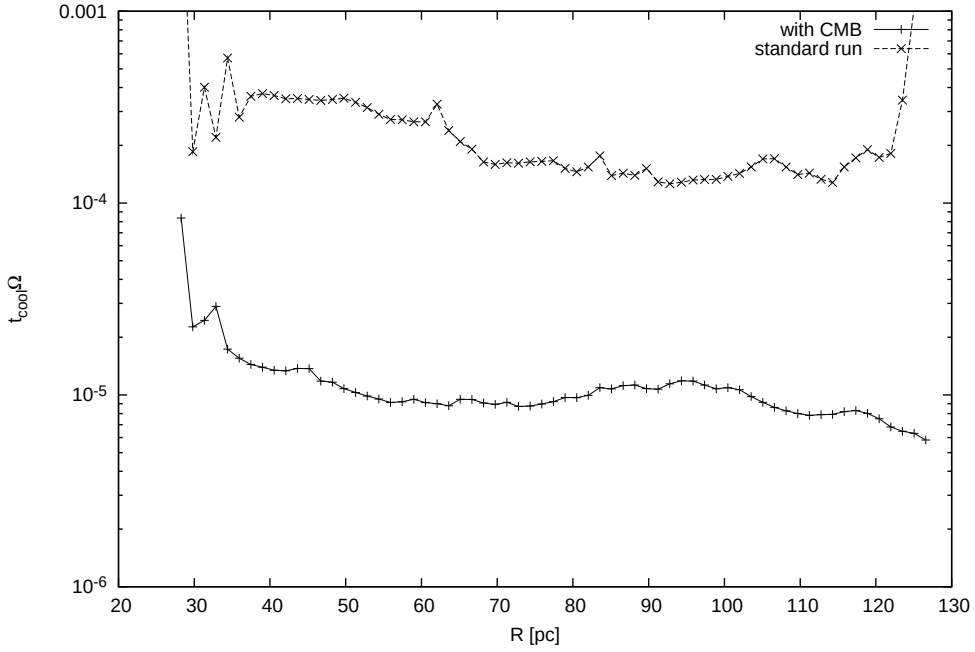

Figure 6.60: Same as Figure 6.58 but for the azimuthal average of the cooling time multiplied by the angular velocity. The dashed line is the same as in Figure 6.27.

6.3.8 Changing γ and μ

In simulation 11 γ and μ were held at $\gamma = \frac{5}{3}$ and $\mu = 0.001\,\mathrm{kg\,mol^{-1}}$, *i.e.*, the atomic values, throughout the simulation and they were not changed to the molecular values where $T < 2000\,\mathrm{K}$ as in the other runs. From Figure 6.23 we see that this affects almost the whole disk. In Figures 6.61 and 6.62 again the accretion at the inner rim and decretion at the outer rim is plotted for run number 11 (solid line) and the standard run (dashed line). The differences in both plots are small.

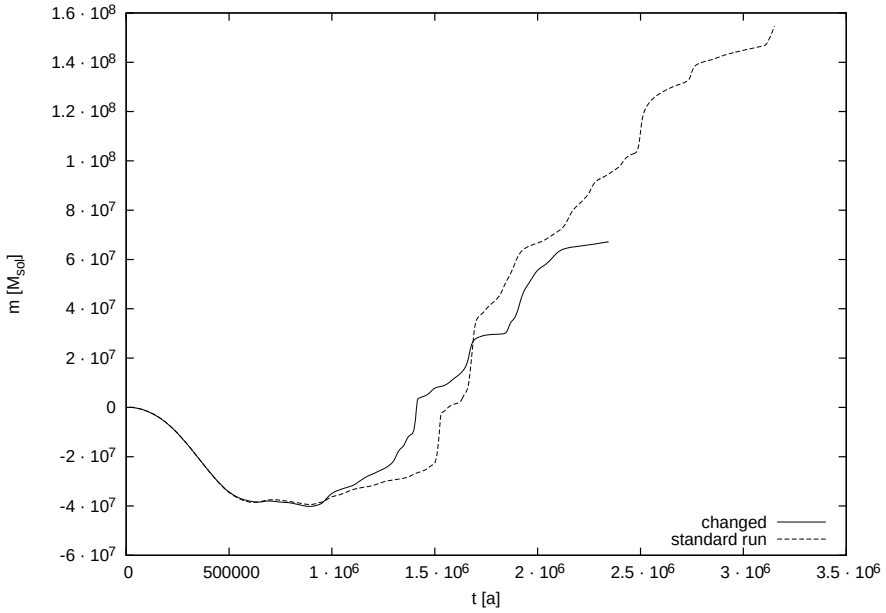

Figure 6.61: The mass in solar masses that passed the inner rim inwards versus time in years for run number 11 where γ and μ were held at the atomic values compared to the standard run.

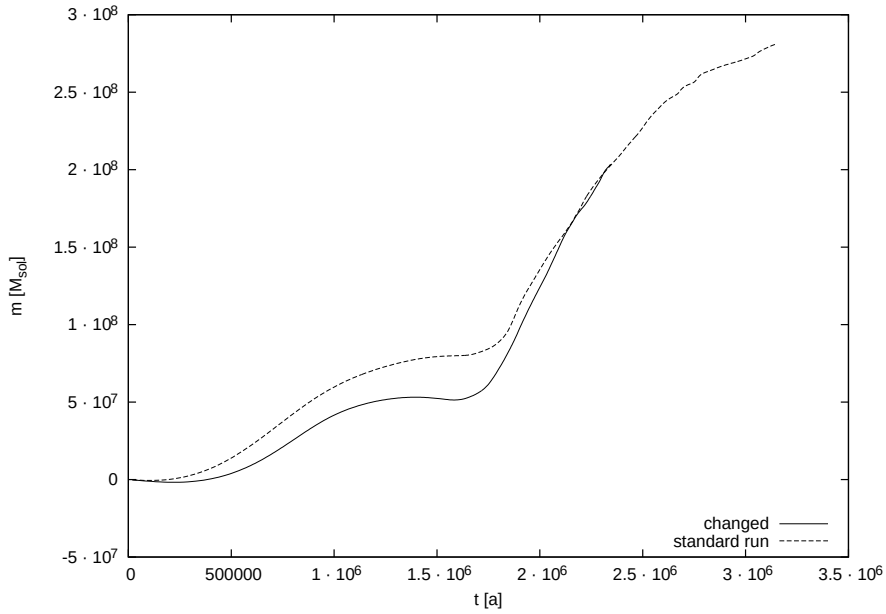

Figure 6.62: The mass in solar masses that passed the outer rim outwards versus time in years for run number 11 where γ and μ were held at the atomic values compared to the standard run.

Chapter 7

Discussion

7.1 Quality of these models

Of course some approximations had to be made in our model. Nevertheless these calculations seem to give some robust results. In the last chapters we have seen that one main result of the model has never changed no matter what parameter we had changed. This result was the high accretion rate at the inner boundary of our calculation domain and the high decretion rate at its outer boundary. In this section we are revisiting some of these parameter changes to see how sensitively the system has reacted to them and how this can affect the conclusions.

7.1.1 Numerical issues

The z-profile and h

As described in Section 4.1.2 the height profile is not always known exactly. Even in the simple case where the z-profile for the local fully self-gravitating case is calculated, this is done under the assumption of an isothermal gas which is probably not completely accurate. Nevertheless with such a thin disk and such low resolution in the z-direction, the deviations cannot be very important.

Similar arguments hold for the height of the disk. But there is an additional issue which is the problem of having the correct Φ boundary condition at $z = z_{\max}$. This can lead to an incorrect potential if the height of the disk is larger than $z_{\max}$ for a high-density region as we have seen in Sections 4.3.3 and 5.2. We have seen in Section 6.2.1 that the heights of the high-density regions have always stayed below $z_{\max}$.

Resolution

We have seen already in Section 5.1 that the simulations are unable to follow the fragmentation correctly due to the resolution. This becomes more serious as the viscosity is reduced and smaller clumps form. On the other hand we were also able to show that a factor of two in resolution does not change the accretion and decretion behavior of the disk. Nevertheless it is reasonable that a higher resolution will possibly reduce the accretion rate since the eddies then have the chance to decrease in size. In the turbulent viscosity picture this would reduce

the viscosity as follows from Equation (2.60). Nevertheless the results are all consistent and agree well with the β-viscosity interpretation (see more about this below). The technical problem with high resolution is of course primarily large CPU-time.

Boundary conditions

As stated in Section 6.1.3 where the boundary conditions are described, the boundary conditions are rather arbitrary and are chosen in a way not to produce spurious flows and clumps at the boundary.

One could argue that the boundary condition that decreases the mass of the inner disk when material is decreted from it at the beginning of a simulation decreases the density and with it the pressure at the boundary, introducing a pressure gradient that sucks the gas into the inner disk and leads to the rapid accretion. But as we have seen in Section 6.2.3 the accretion is mainly due to the clumps, and it continues at the end of the simulations when the density at the inner boundary is orders of magnitude higher than in the disk.

Towards the end of a simulation the boundary conditions for the gravitational potential must become incorrect at some point. The reason is already stated in Section 6.2.1, the mass that dominates the dynamics gravitationally is the mass of the inner disk towards the end of a run. This mass is thought to be spread equally in a disk of radius R_i which is of course a reasonable oversimplification as long as the mass of the inner disk does not dominate the dynamics. This was the reason why the runs were mainly stopped around $t = 3{\cdot}10^6$ a. Already around $t = 2{\cdot}10^6$ a, the radial angular velocity profiles change as shown in Section 6.2.1. Thus to be conservative, the last one million years are not taken into account which does not change the main results of the model,*i.e.*, the strong accretion, if we look at Figure 6.29. A similar argument can be put forward about the correctness of the height calculation towards the end of a simulation since it depends on the disk being fully self-gravitating. Even when the inner disk dominates gravity the height should be calculated approximately correctly since in that case, the gravitational influence of the inner disk is taken into account in the calculation of the height (see Sections 4.1.2 and 4.2.4).

Oscillations in the radial velocity

As already mentioned in Section 4.1.2, the balance between gravitational attraction and centrifugal forces are numerically demanding since it is a subtraction of two very similar large values. This leads to spurious fluctuations in the radial velocity when the flow is in the balance of gravity and centrifugal forces. In Figure 7.1 the radial velocity versus cell number is shown in the case of $M_* = 10^{10}\,\mathrm{M}_\odot$, no self-gravity, no physical or artificial viscosity and initial conditions such that the flow is Keplerian, *i.e.*, in balance. The radial range is the same as in the models used before. The fluctuations have amplitudes of up to about $60\frac{\mathrm{m}}{\mathrm{s}}$. Since this scales with the central mass, these kinds of fluctuations are smaller in our simulations because we used a maximal value of $M_* = 6{\cdot}10^9\,\mathrm{M}_\odot$. In addition the artificial viscosity damps the fluctuations. Finally the amplitude is much smaller

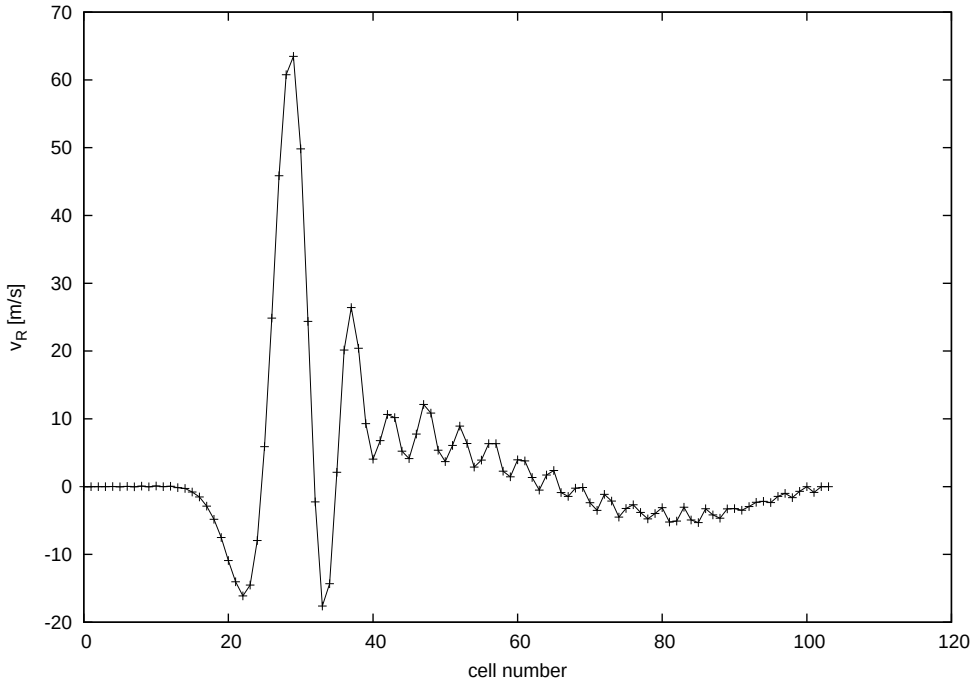

Figure 7.1: The radial velocity in $\mathrm{m\,s^{-1}}$ versus cell number for a run with no self-gravity, no physical or artificial viscosity and a central object mass of $10^{10}\,\mathrm{M_\odot}$. The radial range is the same as in the models of Chapter 6, *i.e.*, 29 pc to 126 pc. The initial conditions are such that $v_R = 0$ and the flow is Keplerian. The radial velocities come from the numerical problem of subtracting similar large numbers which are the gravitational force and the centrifugal force in this case.

than the typical radial velocity in our simulations as shown in Figure 6.5 with even higher velocities at later times (see Figure 6.12). We conclude that such fluctuations do not change the results of the simulations.

Advection at the $\varphi = 0$ boundary

As stated already in Section 4.1.1, there is an imperfection for the angular momentum transport at the $\varphi = 0$ boundary of the calculation domain if the transport is in the positive direction. This problem is the reason why the disk is set to rotate in the negative direction. Unfortunately, the flow becomes turbulent and there are even small regions where the azimuthal velocity becomes positive as can be seen in Figure 7.2 where v_φ is plotted for the standard run at $t = 1.8{\cdot}10^6\,\mathrm{a}$, and the dashed line shows the contours of $v_\varphi = 0$. The third upstream cell gives only a minor correction, the problem occurs only at the $\varphi = 0$ boundary and no anomalies were observed at this boundary. Thus we conclude that this cannot influence the overall results of our simulations.

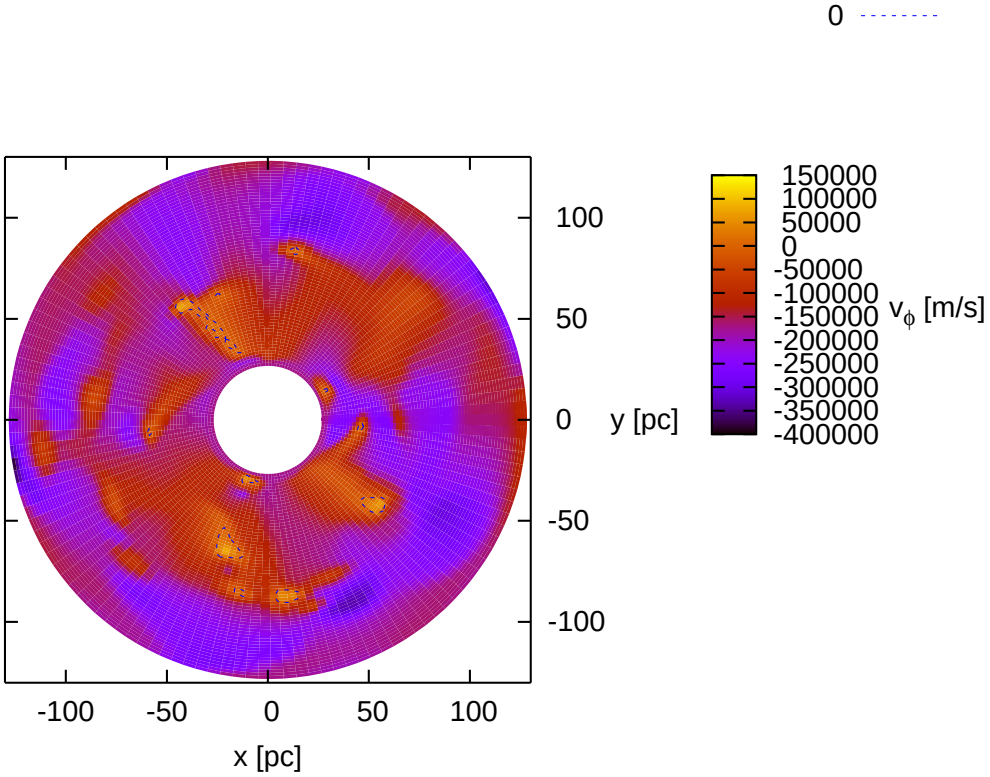

Figure 7.2: The decadic logarithm of the azimuthal velocity in $\mathrm{m\,s^{-1}}$ is plotted for $t = 5.6{\cdot}10^{13}\,\mathrm{s} = 1.8{\cdot}10^{6}\,\mathrm{a}$. The dotted line encloses regions where $v_\varphi > 0$. When such a region passes the $\varphi = 0$ boundary, there might be small imperfections in the angular momentum transport.

7.1.2 Physical issues

Additional heating and star formation

We could show in Section 6.3.7 that heating by the CMB at a redshift of $z = 10$ to $T = 30\,\mathrm{K}$ does not change our main results. Another question would be the heating by hot stars and supernovae that come about due to star formation in the clumps. This can heat up the gas much more and it could in principle change some of our results. It probably would not puff up the disk so that it would become gravitationally stable as we will show in Section 7.1.3. In addition, the supernovae would also introduce more turbulent dynamics. This could also lead to stronger radial and vertical outflows that could affect the accretion.

The third dimension

Our simulations are conducted in two dimensions only. Even when starting from a very thin disk, the clumps that form in it would also scatter into the third dimension when interacting[1]. This is definitely an interesting possibility; but on the other hand, since the disk is very thin, the clumps would need many interactions to give a large effect. Since the clumps have only a few interactions per dynamical time scale and our standard run ran for less than 6 dynamical time scales, the effect would probably be relatively small or only important towards the end of the lifetime of the disk.

Thermal equilibrium

The cooling and the thermodynamics of our simulations are done under the implicit assumption of thermodynamic equilibrium. Here we make a rough estimate to see whether thermal equilibrium is given in the coolest, least dense regions in the standard simulation where there is a chance that it is violated. The thermal equilibrium is given if the typical collision time of the molecules t_{coll} is much smaller than the typical evolution time of the system. First we note from Figure 6.17 that the least dense regions have $\rho \sim 10^{-18}\,\mathrm{kg\,m^{-3}}$ and from Figure 6.23 $T > 1\,\mathrm{K}$ which gives $c_{\mathrm{s}} \sim 60\,\mathrm{m\,s^{-1}}$ using the ideal gas law and $c_{\mathrm{s}}^2 = \frac{P}{\rho}$ with a molecular mean molar weight. With a rough estimate of the collision cross section for a hydrogen molecule or atom of

$$\sigma_{H_2} \sim \pi a_0^2 \approx 0.05\,\mathrm{nm} = 2.5{\cdot}10^{-21}\,\mathrm{m}^2, \tag{7.1}$$

where a_0 is the Bohr radius, we can estimate the mean free path

$$l = \frac{1}{n\sigma_{H_2}} \sim 1.4{\cdot}10^{12}\,\mathrm{m} = 4.7{\cdot}10^{-5}\,\mathrm{pc}. \tag{7.2}$$

Here we used the number density $n = \frac{\rho}{m_{H_2}} = 2.9{\cdot}10^{9}\,\mathrm{m^{-3}}$ with the lower bound for the density from above and a hydrogen molecule mass of $m_{H_2} = 2m_H$ with $m_H = 1.7{\cdot}10^{-27}\,\mathrm{kg}$ being the mass of a hydrogen atom. From this we already see that the mean free path is much smaller than the typical size in our model.

[1] I thank Prof. Dr. Mitchell C. Begelman for pointing this out to me.

Looking at Figure 6.18 where the height in the disk is plotted, which is usually the smallest extent by far, we can see that it can be as small as the mean free path. Those values are reached in high-density regions while in low-density regions the height is always orders of magnitude larger than 10^{-4} pc. Thus one of the main prerequisites for using hydrodynamics and for the hydrostatic equilibrium, *i.e.*, that the mean free path is much smaller than the smallest extent of the calculation domain is given everywhere in the disk.

Coming back to the thermal equilibrium, we need

$$t_{\mathrm{coll}} = \frac{l}{v_{\mathrm{k}}} \approx \frac{l}{c_{\mathrm{s}}} = 2.3{\cdot}10^{10}\,\mathrm{s}, \tag{7.3}$$

where v_{k} is the kinematic velocity of the gas particles which is approximated by the speed of sound. This number is orders of magnitude smaller than the dynamical time scale of $1.7{\cdot}10^{13}$ s of our models. Looking at Figure 6.28 we see that the cooling time for low density regions is mainly of the order of 10^{10} s to 10^{12} s. Thus we cannot guarantee thermal equilibrium for all parts of the disk. On the other hand, it can only be violated in the coolest, least dense regions that are scarce and not the most relevant for our model.

Material constants and optical depths

As shown in Section 6.3.2 a viscosity parameter change of almost two orders of magnitude does change the details of the fragmentation, but it does not change the main, *i.e.*, the strong accretion at the inner boundary and the decretion at the outer boundary. Even the differences in Figure 6.35 where the curves for the simulation with $\beta = 0.01$, and to a less extent that with $\beta = 0.005$, lie somewhat higher than the others, might be explained by the fact that $\beta = 0.01$ is already close to $\beta_{\mathrm{grav}} \approx 0.04$ which we got for the accretion in Section 6.2.3. The two values of the same order of magnitude could change the dynamics.

The choices of $\mu = 0.001\,\mathrm{kg\,mol^{-1}}$ in the atomic case and $\mu = 0.002\,\mathrm{kg\,mol^{-1}}$ in the molecular case as well as the jump from a molecular to an atomic state at $T = 2000\,\mathrm{K}$ are of course relatively crude. There are more realistic numbers for μ depending on the ionization and molecular state etc. but as stated before, the physics of molecule destruction and creation are very complex and so we decided to stick to these relatively crude values and method. In addition, the ratio of specific heats and the molar weight have been changed radically in Section 6.3.8 for the molecular case and thus for almost the whole disk but the accretion and decretion were not really different.

The mean opacities for our disk are similarly uncertain and again they are only used in some approximate form as described in Section 4.6. In addition, the used prerequisite of thermal equilibrium might not be given as we have seen above. On the other hand in Section 6.3.6, we could show that the main result does not change even when changing the cooling time by a factor of ten. Therefore we cannot fully rely on the details of the cooling, but this does not change our qualitative results.

7.1.3 Issues with prerequisites

It was previously stated in Section 2.5 that the gravitational instability of the outer parts of quasar disks is a known problem and also that there are some observations which can be explained by thin self-gravitating disks. We have also seen in the same section that the disk must be thick ($h \gtrsim \frac{1}{3}R$) to be stable. Thus our presumption that the disk is thin is not unreasonable. In addition, we calculate heating, cooling and the height of the disk and we see that indeed it stays thin (see Section 6.2.1). What if there was additional heating, *e.g.*, by star formation? What temperature do we need to make the disk marginally stable? If we require $Q = \frac{c_\mathrm{s}\kappa}{\pi G\Sigma} = 1$, we get

$$T \approx 1.2{\cdot}10^{-4} c_\mathrm{s}^2 = 1.2{\cdot}10^{-4}\left(\frac{\pi G\Sigma}{\kappa}\right)^2 \approx 5{\cdot}10^5\,\mathrm{K} \tag{7.4}$$

using the same relations for c_s as above. We took the following values from the plots in Section 6.2.1: $\Sigma \approx 30\,\mathrm{kg\,m^{-2}}$ and $\kappa \approx \Omega \approx 10^{-13}\,\mathrm{s^{-1}}$. It is hard to imagine a physical process that heats the whole disk to $5{\cdot}10^5\,\mathrm{K}$ at such a long distance from the quasar (which is not necessarily there yet). On the other hand, maybe the disk becomes only stable locally. The star formation that can heat the gas would occur at the clumps; but near and at their location Σ is higher than $30\,\mathrm{kg\,m^{-2}}$. Even for a value of $\Sigma = 100\,\mathrm{kg\,m^{-2}}$, which is almost two orders of magnitude below the maximal value in Figure 6.16, the required temperature for stability is $5{\cdot}10^6\,\mathrm{K}$. So it seems unrealistic that large parts of the disk can become stable.

It can also be shown that the instability of thin fully self-gravitating gas disks is not contradicted by the existence of thin galactic stellar disks as shown by Fuchs (2006). This is due to differences in the physics of gas and star dynamics and because of the existence of a dark halo in galaxies.

Although we could show in Section 6.3.4 that changing the radial Σ-profile at the beginning of the run does not change the qualitative result, we cannot exclude that significantly different initial conditions would give different results. And the initial conditions are obviously not known well, which leads to a phase of adjustment before the accretion at the inner boundary takes over. This adjustment is actually somewhat different when changing the initial conditions (see Figure 6.47, the first $1.5{\cdot}10^6\,\mathrm{a}$). In order to be conservative and to have a result independent of the details of the initial conditions, one would not take into account this first phase. As stated in Section 7.1.1, being conservative we do not trust the last $10^6\,\mathrm{a}$ either; therefore we stick to $10^6\,\mathrm{a} < t < 2{\cdot}10^6\,\mathrm{a}$ which still does not change our qualitative results.

7.2 Comparison with different predictions

7.2.1 The clumpy disk model

Although this model predicts the right scaling of the accretion time scale equal to $\frac{1}{\beta\Omega}$ with some constant β, we have seen in Section 6.2.3 that the order of magnitude does not come out right. This comes about since the proportionality

factor turns out to be $\beta = \frac{R}{l_c}\frac{M_R}{\pi M_t}$. $\frac{R}{l_c}$ is always larger than one and $\frac{M_R}{\pi M_t}$ cannot be much smaller than one either. So in this model, β can never really be smaller than unity which it obviously is.

7.2.2 α-viscosity

From Section 6.2.2, we know that the prediction of the α-disk interpretation that the temperature is constant with radius seems to be in agreement with our models. Actually for a self-gravitating α-disk, it is not the thermodynamic temperature of the disk that is constant with radius but the temperature of the radiation. The prediction that $t_{cool}\Omega$ is constant with R is not fulfilled very well but still not completely wrong. We have tested the predictions for the accretion as introduced in Section 2.5 in different ways. First in Section 6.2.3 we could show that the prediction for the viscous time scale fits the value in the model well. This might only be a coincidence since we could show in Section 6.3.3 that when the disk mass is changed, the accretion time scale does not scale as the α-viscosity interpretation predicts; the factors are a factor of two off. Changing the cooling time artificially as done in Section 6.3.6 even shows that the accretion time scale does not change while it would do so in the α-viscosity interpretation by a factor of four. We observed in Section 6.3.7 that the heating by the CMB should change the accretion rate by a factor of 20 when it didn't change at all. All this taken together lets us conclude that the α-viscosity interpretation does not fit our models. The reasons are probably that first, the process is not local and second that the idea in Section 2.5 that the heating is mainly due to accretion and not fragmentation is not true. We conclude that the viscosity is not dependant on the heating time scale but on the dynamical time scale due to the clump-clump-interaction.

7.2.3 β-viscosity

In different sections we could show that the β-viscosity interpretation fits our results well. In Section 6.2.3 we showed that the accretion time scale gives a β-value that agrees with the value we got for the turbulent velocity which in turn agrees with the value for the turbulent length scale even in the case of higher or lower disk masses (see Section 6.3.3). Unfortunately, these values are orders of magnitude off compared to the value we got in Section 3.4 using the linear stability analysis. Then again as already argued in that section, this value is highly uncertain and thus the discrepancy is not serious although it is large. Then in Section 6.3.3 we have seen that the scaling of the accretion time scale with disk mass is well explained by the β-viscosity interpretation.

In Mejía et al. (2005) a self-gravitating protoplanetary disk with $\frac{M_*}{M_d} = 7.1$ and t_{cool} = constant was simulated. If we use Equation (3.61), replacing the value $6.5{\cdot}10^{-5}$ which is highly uncertain with $\beta_{grav} = 0.04$ from Section 6.2.3, we can predict the β-value for this disk which gives $\beta_{predict} = 6.1{\cdot}10^{-4}$. On the other hand for the run they did where the cooling time was smaller than three dynamical time scales we get $\beta_{mejia} = 1.9{\cdot}10^{-4}$ by using Equations (2.88) (with $\delta = 3$ for Keplerian flow) and (2.58). This is a factor of about three off which is not too bad

regarding the uncertainties. The values from the papers used are for $R = 20\,\mathrm{AU}$: $\dot{M} = 4{\cdot}10^{-6}\,\mathrm{M}_\odot\,\mathrm{a}^{-1}$, $\Sigma = 1000\,\mathrm{kg\,m^{-2}}$ and $v_\varphi = 470\,\mathrm{m\,s^{-1}}$. For the runs where the cooling time is much larger than three times the dynamical time scale, they get accretion rates that are lower and dependant on the cooling. It would be interesting to see runs with different cooling times for the same model which all are smaller than three times the dynamical time scale. A strong dependence of the accretion rate on the cooling time would rule out the β-viscosity interpretation for these disks and strengthen it otherwise. Summarizing it seems that the β-viscosity interpretation can describe self-gravitating accretion in the case that the cooling time is smaller than three dynamical time scales.

Interestingly for the β-viscosity arising from gravitational instability, the dissipation limit does not exist as expected in Section 3.4 since the turbulent velocity (see, *e.g.*, Section 6.2.1) was measured to be around $v_\mathrm{t} \sim 0.2 v_\varphi$ and the Mach number in the φ-direction was several hundreds. Thus the turbulence is highly supersonic.

7.3 Comparison with observations

We could not find direct observations of clumpy disks in literature, only models like in Kumar (1999) or Scoville et al. (1997) where clumpy disk models can fit the observations. The problem is still the resolution of the observations. The real massive disks of that kind which are in ultraluminous infrared galaxies like the one in Arp 220 examined by Scoville et al. (1997) and Scoville (1999) are far away (more than 100 Mpc in the case of Arp 220), and thus the resolution of the mm-observations is about 300 pc which is far too low to resolve the clumps. On the other hand, the disk lifetimes in our models are rather small and thus the probability of observing such a disk is relatively low.

In Scoville et al. (1997) the disk is actually thin in the sense that $h \approx 16\,\mathrm{pc}$ which is much smaller than the radius of 250 pc for which this was calculated, corresponding to $\frac{h}{R} = 0.064$. This is too thin for a fully self-gravitating disk to be stable (see Section 2.5) and indeed in this model, the disk is Toomre unstable at $R < 400\,\mathrm{pc}$. The disk is much thicker than our model disk with $0.02 > \frac{h}{R} > 10^{-6}$ depending on the surface density. The height of the Arp 220 disk was inferred using the velocity dispersion and the assumption that the clumps are in a hydrostatic equilibrium. In section 7.1.2, we have argued against the clumps being in hydrostatic equilibrium in the vertical direction to puff up the disk, so maybe that is the reason for the difference.

The measured velocity dispersion from Scoville et al. (1997) is $90\,\mathrm{km\,s^{-1}}$ which is of the same order of magnitude as in our models as can be seen in Figure 7.3 where the RMS of v_R (corrected by the mean v_R at each radius) is plotted in km s^{-1} for the $M_\mathrm{d} = 6{\cdot}10^9\,\mathrm{M}_\odot$ run. The mass of the disk in the Arp 220 model below $R = 130\,\mathrm{pc}$, *i.e.*, corresponding to our model, is about $2.5{\cdot}10^9\,\mathrm{M}_\odot$ which is between our standard and our most massive model.

Scoville et al. (1997) have also measured the temperature of the molecular disk which comes out to be about 50 K which lies between the mean temperatures of our standard (20 K) and the most massive model (100 K) which fits very well. On

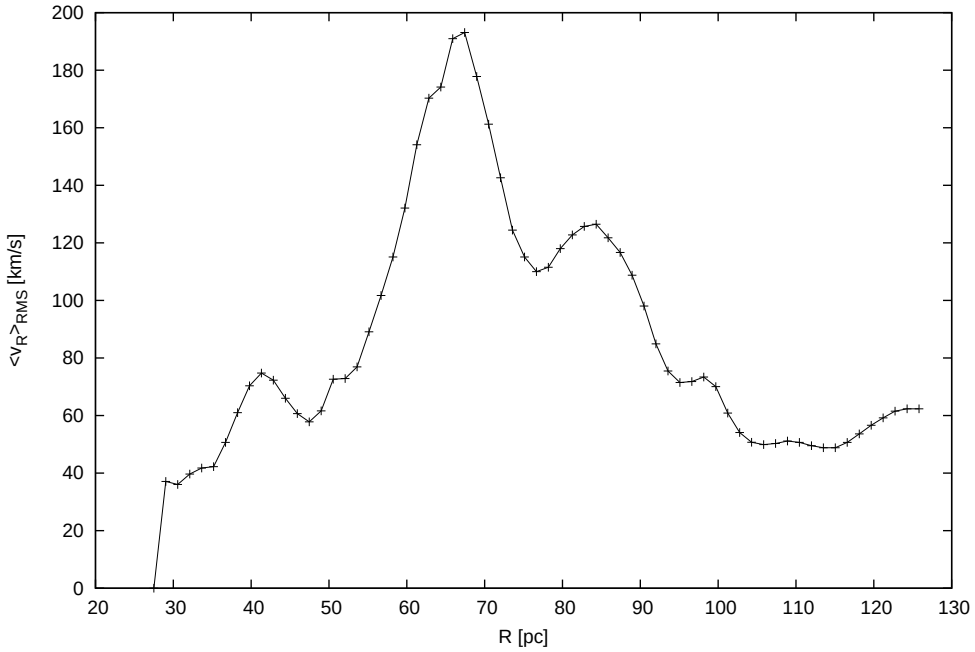

Figure 7.3: The azimuthal average of $\langle v_R \rangle_{\mathrm{RMS}}$ in km s^{-1} corrected by the mean radial velocity at each radius for the run with $M_{\mathrm{d}} = 6{\cdot}10^9\,\mathrm{M}_\odot$. The value is of the same order of magnitude as the value measured for Arp 220 of $90\,\mathrm{km\,s^{-1}}$.

the other hand they measure the filling factor of the molecular gas to be about 0.25 which seems very high compared to what one would estimate, *e.g.*, from Figure 6.16. The clumps which make up the material and are not volume filling might actually be mostly atomic and not molecular. Because the Arp 220 disk seems to be dominated by the molecular gas, such massive clumps of atomic gas are ruled out. Consequently there seems to be a discrepancy between the model and the observation in this point.

Nevertheless our model can indeed explain many of the observed properties of such disks.

7.4 The relevance of our model for the SMBH-formation model

First of all, the models in this work show an accretion whose time scale behavior fits that of the viscous time scale of the β-viscosity on which the SMBH-formation model relies.

As we have seen in Section 6.3.5 where a model with a central mass of $M_* = 0$ was presented, the accretion to the inner disk does not depend on the existence of a point mass at the center. This indicates that the SMBH-formation model of Section 1.3 can indeed not only account for the *growth* but also for the *formation* of SMBHs.

The time scales of the lifetime of such a disk are between a million and ten million years depending on its mass and are much shorter than expected. This

would mean that the time scale of the SMBH-formation would be dominated by the time scale of the galaxy merger and not by that of the disk accretion. Thus the disk accretion could not explain the anti-hierarchical growth of the SMBH (see Sections 1.1 and 1.3) if there was no massive mass flow onto the disk from outside. On the other hand as mentioned in Section 7.1.1, it is possible that the time scale would become larger for higher resolution.

Chapter 8

Conclusions and outlook

8.1 Summary and conclusions

In Chapter 3 we have examined the stability of viscous accretion disks using the linear stability analysis. We arrived at the results that even non-self-gravitating α-disks can become unstable under certain conditions. This is not the case if the turbulence that is responsible for the viscosity not only creates a shear but also creates a bulk viscosity of the same order of magnitude.

For thin fully self-gravitating β-disks, we have been able to show that they are gravitationally unstable. We have also been able to show that if this gravitational instability drives a viscosity, the β-ansatz for this viscosity is a consistent one.

From Chapters 5 and 6 where we ran 2D simulations of fully self-gravitating accretion disks, we have not only seen that these disks indeed become unstable and fragment but also that using any of the tested numerical and physical parameters for the models, we get a strong accretion at the inner rim of the simulation domain and a strong outflow at the outer rim. Although a dependence of the main results on resolution was not observed, the details of the fragmentation cannot be correct with such low resolution. The same is true for the not well constrained viscosity parameter. The accretion time scale for the $M_\mathrm{d} = 6{\cdot}10^8\,\mathrm{M}_\odot$ disk was of the order of $t_\mathrm{acc} \approx 1.2{\cdot}10^7\,\mathrm{a}$ which is much shorter than the time scale for the merger of the galaxies of about $10^8\,\mathrm{a}$ in which such a disk is created. In addition, by comparing runs with different disk masses, we found that the accretion time scale scales roughly with Ω^{-1} as predicted by the β-viscosity interpretation. The β-viscosity also correctly predicts the turbulent velocity and length scale with respect to the accretion time scale. Only the β-value derived from the accretion time scale differs by orders of magnitude from the prediction by the linear calculations, but the numbers of these are highly uncertain so this is not a contradiction. Possibly the β-viscosity can explain the accretion rate for any self-gravitating disk with $t_\mathrm{cool}\Omega < 3$.

The clumpy disk model on the other hand, although predicting correctly the Ω^{-1} dependence of the accretion time scale, does not give the correct accretion time scale derived from the clump and disk geometry. The α-disk interpretation indeed does a good job predicting the accretion time scale in the standard run. Rather, this turns out to be a coincidence since these predictions are wrong by a factor of 2 to 20 when using different disk masses, a changed cooling law or

including the CMB. So the β-viscosity interpretation is much more favorable.

The azimuthal average of the surface density, temperature and thus also the cooling time stay constant except for fluctuations when plotted versus radius. It is not clear why this comes about, but it is consistent.

We have been able to show that the SMBH-formation model described in Section 1.3 can indeed account for forming SMBHs without the need of a seed BH as well as growing them to the size at which they are observed.

Still missing is the star formation which will not only use up part of the gas in the disk but also heat it and introduce an additional turbulence. Due to the fragmentation, it is quite obvious that star formation will take place.

8.2 Outlook

From this it is obvious that a main point of future work will be the inclusion of star formation. An additional important point is to increase the resolution. To achieve this there are two possibilities that should be made use of. First the code should be parallelized to be run on several processors in parallel. In addition, the AMR method mentioned in Section 4.1.1 can be used. This technique is already included in NIRVANA2.0 although it is not tested for curved coordinate systems. The changes described in Chapter 4 would have to be rewritten accordingly.

It would be good to push the inner boundary of the calculation domain as far as possible to smaller radii in order to include the inner parts where the disk becomes Keplerian and to follow the clumps all the way down to the non-self-gravitating disk. To do this, it is necessary to change the z-profile calculation of ρ as well as that of the height of the disk for the Keplerian regime. Then one could also think about using this program to simulate protoplanetary disks; and to examine the accretion in the Keplerian case, with different cooling times in the regime where the cooling is smaller than three times the dynamical time scale as mentioned in Section 7.2.3.

Another interesting question that could be tackled using this code is that of the initial mass function of stars that are formed in circumnuclear disks. There are indications (see, *e.g.*, Nayakshin and Sunyaev, 2005) that the mass function of such stars might be shifted towards the high-mass end.

Appendix A

The movies on a CD

In this appendix, you will find a CD with movies created from the simulations. There are 11 directories on this CD, one for each simulation named accordingly. They contain movies in `avi` files in the `mpeg4` format. The file names start with "sigma", "T", "rho" or "velocity" for the movie showing the surface density, the temperature, the volume density and the velocity respectively. The physical time is always shown at the top of the movie. It is obvious that the frames are not equidistant in physical time but the time between two frames depends on the time step size in the simulation. When the movie slows down due to time step restrictions, the film showing the velocity features very high velocities at some location that are responsible for the small time step sizes. These extreme velocities appear at the same locations where extreme density gradients appear that are responsible for the convergence problems of the self-gravity algorithm.

Bibliography

V. A. Antonov and B. P. Kondratyev. On the oscillations and the stability of a uniformly rotating gaseous gravitating disc, including viscosity and heat exchange. *MNRAS*, **304**:759–766, 1995.

R. Antonucci. Unified models for active galactic nuclei and quasars. *Annu. Rev. Astron. Astrophys.*, 31:473–521, 1993.

I. V. Artemova et al. Structure of accretion disks with optically thick-optically thin transitions. *ApJ*, **456**:119–123, 1996.

S. A. Balbus and J. F. Hawley. A powerful local shear instability in weakly magnetized disks. I - Linear analysis. II - Nonlinear evolution. *ApJ*, 376:214–233, July 1991.

S. A. Balbus, J. F. Hawley, and J. M. Stone. Nonlinear Stability, Hydrodynamical Turbulence, and Transport in Disks. *ApJ*, 467:76–+, August 1996.

J. E. Barnes. Formation of gas discs in merging galaxies. *MNRAS*, 333:481–494, July 2002.

J. E. Barnes and L. Hernquist. Transformations of Galaxies. II. Gasdynamics in Merging Disk Galaxies. *ApJ*, 471:115–+, November 1996.

J. E. Barnes and L. Hernquist. Transformations of Galaxies. II. Gasdynamics in Merging Disk Galaxies: Addendum. *ApJ*, 495:187–+, March 1998.

A. J. Barth, P. Martini, C. H. Nelson, and L. C. Ho. Iron Emission in the z = 6.4 Quasar SDSS J114816.64+525150.3. *ApJL*, 594:L95–L98, September 2003.

M. C. Begelman, M. Volonteri, and M. J. Rees. Formation of Supermassive Black Holes by Direct Collapse in Pregalactic Halos. *ArXiv Astrophysics e-prints*, arXiv:astro-ph/0602363, February 2006.

K. R. Bell and D. N. C. Lin. Using FU Orionis outbursts to constrain self-regulated protostellar disk models. *ApJ*, 427:987–1004, June 1994.

G. Bertin and G. Lodato. A class of self-gravitating accretion disks. *A & A*, 350: 694–704, October 1999.

M. Biermann. *Akkretionsscheiben-Modelle mit einer verallgemeinerten, Reynolds-kritischen Turbulenz in aktiven galaktischen Kernen und um Protosterne*. PhD thesis, Universität Heidelberg, 2001.

J. Binney and S. Tremaine. *Galactic Dynamics*. Princeton University Press, first edition, 1987.

G. Bodo and A. Curir. Models of self-gravitating accretion disks. *A & A*, 253: 318–328, January 1992.

A. P. Boss. Possible Rapid Gas Giant Planet Formation in the Solar Nebula and Other Protoplanetary Disks. *ApJL*, 536:L101–L104, June 2000.

G. D. Chagelishvili, J.-P. Zahn, A. G. Tevzadze, and J. G. Lominadze. On hydrodynamic shear turbulence in Keplerian disks: Via transient growth to bypass transition. *A & A*, 402:401–407, May 2003.

J. Douglas, Jr. Alternating direction method for three space variables. *Numerische Mathematik*, **4**:41–63, 1962.

R. Durisen, A. Boss, L. Mayer, A. Nelson, T. Quinn, and K. Rice. Gravitational Instabilities in Gaseous Protoplanetary Disks and Implications for Giant Planet Formation. *ArXiv Astrophysics e-prints*, arXiv:astro-ph/0603179, March 2006.

W. J. Duschl and M. Britsch. A gravitational instability-driven viscosity in self-gravitating accretion disks, submitted to ApJL, 2006. Available as preprint: arXiv:astro-ph/0607610.

W. J. Duschl and P. A. Strittmatter. The Cosmogony of Super-Massive Black Holes. *ArXiv Astrophysics e-prints*, arXiv:astro-ph/0602009, February 2006.

W. J. Duschl, P. A. Strittmatter, and P. L. Biermann. A note on hydrodynamic viscosity and selfgravitation in accretion disks. *A & A*, 357:1123–1132, May 2000.

R. Ebert. The production of turbulence by gravitational instabilities in self-gravitating differentially rotating disks. *A & A*, 286:997–1005, June 1994.

G. Engeln-Müllges and F. Reutter. *Numerik-Algorithmen*. DVI Verlag, eighth edition, 1996.

K. Fathi, T. Storchi-Bergmann, R. A. Riffel, C. Winge, D. J. Axon, A. Robinson, A. Capetti, and A. Marconi. Streaming Motions toward the Supermassive Black Hole in NGC 1097. *ApJL*, 641:L25–L28, April 2006.

T. Fliessbach. *Allgemeine Relativitätstheorie*. Spektrum Akademischer Verlag GmbH, second edition, 1995.

J. Frank, A. King, and D. Raine. *Accretion Power in Astrophysics*. Cambridge University Press, third edition, 2002.

A. M. Fridman and V. L. Polyachenko. *Physics of Gravitating Systems II*. Springer-Verlag, first edition, 1984.

B. Fuchs. Private comunication, 2006.

H.-P. Gail. Private comunication, 2003.

C. F. Gammie. Linear Theory of Magnetized, Viscous, Self-gravitating Gas Disks. *ApJ*, 462:725–+, May 1996.

C. F. Gammie. Nonlinear Outcome of Gravitational Instability in Cooling, Gaseous Disks. *ApJ*, 553:174–183, May 2001.

P. Goldreich and D. Lynden-Bell. I. Gravatational stability of uniformly rotating disks. *MNRAS*, 130:97–+, 1965.

J. Goodman. Self-gravity and quasi-stellar object discs. *MNRAS*, 339:937–948, March 2003.

I. S. Gradshteyn and I. M. Ryzhik. *Table of integrals series and products*. Academic Press, sixth edition, 2000.

S. Grossmann. The onset of shear flow turbulence. *Reviews of Modern Physics*, 72:603–618, April 2000.

W. Hackbusch. *Multi-Grid Methods and Applications*. Springer-Verlag, first edition, 1985.

G. Hasinger, T. Miyaji, and M. Schmidt. Luminosity-dependent evolution of soft X-ray selected AGN. New Chandra and XMM-Newton surveys. *A & A*, 441: 417–434, October 2005.

C. Hirsch. *Numerical Computation of Internal and External Flows, Vol I*. John Wiley & Sons Ltd., first edition, 1988.

C. Hirsch. *Numerical Computation of Internal and External Flows, Vol II*. John Wiley & Sons Ltd., first edition, 1990.

I. Hubeny. Vertical structure of accretion disks: A simplified analytical model. *ApJ*, **351**:632–641, 1990.

J. H. Hunter and T. Horak. The development of structure in shearing, viscous media. II. *ApJ*, 265:402–416, February 1983.

J. H. Hunter and K. S. Schweiker. On the development of vorticity and waves in shearing media with preliminary application to the solar nebula. *ApJ*, 243: 1030–1039, February 1981.

T. Illenseer. *Zur Theorie von Scheibenwinden*, Diplomarbeit, Universität Heidelberg, 2002.

J. D. Jackson. *Classical Electrodynamics*. John Wiley & Sons, sixth edition, 1967.

B. M. Johnson and C. F. Gammie. Nonlinear Outcome of Gravitational Instability in Disks with Realistic Cooling. *ApJ*, 597:131–141, November 2003.

S. Kato and S. S. Kumar. The Gravitational Instability of an Infinite Homogeneous Medium having Viscosity and Thermal Conductivity. *Pub. Astro. Soc. of Japan*, 12:290–+, 1960.

R. Kippenhahn and A. Weigert. *Stellar Structure and Evolution*. Springer-Verlag, first edition, 1990.

P. Kumar. The Structure of the Central Disk of NGC 1068: A Clumpy Disk Model. *ApJ*, 519:599–604, July 1999.

S. S. Kumar. On Gravitational Instability, II. *Pub. Astro. Soc. of Japan*, 12: 552–+, 1960.

F. Kuypers. *Klassische Mechanik*. Wiley-CVH, fifth edition, 1997.

L. D. Landau and E. M. Lifshitz. *Fluid Mechanics*. Pergamon Press LTD., first edition, 1959.

G. Lesur and P.-Y. Longaretti. On the relevance of subcritical hydrodynamic turbulence to accretion disk transport. *A & A*, 444:25–44, December 2005.

R. J. LeVeque. Nonlinear conservation laws and finite volume methods. In R. J. LeVeque et al., editors, *Saas-Fee Advanced Course 27: Computational Methods for Astophysical FLuid Flow*. Springer, 1997.

D. N. C. Lin and J. E. Pringle. A viscosity prescription for a self-gravitating accretion disc. *MNRAS*, 225:607–613, April 1987.

G. Lodato and W. K. M. Rice. Testing the locality of transport in self-gravitating accretion discs. *MNRAS*, 351:630–642, June 2004.

G. Lodato and W. K. M. Rice. Testing the locality of transport in self-gravitating accretion discs - II. The massive disc case. *MNRAS*, 358:1489–1500, April 2005.

D. Lynden-Bell and J. E. Pringle. The evolution of viscous discs and the origin of the nebular variables. *MNRAS*, 168:603–637, September 1974.

W. D. MacMillan. *The Theory of the Potential*. Dover Publications, second edition, 1958.

M. Mayer. *Die Absorbtionseigenschaften primordialer Materie und ihre Anwendung auf die Struktur und Stabilität stationärer Akkretionsscheiben*. PhD thesis, Universität Heidelberg, 2004.

A. C. Mejía, R. H. Durisen, M. K. Pickett, and K. Cai. The Thermal Regulation of Gravitational Instabilities in Protoplanetary Disks. II. Extended Simulations with Varied Cooling Rates. *ApJ*, 619:1098–1113, February 2005.

L. Mestel. On the galactic law of rotation. *MNRAS*, 126:553–+, 1963.

S. Mineshige and M. Umemura. Self-similar Collapse of a Self-gravitating Viscous Disk. *ApJ*, 480:167–+, May 1997.

Y. N. Mishurov, V. M. Peftiev, and A. A. Suchkov. Instability of gravitating, rotating, viscous gaseous systems, and the origin of ring structure in galaxies. *Soviet Astronomy*, 20:152–+, April 1976.

S. Nayakshin and R. Sunyaev. The 'missing' young stellar objects in the central parsec of the Galaxy: evidence for star formation in a massive accretion disc and a top-heavy initial mass function. *MNRAS*, 364:L23–L27, November 2005.

C. R. O'dell, Z. Wen, and X. Hu. Discovery of new objects in the Orion nebula on HST images - Shocks, compact sources, and protoplanetary disks. *ApJ*, 410: 696–700, June 1993.

B. Paczyński. A model of selfgravitating accretion disk. *Acta Astronomica*, **28**: 91–109, 1978.

J. Papaloizou and J. E. Pringle. Tidal torques on accretion discs in close binary systems. *MNRAS*, **181**:441– 454, 1977.

W. H. Press et al. *Numerical Recipes in C*. Cambridge University Press, second edition, 1992.

J. E. Pringle. Accretion discs in astrophysics. *Annu. Rev. Astron. Astrophys.*, 19:137–162, 1981.

W. K. M. Rice, P. J. Armitage, M. R. Bate, and I. A. Bonnell. The effect of cooling on the global stability of self-gravitating protoplanetary discs. *MNRAS*, 339: 1025–1030, March 2003.

W. K. M. Rice, G. Lodato, and P. J. Armitage. Investigating fragmentation conditions in self-gravitating accretion discs. *MNRAS*, 364:L56–L60, November 2005.

D. Richard. *Instablités hydrodynamiques dans les écoulements en rotation différentielle*. PhD thesis, Université Paris VII, 2001.

D. Richard and J.-P. Zahn. Turbulence in differentially rotating flows. What can be learned from the Couette-Taylor experiment. *A & A*, 347:734–738, July 1999.

A. G. Riess, W. Li, P. B. Stetson, A. V. Filippenko, S. Jha, R. P. Kirshner, P. M. Challis, P. M. Garnavich, and R. Chornock. Cepheid Calibrations from the Hubble Space Telescope of the Luminosity of Two Recent Type Ia Supernovae and a Redetermination of the Hubble Constant. *ApJ*, 627:579–607, July 2005.

A. Sandu. A positive numerical integration method for chemical kinetic systems. *Journal of Computational Physics*, **170**:1–14, 2001. As a preprint taken from: `http://people.cs.vt.edu/~asandu/Deposit/positive_projection.pdf`.

U. Schmit and W. M. Tscharnuter. A fluid dynamical treatment of the common action of self-gravitation, collision, and rotation in saturn's b-ring. *Icarus*, **115**: 304–319, 1995.

N. Z. Scoville. Massive accretion disks. *Astrophys. and Space Science*, 266:149–155, 1999.

N. Z. Scoville, M. S. Yun, and P. M. Bryant. Arcsecond Imaging of CO Emission in the Nucleus of ARP 220. *ApJ*, 484:702–+, July 1997.

N. I. Shakura and R. A. Sunyaev. Black holes in binary systems. Observational appearance. *A & A*, 24:337–355, 1973.

G. D. Smith. *Numerische Lösungen von partiellen Differentialgleichungen*. Friedr. Vieweg + Sohn, first edition, 1970.

D. N. Spergel, R. Bean, O. Dore', M. R. Nolta, C. L. Bennett, G. Hinshaw, N. Jarosik, E. Komatsu, L. Page, H. V. Peiris, L. Verde, C. Barnes, M. Halpern, R. S. Hill, A. Kogut, M. Limon, S. S. Meyer, N. Odegard, G. S. Tucker, J. L. Weiland, E. Wollack, and E. L. Wright. Wilkinson Microwave Anisotropy Probe (WMAP) Three Year Results: Implications for Cosmology. *ArXiv Astrophysics e-prints*, arXiv:astro-ph/0603449, March 2006.

J. H. Spurk. *Strömungslehre*. Springer, 1996.

G. Stephenson. The gravitational instability of an infinite homogeneous rotating viscous medium in the presence of a magnetic field. *MNRAS*, 122:455–+, 1961.

G. I. Taylor. *Phil. Trans. Roy. Soc. London A*, 223:289, 1923.

G. I. Taylor. *Proc. Roy. Soc. London A*, 157:546, 1936.

A. G. Tevzadze, G. D. Chagelishvili, J.-P. Zahn, R. G. Chanishvili, and J. G. Lominadze. On hydrodynamic shear turbulence in stratified Keplerian disks: Transient growth of small-scale 3D vortex mode perturbations. *A & A*, 407: 779–786, September 2003.

A. Toomre. On the gravitational stability of a disk of stars. *ApJ*, 139:1217–1238, May 1964.

J. K. Truelove, R. I. Klein, C. F. McKee, J. H. Holliman, L. H. Howell, and J. A. Greenough. The Jeans Condition: A New Constraint on Spatial Resolution in Simulations of Isothermal Self-gravitational Hydrodynamics. *ApJL*, 489: L179+, November 1997.

W. M. Tscharnuter and K.-H. Winkler. A method for computing selfgravitating gas flows with radiation. *Computer Physics Communications*, 18:171–199, October 1979.

A. Unsöld and B. Baschek. *Der Neue Kosmos*. Springer Verlag Heidelberg, seventh edition, 2002.

S. Veilleux, D.-C. Kim, C. Y. Peng, L. C. Ho, L. J. Tacconi, K. M. Dasyra, R. Genzel, D. Lutz, and D. B. Sanders. A Deep Hubble Space Telescope H-Band Imaging Survey of Massive Gas-rich Mergers. *ApJ*, 643:707–723, June 2006.

M. Vestergaard. Early Growth and Efficient Accretion of Massive Black Holes at High Redshift. *ApJ*, 601:676–691, February 2004.

J. von Neumann and R. D. Richtmyr. A Method for the Numerical Calculation of Hydrodynamic Shocks. *J. Appl. Phys.*, 21:232–237, 1950.

F. Wendt. *Ing. Arch.*, 4:577, 1933.

Wolfram Research. *Mathematica5.1.* Wolfram Research, 2005.

U. Ziegler. Nirvana+: An adaptive mesh refinement code for gas dynamics and mhd. *Comp. Phys. Comm.*, **109**:111–134, 1998.

U. Ziegler. A three-dimensional cartesian adaptive mesh code for compressible magnetohydrodynamics. *Comp. Phys. Comm.*, **116**:65–77, 1999.

U. Ziegler. Nirvana2.0, `http://nirvana-code.aip.de/nirvana2.0.tar.gz` as of, October 2003.

Danksagung

Ich möchte meinem Betreuer Prof. Dr. Wolfgang J. Duschl danken für die interessante Aufgabenstellung und dass er mich hat eigenständig arbeiten lassen mir aber trotzdem immer mit Rat zur Seite stand wenn es nötig war. Dank bin ich ihm auch schuldig für die gute Arbeitsatmosphäre und seinen Einsatz bei der Finanzierung meiner Arbeit und der Stellensuche am Ende der Arbeit.

Ich danke Prof. Dr. Burkhard Fuchs für interessante fachliche Diskussionen und die Übernahme des Zweitgutachtens. Prof. Dr. Werner M. Tscharnuter, Prof. Dr. Hans-Peter Gail und Prof. Dr. Rainer Wehrse danke ich für hilfreiche und anregende Diskussionen.

Ich bedanke mich beim SFB 439 für die Teilfinanzierung meiner Arbeit.

Ich möchte mich auch bei Frau Anna Zacheus, Frau Ellen Jensen und Frau Martina Buchhaupt für die unkomplizierte Erledigung von Verwaltungsaufgaben und die freundliche Atmosphäre im Sekretariat bedanken.

Besonderer Dank gilt Dr. Christof Keller für seine Hilfe in der Anfangsphase meiner Arbeit. Auch Dr. Udo Ziegler möchte ich für seine Hilfe mit dem NIRVANA2.0-Code und meinem Aufenthalt in Potsdam danken.

Je veux dire merci à Dr. Franck Hersant pour des discussions astrophysique et non-astrophysique.

Danke auch an Dr. Michael Mayer für fachliche Diskussionen und die Hilfe und Gastfreundschaft in Cambridge. Also many thanks to Dr. Francesca de Angeli, Dr. Marco Riello, Dr. Jasinta Dewi, Dr. Marc Freitag, Dr. Bram Venemans and all the others in Cambridge for hospitality!

I would like to thank Dr. Giuseppe Lodato and Dr. Cathie J. Clarke for supervising me in Cambridge at the IoA and the Marie Curie Early Training Site program for funding my four month stay at the IoA.

Danke auch an Farid Gamgami für viele fachliche und nicht fachliche Diskussionen.

Ich danke der ganzen WJD-Arbeitsgruppe für das gute Arbeitsklima, interessante Diskussionen und die netten Kaffeepausen; insbesondere ein Dank an Jan Hofmann für den Tipp mit den eps-Dateien.

A big thank you goes to Lisa Kaufman for proofreading my thesis with regard to the language. Danke auch an Mario Verschl fürs Korrekturlesen.

Ganz besonderer Dank gilt Tobias Illenseer mit dem ich mein Büro teilen durfte. Danke für die Hilfe mit allem was mit Computern zu tun hat, Anregungen und Diskussionen zu meiner Arbeit und natürlich auch Gespräche über andere Themen. Es war sehr angenehm mit Dir das Büro zu teilen.

Danke an meinen Bruder Volker Britsch, der mir früh das Rechnen beigebracht

hat (mit dem Schreiben hat das nicht so funktioniert) und meine Faszination für Physik und Astronomie geweckt hat.

Und schließlich danke ich meinen Eltern Hanne und Axel Britsch für alles, was sie für mich getan haben. Darunter, dass sie früh meine Neugierde geweckt haben, dass sie mir immer meine Entscheidungsfreiheit gelassen und mir mein Studium ermöglicht haben.